TESIS DE LA UNIVERSIDAD DE ZARAGOZA

2025 209

Juan Román Roche

Large-n theories for Cavity-QED materials VERSIÓN CORREGIDA

Director/es
Luis Vitalla, Fernando
Zueco Lainez, David

ISSN 2254-7606

Prensas de la Universidad Universidad Zaragoza

Universidad de Zaragoza
Servicio de Publicaciones

ISSN 2254-7606

Universidad Zaragoza
1542

Tesis Doctoral

LARGE-N THEORIES FOR CAVITY-QED MATERIALS
VERSIÓN CORREGIDA

Autor

Juan Román Roche

Director/es

Luis Vitalla, Fernando
Zueco Lainez, David

UNIVERSIDAD DE ZARAGOZA
Escuela de Doctorado

Programa de Doctorado en Física

2025

Universidad Zaragoza
1542

Tesis Doctoral

LARGE-N THEORIES FOR CAVITY-QED MATERIALS

Autor

Juan Román Roche

Directores

David Zueco Láinez
Fernando Luis Vitalla

Universidad de Zaragoza
Escuela de Doctorado

Programa de Doctorado en Física
2024

Contents

Resumen

Cavity QED materials es un campo en la intersección de la física de la materia condensada y la óptica cuántica que estudia la modificación de las propiedades de los materiales por el acoplamiento con luz cuántica. La luz cuántica es generada por una estructura tipo cavidad que confina el campo electromagnético, aumentando el acoplamiento luz-materia hasta el punto en que es significativo en el límite de pocos o ningún fotón.

En esta tesis mostramos que la mayoría de los modelos microscópicos utilizados en *cavity QED materials* pueden ser expresados como un modelo de Dicke generalizado. Estudiamos el modelo de Dicke generalizado utilizando una expansión de N grande. Aquí, N es el número de grados de libertad de la materia, por lo que el límite de N grande es el límite termodinámico, el cual es natural en el estudio de las propiedades macroscópicas de materiales. Obtenemos teorías de equilibrio y de respuesta lineal para el modelo de Dicke generalizado en términos de un Hamiltoniano efectivo de campo medio solo para la materia.

Usando estas teorías, estudiamos varios problemas y sistemas. Revisitamos el problema de la superradiancia en equilibrio, unificando y generalizando los teoremas previos de imposibilidad y las condiciones críticas. Estudiamos la modificación de las propiedades de conducción del gas de electrones en dos dimensiones acoplado a una cavidad, incluyendo el efecto Hall cuántico entero. Resolvemos los modelos de Dicke, Dicke-Lipkin-Meshkov-Glick (Dicke-LMG) y Dicke-Ising. En este último, describimos la formación de estados ligados de polaritones y proporcionamos la condición para su existencia. Inspirados por el modelo de Dicke-LMG longitudinal, proponemos una plataforma experimental para el observar ferromagnetismo potenciado por la cavidad y la superradiancia en equilibrio, basada en nanoimanes moleculares acoplados a una cavidad de microondas. Finalmente, calculamos la modificación de la ecuación de Landau-Lifshitz-Gilbert por una cavidad e implementamos el resultado en el software de simulación micromagnética de código abierto Mumax3-cQED.

Las teorías de N grande también pueden aplicarse a modelos cuánticos con

fuertes interacciones de largo alcance. Definimos la cadena de Ising antiferromagnética no frustrada y mostramos que presenta un punto tricrítico. Nuestros resultados indican que las transiciones de fase cuánticas de primer orden se generan en modelos con interacciones antiferromagnéticas de largo alcance no frustradas por la presencia simultánea de interacciones antiferromagnéticas intersubred y ferromagnéticas intrasubred de intensidad comparable.

Abstract

Cavity QED materials is a field at the intersection of condensed matter physics and quantum optics that studies the modification of material properties by coupling to quantum light. The quantum light is generated by a cavity-like structure that confines the electromagnetic field, increasing the light-matter coupling to the point where it is significant in the few or no photon limit.

In this thesis we show that most of the microscopic models used in cavity QED materials can be cast into the form of a generalized Dicke model. We study the generalized Dicke model using a large-N expansion. Here N is the number of matter degrees of freedom and thus the large-N limit is the thermodynamic limit, which is natural in the study of bulk materials. We obtain equilibrium and linear response theories for the generalized Dicke model in terms of a matter-only mean-field effective Hamiltonian.

Using these theories we study several problems and systems. We revisit the problem of equilibrium superradiance, unifying and generalizing previous no-go theorems and critical conditions. We study the modification of the conduction properties of the two-dimensional electron gas coupled to a cavity, including the integer quantum Hall effect. We solve the Dicke, Dicke-Lipkin-Meshkov-Glick (Dicke-LMG) and Dicke-Ising models. In the latter, we describe the formation of bound polariton states and provide the condition for their existence. Inspired by the longitudinal Dicke-LMG model, we propose an experimental platform for cavity-enhanced ferromagnetism and equilibrium superradiance, based on molecular nanomagnets coupled to a microwave cavity. Finally, we compute the modification of the Landau-Lifshitz-Gilbert equation by a cavity and implement the result into the open-source micromagnetic simulation software Mumax3-cQED.

The large-N theories can also be applied to quantum models with strong long-range interactions. We define the unfrustrated antiferromagnetic Ising chain and show that it presents a tricritical point. Our results indicate that first-order quantum phase transitions are generated in models with unfrustrated antiferromagnetic long-range interactions by the simultaneous presence of

antiferromagnetic intersublattice and ferromagnetic intrasublattice interactions of similar strength.

Introduction

Condensed matter physics describes the properties of matter stemming from the electromagnetic forces acting on electrons and nuclei. It is in this field that we find some of the more resounding successes of quantum theory. Early applications revealed foundational concepts, like the electronic band structure or the exchange interaction, that explain some of the more mundane properties of materials, such as electrical conductivity or ferromagnetism. These were pivotal developments for the semiconductor industry that powers the digital world that we now take for granted. More recently, quantum many-body theory has allowed physicists to describe less ordinary phenomena, like superconductivity and the quantum Hall effect, which are rooted in concepts such as Bose-Einstein condensation, topological invariants and fractional statistics in two-dimensional materials.

One of the core concepts of quantum physics is the wave-particle duality, which states that quantum entities exhibit wave-like or particle-like properties depending on the circumstances. Quantum condensed matter physics was able to go beyond classical theories precisely by acknowledging the wave-like nature of the electrons and nuclei that constitute matter. Likewise, the field of quantum optics stems from the acknowledgement that some properties of light have to be described in terms of particle-like photons.

Quantum optics studies the interaction of atoms and molecules with quantum light, which is described by (non-relativistic) quantum electrodynamics (QED). Quantum electrodynamic effects only arise in certain scenarios, like high-energy particle collisions or when the electromagnetic field is confined in the vicinity of atoms or molecules to enhance their interaction. The latter case is exploited in the field of cavity QED, which has provided a true playground for quantum mechanical effects. Perhaps the simplest is the coherent exchange of energy between an atom and a cavity in what are called quantum Rabi oscillations, which is the hallmark of strong atom-cavity coupling, when quantum effects start to overcome dissipation.

Given the independent success of cavity QED and quantum condensed

matter physics it is natural to consider their interplay. Indeed, there is a growing interest in the field of *cavity QED materials*, which is dedicated to studying how material properties are affected by their interaction with quantum light, such as provided by a cavity environment. Quantum light can provide an additional tuning knob to the many phenomena of traditional condensed matter and perhaps unlock new physics. From the theoretical side, it is an opportunity to hone our understanding of quantum systems and light-matter interaction and the models with which we describe them.

Many of the latter advances in theoretical condensed matter physics have occurred in the context of a unification of tools and concepts with the field of high energy physics. In particular, under the umbrella of quantum field theory, with all that it entails. It seems reasonable then to reexamine the toolbox of quantum field theory when faced with the description of cavity QED materials. In particular, in this thesis we apply the large-N expansion to the study of cavity QED materials.

In quantum field theory, the large-N expansion is an alternative to conventional perturbation theory on the coupling parameter. It consists on an expansion of the relevant quantities in powers of $1/N$, where N is the rank of the symmetry group of the theory, for instance $\mathrm{SU}(N)$ in quantum chromodynamics (QCD). It is particularly useful in the study of asymptotically free theories like QCD, for which the effective coupling parameter decreases as energy increases. At low energies, these become strongly coupled and standard perturbation theory is compromised. As it will become clear throughout this thesis, in a path-integral formulation, the large-N limit can be seen as a self-consistent mean-field theory in which corrections can be computed as successive powers of $1/N$ in the expansion.

In this thesis we develop a large-N theory of cavity QED materials. We consider the strict $N \to \infty$ limit to describe the equilibrium and, in particular cases, the dynamics and then the $(1/N)^2$ correction that provides the linear response theory. In the process, we clarify the validity of mean-field theory for cavity QED materials and also for quantum systems with long-range interactions. We use the theory to revisit the problem of equilibrium superradiance, to study several paradigmatic models coupled to a cavity, such as the two-dimensional (2D) electron gas, the Dicke model, the Lipkin-Meshkov-Glick (LMG) model or the Ising model, to solve the dynamics of magnetic materials coupled to a cavity and to solve quantum strong long-range models. The thesis is organized as follows.

Chapter 1 is dedicated to introducing the relevant aspects of cavity QED materials. First, we define and review the field, with an emphasis on the latest developments. Then, we present the microscopic models that are typically

considered as the starting point in the description of cavity QED materials. We show that these are particular instances of the generalized Dicke model, which we define. Next, we review previous theories involving large-N expansions that have been used to describe cavity QED materials. We finish by acknowledging other field-theoretical approaches to cavity QED materials that are contemporary to this thesis.

Chapter 2 is dedicated to the equilibrium theory. First, we present the path integral formalism and compute the effective action for the generalized Dicke model. Then we apply the large-N limit to reveal the equilibrium properties of the model in terms of a mean-field effective Hamiltonian. Using again the large-N limit, we promote this mean-field Hamiltonian to a proper effective Hamiltonian. Finally, we test the finite-size scaling of the effective Hamiltonian and compare it against other effective theories.

Chapter 3 is dedicated to the linear response theory. We pick up where we left off in Chap. 2 and we compute the next term on the large-N expansion to reveal the response functions of the generalized Dicke model. Then, we switch gears and present an alternative derivation for the linear response theory, by solving the equations of motion of the retarded Green functions. We finish by comparing the two approaches and then draw conclusions on the validity of mean-field theory for the generalized Dicke model and more generally for collective interactions.

Chapter 4 is dedicated to the application of the theory to electronic systems. First, we discuss the issue of equilibrium superradiance and derive a critical condition. Then, we study the 2D electron gas coupled to a cavity, in particular the modification of the electric conductivity and the integer quantum Hall effect.

Chapter 5 is dedicated to the application of the theory to several spin models. We start with the Dicke model and then introduce interactions in an increasingly complex manner. We consider the Dicke-LMG and Dicke-Ising model. We argue that the former can describe dipolar magnets coupled to a cavity and propose an experimental realization that can in principle display cavity-enhanced dipolar ferromagnetism. In the latter, we focus on the hybrid excitation spectrum and describe the formation of what we call bound polariton states. We finish by considering a Heisenberg ferromagnet coupled to a cavity.

Chapter 6 is dedicated to extending the Landau-Lifshitz-Gilbert (LLG) equation for a magnetic material coupled to a cavity. First, we present the LLG equation and discuss its application in micromagnetic simulations. Then we discuss its extension to account for a cavity and the implementation of the resulting modified LLG equation into the open-source micromagnetic simulation

software Mumax3, which we have released as Mumax3-cQED. We finish by benchmarking Mumax3-cQED and showcasing a couple of use cases. The results presented in this chapter have been a joint effort in collaboration with undergraduate student Andrés Martín-Megino and fellow PhD candidate Sergio Martínez-Losa del Rincón.

Chapter 7 is dedicated to quantum long-range models. First, we present the field of long-range interactions and discuss its different regimes. Then, we show how the theory developed in the thesis for cavity QED materials can also be applied to provide an exact solution for quantum strong long-range models. As a first application we use it to solve the ferromagnetic strong long-range Ising model. Then, we define the unfrustrated antiferromagnetic long-range Ising model. We solve it analytically in the strong long-range regime and then numerically in the full range of interactions. The results presented for the unfrustrated antiferromagnetic Ising model have been a joint effort in collaboration with undergraduate students Victor Herráiz-López and Ramón Ferrández and fellow PhD candidates Sebastián Roca-Jerat and Manuel Gallego. In particular, Sebastián Roca-Jerat did the brunt of the numerical work.

Chapter 1

Cavity QED materials

In this chapter we will introduce the field of cavity QED materials and set the context for the remainder of the thesis. First, we will define the field and review its state of the art. Then, we will introduce the microscopic models that are used for the theoretical description of cavity QED materials and show how they can be understood as generalized Dicke models. The generalized Dicke model will be the central model of this thesis, on which the main theoretical derivations are based. Next, we will review some large-N theories that have been used to describe cavity QED materials. These are the precursors to the large-N theories developed in this thesis. Finally, we will comment on other field-theoretical approaches that are contemporary to this thesis.

1.1 Review

Cavity QED materials is a field at the crossroads of quantum optics and condensed matter physics. Typical cavity QED setups consider a few atoms or molecules interacting with quantum light in the form of the vacuum fluctuations of the electromagnetic field or a few of its excitations: photons. Quantum condensed-matter physics describes the collective properties of materials stemming from their quantum many-body nature, such as superconductivity, the quantum Hall effect or magnetism. In traditional condensed-matter physics, the effect of the electromagnetic field as a mediator of interactions is introduced phenomenologically, in the form of electrostatic Coulomb interactions or magnetic dipole-dipole interactions. Alternatively, light is also considered as a probing or driving tool, often in the form of lasers, and described classically as a consequence of the high photon count. The resulting phenomenology is described by Floquet theory [1]. The field of cavity QED materials seeks

to describe how the properties of materials are modified by the coupling to quantum light [2–4]. Following the spirit of cavity QED, this is achieved by confining the electromagnetic field in cavities, to reduce the mode volume and enhance the otherwise weak light-matter coupling.

We can distinguish two fundamentally different mechanisms by which the cavity can modify the material. The simplest is by a hybridization of the cavity photons with one or more collective excitations in the material, forming polaritons with attractive mixed light-matter properties. This is already commonly achieved with quasiparticle excitations such as magnon, phonons or excitons and has given rise to a full zoo of polariton physics [5]. In this regard, the field of cavity QED materials is actively exploring new polaritonic flavors in novel platforms. Chemical reactivity has been modified in molecules under vibrational [6, 7] and electronic [8] strong coupling to cavity vacuum fields, giving rise to the field of polaritonic chemistry [9, 10]. Transport properties have been modified by polariton formation in organic semiconductors [11] and excitons [12] and in two-dimensional electron gasses via Landau polaritons [13, 14]. Besides the engineering of hybrid light-matter excitations, the second mechanism is the modification of (thermal) equilibrium or ground-state properties. This is a much more nuanced research question that is deeply tied (we will argue that it is synonymous) to the phenomenon of equilibrium superradiance, where the light-matter coupling induces a phase transition leading to a polarized material and a macroscopic population of photons in the cavity. Equilibrium superradiance was first described in the Dicke model [15–17]. Fifty years after its theoretical prediction it has been realized in driven-dissipative systems serving as analog simulators for the Dicke model, but there are no clear demonstrations in proper equilibrium [18]. To this regard, it is worth mentioning that a magnonic superradiant phase transition has been achieved in $ErFeO_3$. Here, the role of the cavity is played by an Fe^{3+} magnon, which is coupled to Er^{3+} spins.

There have been several experiments in recent years showing modifications of material properties by coupling to a cavity where the underlying mechanism is unclear, so we cannot rule out modifications of the equilibrium properties. First, the modification of the quantum Hall effect [19]. The quantum Hall effect is a phenomenon of electric conductivity, and thus of the electric response, so it is likely related to the formation of Landau polaritons and not to a modification of the ground-state properties of the metal. However, a microscopic model explaining these experimental findings is still lacking. Second, changes to the superconducting critical temperature of YBCO nanoparticles have been reported [20], underlain by an enhancement of ferromagnetism [21]. It must be noted that in this system the interaction between the light, in the form of surface plasmons in a gold surface, and the YBCO nanoparticles is mediated

by vibrational excitations in the polymer that hosts the nanoparticles. Again, a microscopic theory is needed, but the authors rationalize the results in terms of hybridized plasmon-phonon excitations. Finally, the metal-to-insulator transition of 1T-TaS_2 has also been tuned by coupling to a terahertz cavity [22]. Although the metal-to-insulator transition is typically understood as a quantum phase transition, here it is a temperature-driven transition. The cavity is theorized to modify the dissipation properties of the 1T-TaS_2 sample in a Purcell-like effect, leading to a change of the effective temperature of the sample and thus driving the phase transition.

In the theoretical front, there have been a host of proposals describing novel phenomenology or attempting to explain the aforementioned experimental demonstrations, such as changes in the critical temperature in superconductivity [23, 24], or alterations in magnetism [25–28], the Kondo effect [29], topological phases [30–40], ferroelectricity [41–45] and transport in excitonic [46, 47], molecular [48] and (disordered) electronic systems [49–55].

Beyond concrete proposals, other works have focused on providing relatively general theories for certain aspects of cavity QED materials. In no particular order, we have theories on the light-matter coupling and quantum geometrical effects on moiré materials [56], on the quantum to classical crossover of Floquet engineering [57], on the collective light-matter hybrid modes of transition dipoles in a solid [58, 59], on the electro- and magnetostatic nature of cavity-mediated interactions [60, 61], on the equilibrium and linear response properties of cavity QED materials in the thermodynamic limit [62–64], on a unitary transformation to study cavity QED systems at arbitrary interaction strengths [65], on the modification of Landau-Lifshitz-Gilbert dynamics by a cavity [66], on using hyperbolic van der Waals materials as cavities [67], on the extension of the Bloch theorem to cavity QED materials [68], on mass-renormalization effects in electronic cavity QED materials [69, 70], on the extension of density functional theory (DFT) to cavity QED materials [71–73], on Amperean superconductivity in two-dimensional materials coupled to deep subwavelength cavities [74], on fractional quantum Hall liquids coupled to quantum light [75], on equilibrium superradiance (also called photon condensation) [76–85], on cavity-induced charge transfer in the length-gauge [86] and on light-matter interactions for extended systems within the long-wavelength approximation [87].

Finally, more fundamentally, there has been a theoretical effort to identify pitfalls in the microscopic models underlying the field, which could lead to wrong predictions and explain the lack of experimental confirmation for many of the proposed phenomena, and more generally of the superradiant phase transition. The main issue has been ensuring the gauge invariance of the models, which can be broken by disregarding diamagnetic (A^2) or self-polarization (P^2) terms in

the light-matter Hamiltonian [88–90], or by a projection to a subset of material energy levels or the truncation of the photonic Hilbert space [91–96]. A related issue is the fact that although proper models are gauge-invariant, particular operators need not be. This can have consequences in the interpretation of certain phenomena like equilibrium superradiance when a gauge-dependent operator is used as the order parameter. Likewise, a particular experimentally measurable observable corresponds to a certain gauge-dependent operator only in the appropriate gauge [97–99]. Finally, the importance of considering the totality of the electromagnetic modes, going beyond models that consider only a few resonant or near resonant levels, has also been emphasized [60, 61, 84, 100]. In this thesis, we continue this effort, by deriving exact non-perturbative theories for gauge-invariant microscopic models of cavity QED materials.

1.2 Microscopic models of cavity QED materials

A microscopic description of cavity QED materials requires that we fix a material subsystem, whose properties are well described by some microscopic theory, and develop a theory of how such a material couples to the electromagnetic field of a cavity. It is common to assume that the matter subsystem is composed of N identical particles. Then, depending on the spatial confinement of the particles we can distinguish two different families of systems. Gases and liquids, where the particles are free to occupy any position of space, like an electron liquid in a conductor; and systems of emitters where each particle or group of particles is bounded to a non-dynamical core, such as a system of neutral atoms or molecules where the motion of the nucleus is disregarded, and the focus is placed on the electron(s) motion. The two families differ slightly in the way they couple to the electromagnetic field, so we will consider them separately. Our goal in this section is to show that in both cases it is possible to cast the Hamiltonian into the form of a generalized Dicke model, which we will define. The importance of the generalized Dicke model lies in the fact that it features a light-matter coupling that is linear in matter operators, which facilitates later analytical treatments based on a coherent-state path-integral formulation where the trace over photonic modes becomes a Gaussian integral.

Before proceeding, we must note that the ensuing microscopic models do not include fermionic tight-binding models where the light-matter coupling appears in the form of Peierls phase factors, which are also commonly considered in the literature of cavity QED materials. This is because this type of coupling can be seen to arise from a projection of the usual minimal coupling Hamiltonian that we consider in the following onto a subset of electronic energy levels [96]. The trade-off for this simplified description of the electronic subsystem is that

the light-matter coupling takes the highly non-linear form of a Peierls phase factor. With our formulation, we do not resort to simplified descriptions of the electronic subsystem, at least initially. Instead, we consider the full electronic spectrum at the beginning such that the light-matter coupling is linear, as we will show in this section. This allows us to apply the equilibrium and linear response theories that we develop in Chaps. 2 and 3, in which the cavity is eliminated as a degree of freedom, and the properties of the hybrid system are given as a function of the properties of an effective matter-only Hamiltonian. At that point, we will be free to solve the effective matter Hamiltonian with the usual approximations employed in many-body problems.

1.2.1 An electron liquid coupled to a cavity

An electron liquid is generally described by a Hamiltonian of the form

$$H_{\mathrm{m}} = \sum_j \frac{\boldsymbol{p}_j^2}{2m} + V_C + V\,. \tag{1.1}$$

Here, m is the electron mass and $\boldsymbol{r}_j$ and $\boldsymbol{p}_j$ are the canonical position and momentum operators of the j-th electron, such that $[\boldsymbol{r}_{i,\alpha}, \boldsymbol{p}_{j,\beta}] = i\delta_{ij}\delta_{\alpha\beta}$. Note that $\hbar = 1$ throughout the text, unless otherwise specified. We also include two potential terms. Electrostatic Coulomb interactions between charges, including self-interactions, electron-electron interactions and electron-ion interactions, are encapsulated in V_C. The potential V accounts for additional unspecified single- and two-particle interactions. These potential terms would be absent in the description of a gas. Note that this Hamiltonian can also describe quasiparticles, such as electron-hole pairs in the Fermi surface of a metal, in which case m would stand for an effective mass. We are interested in the effects of coupling this material subsystem to the quantized electromagnetic field in a confined region of space, i.e., a cavity. Following the minimal coupling prescription, one obtains the Hamiltonian for the complete system

$$H = \sum_j \frac{(\boldsymbol{p}_j + e\boldsymbol{A}(\boldsymbol{r}_j))^2}{2m} + V_{\mathrm{C}}' + V + H_{\mathrm{em}} + \frac{g_{\mathrm{e}}\mu_{\mathrm{B}}}{2}\sum_j \boldsymbol{\sigma}_j \cdot \boldsymbol{B}(\boldsymbol{r}_j)\,. \tag{1.2}$$

The effect of the coupling is fourfold. Most trivially, we must account for the energy of the electromagnetic field, hence H_{em}, which we will specify later. Secondly, the canonical momentum now differs from the mechanical momentum, this is apparent in the kinetic term, which now includes the vector potential $\boldsymbol{A}(\boldsymbol{r}_j)$ at each particles' position, here $-e$ is the electron's charge. The third and perhaps more subtle effect is the modification of the Coulomb potential between charges $V_{\mathrm{C}} \to V_{\mathrm{C}}'$, to include direct as well as image-charge-mediated

interactions [101, 102]. The latter arise as an electrostatic effect of imposing the cavity boundary conditions on the Coulomb potential. Finally, we include the Zeeman coupling between the electron spin and the magnetic field $\boldsymbol{B}(\boldsymbol{r}_j)$. Here $\boldsymbol{\sigma}_j = (\sigma_j^x, \sigma_j^y, \sigma_j^z)$ is the Pauli vector, whose components are the Pauli matrices, $\mu_{\mathrm{B}} = e/(2m)$ is the Bohr magneton and g_{e} the electron's Landé factor. Equation (1.2) is the many-particle generalization of the Pauli-Fiertz Hamiltonian for non-relativistic electrons, bar the spin-orbit coupling.

In the Coulomb gauge, the vector potential is transverse, $\nabla \cdot \boldsymbol{A} = 0$, and given by

$$\boldsymbol{A}(\boldsymbol{r}) = \sum_{\kappa} A_{\boldsymbol{k}} \boldsymbol{u}_{\kappa}(\boldsymbol{r}) a_{\kappa} + \mathrm{h.c.}\,, \tag{1.3}$$

where κ is a four-vector containing the polarization index $\sigma = 1, 2$ and the wavevector $\boldsymbol{k}$: $\kappa \equiv \{\boldsymbol{k}, \sigma\}$. The mode amplitude is $A_{\boldsymbol{k}} = \sqrt{1/(2\epsilon_0 V \omega_{\boldsymbol{k}})}$. The V and ϵ_0 are respectively the cavity mode volume and the dielectric constant. We also introduce the bosonic annihilation and creation operators of the κ-th mode: a_κ, $a_\kappa^\dagger$, which obey the canonical commutation relations $[a_\kappa, a_{\kappa'}^\dagger] = \delta_{\kappa\kappa'}$. To maintain as much generality as possible, we have refrained from using a particular spatial dependence for the vector potential. For a specific model, the geometry of the cavity will determine the spatial quantization of the wavevector $\boldsymbol{k}$ and in turn, the functional form of the mode functions $\boldsymbol{u}_\kappa(\boldsymbol{r})$ [103]. In any case, the following properties hold for the mode functions: $\boldsymbol{u}_{-\boldsymbol{k},\sigma}(\boldsymbol{r}) = \boldsymbol{u}_{\boldsymbol{k},\sigma}^*(\boldsymbol{r})$, $\boldsymbol{u}_{\boldsymbol{k},\sigma}(\boldsymbol{r}) \cdot \boldsymbol{k} = 0$, $\int_V dV \boldsymbol{u}_\kappa^*(\boldsymbol{r}) \cdot \boldsymbol{u}_{\kappa'}(\boldsymbol{r}) = \delta_{\kappa\kappa'}$. Note that in Eq. (1.3) the mode functions have been promoted to mode operators, since they depend on the position operator of each particle (Cf. Sec. 1.2.2). By definition, $\boldsymbol{B} = \nabla \times \boldsymbol{A}$, so

$$\boldsymbol{B}(\boldsymbol{r}) = \sum_{\kappa} B_{\boldsymbol{k}} \boldsymbol{u}_{\perp,\kappa}(\boldsymbol{r}) a_{\kappa} + \mathrm{h.c.}\,, \tag{1.4}$$

where we have defined the transverse mode functions $\boldsymbol{u}_{\perp,\kappa}(\boldsymbol{r}) = |\boldsymbol{k}|^{-1} \nabla \times \boldsymbol{u}_\kappa(\boldsymbol{r})$ and $B_{\boldsymbol{k}} = A_{\boldsymbol{k}} |\boldsymbol{k}| = A_{\boldsymbol{k}} \omega_{\boldsymbol{k}} / c$. Finally, we can express H_{em} as

$$H_{\mathrm{em}} = \sum_{\kappa} \omega_{\boldsymbol{k}} a_\kappa^\dagger a_\kappa\,. \tag{1.5}$$

To facilitate the analytical treatment of the Hamiltonian, it is convenient to expand the kinetic term and make uso of Eqs. (1.3), (1.4) and (1.5):

$$\begin{aligned} H = H'_{\mathrm{m}} &+ \sum_{\kappa} \omega_{\boldsymbol{k}} a_\kappa^\dagger a_\kappa + \sum_j \sum_{\kappa} \frac{e}{m} A_{\boldsymbol{k}} \boldsymbol{p}_j \cdot (\boldsymbol{u}_\kappa(\boldsymbol{r}_j) a_\kappa + \mathrm{h.c.}) \\ &+ \sum_j \frac{e^2}{2m} \sum_{\kappa,\kappa'} A_{\boldsymbol{k}} A_{\boldsymbol{k}'} \, (\boldsymbol{u}_\kappa(\boldsymbol{r}_j) a_\kappa + \mathrm{h.c.}) \cdot (\boldsymbol{u}_{\kappa'}(\boldsymbol{r}_j) a_{\kappa'} + \mathrm{h.c.}) \\ &+ \frac{g_{\mathrm{e}} \mu_{\mathrm{B}}}{2} \sum_{\kappa} \sum_j B_{\boldsymbol{k}} \boldsymbol{\sigma}_j \cdot (\boldsymbol{u}_{\perp,\kappa}(\boldsymbol{r}_j) a_\kappa + \mathrm{h.c.})\,. \end{aligned} \tag{1.6}$$

Here, H'_{m} is just H_{m} but with V_{C} replaced by V'_{C}. The third term describes the interaction of the electronic momentum with the electromagnetic field and is typically referred to as the paramagnetic coupling. The fourth term is referred to as the diamagnetic contribution or A^2 term. It can be eliminated with a Bogoliubov transform, leading to a renormalization of the cavity frequencies and the paramagnetic coupling strength. To condense the notation, we define the operators

$$U_{\kappa,\kappa'} = N^{-1} \sum_j \boldsymbol{u}_\kappa(\boldsymbol{r}_j) \cdot \boldsymbol{u}_{\kappa'}(\boldsymbol{r}_j)\,, \tag{1.7}$$

$$\bar{U}_{\kappa,\kappa'} = N^{-1} \sum_j \boldsymbol{u}_\kappa(\boldsymbol{r}_j) \cdot \boldsymbol{u}^*_{\kappa'}(\boldsymbol{r}_j)\,, \tag{1.8}$$

and the constants

$$\Delta_{\boldsymbol{k},\boldsymbol{k}'} = \frac{\omega_{\mathrm{p}}^2}{4\sqrt{\omega_{\boldsymbol{k}}\omega_{\boldsymbol{k}'}}} \tag{1.9}$$

$$g^{\mathrm{e}}_{\boldsymbol{k}} = \frac{\omega_{\mathrm{p}}}{\sqrt{N}} \sqrt{\frac{\omega_{\mathrm{p}}}{\omega_{\boldsymbol{k}}}}\,, \tag{1.10}$$

$$g^{\mathrm{m}}_{\boldsymbol{k}} = \mu_{\mathrm{B}} B_{\boldsymbol{k}} = \frac{\omega_{\mathrm{p}}}{\sqrt{N}} \sqrt{\frac{\omega_{\boldsymbol{k}}}{8mc^2}}\,, \tag{1.11}$$

where $\omega_{\mathrm{p}} = \sqrt{e^2\rho/(m\epsilon_0)}$ the electron plasma frequency, with $\rho = N/V$ the electron density. With these, we write the terms that depend quadratically on the bosonic operators as

$$H_{\mathrm{ph}} = \sum_\kappa \omega_{\boldsymbol{k}} a^\dagger_\kappa a_\kappa + \sum_{\kappa,\kappa'} \Delta_{\boldsymbol{k},\boldsymbol{k}'} \left(U_{\kappa,\kappa'} a_\kappa a_{\kappa'} + \bar{U}_{\kappa,\kappa'} a_\kappa a^\dagger_{\kappa'} + \mathrm{h.c.} \right)\,. \tag{1.12}$$

Analytical tractability demands that we neglect mode-mode interactions (Cf. Sec. 1.2.2), i.e., that we assume $U_{\boldsymbol{k},\sigma,\boldsymbol{k}',\sigma'} = \delta_{\boldsymbol{k},-\boldsymbol{k}'}\delta_{\sigma\sigma'}\mathbb{I}$ and $\bar{U}_{\boldsymbol{k},\sigma,\boldsymbol{k}',\sigma'} = \delta_{\boldsymbol{k},\boldsymbol{k}'}\delta_{\sigma\sigma'}\mathbb{I}$, leaving only the momentum-conserving terms, and without spatial dependence

$$H_{\mathrm{ph}} \approx \sum_\kappa \omega_{\boldsymbol{k}} a^\dagger_{\boldsymbol{k},\sigma} a_{\boldsymbol{k},\sigma} + \sum_\kappa \Delta_{\boldsymbol{k}} \left(a_{\boldsymbol{k},\sigma} a_{-\boldsymbol{k},\sigma} + a_{\boldsymbol{k},\sigma} a^\dagger_{\boldsymbol{k},\sigma} + \mathrm{h.c.} \right)\,, \tag{1.13}$$

where $\Delta_{\boldsymbol{k}} \equiv \Delta_{\boldsymbol{k},\boldsymbol{k}}$. The approximation is exact for a homogeneous electron system. Furthermore, for systems that have a second order phase transition to a non-homogeneous phase, the approximation is valid in the vicinity of the transition [77]. This suggests that the resulting model can be used to predict and locate transitions to non-homogeneous phases. It is expected that the effect of the approximation will be quantitative and will skew the calculation

of observables in the non-homogeneous phase. $H_{\rm ph}$ can now be diagonalized with a Bogoliubov transformation

$$a^\dagger_{\boldsymbol{k},\sigma} = \cosh(\theta_{\boldsymbol{k}}) b^\dagger_{\boldsymbol{k},\sigma} - \sinh(\theta_{\boldsymbol{k}}) b_{-\boldsymbol{k},\sigma} \,. \tag{1.14}$$

One finds that $\cosh(\theta_{\boldsymbol{k}}) = (\lambda_{\boldsymbol{k}} + 1)/(2\sqrt{\lambda_{\boldsymbol{k}}})$ and $\sinh(\theta_{\boldsymbol{k}}) = (\lambda_{\boldsymbol{k}} - 1)/(2\sqrt{\lambda_{\boldsymbol{k}}})$ and $\lambda_{\boldsymbol{k}} = \tilde{\omega}_{\boldsymbol{k}}/\omega_{\rm p}$, with $\tilde{\omega}_{\boldsymbol{k}} = \sqrt{\omega^2_{\boldsymbol{k}} + \omega^2_{\rm p}}$. As a result, the complete Hamiltonian can be written as

$$\begin{aligned} H = H'_{\rm m} + \sum_\kappa \tilde{\omega}_{\boldsymbol{k}} b^\dagger_\kappa b_\kappa + \sum_\kappa \sum_j \sqrt{\frac{\omega_{\boldsymbol{k}}}{\tilde{\omega}_{\boldsymbol{k}}}} g^{\rm m}_{\boldsymbol{k}} \frac{g_{\rm e}}{2} \boldsymbol{\sigma}_j \cdot (\boldsymbol{u}_{\perp,\kappa}(\boldsymbol{r}_j) b_\kappa + \text{h.c.}) \\ + \sum_\kappa \sum_j \sqrt{\frac{\omega_{\boldsymbol{k}}}{\tilde{\omega}_{\boldsymbol{k}}}} g^{\rm e}_{\boldsymbol{k}} \sqrt{\frac{1}{2m\omega_{\rm p}}} \boldsymbol{p}_j \cdot (\boldsymbol{u}_\kappa(\boldsymbol{r}_j) b_\kappa + \text{h.c.}) \,. \end{aligned} \tag{1.15}$$

Defining the coupling operator and coupling constant

$$g_{\boldsymbol{k}} C_\kappa = \sum_j \sqrt{\frac{\omega_{\boldsymbol{k}}}{\tilde{\omega}_{\boldsymbol{k}}}} \left(g^{\rm e}_{\boldsymbol{k}} \sqrt{\frac{1}{2m\omega_{\rm p}}} \boldsymbol{p}_j \cdot \boldsymbol{u}_\kappa(\boldsymbol{r}_j) + g^{\rm m}_{\boldsymbol{k}} \frac{g_{\rm e}}{2} \boldsymbol{\sigma}_j \cdot \boldsymbol{u}_{\perp,\kappa}(\boldsymbol{r}_j) \right) \,, \tag{1.16}$$

we can finally write the Hamiltonian as

$$H = H'_{\rm m} + \sum_\kappa \tilde{\omega}_{\boldsymbol{k}} b^\dagger_\kappa b_\kappa + \sum_\kappa g_{\boldsymbol{k}} \left(C_\kappa b_\kappa + \text{h.c.} \right) \,. \tag{1.17}$$

1.2.2 A system of neutral atoms coupled to a cavity

The main difference between an electron liquid and a system of localized emitters lies on the fact that in the former case the electrons are free to move on the entire volume of the system, whereas in the latter their movement is bounded to a non-dynamical core.

For simplicity, we consider a system of N neutral single-electron atoms, each with a non-dynamical nucleus with charge e at position $\boldsymbol{R}_j$ and a dynamical electron with charge $-e$, bound to the nucleus, at position $\boldsymbol{R}_j + \boldsymbol{r}_j$. The derivation can be readily extended to multi-electron atoms or molecules. Note that $\boldsymbol{R}_j$ is a classical variable and $\boldsymbol{r}_j$ is an operator. The charge density of the system reads

$$\rho(\boldsymbol{r}) = -e \sum_j \delta^3(\boldsymbol{r} - \boldsymbol{R}_j - \boldsymbol{r}_j) + e \sum_j \delta^3(\boldsymbol{r} - \boldsymbol{R}_j) \,, \tag{1.18}$$

and one can define polarization

$$\boldsymbol{P}(\boldsymbol{r}) = -e \sum_j \boldsymbol{r}_j \int_0^1 ds \delta^3(\boldsymbol{r} - \boldsymbol{R}_j - s\boldsymbol{r}_j) \tag{1.19}$$

and magnetization

$$\boldsymbol{M}(\boldsymbol{r}) = -e\sum_j \boldsymbol{r}_j \times \dot{\boldsymbol{r}}_j \int_0^1 dss\delta^3(\boldsymbol{r} - \boldsymbol{R}_j - s\boldsymbol{r}_j) \tag{1.20}$$

fields that satisfy $\nabla \cdot \boldsymbol{P} = -\rho$ and $\nabla \times \boldsymbol{M} = \boldsymbol{j} - \delta_t \boldsymbol{P}$, with the current density $\boldsymbol{j}(\boldsymbol{r}) = -e\sum_j \dot{\boldsymbol{r}}_j \delta^3(\boldsymbol{r} - \boldsymbol{R}_j - \boldsymbol{r}_j)$. Here $\delta^3(\boldsymbol{r})$ is the three-dimensional Dirac delta function.

Description in the Coulomb gauge

In terms of the nucleus and relative electron coordinates, the Hamiltonian in the Coulomb gauge reads

$$H = \sum_j \frac{\left(\boldsymbol{p}_j + e\boldsymbol{A}(\boldsymbol{R}_j + \boldsymbol{r}_j)\right)^2}{2m} + V_{\mathrm{C}} + V + H_{\mathrm{em}} + \frac{g_{\mathrm{e}}\mu_{\mathrm{B}}}{2}\sum_j \boldsymbol{\sigma}_j \cdot \boldsymbol{B}(\boldsymbol{R}_j + \boldsymbol{r}_j)\,, \tag{1.21}$$

Note that we are disregarding image-charge effects in V_{C} in this case. To take them into account consistently we would have to include them also in the charge density and the polarization and magnetization fields.

If the length scale of the bounded motion is much smaller than the wavelength of the electromagnetic field, one can consider that the EM field is constant and equal at any point in the trajectory of an individual electron $\boldsymbol{A}(\boldsymbol{r}_j + \boldsymbol{R}_j) \approx \boldsymbol{A}(\boldsymbol{R}_j)$. This is the long-wavelength approximation in its crudest form. Assuming that we can work within this long-wavelength limit, the field operators $\boldsymbol{A}$, $\boldsymbol{B}$ act only on the Hilbert space of the photons, i.e., they do not contain position operators acting on the Hilbert space of the matter. Instead, they are parametrized by the positions of the nuclei. This subtle difference implies that, unlike for the liquid, the terms in the Hamiltonian quadratic in bosonic operators can be exactly diagonalized by a Bogoliubov transformation. The final Hamiltonian (1.17) (See Fig. 2.1(b)) has the same functional form in both cases, the differences are encoded in the frequencies $\{\Omega_{\boldsymbol{k}}\}$, coupling constants $\{g_{\boldsymbol{k}}\}$ and coupling operators $\{C_\kappa\}$, and of course in H_{m}. For the sake of completeness we include a detailed derivation in App. A. However, in the case of localized emitters it is possible and convenient to apply a unitary transformation to the Coulomb gauge Hamiltonian and move to the multipolar gauge, in order to then have more control on the long-wavelength approximation.

Description in the multipolar gauge

To move to the multipolar gauge we will use the Power-Zienau-Woolley (PZW) transformation, defined as

$$U = e^{-i\int d^3r \boldsymbol{P}(\boldsymbol{r})\cdot\boldsymbol{A}(\boldsymbol{r})}. \tag{1.22}$$

Accordingly, the operators transform as

$$\boldsymbol{p}_j \to U\boldsymbol{p}_j U^\dagger = \boldsymbol{p}_j - e\boldsymbol{A}(\boldsymbol{R}_j + \boldsymbol{r}_j) - e\boldsymbol{r}_j \times \int_0^1 ds s \boldsymbol{B}(\boldsymbol{R}_j + s\boldsymbol{r}_j)\,, \tag{1.23}$$

$$a_\kappa \to U a_\kappa U^\dagger = a_\kappa + i\int d^3r \boldsymbol{P}(\boldsymbol{r})\cdot\boldsymbol{A}(\boldsymbol{r})\,. \tag{1.24}$$

The resulting Hamiltonian in the multipolar gauge reads

$$\begin{aligned} H = \sum_j \frac{\left(\boldsymbol{p}_j - e\boldsymbol{r}_j \times \int_0^1 ds s \boldsymbol{B}(\boldsymbol{R}_j + s\boldsymbol{r}_j)\right)^2}{2m} + V_\mathrm{C} + V \\ + \sum_\kappa \omega_{\boldsymbol{k}} a_\kappa^\dagger a_\kappa - i\sum_\kappa \omega_{\boldsymbol{k}} A_{\boldsymbol{k}} \int d^3r \boldsymbol{P}(\boldsymbol{r})\cdot(\boldsymbol{u}_\kappa(\boldsymbol{r})a_\kappa - \mathrm{h.c.}) \\ + \sum_\kappa \omega_{\boldsymbol{k}} \left| A_{\boldsymbol{k}} \int d^3r \boldsymbol{P}(\boldsymbol{r})\cdot\boldsymbol{u}_\kappa(\boldsymbol{r})\right|^2 + \frac{g_\mathrm{e}\mu_\mathrm{B}}{2}\sum_j \boldsymbol{\sigma}_j\cdot\boldsymbol{B}(\boldsymbol{R}_j + \boldsymbol{r}_j)\,. \end{aligned} \tag{1.25}$$

We can now perform the long-wavelength approximation for the electromagnetic field. Instead of taking the crudest approximation, we will perform a multipolar expansion of the polarization and the magnetic field up to the electric quadrupole and magnetic dipole terms. Although negligible in comparison with the electric dipole, these terms, particularly the magnetic dipole, will prove relevant in Chaps. 2 and 4 when we construct a matter-only effective Hamiltonian and examine the resulting effective interactions. For the polarization we approximate

$$\delta^3(\boldsymbol{r} - \boldsymbol{R}_j - s\boldsymbol{r}_j) \approx \delta^3(\boldsymbol{r} - \boldsymbol{R}_j) - s(\boldsymbol{r}_j\nabla)\delta^3(\boldsymbol{r} - \boldsymbol{R}_j) \tag{1.26}$$

and subsequently

$$\boldsymbol{P}(\boldsymbol{r}) = -e\sum_j \boldsymbol{r}_j\delta^3(\boldsymbol{r} - \boldsymbol{R}_j) + \frac{1}{2}e\sum_j \boldsymbol{r}_j(\boldsymbol{r}_j\cdot\nabla)\delta^3(\boldsymbol{r} - \boldsymbol{R}_j)\,. \tag{1.27}$$

With this

$$\int d^3r \boldsymbol{P}(\boldsymbol{r})\cdot\boldsymbol{u}_\kappa(\boldsymbol{r}) = -e\sum_j \boldsymbol{r}_j\cdot\boldsymbol{u}_\kappa(\boldsymbol{R}_j) + \frac{1}{2}e\sum_j \boldsymbol{r}_j\cdot[(\boldsymbol{r}_j\cdot\nabla)\boldsymbol{u}_\kappa(\boldsymbol{r})]_{\boldsymbol{r}=\boldsymbol{R}_j}\,. \tag{1.28}$$

Similarly, we approximate the magnetic field as $\boldsymbol{B}(\boldsymbol{R}_j + \boldsymbol{r}_j) \approx \boldsymbol{B}(\boldsymbol{R}_j)$. The resulting Hamiltonian reads

$$\begin{aligned} H = H_{\mathrm{m}} &- \sum_j \boldsymbol{m}_j \cdot \boldsymbol{B}(\boldsymbol{R}_j) + \frac{1}{8m}\sum_j \left(\boldsymbol{d}_j \times \boldsymbol{B}(\boldsymbol{R}_j)\right)^2 \\ &+ \sum_k \omega_{\boldsymbol{k}} a_\kappa^\dagger a_\kappa - i\sum_\kappa \omega_{\boldsymbol{k}} A_{\boldsymbol{k}} \sum_j \boldsymbol{d}_j \cdot \left(\boldsymbol{u}_\kappa(\boldsymbol{R}_j) a_\kappa - \mathrm{h.c.}\right) \\ &+ i\sum_\kappa \frac{\omega_{\boldsymbol{k}}^2}{c} A_{\boldsymbol{k}} \sum_j \left(\mathrm{Tr}(Q_j U_\kappa(\boldsymbol{R}_j) a_\kappa - \mathrm{h.c.}\right) \\ &+ \sum_\kappa \omega_{\boldsymbol{k}} \left| A_{\boldsymbol{k}} \sum_j \boldsymbol{d}_j \cdot \boldsymbol{u}_\kappa(\boldsymbol{R}_j) - A_{\boldsymbol{k}} \frac{\omega_{\boldsymbol{k}}}{c} \sum_j \mathrm{Tr} Q_j U_\kappa(\boldsymbol{R}_j) \right|^2 , \end{aligned} \tag{1.29}$$

with

$$\boldsymbol{d}_j = -e\boldsymbol{r}_j \,, \tag{1.30}$$

$$Q_{j,\alpha\beta} = -\frac{1}{2} e \left(r_{j,\alpha} r_{j,\beta} - \frac{\boldsymbol{r}_j^2}{3} \delta_{\alpha\beta} \right) , \tag{1.31}$$

$$\boldsymbol{m}_j = -\mu_{\mathrm{B}} \left(\boldsymbol{r}_j \times \boldsymbol{p}_j + \frac{g_{\mathrm{e}}}{2} \boldsymbol{\sigma}_j \right) \tag{1.32}$$

the electric dipole, electric quadrupole and magnetic dipole operators, respectively. To simplify notation, we have defined $U_\kappa(\boldsymbol{R}_j) = |\boldsymbol{k}|^{-1} J_{\boldsymbol{u}_\kappa}(\boldsymbol{R}_j)$ with $J_{\boldsymbol{u}_\kappa}$ the Jacobian matrix of $\boldsymbol{u}_\kappa$ at $\boldsymbol{R}_j$. This simplified Hamiltonian (1.29) reveals the main forms of atom-light interaction. The second term corresponds to the Zeeman coupling between the total magnetic moment of the electron and the magnetic field. The third term, coupling the electric dipole to the magnetic field, is known as the diamagnetic term. We will disregard it as it is negligible when compared to the others for small per-particle couplings [104]. Besides, it is biquadratic in matter and bosonic operators and thus intractable with the theories that we develop in this thesis. The other coupling terms are linear in bosonic operators and thus tractable. Note that we could have identified

$$\boldsymbol{E}^\perp(\boldsymbol{r}) = -\partial_t \boldsymbol{A}(\boldsymbol{r}) = i\sum_\kappa \omega_{\boldsymbol{k}} A_{\boldsymbol{k}} \left(\boldsymbol{u}_\kappa(\boldsymbol{r}) a_\kappa - \mathrm{h.c.} \right) , \tag{1.33}$$

in the fifth and sixth terms, which couple the electric dipole and quadrupole to the transverse electric field, respectively. We keep them as they are for later convenience. The last term corresponds to a self-interaction of the polarization field, and it is typically referred to as the P^2 term. It contains emitter self-energies as well as electrostatic interactions between emitters. In some formulations of the multipolar gauge Hamiltonian these interactions are written

explicitly and shown to cancel the electrostatic interactions present in V_{C} [98]. From this point of view, all electromagnetic interactions between the emitters are field-mediated in the multipolar gauge, eliminating the apparent paradox of instantaneous electrostatic interactions of the Coulomb gauge. However, we choose to keep the P^2 term intact in this case, as we will later use it to cancel some of the light-mediated interactions that will appear when we construct a matter-only effective Hamiltonian in Chaps. 2 and 4. With this, and defining the constants

$$g^{\mathrm{d}}_{\boldsymbol{k}} = \frac{\omega_{\boldsymbol{k}}}{\sqrt{N}}\sqrt{\frac{\omega_{\mathrm{p}}}{\omega_{\boldsymbol{k}}}}\,, \tag{1.34}$$

$$g^{\mathrm{q}}_{\boldsymbol{k}} = \frac{\omega_{\boldsymbol{k}}}{\sqrt{N}}\sqrt{\frac{2\omega_{\boldsymbol{k}}}{mc^2}}\,, \tag{1.35}$$

we can put together the interaction terms to define the coupling operators and coupling constant

$$\begin{aligned} g_{\boldsymbol{k}}C_\kappa = -\sum_j \Bigg(& g^{\mathrm{m}}_{\boldsymbol{k}}\frac{1}{\mu_{\mathrm{B}}}\boldsymbol{m}_j\cdot\boldsymbol{u}_{\perp,\kappa}(\boldsymbol{R}_j) + ig^{\mathrm{d}}_{\boldsymbol{k}}\sqrt{\frac{m\omega_{\mathrm{p}}}{2}}\boldsymbol{d}_j\cdot\boldsymbol{u}_\kappa(\boldsymbol{R}_j) \\ & - ig^{\mathrm{q}}_{\boldsymbol{k}}\frac{m\omega_{\mathrm{p}}}{2}\mathrm{Tr}(U_\kappa(\boldsymbol{R}_j)Q_j)\Bigg) \end{aligned} \tag{1.36}$$

to finally write the Hamiltonian as

$$\begin{aligned} H = {} & H_{\mathrm{m}} + \sum_\kappa \omega_{\boldsymbol{k}} a^\dagger_\kappa a_\kappa + \sum_\kappa g_{\boldsymbol{k}}\left(C_\kappa a_\kappa + \mathrm{h.c.}\right) \\ & + \sum_\kappa \frac{1}{\Omega_{\boldsymbol{k}}}\left| g^{\mathrm{d}}_{\boldsymbol{k}}\sqrt{\frac{m\omega_{\mathrm{p}}}{2}}\boldsymbol{d}_j\cdot\boldsymbol{u}_\kappa(\boldsymbol{R}_j) - g^{\mathrm{q}}_{\boldsymbol{k}}\frac{m\omega_{\mathrm{p}}}{2}\mathrm{Tr}(U_\kappa(\boldsymbol{R}_j)Q_j)\right|^2 . \end{aligned} \tag{1.37}$$

We have left the P^2 term explicit here, but note that it only depends on matter operators and could be incorporated into H_{m}. With that, the Hamiltonian (1.37) acquires the same form as for the electron liquid in Eq. (1.17).

1.2.3 The generalized Dicke model as the starting point for our large-N theories

The Dicke model

R. H. Dicke introduced the model that now bears his name to describe superradiance in the spontaneous emission of an ensemble of molecules [15]. It is a toy model describing an ensemble of N independent two-level systems interacting

with a quantized electromagnetic field with a wavelength much larger than the spatial extension of the ensemble. The Hamiltonian reads [16]

$$H = \frac{\omega_z}{2}\sum_j \sigma_j^z + \Omega a^\dagger a + \frac{\lambda}{\sqrt{N}}(a + a^\dagger)\sum_j \sigma_j^x \,, \tag{1.38}$$

where ω_z is the transition frequency between two molecular energy levels, Ω is the frequency of an electromagnetic mode and $\lambda/\sqrt{N}$ is the per-particle coupling to the electric field of the quantum electromagnetic mode. Here a, $a^\dagger$ are bosonic creation and destruction operators, $[a, a^\dagger] = 1$, and $\sigma^{x,z}$ are Pauli matrices. The model was later solved at equilibrium in the thermodynamic limit, $N \to \infty$, by Hepp and Lieb and Wang and Hioe [16, 17, 105]. They showed that the model exhibits a second-order phase transition between a normal phase where the dipoles are paramagnetic and the number of photons is zero and a superradiant (also known as photon-condensed) phase where the dipoles are ferromagnetic along x and the number of photons is non-zero.

The relevance of the Dicke model for cavity QED materials lies in the fact that it can be considered as the first and simplest model of a material coupled to a cavity. In fact, one can reach the Dicke model from the many-particle Pauli-Fierz Hamiltonian (1.2) following a series of approximations: neglecting all electron-electron interactions, assuming a uniform vector potential, neglecting the A^2 and Zeeman terms and restricting the Hilbert space to the two electronic energy levels closer to resonance with the fundamental cavity mode. Alternatively, the same is possible from the multipolar gauge formulation of the Hamiltonian, but then it is the P^2 term, instead of the A^2 term, that has to be neglected. These approximations break gauge-invariance and lead to the unphysical prediction of the superradiant phase transition. Thus, the bare Dicke model is nowadays considered inadequate to describe the coupling of electronic dipole transitions to the electromagnetic field [106, 107]. In Chaps. 4 and 5 we will argue that it is a valid starting point to describe the coupling of magnetic molecules to a cavity. In any case, the Dicke model remains a convenient starting point in the theoretical study of cavity QED materials due to its simplicity and the fact that it can be solved analytically.

The generalized Dicke model

Importantly, Hamiltonians (1.17) and (1.37) that we have obtained for an electron liquid and a system of emitters constitute generalized Dicke models. At the risk of repeating ourselves, but for the sake of completeness and future reference, let us rewrite those generalized Dicke model (GDM) Hamiltonians

here as

$$H = H_{\mathrm{m}} + \sum_k \Omega_k b_\kappa^\dagger b_\kappa + \sum_k g_k \left(C_k b_k + \mathrm{h.c.}\right) . \tag{1.39}$$

The cavity is multimode (note that k here is an index over arbitrary modes) and the cavity system remains unspecified in the matter Hamiltonian H_{m} and the coupling operators C_k. Crucially, the coupling term is linear in cavity operators and the material system has N degrees of freedom, with the matter coupling operators being collective, $C_k \sim N$, and the coupling constants scaling as $1/\sqrt{N}$, i.e., $g_k = \lambda_k/\sqrt{N}$ with λ_k the collective coupling per mode, just like in the original Dicke model. The scaling $g_k \sim 1/\sqrt{N}$ stems from the thermodynamic limit. By default, the cavity fields depend on the inverse square root of the mode volume $\boldsymbol{A}(\boldsymbol{r}) \sim 1/\sqrt{V}$. To ensure a well-defined thermodynamic limit, we assume a finite density of material degrees of freedom in the cavity, $\rho = N/V = \mathrm{cst.}$. Accordingly, we find that the cavity volume must scale as $V \sim N$ and thus that the cavity field must scale as $\boldsymbol{A}(\boldsymbol{r}) \sim 1/\sqrt{N}$ for $N \to \infty$. With this and the fact that all the coupling constants are proportional to the vector potential [Cf. the expressions of $g^{\mathrm{e}}_{\boldsymbol{k}}$ (1.10), $g^{\mathrm{m}}_{\boldsymbol{k}}$ (1.11), $g^{\mathrm{d}}_{\boldsymbol{k}}$ (1.34) and $g^{\mathrm{q}}_{\boldsymbol{k}}$ (1.35)], we get that $g_k \sim 1/\sqrt{N}$. Note that the original Dicke model is a particular case of the GDM with $H_{\mathrm{m}} = \omega_z/2 \sum_j \sigma_j^z$, $C_0 = \sum_j \sigma_j^x$ and $g_0 = \lambda/\sqrt{N}$.

Other generalizations of the Dicke model have been considered previously. Some of these generalizations already include inhomogeneous couplings, multimode cavities or intrinsic interactions [108, 109]. The generalized Dicke model presented here goes beyond previous models by being completely agnostic of the material subsystem, besides the aforementioned scaling assumptions.

Note that although here we have arrived to the GDM from a microscopic theory of electronic cavity QED materials it can also be applied to other systems. Most trivially, it can describe a material coupled to other bosonic excitations, such as quantized LC circuits (See Sec. 5.2.2), magnons [110] or phonon-polaritons [28]. Furthermore, it can also describe models in which N material bosonic excitations, such as optical phonons [42], couple linearly to the cavity modes.

1.3 Previous large-N theories of cavity QED materials

In this section, we will review some works than can be considered precursors of the results laid out in this thesis, in the sense that they also constitute large-N theories of cavity QED materials or the Dicke model.

1.3.1 The thermodynamic limit of the Dicke model

We will start by reviewing different solutions of the Dicke model which rely on the thermodynamic limit.

Hepp and Lieb's solution: Lieb-Berezin inequalities

In their seminal papers [16, 105] Hepp and Lieb provide an exact solution for the Dicke model (1.38) based on a Lieb-Berezin inequality. Lieb-Berezin inequalities provide lower and upper bounds for the partition function of a quantum system [111, 112]. In the particular case of the Dicke model, these read

$$\tilde{Z} \leq Z \leq e^{\beta\Omega}\tilde{Z}\,, \tag{1.40}$$

where Z is the true partition function of the Dicke model, which written in terms of bosonic coherent states reads

$$Z = \mathrm{Tr}_{\mathrm{m}}\left[\int \frac{d^2\alpha}{\pi}\langle\alpha|e^{-\beta H}|\alpha\rangle\right], \tag{1.41}$$

and $\tilde{Z}$ is the simpler

$$\tilde{Z} = \mathrm{Tr}_{\mathrm{m}}\left[\int \frac{d^2\alpha}{\pi}e^{-\beta\langle\alpha|H|\alpha\rangle}\right]. \tag{1.42}$$

Crucially, in the thermodynamic limit, $N \to \infty$, the exponential prefactor in the right-hand side of Eq. (1.40) is negligible, and the partition function is given by $Z = \tilde{Z}$. Note that

$$\langle\alpha|H|\alpha\rangle = \frac{\omega_z}{2}\sum_j \sigma_j^z + \Omega|\alpha|^2 + \frac{2\lambda}{\sqrt{N}}\,\mathrm{Re}(\alpha)\sum_j \sigma_j^x \tag{1.43}$$

is the Hamiltonian of a collection of free spins, such that taking the trace over the matter, the partition function can be written as

$$\tilde{Z} = \int \frac{d^2\alpha}{\pi}e^{-\beta(\Omega|\alpha|^2 + N\log[2\cosh(\beta\epsilon)])}\,, \tag{1.44}$$

with

$$2\epsilon = \sqrt{\omega_z^2 + \left(4\frac{\lambda}{\sqrt{N}}\,\mathrm{Re}(\alpha)\right)^2}\,. \tag{1.45}$$

Performing the trivial integration over the imaginary part of α and rescaling the real part as $u = \mathrm{Re}(\alpha)/\sqrt{N}$, the remaining integral over the real part can be written as

$$\tilde{Z} \propto \int du e^{-N\beta f(u)} \tag{1.46}$$

with $f(u)$ independent of N

$$f(u) = \Omega u^2 - \frac{1}{\beta}\log[2\cosh(\beta\epsilon)]\,. \tag{1.47}$$

In the thermodynamic limit, $N \to \infty$, the integral can be computed via the saddle-point method in terms of the minimum of $f(u)$, which is revealed to be a variational free energy of the Dicke model. A minimization yields the equilibrium free energy [108]

$$-\beta f = \begin{cases} \ln\left[2\cosh\left(\beta\dfrac{\omega_z}{2}\right)\right] & \text{if} \quad \lambda < \lambda_{\rm c}/\tanh(\beta\omega_z/2)\,, \\ \ln\left[2\cosh\left(\beta\bar{\epsilon}\right)\right] - \beta\Omega\bar{u}^2 & \text{if} \quad \lambda > \lambda_{\rm c}/\tanh(\beta\omega_z/2)\,, \end{cases} \tag{1.48}$$

where $\lambda_{\rm c} = \sqrt{\Omega\omega_z}/2$ is the zero-temperature critical coupling, $\bar{\epsilon} = \epsilon(\bar{u})$ and $\bar{u}$ is determined by solving

$$\Omega\bar{\epsilon} = 2\lambda^2\tanh(\beta\bar{\epsilon})\,, \tag{1.49}$$

which corresponds to the non-trivial solution of the vanishing-gradient condition for $f(u)$. The simultaneous photon-field and spin flip symmetry, $a \to -a$ and $\sigma_j^x \to -\sigma_j^x$, of the Dicke model is spontaneously broken in a second-order quantum phase transition between a normal phase with $u = 0$ and a superradiant phase with $u \neq 0$. In the symmetry-broken phase the number of photons is macroscopic, since it grows as $n_{\rm ph} = Nu^2$, hence the name superradiant.

Wang and Hioe's solution: Commuting rescaled bosonic operators

Wang and Hioe's solution of the Dicke model is similar to that of Hepp and Lieb, in the sense that it also stems from proving that $Z = \tilde{Z}$. However instead of invoking the Lieb-Berezin bounds, they argue in terms of the commutation properties of rescaled bosonic operators [17].

The Hamiltonian of the Dicke model can be written in terms of rescaled bosonic operators, $b = a/\sqrt{N}$ and $b^\dagger = a^\dagger/\sqrt{N}$, which we assume to have a well-defined thermodynamic limit, $N \to \infty$. Then, we can see that their commutator is $[b, b^\dagger] = 1/N$ and vanishes for $N \to \infty$. With this, we can expand the exponential

$$e^{-\beta H} = \sum_n \frac{(-\beta H)^n}{n!}\,. \tag{1.50}$$

A typical term in the expansion will consist of a disordered collection of rescaled creation and annihilation operators. Using Wick's theorem, such a term can be expressed as a sum of normal-ordered strings of rescaled operators and the

terms in the sum corresponding to single, double, and higher order contractions will carry factors $1/N$ stemming from the commutation relation. For instance

$$b^\dagger b b^\dagger b b^\dagger b = b^\dagger b^\dagger b^\dagger b b b + \frac{3}{N} b^\dagger b^\dagger b b + \frac{1}{N^2} b^\dagger b \,. \tag{1.51}$$

In the thermodynamic limit, all the terms proportional to some power of $1/N$ can be neglected, such that

$$\langle \alpha | e^{-\beta H} | \alpha \rangle = \sum_n \frac{(-\beta \langle \alpha | H | \alpha \rangle)^n}{n!} = e^{-\beta \langle \alpha | H | \alpha \rangle} \,, \tag{1.52}$$

and thus $Z = \tilde{Z}$. From here, the partition function can be computed as outlined in Sec. 1.3.1.

Emary and Brandes' solution: Bosonization of the emitters

Emary and Brandes' solution of the Dicke model differs from the previous ones in that it is only valid at zero temperature, and it only solves the maximum total spin subspace of the Dicke Hamiltonian, which is the most interesting, since it contains the ground and first-excited states. It does so by bosonizing the total spin operators with a Holstein-Primakov transformation.

The Hamiltonian of the Dicke model (1.38) can be written in terms of total spin operators

$$H = \omega_z S_z + \Omega a^\dagger a + \frac{\lambda}{\sqrt{N}} (S_- + S_+)(a + a^\dagger) \,, \tag{1.53}$$

with $S_\alpha = \sum_j \sigma_j^\alpha / 2$. Since the total spin $\boldsymbol{S}^2$ commutes with the Hamiltonian, $[\boldsymbol{S}^2, H] = 0$, the Hamiltonian is divided in non-interacting subspaces of fixed total spin S. In particular, we can focus on solving the subspace of maximum total spin $S = N/2$. Thus, in the following we take the total spin operators S_α to be spin $S = N/2$ operators. The Holstein-Primakov transformation provides a mapping between bosonic annihilation and creation operators and spin operators

$$S_z = b^\dagger b - N \,, \tag{1.54}$$

$$S_+ = \sqrt{N} b^\dagger \sqrt{1 - \frac{b^\dagger b}{N}} \,, \tag{1.55}$$

$$S_- = \sqrt{N} \sqrt{1 - \frac{b^\dagger b}{N}} b \,, \tag{1.56}$$

with $[b, b^\dagger] = 1$. Ignoring constants, the resulting bosonic Hamiltonian reads

$$H = \omega_z b^\dagger b + \Omega a^\dagger a + \lambda \left(b^\dagger \sqrt{1 - \frac{b^\dagger b}{N}} + \sqrt{1 - \frac{b^\dagger b}{N}} b \right) \left(a + a^\dagger \right) \,. \tag{1.57}$$

To allow for the description of both a normal and a symmetry-broken phase, in which the bosonic degrees of freedom acquire macroscopic occupations, we displace the bosonic operators as

$$a^\dagger \to c^\dagger + \sqrt{\alpha}\,, \tag{1.58}$$

$$b^\dagger \to d^\dagger - \sqrt{\beta}\,, \tag{1.59}$$

with α and β real parameters whose value we will determine later but which are assumed to scale as N. This is equivalent to assuming that in the symmetry broken phases the two modes acquire a macroscopic occupation. Note that this constitutes an ansatz as to what are the quasiparticle excitations in the ordered phase. With these displacements and ignoring constants, the Hamiltonian becomes

$$\begin{aligned} H = {} & \omega_z \left(d^\dagger d - \sqrt{\beta}(d + d^\dagger) \right) + \Omega \left(c^\dagger c + \sqrt{\alpha}(c + c^\dagger) \right) \\ & + \lambda \sqrt{\frac{k}{N}} \left(d^\dagger \sqrt{\xi} + \sqrt{\xi} d - 2\sqrt{\beta}\sqrt{\xi} \right) \left(c + d^\dagger + 2\sqrt{\alpha} \right) , \end{aligned} \tag{1.60}$$

with

$$\sqrt{\xi} = \sqrt{1 - \frac{d^\dagger d - \sqrt{\beta}(d + d^\dagger)}{k}}\,, \tag{1.61}$$

and $k = N - \beta$. From here, the Hamiltonian can be solved in three steps. First, taking the thermodynamic limit by expanding the square root $\sqrt{\xi}$ and setting terms with overall powers of N in the denominator to zero. Then, imposing that the linear terms of the resulting Hamiltonian vanish, which yields the ground-state values of the occupations $\sqrt{\alpha}$ and $\sqrt{\beta}$. These are in agreement with the expectation values that can be computed in the exact solution of Sec. 1.3.1. The resulting model is quadratic, and its coefficients depend on the values of $\sqrt{\alpha}$ and $\sqrt{\beta}$. It can be diagonalized with a Bogoliubov transformation to reveal the excitation energies of the system. More details about the method can be found in App. G, where we generalize it for models that also feature intrinsic collective interactions.

1.3.2 Neglecting light-matter entanglement in the thermodynamic limit of electron liquids

In Refs. [76, 77], Andolina *et al.* introduce a theory for equilibrium superradiance (which they call photon condensation) in electron liquids. Similarly to Wang and Hioe's solution of the Dicke model, their theory relies on the commutation properties of conveniently rescaled operators.

For simplicity and following Ref. [76], we consider a single uniform cavity and disregard the Zeeman coupling. Following Sec. 1.2.1, its Hamiltonian is

given by

$$H = H_{\rm m} + \tilde{\omega} b^\dagger b + \frac{\omega_{\rm p}}{\sqrt{N}} \sqrt{\frac{1}{2m\tilde{\omega}}} \sum_j \boldsymbol{p}_j \cdot \boldsymbol{u} \left(b + b^\dagger \right) , \tag{1.62}$$

with $\tilde{\omega}^2 = \Omega^2 + \omega_{\rm p}^2$. We can separate the Hamiltonian into matter, photon and interaction terms $H = H_{\rm m} + H_{\rm ph} + H_{\rm int}$ and assume that $H_{\rm m}/N$, $H_{\rm ph}/N$ and $H_{\rm int}/N$ have well-defined $N \to \infty$ limits. Then, it can be shown that $\lim_{N\to\infty}[H_{\rm m}/N, H_{\rm int}/N] = \lim_{N\to\infty}[H_{\rm ph}/N, H_{\rm int}/N] = 0$, which is used to justify the approximation that there is no light-matter entanglement in the thermodynamic limit and that we can write the ground state as $|\Psi\rangle = |\psi\rangle \otimes |\alpha\rangle$, with $|\psi\rangle$ the electronic wavefunction and $|\alpha\rangle$ a bosonic coherent state. With this, the ground state energy is given by

$$E_\psi(\alpha) = \langle\psi|H_{\rm m}|\psi\rangle + \tilde{\omega}|\alpha|^2 + 2\,{\rm Re}(\alpha) \frac{\omega_{\rm p}}{\sqrt{N}} \sqrt{\frac{1}{2m\tilde{\omega}}} \sum_j \langle\psi|\boldsymbol{p}_j \cdot \boldsymbol{u}|\psi\rangle \, . \tag{1.63}$$

Minimizing with respect to α shows that $\alpha = {\rm Re}(\alpha)$ and yields the relation

$$\alpha = -\frac{\omega_{\rm p}}{\sqrt{N}} \sqrt{\frac{1}{2m\tilde{\omega}^3}} \sum_j \langle\psi|\boldsymbol{p}_j \cdot \boldsymbol{u}|\psi\rangle \, . \tag{1.64}$$

Now, the minimization with respect to the electronic state is constrained to satisfy Eq. (1.64). The condition for equilibrium superradiance to occur is that a state with a non-zero value of α is the true ground state, i.e., that $E_{\psi_\alpha}(\alpha) \leq E_{\psi_0}(0)$, or equivalently

$$\langle\psi_\alpha|H_{\rm m}|\psi_\alpha\rangle - \langle\psi_0|H_{\rm m}|\psi_0\rangle \leq \tilde{\omega}\alpha^2 \, . \tag{1.65}$$

Note that $|\psi_0\rangle$ is the ground state of the bare electron liquid. Here, the stiffness theorem allows us to expand the left-hand side in powers of α [113, Chap. 3]. In the proximity of a second-order phase transition, for small α, the expansion can be truncated at second order to yield $\langle\psi_\alpha|H_{\rm m}|\psi_\alpha\rangle - \langle\psi_0|H_{\rm m}|\psi_0\rangle \approx -\alpha^2/(2\chi(0))$, with

$$\chi(0) = -\frac{\omega_{\rm p}^2}{Nm\tilde{\omega}^3} \sum_n \frac{|\langle\psi_n| \sum_j \boldsymbol{p}_j \cdot \boldsymbol{u}|\psi_0\rangle}{E_n - E_0} \, , \tag{1.66}$$

proportional to the static paramagnetic current-current response function of the bare electron liquid. Here $|\psi_n\rangle$ and E_n are, respectively, the eigenvectors and eigenvalues of the bare electron liquid. This yields the critical condition for equilibrium superradiance

$$1 \leq \frac{\omega_{\rm p}^2}{\Omega^2 + \omega_{\rm p}^2} \frac{2}{Nm} \sum_n \frac{|\langle\psi_n| \sum_j \boldsymbol{p}_j \cdot \boldsymbol{u}|\psi_0\rangle|^2}{E_n - E_0} \, . \tag{1.67}$$

This critical condition is unsatisfiable, since it can be shown that

$$\frac{2}{Nm}\sum_n \frac{|\langle\psi_n|\sum_j \boldsymbol{p}_j\cdot\boldsymbol{u}|\psi_0\rangle|^2}{E_n-E_0}=1\,. \tag{1.68}$$

This is a no-go theorem for equilibrium superradiance with electron liquids homogeneously coupled to the electromagnetic field. The critical condition can be extended to the case of inhomogeneous fields and to include the Zeeman coupling [77]. The no-go theorem can also be proven for a first-order superradiant phase transition by different means [78].

1.4 Field-theoretical approaches to cavity QED materials

In Chaps. 2 and 3 of this thesis we will develop equilibrium and linear response theories for cavity QED materials that rely on a coherent-state path integral formulation of the partition function of the GDM. To contextualize these chapters, we discuss here related field-theoretical approaches that have been put forth in the last years.

Several works have taken this approach to compute response functions of electronic systems under the assumption of a trivial ground state [32, 36, 80, 86, 96, 114] and also to compute the critical condition to a superradiant scenario [80]. Alternatively, the response functions of dipolar systems have been computed in the large-N limit [59] and with dynamical mean-field theory [45]. In the case of magnetic materials, progress has been more limited, with notable exceptions such as Ref. [115], where ferromagnetic systems were treated within the random phase approximation (RPA).

This thesis, among other contributions, aims to provide a unified theory for electronic, dipolar, and magnetic materials coupled to a cavity, with and without trivial ground states, for both equilibrium properties, e.g. the occurrence of superradiance, and linear response theory.

Chapter 2

Equilibrium theory

Our goal in this chapter is to take the Hamiltonian of the generalized Dicke model (GDM) (1.39) and trace out the photonic degrees of freedom in order to derive a Hamiltonian for the material with effective interactions induced by the coupling to the cavity. To do so, we will formulate the partition function as an integral over coherent light and matter fields. The model being quadratic in the photonic degrees of freedom will allow us to integrate over the photonic fields to obtain an effective matter action. One can foresee that the light-matter coupling present in (1.39) will translate into an effective matter-matter coupling that will appear in the effective action. The effective action will reveal important properties of the light-mediated interaction and will be a key stepping stone in the development of the linear response theory in Chap. 3. In the remainder of the chapter we will abandon the effective action. First, we will show that for $N \to \infty$ it is possible to decouple the effective action and yield a mean-field effective matter Hamiltonian. Then, by invoking the thermodynamic limit again, we will show that this Hamiltonian can be promoted to a regular Hamiltonian. We will thus obtain an effective Hamiltonian, with a structure analogous to the previously obtained effective action, that exactly captures the equilibrium properties of the GDM in the thermodynamic limit. This process is summarized in Fig. 2.1. Finally, we will test the finite size scaling of this effective Hamiltonian, and we will compare it to other effective Hamiltonians.

This chapter is based on parts of Refs. [62, 63].

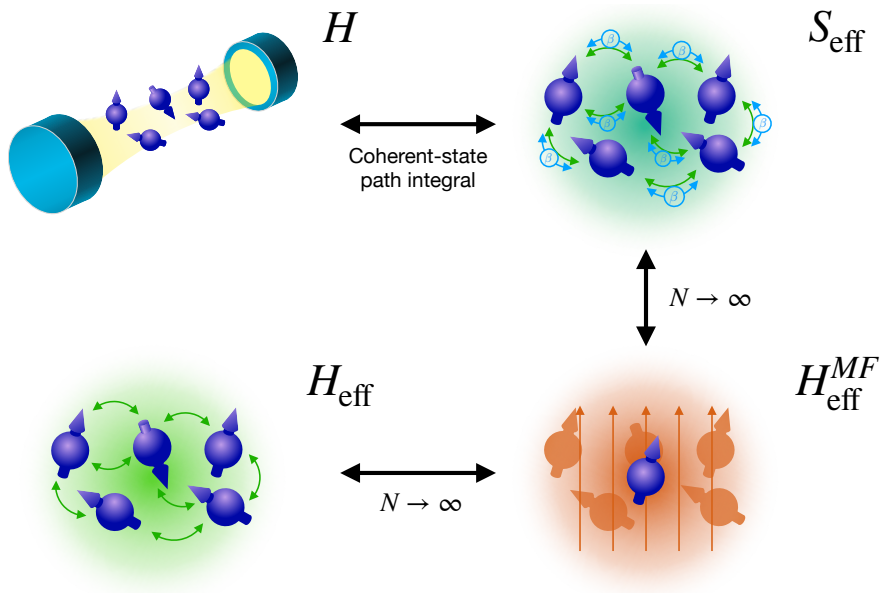

Figure 2.1: Schematic summary of the derivation of the effective Hamiltonian for cavity QED materials. Starting from the GDM we formulate its partition function as a path integral over coherent-state fields. Then, we trace out the cavity to arrive to an effective action. Invoking the thermodynamic limit, we decouple the effective action to produce a mean-field effective Hamiltonian. Finally, invoking the thermodynamic limit again, we promote the mean-field effective Hamiltonian to a proper Hamiltonian.

2.1 Effective action

The partition function of a single-mode bosonic system described by a Hamiltonian H can be written as a path integral over coherent-state fields as

$$Z = \int \mathcal{D}[a, \bar{a}] e^{-S}\,, \tag{2.1}$$

with Euclidean action

$$S = \int_0^\beta \left(\bar{a}(\tau)\partial_\tau a(\tau) + H(a, \bar{a})\right) d\tau\,, \tag{2.2}$$

where $\beta = 1/(k_\mathrm{B}T)$ with k_B the Boltzmann constant and T the temperature, $a(\tau)$ and $\bar{a}(\tau)$ are complex-valued continuous fields over coherent states and $\mathcal{D}[a, \bar{a}]$ is the differential over the fields satisfying the boundary condition $\bar{a}(0) = \bar{a}(\beta)$, $a(0) = a(\beta)$ [116, chapter 4]. Here, $H(a, \bar{a})$ is obtained by replacing the bosonic operators, a and $a^\dagger$, by the fields, $a(\tau)$ and $\bar{a}(\tau)$, in the normal-ordered form of H. This result is readily generalized to the multimode case

$$Z = \int \mathcal{D}[a_k, \bar{a}_k] e^{-S_k} \tag{2.3}$$

with

$$S_k = \int_0^\beta \left(\bar{a}_k \partial_\tau a_k + H_k(a_k, \bar{a}_k)\right) d\tau \,. \tag{2.4}$$

We now focus our attention on a hybrid light-matter system such as the GDM (1.39). We assume that one could formulate a coherent-path-integral partition function for the full system, so we assign an action to the matter Hamiltonian $H_\mathrm{m} \to S_\mathrm{m}$ and a field to the coupling operator $C_k \to C_k(\tau)$, $C_k^\dagger \to \bar{C}_k(\tau)$. We will denote the matter coherent fields by c and the differential over them as $\mathcal{D}[c]$. Knowledge of the precise dependence of S_m, C_k and $\bar{C}_k$ on material coherent fields is not required for what follows. With these definitions, the total action can be written as

$$S = S_\mathrm{m} + \sum_k S_k \,, \tag{2.5}$$

with

$$S_k = \int_0^\beta \left(\bar{a}_k \partial_\tau a_k + \Omega_k \bar{a}_k a_k + g_k \left(C_k a_k + \bar{C}_k \bar{a}_k\right)\right) d\tau \,, \tag{2.6}$$

For such a system, we can define an effective matter action by tracing only over the light degrees of freedom in the full partition function

$$Z = \int \mathcal{D}[a_k, \bar{a}_k]\mathcal{D}[c] e^{-S} =: Z_\mathrm{ph} \int \mathcal{D}[c] e^{-S_\mathrm{eff}} \,. \tag{2.7}$$

It should be noted that S_eff is useful because it makes explicit the influence of the cavity on the matter degrees of freedom. In particular, the type of interactions that emerge. In addition, as we show in Sec. 2.4, no information is lost because light observables can be written in terms of matter observables, which can be calculated from S_eff.

We are thus interested in computing

$$\int \mathcal{D}[a_k, \bar{a}_k] e^{-\sum_k S_k} \,. \tag{2.8}$$

Since the trajectories are periodic $a(0) = a(\beta)$, $\bar{a}(0) = \bar{a}(\beta)$, we can expand the fields as a Fourier series

$$a_k(\tau) = \frac{1}{\beta} \sum_n a_k(\omega_n) e^{-i\omega_n \tau} \,, \tag{2.9}$$

$$\bar{a}_k(\tau) = \frac{1}{\beta} \sum_n \bar{a}_k(\omega_n) e^{i\omega_n \tau} \,. \tag{2.10}$$

with the Matsubara frequencies $\omega_n = \frac{2\pi n}{\beta}$. Inserting Eqs. (2.9), (2.10) in the action (2.6) yields

$$S_k = \frac{1}{\beta} \sum_n \left(\left(-i\omega_n + \Omega_k\right) \bar{a}_k(\omega_n) a_k(\omega_n) - g_k (a_k(\omega_n) C_k(\omega_n) + \text{c.c.})\right) \,, \tag{2.11}$$

where

$$C_k(\omega_n) = \int_0^\beta d\tau C_k(\tau) e^{-i\omega_n \tau}\,, \tag{2.12}$$

$$\bar{C}_k(\omega_n) = \int_0^\beta d\tau \bar{C}_k(\tau) e^{i\omega_n \tau}\,. \tag{2.13}$$

The functional differential over temperature trajectories in Eq. (2.8) is replaced with the differential over frequency trajectories. The result is simply a collection of n-dimensional Gaussian integrals for each mode k, yielding

$$\int \mathcal{D}[a_k, \bar{a}_k] e^{-\sum_k S_k} = Z_{\rm ph} \exp\left[-\sum_k g_k^2 \int_0^\beta d\tau d\tau' C_k(\tau) D_{k,0}(\tau - \tau') \bar{C}_k(\tau') \right], \tag{2.14}$$

where $D_{k,0}$ is the free propagator of the k-th photonic mode

$$D_{k,0}(\tau) = \frac{1}{\beta} \sum_n D_{k,0}(\omega_n) e^{-i\omega_n \tau}\,, \tag{2.15}$$

with

$$D_{k,0}(\omega_n) = \frac{1}{i\omega_n - \Omega_k}\,. \tag{2.16}$$

At this point, the prefactor $Z_{\rm ph}$ defined in Eq. (2.7) acquires meaning: $Z_{\rm ph} = \prod_k Z_k$, where $Z_k = [1 - \exp(-\beta\Omega_k)]^{-1}$ is the partition function of a harmonic oscillator of frequency Ω_k. We can now put together the effective action as defined in Eq. (2.7)

$$S_{\rm eff} = S_{\rm m} + \sum_k \lambda_k^2 \iint_0^\beta d\tau d\tau' C_k(\tau) \frac{1}{N} D_{k,0}(\tau - \tau') \bar{C}_k(\tau')\,. \tag{2.17}$$

After tracing out the light degrees of freedom, the light-matter interaction appears translated into an induced retarded collective interaction between matter degrees of freedom [117, 118]. The elimination of the cavity allows us to study the modification of material properties from the point of view of the matter subsystem. However, the non locality of the effective interaction implies that Eq. 2.17 does not have straightforward analytical applicability. In particular, we cannot recover an equivalent Hamiltonian. That is, we cannot undo our agnostic substitutions $H_{\rm m} \to S_{\rm m}$, $C_k \to C_k$ and $C_k^\dagger \to \bar{C}_k$, to revert the description of the matter subsystem from an action-based one to a Hamiltonian-based one. This is because not all fields depend on the same temperature in this non-local action. This should not come as a surprise, since in classical statistical mechanics when integrating a subpart of the whole system the magnitudes that involve the remaining degrees of freedom can be calculated from a temperature-dependent effective Hamiltonian [119]. Equivalently, in

bipartite quantum systems, the (temperature dependent) Hamiltonian of mean force describes the equilibrium properties of a partition [120, 121]. On the other hand, (2.17) is formally analogous to the effective action after tracing out the environment degrees of freedom in the path integral formulation of open quantum systems [118, 122].

We will show next how this effective action can be decoupled to arrive to a mean-field effective Hamiltonian in the thermodynamic limit $N \to \infty$.

2.2 Mean-field effective Hamiltonian in the thermodynamic limit

Since we have already familiarized ourselves with the path-integral formalism in the last section, it is convenient to introduce henceforth a more concise notation. We will use $\oint_c \equiv \int \mathcal{D}[c]$ to indicate the path integrals over periodic coherent-state paths and $\int_\tau \equiv \int_0^\beta d\tau$ to indicate integrals over imaginary time.

The effective interaction can be decoupled with a Hubbard-Stratonovich transformation that introduces complex conjugate auxiliary scalar fields for each mode, φ_k and $\bar{\varphi}_k$ [45, 59]:

$$e^{-S_{\rm eff}} = e^{-S_{\rm m}} \frac{1}{Z_\varphi} \oint_{\varphi,\bar{\varphi}} \exp\Big(-N \sum_k \int_{\tau,\tau'} \bar{\varphi}_k(\tau) D^{-1}_{k,0}(\tau-\tau')\varphi_k(\tau') - i \sum_k \lambda_k \int_\tau (\varphi_k(\tau) C_k(\tau) + \bar{\varphi}(_k\tau)\bar{C}_k(\tau))\Big) . \tag{2.18}$$

Note that, with this definition, the auxiliary fields do not scale with N, i.e., $\varphi_k, \bar{\varphi}_k \sim \mathcal{O}(1)$. We can now define $\mathcal{G}^0_{\rm m}[\xi_k, \bar{\xi}_k] = -N^{-1} \log Z_{\rm m}[\xi_k, \bar{\xi}_k]$, with

$$Z_{\rm m}[\xi_k, \bar{\xi}_k] = \oint_c \exp\left[- \left(S_{\rm m} + i \sum_k \int_\tau (\xi_k(\tau) C_k(\tau) + \bar{\xi}_k \bar{C}_k(\tau)) \right) \right] . \tag{2.19}$$

We will see in Chap. 3 that objects such as $\mathcal{G}^0_{\rm m}$ are the generators of connected correlation functions, but for now it suffices to know that its first derivatives provide expectation values of the matter coupling operators

$$\left. \frac{\delta \mathcal{G}^0_{\rm m}}{\delta \xi_k(\tau)} \right|_{\xi_k, \bar{\xi}_k = 0} = \frac{i}{N} \langle C_k(\tau) \rangle , \tag{2.20}$$

$$\left. \frac{\delta \mathcal{G}^0_{\rm m}}{\delta \bar{\xi}_k(\tau)} \right|_{\xi_k, \bar{\xi}_k = 0} = \frac{i}{N} \langle \bar{C}_k(\tau) \rangle^{\rm c} . \tag{2.21}$$

With this, the partition function can be written as [59]

$$Z = \frac{Z_{\rm ph}}{Z_\varphi} \oint_{\varphi_k, \bar{\varphi}_k} e^{-N\beta f[\varphi_k, \bar{\varphi}_k]} , \tag{2.22}$$

with

$$f[\varphi_k, \bar{\varphi}_k] = \frac{1}{\beta} \sum_k \int_{\tau,\tau'} \bar{\varphi}_k(\tau) D^{-1}_{k,0}(\tau - \tau') \varphi_k(\tau') + \frac{1}{\beta} \mathcal{G}^0_{\mathrm{m}}[\lambda_k \varphi_k, \lambda_k \bar{\varphi}_k] \,. \quad (2.23)$$

The exponent is explicitly proportional to N, with f being an intensive quantity. This suggests that it can be treated with the saddle-point method for large N: the integral can be well approximated by expanding f around the minimizing paths $\varphi_{k,\mathrm{sp}}$. The number of terms required for a good approximation will be determined by the value of N. In the thermodynamic limit, $N \to \infty$, it will be justified to truncate the expansion at the quadratic term, yielding an integrable action. To check the validity of the truncation, the correction stemming from the quadratic term must be negligible with respect to the constant term. This is true provided that the number of auxiliary fields M is negligible with respect to N in the thermodynamic limit, i.e., provided that $\lim_{N\to\infty} M/N = 0$. See App. B for a detailed explanation. The number of auxiliary fields M required in the Hubbard-Stratonovich transformation to eliminate the effective coupling in the action, is given by the number of distinct interaction channels, i.e., the number of distinct $\{C_k\}$. Generally, we associate one distinct C_k per cavity mode, and hence the condition $\lim_{N\to\infty} M/N = 0$ poses a limitation to the number of cavity modes that we can consider with this formalism. However, it is also possible to consider situations in which $C_k = C \; \forall k$ [50, 70], in which case only one auxiliary field is necessary, and the number of modes is unrestricted. This is the case under a zeroth-order long-wavelength approximation, where the spatial dependence of the light-matter coupling is disregarded completely. Under these conditions, this formalism could also be applied to waveguide QED setups, where a continuum of electromagnetic modes is considered.

With this, we find that in the thermodynamic limit $f[\varphi_{k,\mathrm{sp}}, \bar{\varphi}_{k,\mathrm{sp}}]$ is precisely the free energy per particle

$$f[\varphi_{k,\mathrm{sp}}, \bar{\varphi}_{k,\mathrm{sp}}] = -\lim_{N\to\infty} \frac{1}{\beta N} \log Z \,, \quad (2.24)$$

and thus the equilibrium properties of the system are determined by it. The saddle point is defined by the condition of vanishing gradient of the action

$$\int_{\tau'} D^{-1}_{k,0}(\tau - \tau') \varphi_{k,\mathrm{sp}}(\tau') + \frac{i\lambda_k}{N} \langle C_k(\tau) \rangle_{\lambda_k \varphi_{k,\mathrm{sp}}, \lambda_k \bar{\varphi}_{k,\mathrm{sp}}} = 0 \,, \quad (2.25)$$

$$\int_{\tau} \bar{\varphi}_{k,\mathrm{sp}}(\tau) D^{-1}_{k,0}(\tau - \tau') + \frac{i\lambda_k}{N} \langle C_k(\tau) \rangle_{\lambda_k \varphi_{k,\mathrm{sp}}, \lambda_k \bar{\varphi}_{k,\mathrm{sp}}} = 0 \quad (2.26)$$

or in Matsubara-frequency space

$$\varphi_{k,\mathrm{sp}}(\omega_n) = -\frac{i\lambda_k}{N} D_{k,0}(\omega_n) \langle C_k(\omega_n) \rangle_{\lambda_k \varphi_{k,\mathrm{sp}}, \lambda_k \bar{\varphi}_{k,\mathrm{sp}}} \,, \quad (2.27)$$

$$\bar{\varphi}_{k,\mathrm{sp}}(\omega_n) = -\frac{i\lambda_k}{N} D_{k,0}(\omega_n) \langle \bar{C}_k(\omega_n) \rangle_{\lambda_k \varphi_{k,\mathrm{sp}}, \lambda_k \bar{\varphi}_{k,\mathrm{sp}}} \,. \quad (2.28)$$

Note that, following Eq. (2.19), $\langle\cdot\rangle_{\xi_k,\bar{\xi}_k}$ indicates a bare matter average but subject to fields $i\xi_k$ and $i\bar{\xi}_k$.

We look for constant solutions to these saddle point equations

$$\varphi_{k,\mathrm{sp}}(\tau) = \varphi_{k,\mathrm{sp}} = \varphi_{k,\mathrm{sp}}(\omega_n = 0)\,. \tag{2.29}$$

Then, from Eqs. 2.27 and 2.28 we find

$$\varphi_{k,\mathrm{sp}} = -\frac{i\lambda_k}{N} D_{k,0}(\omega_n = 0)\langle C_k\rangle_{\lambda_k\varphi_{k,\mathrm{sp}},\lambda_k\bar{\varphi}_{k,\mathrm{sp}}}\,, \tag{2.30}$$

$$\bar{\varphi}_{k,\mathrm{sp}} = -\frac{i\lambda_k}{N} D_{k,0}(\omega_n = 0)\langle \bar{C}_k\rangle_{\lambda_k\varphi_{k,\mathrm{sp}},\lambda_k\bar{\varphi}_{k,\mathrm{sp}}}\,. \tag{2.31}$$

This tells us that the $\varphi_{k,\mathrm{sp}}$ and $\bar{\varphi}_{k,\mathrm{sp}}$ are self-consistently proportional to $\langle C_k\rangle_{\lambda_k\varphi_{k,\mathrm{sp}},\lambda_k\bar{\varphi}_{k,\mathrm{sp}}}$ and $\langle \bar{C}_k\rangle_{\lambda_k\varphi_{k,\mathrm{sp}},\lambda_k\bar{\varphi}_{k,\mathrm{sp}}}$, i.e., to the expectation value of C_k and $\bar{C}_k$ for the bare matter subject to fields

$$i\lambda_k\varphi_{k,\mathrm{sp}} = -\frac{\lambda_k^2}{N\Omega_k}\langle C_k\rangle\,, \tag{2.32}$$

$$i\lambda_k\bar{\varphi}_{k,\mathrm{sp}} = -\frac{\lambda_k^2}{N\Omega_k}\langle \bar{C}_k\rangle\,. \tag{2.33}$$

These are precisely the self-consistent conditions that arise from computing $\langle C_k\rangle$ and $\langle \bar{C}_k\rangle$ from the mean-field Hamiltonian

$$H_{\mathrm{eff}}^{\mathrm{MF}} = H_{\mathrm{m}} - \sum_k \frac{\lambda_k^2}{N\Omega_k}\left(\langle C_k^\dagger\rangle C_k + \langle C_k\rangle C_k^\dagger\right) + \sum_k \frac{\lambda_k^2}{N\Omega_k}|\langle C_k\rangle|^2\,, \tag{2.34}$$

by minimizing the free energy variationally with respect to $\langle C_k\rangle$.

The same conclusion can be reached by plugging the saddle point equations, Eqs. (2.30) and (2.31), into $f[\varphi_{k,\mathrm{sp}},\bar{\varphi}_{k,\mathrm{sp}}]$. Doing so makes it evident that it is precisely the free energy per particle of the mean-field effective Hamiltonian (2.34).

The fact that we can describe the equilibrium properties of the GDM in terms of a mean-field matter-only Hamiltonian implies that we will be able to provide an exact solution for the GDM provided that H_{m} is solvable and remains so after the addition of the mean field. In Chap. 5 we will see some non-trivial examples of this.

2.3 Promoting the mean-field effective Hamiltonian to a full Hamiltonian

We will now show that the equilibrium properties of a system described by a Hamiltonian of the form

$$H_{\rm eff} = H_{\rm m} - \sum_k \frac{g_k^2}{\Omega_k} C_k C_k^\dagger \,, \tag{2.35}$$

where the sum runs over M collective interactions, are also described exactly by $H_{\rm eff}^{\rm MF}$ (2.34) in the thermodynamic limit, $N \to \infty$. In other words, we will show that the mean-field effective Hamiltonian, $H_{\rm eff}^{\rm MF}$ (2.34), can be promoted to a proper effective Hamiltonian, $H_{\rm eff}$ (2.35). The proof follows the same logic that we used in the previous section for the GDM, so we will be concise this time around.

The partition function can be formulated as a path integral over coherent state fields with action

$$S = S_{\rm m} + \sum_k \int_{\tau\tau'} C_k(\tau) \frac{1}{N} K_k(\tau - \tau') \bar{C}_k(\tau') \,, \tag{2.36}$$

with

$$K_k(\tau) = -\frac{\lambda_k^2}{\Omega_k} \delta(\tau) \tag{2.37}$$

and so

$$K_k(\omega_n) = \frac{\lambda_k^2}{\Omega_k} \,. \tag{2.38}$$

The interaction can be decoupled with a Hubbard-Stratonovich transformation and after a partial integration over the matter coherent fields we can write the partition function as

$$Z = \frac{1}{Z_\phi} \oint_{\phi_k, \bar{\phi}_k} e^{-N\beta f[\phi_k, \bar{\phi}_k]} \,, \tag{2.39}$$

with

$$f[\phi_k, \bar{\phi}_k] = \frac{1}{\beta} \sum_k \int_{\tau,\tau'} \bar{\phi}_k(\tau) K_k^{-1}(\tau - \tau') \phi_k(\tau') + \frac{1}{\beta} \mathcal{G}_{\rm m}^0[\phi_k, \bar{\phi}_k] \,. \tag{2.40}$$

The exponent being explicitly proportional to N we can apply the saddle point method to reveal that in the thermodynamic limit, $N \to \infty$, the free energy per particle is given by $f[\phi_{k,\rm sp}, \bar{\phi}_{k,\rm sp}]$, with

$$\phi_{k,\rm sp}(\omega_n) = -\frac{i}{N} K_k(\omega_n) \langle C_k(\omega_n) \rangle_{\phi_{k,\rm sp}, \bar{\phi}_{k,\rm sp}} \,, \tag{2.41}$$

$$\bar{\phi}_{k,\rm sp}(\omega_n) = -\frac{i}{N} K_k(\omega_n) \langle \bar{C}_k(\omega_n) \rangle_{\phi_{k,\rm sp}, \bar{\phi}_{k,\rm sp}} \,, \tag{2.42}$$

provided that the number of interaction channels M satisfies $\lim_{N\to\infty} M/N = 0$ (See App. B for details). Assuming a constant solution to the saddle point equations we find that the $\phi_{k,\mathrm{sp}}$ and $\bar{\phi}_{k,\mathrm{sp}}$ are self-consistently proportional to $\langle C_k\rangle_{\phi_{k,\mathrm{sp}},\bar{\phi}_{k,\mathrm{sp}}}$ and $\langle \bar{C}_k\rangle_{\phi_{k,\mathrm{sp}},\bar{\phi}_{k,\mathrm{sp}}}$, i.e., to the expectation value of C_k and $\bar{C}_k$ for the bare matter subject to fields

$$i\phi_{k,\mathrm{sp}} = -\frac{\lambda_k^2}{N\Omega_k}\langle C_k\rangle\,, \tag{2.43}$$

$$i\bar{\phi}_{k,\mathrm{sp}} = -\frac{\lambda_k^2}{N\Omega_k}\langle \bar{C}_k\rangle\,. \tag{2.44}$$

These are precisely the self-consistent conditions that arise from computing $\langle C_k\rangle$ and $\langle \bar{C}_k\rangle$ from the mean-field effective Hamiltonian (2.34).

With this, we have shown that the equilibrium properties of the original GDM and of the matter only model described by H_{eff} (2.35) are the same, in the sense that the interactions in both are of mean-field nature and lead to the same mean-field effective Hamiltonian (2.34). In particular, the effect that the cavity has on the material subsystem is revealed explicitly in the induced interaction in the second term of the right-hand side of Eq. (2.35). Sometimes similar effective interactions are obtained by invoking approximations such as perturbation theory. Here we show that they are exact in the thermodynamic limit for the matter. Besides, this is a rather general result. We emphasize that the cavity-matter coupling has been discussed under general grounds in Chapter 1, and Eq. (2.35) follows from it.

At the same time, our derivation has revealed that the interactions mediated by the cavity are collective and in that sense they can be treated is the same fashion as intrinsic collective interactions. We will exploit this fact further in Chapter 3. We have also shown that a model with a finite number of collective interactions [Eq. (2.35)] can be solved in the thermodynamic limit, since it is exactly described by mean-field theory. We will apply this to solve quantum strong long-range models in Chap. 7.

2.4 Relation between light and matter observables

Our effective theory puts emphasis on the behavior of the matter subsystem, to the point where the cavity is eliminated from the Hamiltonian. However, for a complete characterization of the full system one must be able to compute photonic observables and expectation values, such as $\langle a_k\rangle$ and $\langle a_k^\dagger\rangle$, which determine the intensity of the electromagnetic fields in the cavity. We reconcile this necessity with our formalism by noting that in the process of tracing out the photonic degrees of freedom we can extract a relationship between the

expectation values of matter and light observables. To illustrate the idea, let us work out the case of computing $\langle a_p + a_p^\dagger \rangle$. We extend our Hamiltonian to the form

$$H(\eta) = H - \eta(a_p + a_p^\dagger)\,, \tag{2.45}$$

where H is the GDM, such that we can write, as is customary in statistical mechanics, $\beta\langle a_p + a_p^\dagger\rangle = \lim_{\eta\to 0}\partial_\eta \ln Z(\eta)$, with

$$Z(\eta) = \mathrm{Tr}(\exp[-\beta H(\eta)])\,. \tag{2.46}$$

At the same time, we can rewrite $H(\eta)$ as

$$H(\eta) = H_\mathrm{m} + \sum_k \Omega_k a_k^\dagger a_k - \sum_k g_k\left(C_k(\eta)a_k + h.c.\right)\,, \tag{2.47}$$

where $C_k(\eta) = C_k - \delta_{k,p}\eta/g_k$. Following our theory, the corresponding effective Hamiltonian is given by

$$H_\mathrm{eff}(\eta) = H_\mathrm{m} - \sum_k \frac{g_k^2}{\Omega_k} C_k(\eta)C_k^\dagger(\eta)\,. \tag{2.48}$$

Then, following our definition of the effective Hamiltonian (2.35), we can express the partition function as

$$Z(\eta) = \mathrm{Tr}_\mathrm{m}\left(\exp[-\beta H_\mathrm{eff}(\eta)]\right)\,, \tag{2.49}$$

such that

$$\langle a_p + a_p^\dagger\rangle = \frac{1}{\beta}\lim_{\eta\to 0}\partial_\eta \log Z(\eta) = -\frac{g_p}{\Omega_p}\langle C_p + C_p^\dagger\rangle_\mathrm{eff}\,. \tag{2.50}$$

Proceeding in similar fashion, we can compute other observables such as

$$\langle a_p - a_p^\dagger\rangle = \frac{g_p}{\Omega_p}\langle C_p - C_p^\dagger\rangle_\mathrm{eff}\,. \tag{2.51}$$

Here $\langle\cdot\rangle_\mathrm{eff}$ indicates an average computed with the effective Hamiltonian. Another observable of interest is the photon number of the k-th mode

$$\left\langle a_p^\dagger a_p\right\rangle = -\frac{1}{\beta}\partial_{\Omega_p}\ln Z = \left(\frac{g_p}{\Omega_p}\right)^2\langle C_p C_p^\dagger\rangle_\mathrm{eff}\,. \tag{2.52}$$

These relations are important because they show that the expectation value of the cavity fields and the cavity photon number are proportional to the expectation value of the matter coupling operator. If the system undergoes a transition into a phase where $\langle C_p\rangle$ in finite, the cavity develops a photon population proportional to the number of matter degrees of freedom N. In

the context of equilibrium superradiance, that we will discuss in depth in Sec. 4.1, this implies that the superradiant phase transition is synonymous with the phase transition corresponding to the symmetry breaking of the matter coupling operators C_p.

In Chap. 3 we will obtain further relationships between the light and matter subsystems. In particular between two-point correlators, which are the subject of linear response theory.

2.5 Effective Hamiltonian put to the test

Effective theories are a common tool in theoretical physics. To contextualize ours we perform a numerical analysis of its finite-size scaling, and we compare it against other common ones in the fields of condensed matter and quantum optics. Because other effective theories are model dependent and to facilitate the numerical analysis, our testbed here will be the Dicke model (1.38).

The total spin is conserved in the Dicke model (See Sec. 1.3.1) such that it can be solved numerically by diagonalizing each spin-S sector separately. The total partition function is given by

$$Z = \sum_{S=s_0}^{N/2} Y(S,N) Z_S \,, \tag{2.53}$$

where $s_0 = 0$ $(1/2)$ if N is even (odd), Z_S is the partition function of the total spin Hamiltonian (1.53) in the spin-S sector and

$$Y(S,N) = \frac{N!(2S+1)}{(N/2-S)!\,(N/2+S+1)!} \,. \tag{2.54}$$

Numerical diagonalization can be further facilitated by a Polaron transformation, given by $U_{\mathrm{P}} = \exp(-\alpha S_x)$ with $\alpha = 2\zeta(a^\dagger - a)$ and $\zeta = g/\Omega$. The resulting effective Hamiltonian $H_{\mathrm{P}} = U_{\mathrm{P}}^\dagger H U_{\mathrm{P}}$ reads

$$H_{\mathrm{P}} = \omega_z \left(S_z \cosh\alpha - i S_y \sinh\alpha\right) + \Omega a^\dagger a - \frac{4g^2}{\Omega} S_x^2 \,. \tag{2.55}$$

The Polaron frame is particularly well-suited for exact diagonalization because the displacement of the bosons by S_x cancels the finite expectation value of a, $a^\dagger$ in the ordered phase. As a result, the number of bosons in the Polaron frame is only dependent on temperature and the bosonic state-space can be truncated to a much smaller excitation cutoff than would otherwise be required [123, 124]. This, paired with the conservation of the total spin, allows one to

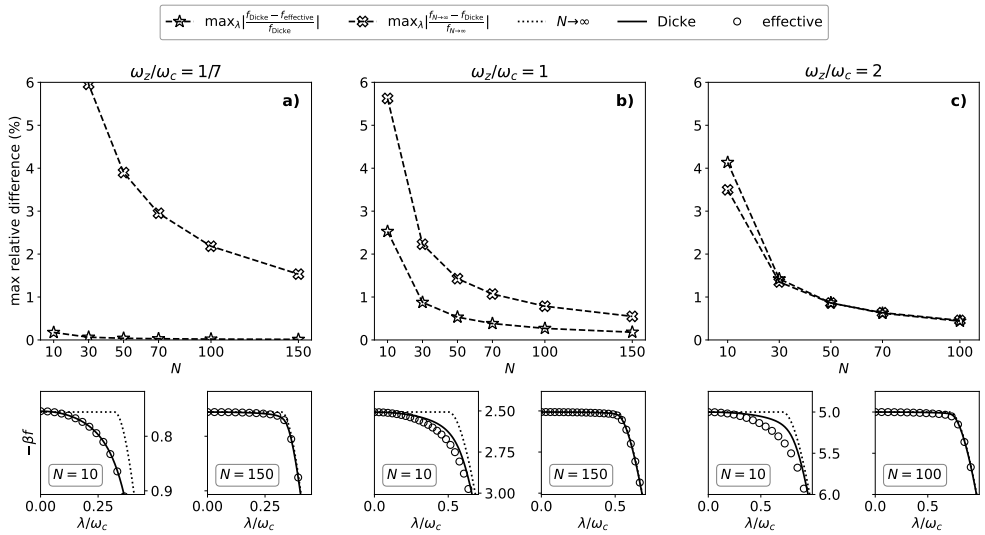

Figure 2.2: Finite-size scaling of the free energy per site computed with our effective theory. Top: Maximum relative difference between the free energies computed by exact diagonalization of our effective Hamiltonian, exact diagonalization of the Dicke model in the Polaron frame and the exact analytical solution in the thermodynamic limit. Bottom: Plots of the free energy at small and large system sizes. a) In the fast-cavity regime $\omega_z/\Omega = 1/7$. b) At resonance $\omega_z/\Omega = 1$. c) In the slow-cavity regime $\omega_z/\Omega = 2$. For reasons of numerical intractability, values for $N = 150$ were unattainable in the slow-cavity regime, which would have required a larger photon cutoff. The temperature is $\beta\Omega = 5$ and the cutoff is $N_{\rm ph} = 10$ throughout.

reach system sizes of $N \sim 100$. As we show below, this is effectively close to the thermodynamic limit. For this reason, we use the Hamiltonian in the Polaron frame (2.55) to do exact diagonalization of the full Dicke model.

In terms of total spin operators, the effective Hamiltonian of the Dicke model reads

$$H_{\rm eff} = \omega_z S_z - \frac{4g^2}{\Omega} S_x^2 \,. \tag{2.56}$$

2.5.1 Validity of the effective Hamiltonian for finite sizes

For an effective Hamiltonian that is only exact in the thermodynamic limit, it is interesting to test its finite-size scaling. In Fig. 2.2 we compare exact diagonalization results for the free energy per particle of the Dicke model at finite N obtained with our effective Hamiltonian (2.56) and with the full Hamiltonian (2.55). We also include the free energy computed analytically in the thermodynamic limit (1.48). We distinguish three regimes of fast cavity, resonance and slow cavity and find that each presents a characteristic finite-size

scaling. In the fast-cavity limit, the effective theory quickly converges to the full Dicke model, already for $N = 30$, and then they both slowly converge to the $N \to \infty$ analytical solution later, with relative differences of $\sim 2\%$ at the critical point for $N = 150$. As one moves towards the slow-cavity regime, the convergence of the effective theory to the full Dicke model slows down, whereas the convergence of the full Dicke model to the $N \to \infty$ analytical solution accelerates. Here we have focused on the free energy at low temperature, which for $\beta\Omega = 5$ is practically equivalent to the ground-state energy, because it is the regime in which the effective theory is most challenged to meet the full Dicke model. In contrast, at high temperature convergence is obtained much faster, akin to the fast-cavity regime at low temperature, as can be seen in the top row of Fig. 2.3 already at $N = 30$. In summary, we find that the effective theory scales well with N, with relative differences with the full Dicke model $< 1\%$ at the critical point for $N \sim 100$ in every regime. In the high-temperature and/or fast-cavity regime, the convergence is even faster, occurring at $N \sim 30$. This finite-size scaling behavior can be explained with a diagrammatic analysis of the first correction to the thermodynamic limit [59].

2.5.2 Comparison with other effective theories

First, let us discuss the taxonomy of effective theories. We can distinguish two families: Hamiltonian theories, with unitary dynamics; and descriptions based on master equations and non-Hermitian Hamiltonians, with dissipative dynamics [125]. Because our theory belongs to the former, we will only consider other Hamiltonian theories in the comparison. We can also distinguish between perturbative and non-perturbative theories. In this regard, it must be noted that our effective Hamiltonian was derived in the $N \to \infty$ limit. As such, it can be regarded as a zeroth order perturbation theory with $1/N$ as the perturbative parameter. The extension to a full-fledged perturbation theory that can be taken to any order in $1/N$ is discussed in Chap. 3. However, in this context we will use the term perturbative to refer only to parameters that affect the light-matter coupling regime, such as the light-matter coupling strength or the detuning between the cavity frequency and the characteristic energy scale of the matter subsystem. It is in this sense that our theory is non-perturbative. The simplest example of a perturbative theory would be standard perturbation theory on the light-matter coupling. To yield an effective Hamiltonian with perturbation theory, a separation of energy scales (large detuning) is required, with the more energetic sector of the spectrum mediating effective interactions on a low-energy subspace [126, 127]. A systematic way to obtain the same effective description as with standard perturbation theory is by means of a Schrieffer–Wolff unitary transformation [128]. We will thus use the latter in our

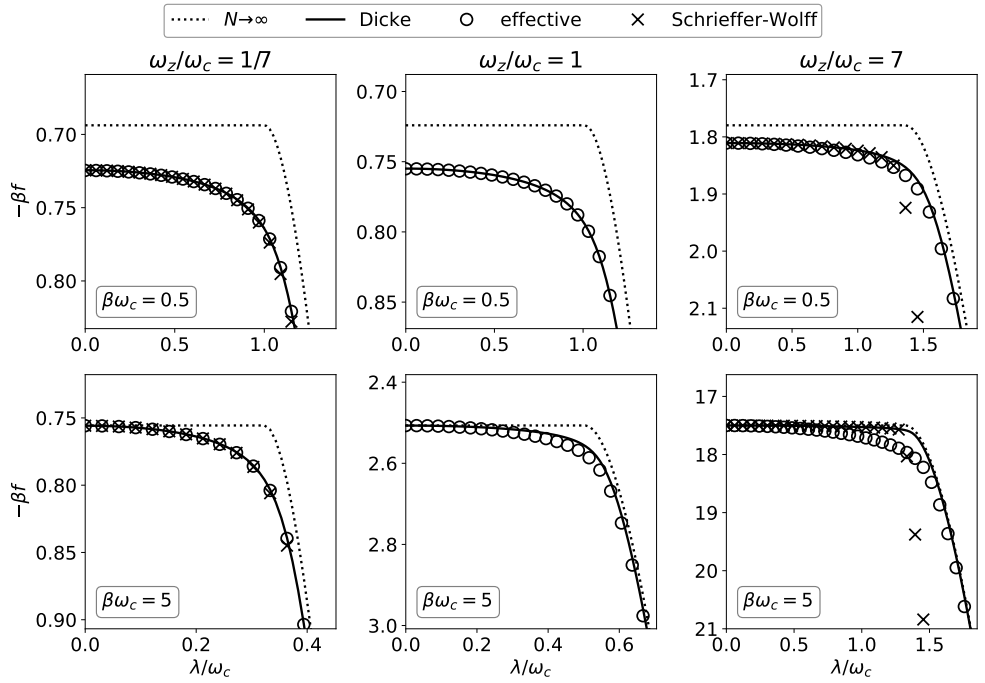

Figure 2.3: Comparison of the free energy per site computed by exact diagonalization of our effective Hamiltonian, exact diagonalization of the Schrieffer–Wolff Hamiltonian, exact diagonalization of the Dicke model in the Polaron frame and the exact analytical solution in the thermodynamic limit. The system size is $N = 30$ and the cutoff is $N_{\mathrm{ph}} = 100$ throughout.

comparison. Regarding non-perturbative alternatives to our effective theory, it is interesting to consider the Polaron transformation itself [123]. For the Dicke model, $\langle a^\dagger - a \rangle$ vanishes in the thermodynamic limit, so we can assume α in Eq. (2.55) to vanish as well. This means that, in the $N \to \infty$ limit, light and matter decouple in the Polaron Hamiltonian (2.55), and it coincides with our effective Hamiltonian (2.56).

The Schrieffer–Wolff transformation has the downside of being model-dependent. This is because the application of the unitary transformations onto the original Hamiltonian requires knowledge about the commutation relation between the matter part of the Hamiltonian and the matter part of the transformations. The matter subsystem must be specified a priori because knowledge of its algebra is required to obtain the effective theory. In contrast, our effective theory was obtained in a model-independent fashion. In all fairness, standard perturbation theory in the fast-cavity limit can also yield an effective matter model without knowledge of the matter subsystem. But in general, perturbation theory is model dependent [127].

For the Dicke model, the Schrieffer-Wolf transformation is given by $U_{\mathrm{SW}} = \exp(-\xi_- X_- - \xi_+ Y_-)$, with $\xi_\pm = g/(\Omega \pm \omega_z)$ and

$$X_\pm = S_- a^\dagger \pm S_+ a\,, \tag{2.57}$$

$$Y_\pm = S_+ a^\dagger \pm S_- a\,. \tag{2.58}$$

The resulting effective Hamiltonian $H_{\mathrm{SW}} = U_{\mathrm{SW}}^\dagger H U_{\mathrm{SW}}$ can be expanded perturbatively and truncated at first order in $\xi_\pm$, yielding

$$H_{\mathrm{SW}} \approx \omega_z S_z + \Omega a^\dagger a - \frac{2g^2\omega_z}{\Omega^2 - \omega_z^2} S_z \left(a + a^\dagger\right)^2 - \frac{4g^2\Omega}{\Omega^2 - \omega_z^2} S_x^2\,. \tag{2.59}$$

Consequently, the parameters $\xi_\pm$ must be small, which requires a large detuning $|\Omega - \omega_z| \gg g$.

In the fast-cavity limit $\Omega \gg \omega_z$, the Hamiltonian simplifies to

$$H_{\mathrm{SW}} \approx \omega_z S_z + \Omega a^\dagger a - \frac{4g^2}{\Omega} S_x^2\,. \tag{2.60}$$

The spin and the cavity decouple and the matter part coincides with H_{eff} (2.56).

The slow-cavity regime is rather nuanced. For starters, there is no light-matter decoupling in this limit

$$H_{\mathrm{SW}} \approx \omega_z S_z + \Omega a^\dagger a + \frac{2g^2}{\omega_z} S_z \left(a + a^\dagger\right)^2\,. \tag{2.61}$$

In addition, the resulting model is ill-defined. The Hamiltonian commutes with S_z, so one can fix the quantum number m_z, defined as $S_z\,|S, m_z\rangle = m_z\,|S, m_z\rangle$. The Hamiltonian for an m_z sector is quadratic in bosonic operators and can be diagonalized with a Bogoliubov transformation, $H_{\mathrm{SW}}(m_z) = \epsilon(m_z) b^\dagger b$. The resulting boson has a frequency

$$\epsilon(m_z) = \sqrt{\Omega^2 + \frac{8g^2\Omega}{\omega_z} m_z}\,, \tag{2.62}$$

that vanishes for $m_z = -S$ at the critical coupling of the Dicke model ($4\lambda_{\mathrm{c}}^2 = \Omega\omega_z$) and is imaginary thereafter. The vanishing is a proper signature of the phase transition but becoming imaginary after is a symptom of the Hamiltonian being ill-defined. This is prevented by keeping the S_x^2 term of H_{SW} that was neglected in passing from Eq. (2.59) to Eq. (2.61). Thus, in the slow-cavity limit the Schrieffer–Wolff Hamiltonian does not admit simplifications nor does it coincide with our effective Hamiltonian. This is a manifestation of the underlying perturbation theory, which requires a separation of energy scales that is unattainable when the cavity is taken as the less energetic subsystem,

because its number of excitations (its energy) its unbounded. Additionally, the regime of resonant cavity and spins is not accessible to the Schrieffer–Wolff theory. These differences are numerically confirmed in Fig. 2.3 for the free energy per site of the Dicke model at high and low temperatures. We observe that the two theories agree in the fast-cavity regime, as expected, and deviate in the slow-cavity regime. Importantly, it is the Schrieffer–Wolff theory that deviates significantly from the full Dicke model past the critical point, whereas our effective theory shows the correct asymptotic behavior. Let us emphasize again that the Schrieffer–Wolff theory is being used as a convenient proxy for standard perturbation theory.

The Schrieffer–Wolff Hamiltonian (2.59) requires a larger cutoff than the Polaron Hamiltonian, specially in the slow-cavity regime. For this reason, the system size has been kept at a conservative $N = 30$ for the comparison in Fig. 2.3 and the bosonic cutoff has been adjusted to reach convergence of the free energy. In practice, this meant a cutoff of $N_{\mathrm{ph}} = 100$ in the worst case.

These numerical results imply an important advantage of our effective theory regarding its applicability to any light-matter coupling regime, hence the surname non-perturbative. They also prove that it is not equivalent to standard perturbation theory. As a caveat, we acknowledge that the theory has only been numerically compared and tested in the Dicke model, although we expect the theory to be equally applicable to other systems. As a matter of fact, in Chaps. 4 and 5 we employ the effective Hamiltonian successfully in other models.

Chapter 3

Linear response theory

Throughout this chapter, we will compute linear response functions [116, Chap. 7], i.e., retarded Green functions, for the light and matter subsystems of the generalized Dicke model (GDM) (1.39) with two different approaches: a path-integral and an equations-of-motion formulation. For convenience, we will consider a slight simplification of the GDM. First, we consider only a single mode for the cavity, this is to alleviate notation, the extension to the multimode case is discussed in App. C. Second we consider either electric or magnetic light-matter interactions, but not both simultaneously. This suffices for the particular systems that we will study later on this thesis (See the discussion in Sec. 4.1.2) From Eqs. (1.17) and (1.37) we can see that the implication of this second simplification is twofold. On the one hand the matter coupling operator, which we denote C_x in the single-mode case, becomes Hermitian $C_x^\dagger = C_x$. On the other hand, in the case of localized emitters, the P^2 term is precisely the square of the matter coupling operator. This will allow us to handle the P^2 term -which is essentially a collective interaction- and the light-mediated interactions in parallel along this chapter, following what we learned in Chap. 2 about how they both lead to mean-field equilibrium properties. The resulting simplification of the GDM can be written as

$$H = H_{\mathrm{m}} + \Omega a^\dagger a + g\left(a + a^\dagger\right) C_x + \zeta \frac{g^2}{\Omega} C_x^2 \,. \tag{3.1}$$

Depending on the choice of H_{m}, C_x, Ω, g and ζ this Hamiltonian can describe several distinct microscopic systems. The Pauli-Fierz Hamiltonian in the Coulomb gauge (1.2) can be brought to the form of the Hamiltonian in Eq. (3.1) by invoking the long-wavelength approximation and diagonalizing the photonic sector with a Bogoliubov transformation to eliminate the A^2 term as we discussed in Sec. 1.2.1 [50, 76]. It would correspond to setting $\zeta = 0$ and associating the electronic collective momenta to C_x and renormalized frequency

and couplings, stemming from the Bogoliubov transform, to Ω and g (See Sec. 4.3 for an example). Localized electric dipoles can be described in the dipole gauge by setting $\zeta = 1$ and associating the collective dipole operator to C_x, this corresponds to the zeroth order long-wavelength limit of the system of localized emitters discussed in Sec. 1.2.2 [129]. Since the inclusion of the P^2 term to ensure gauge invariance in dipolar systems is not always respected, toggling off ζ will clarify its effects within linear response theory. Furthermore, we consider ζ a binary parameter here, but promoting it to take arbitrary values also allows to study a model where the P^2 term amplitude is not fixed by the light-matter coupling and cavity frequency. To describe magnetic dipoles instead, one can associate a collective spin operator to C_x and toggle off the P^2 term by setting $\zeta = 0$ [115, 130].

Following the spirit of the thesis, we will not specify the matter subsystem in our derivation; instead, we will derive relationships between the Green functions for the hybrid light-matter system with the bare matter and photonic Green functions. The bare photonic Green function is a well-known quantity that is trivial to compute. A full solution will thus be contingent on being able to compute the Green function of the bare matter, subject to some additional mean fields, as we will gather from the derivation. The retarded Green function for operators A and B is defined as

$$G^{\mathrm{r}}_{A,B}(t,t') = -i\theta(t-t')\langle[A(t),B(t')]\rangle\,. \tag{3.2}$$

With $\theta(t)$ the Heaviside step function. We will be particularly concerned with the photonic propagator

$$D(t) = G^{\mathrm{r}}_{a,a^\dagger}(t,0) \tag{3.3}$$

and matter response functions

$$\chi_{rs}(t) = -\frac{1}{N}G^{\mathrm{r}}_{C_r,C_s}(t,0)\,, \tag{3.4}$$

where C_r might be C_x or any other collective matter operator.

This chapter is based on parts of Ref. [63].

3.1 Imaginary-time path integral formulation: Thermal Green function

One way to compute retarded Green functions is to obtain them by analytic continuation from the thermal Green function, which can be computed from the imaginary-time path integral formulation of the partition function that we

developed in Chap. 2. The thermal Green function for operators A and B reads

$$G^{\mathrm{t}}_{A,B}(\tau-\tau') = -\langle \mathcal{T}_\tau A(\tau)B(\tau')\rangle \tag{3.5}$$

Within the coherent-state path-integral formalism, we will obtain the thermal Green functions in terms of imaginary time τ or Matsubara frequencies ω_m. The retarded Green function is then obtained with the replacement

$$G^{\mathrm{r}}_{A,B}(\omega) = G^{\mathrm{t}}_{A,B}(\omega_m)|_{i\omega_m\to\omega_+=\omega+i0^+}\ , \tag{3.6}$$

for all positive Matsubara frequencies [116, Chap. 7].

3.1.1 Auxiliary field propagator

Here we will follow the same approach used to derive the equilibrium effective Hamiltonian in Chap. 2. Now, instead of focusing on the zeroth-order term of the saddle-point expansion that determines the equilibrium properties, we will focus on the second-order term, which gives the propagator for the auxiliary field. Also, following our simplification to write the GDM Hamiltonian as in Eq. (3.1), we will be handling the light-matter coupling and the P^2 term in parallel.

Following Chap. 2.1, we write the effective action for Hamiltonian (3.1) as $S_{\mathrm{eff}} = S_{\mathrm{m}} + S_{\mathrm{ind}}$ with

$$S_{\mathrm{ind}} = \frac{1}{2}\int_{\tau,\tau'} C_x(\tau)\frac{1}{N}V_{\mathrm{ind}}(\tau-\tau')C_x(\tau')\,, \tag{3.7}$$

with

$$V_{\mathrm{ind}}(\tau) = \lambda^2(D_0(\tau)+D_0(\beta-\tau)) + 2\zeta\frac{\lambda^2}{\Omega}\delta(\tau)\,, \tag{3.8}$$

or in Matsubara frequency space

$$V_{\mathrm{ind}}(\omega_m) = 2\lambda^2\frac{\Omega^2(\zeta-1)+\zeta\omega_m^2}{\Omega(\omega_m^2+\Omega^2)}\,. \tag{3.9}$$

Note that we symmetrize V_{ind} with respect to τ. It can be seen that the odd part of V_{ind} does not contribute to the action. This will be justified later, when we relate V_{ind} to the propagator of an auxiliary real scalar field, which must be even.

Once again, the effective interaction can be eliminated with a Hubbard-Stratonovich transformation that introduces an auxiliary scalar field which, owing to the fact that $C_x = C_x^\dagger$, is real in this case. We define the propagator of the auxiliary field as

$$W(\tau) = \langle\varphi(\tau)\varphi(0)\rangle^{\mathrm{c}}\,. \tag{3.10}$$

With this, after partial integration over the matter degrees of freedom, we obtain

$$f[\varphi] = \frac{1}{2\gamma}\int_{\tau,\tau'} \varphi(\tau) V_{\mathrm{ind}}^{-1}(\tau-\tau')\varphi(\tau') + \frac{1}{\gamma}\mathcal{G}_{\mathrm{m}}^{0}[\varphi]\,. \tag{3.11}$$

Here, $\mathcal{G}_{\mathrm{m}}^{0}[\xi] = -N^{-1}\log Z_{\mathrm{m}}[\xi]$ is the generating functional for bare connected correlation functions of the matter coupling operator C_x, with

$$Z_{\mathrm{m}}[\xi] = \oint_c e^{-(S_{\mathrm{m}} + i\int_\tau \xi(\tau) C_x(\tau))}\,. \tag{3.12}$$

Its derivatives provide connected correlation functions at all orders

$$\frac{\delta}{\delta\xi(\tau_1)}\cdots\frac{\delta}{\delta\xi(\tau_n)}\mathcal{G}_{\mathrm{m}}^{0}[\xi]\Big|_{\xi=0} = -\frac{(-i)^n}{N}\langle C_x(\tau_1)\cdots C_x(\tau_n)\rangle_{\mathrm{m}}^{\mathrm{c}} \equiv \chi_{xx,0}^{(n)}(\tau_1,\ldots,\tau_n)\,, \tag{3.13}$$

such that $\mathcal{G}_{\mathrm{m}}^{0}$ can itself be written as a series expansion in terms of correlators

$$\mathcal{G}_{\mathrm{m}}^{0}[\xi] = \sum_n \frac{1}{n!}\int_{\tau_1,\ldots,\tau_n} \xi(\tau_1)\cdots\xi(\tau_n)\,\chi_{xx,0}^{(n)}(\tau_1,\ldots,\tau_n)\,. \tag{3.14}$$

In the following we will denote $\chi_{xx,0}^{(2)} \equiv \chi_{xx,0}$.

The saddle-point is now obtained from the mean-field effective Hamiltonian

$$H_{\mathrm{eff}}^{\mathrm{MF}} = H_{\mathrm{m}} + \frac{2\lambda^2(\zeta-1)}{N\Omega}\langle C_x\rangle C_x - \frac{\lambda^2(\zeta-1)}{N\Omega}\langle C_x\rangle^2\,, \tag{3.15}$$

with $i\varphi_{\mathrm{sp}} = 2\lambda^2(\zeta-1)/(\Omega N)\langle C_x\rangle$. By virtue of φ_{sp} being a minimum of f, f is locally quadratic in its vicinity

$$f[\varphi] - f[\varphi_{\mathrm{sp}}] = \frac{1}{2\gamma}\int_{\tau,\tau'} \delta\varphi(\tau)(NW_0)^{-1}(\tau-\tau')\delta\varphi(\tau') + \mathcal{O}(\delta\varphi^4)\,. \tag{3.16}$$

Here $\delta\varphi = \varphi - \varphi_{\mathrm{sp}}$ and

$$(NW_0)^{-1} = V_{\mathrm{ind}}^{-1} + \tilde{\chi}_{xx,0}\,, \tag{3.17}$$

with

$$\tilde{\chi}_{xx,0}(\tau,\tau') = \frac{\delta}{\delta\varphi_{\mathrm{sp}}(\tau)}\frac{\delta}{\delta\varphi_{\mathrm{sp}}(\tau')}\mathcal{G}_{\mathrm{m}}^{0}[\varphi_{\mathrm{sp}}] = \frac{1}{N}\langle C_x(\tau)C_x(\tau')\rangle_{\mathrm{eff}}^{\mathrm{c}}\,. \tag{3.18}$$

Note that in the absence of symmetry breaking, i.e., when $\langle C_x\rangle = 0$, or if $\zeta = 1$, the effective matter Hamiltonian is just the bare matter Hamiltonian and thus $\tilde{\chi}_{xx,0} = \chi_{xx,0}$ is just the bare matter response. At this point we note that W_0, which is the free propagator of φ, a real scalar field, is a function of V_{ind}. It is now clear why we symmetrize V_{ind}, W_0 must be even in time. The importance of Eq. (3.17) stems from the fact that for $N\to\infty$ one can safely truncate the saddle-point expansion to second order, which implies that $W = W_0$. We can now obtain relations between the auxiliary field propagator W the photonic propagator D and matter response functions.

3.1.2 Dressed response functions in terms of bare response functions

In the following we will define generating functionals for connected correlators in imaginary time. These differ from the thermal Green function as defined in Eq. (3.5) when the expectation value of the operator for which one is computing the connected correlator acquires a finite value. However, this difference only affects the zero frequency component of the correlator and is thus unimportant for the analytic continuation to real frequencies.

Let us define the generating functional for photonic connected correlators by introducing a complex field to the original action: $\mathcal{G}_{\mathrm{ph}}[\eta,\bar{\eta}] = -\log Z[\eta,\bar{\eta}]$, with

$$Z[\eta,\bar{\eta}] = \oint_{a,\bar{a},c} e^{-(S+\int_\tau (a(\tau)\bar{\eta}(\tau)+\bar{a}(\tau)\eta(\tau))}\,. \tag{3.19}$$

After partial integration of the cavity fields, this yields

$$Z[\eta,\bar{\eta}] = \oint_c \exp -\left(S_{\mathrm{m}} + \zeta\frac{g^2}{\Omega}\int_\tau C_x^2(\tau) + \int_{\tau,\tau'}\bar{m}(\tau)D_0(\tau-\tau')m(\tau)\right)\,, \tag{3.20}$$

with $m(\tau) = \eta(\tau) + gC_x(\tau)$. With this

$$\begin{aligned} D(\tau-\tau') &= \frac{\delta}{\delta\bar{\eta}(\tau)}\frac{\delta}{\delta\eta(\tau')}\mathcal{G}_{\mathrm{ph}}[\eta,\bar{\eta}]\Big|_{\eta=\bar{\eta}=0} \\ &= D_0(\tau-\tau') - \lambda^2\int_{u,v} D_0(\tau-u)\chi_{xx}(u-v)D_0(v-\tau')\,, \end{aligned} \tag{3.21}$$

or in Matsubara frequency space

$$D(\omega_m) = D_0(\omega_m) - \lambda^2 D_0(\omega_m)\chi_{xx}(\omega_m)D_0(\omega_m)\,. \tag{3.22}$$

Likewise, we can define the generating functional for matter connected correlators. Since we are interested in response functions, i.e., two-point correlators, we can rather generally consider correlations of three distinct matter operators, the matter coupling operator C_x and two others, that we label C_y and C_z. Note that x, y and z are simply indices here, and they do not necessarily indicate spatial direction. The generating functional is $\mathcal{G}_{\mathrm{m}}[\xi_x,\xi_y,\xi_z] = -N^{-1}\log Z[\xi_x,\xi_y,\xi_z]$, with

$$Z[\xi_x,\xi_y,\xi_z] = \oint_{c,\varphi} e^{-(S_{\mathrm{eff}}+i\int_\tau\sum_r \xi_r(\tau)C_r(\tau))}\,. \tag{3.23}$$

After partial integration over the matter fields, this yields

$$Z[\xi_x,\xi_y,\xi_z] = \oint_\varphi e^{-N\beta f[\varphi,\xi_x,\xi_y,\xi_z]}\,, \tag{3.24}$$

with

$$f[\varphi,\xi_x,\xi_y,\xi_z] = \frac{1}{2\gamma}\int_{\tau,\tau'}\varphi(\tau)V_{\rm ind}^{-1}(\tau-\tau')\varphi(\tau') + \frac{1}{\gamma}\mathcal{G}_{\rm m}^0[\xi_x+\varphi,\xi_y,\xi_z]\,, \quad (3.25)$$

Here $\mathcal{G}_{\rm m}^0[\xi_x,\xi_y,\xi_z] = -N^{-1}\log Z_{\rm m}[\xi_x,\xi_y,\xi_z]$ is the generalization of $\mathcal{G}_{\rm m}^0[\xi]$ (3.12), with

$$Z_{\rm m}[\xi_x,\xi_y,\xi_z] = \oint_c e^{-(S_{\rm m}+i\int_\tau\sum_r\xi_r(\tau)C_r(\tau))}\,. \quad (3.26)$$

Then a second-order expansion of $f[\varphi,\xi_x,\xi_y,\xi_z]$ around $\varphi_{\rm sp}$ yields

$$\begin{aligned} &f[\varphi,\xi_x,\xi_y,\xi_z] - f[\varphi_{\rm sp},0,0,0] = \\ &\frac{1}{2\gamma}\int_{\tau,\tau'}\Big(\delta\varphi(\tau)(NW)^{-1}(\tau-\tau')\delta\varphi(\tau') + \sum_{rs}\xi_r(\tau)\tilde{\chi}_{rs,0}(\tau-\tau')\xi_s(\tau') \\ &\quad + \delta\varphi(\tau)\sum_r\tilde{\chi}_{xr,0}(\tau-\tau')\xi_r(\tau') + \sum_r\xi_r(\tau)\tilde{\chi}_{rx,0}(\tau-\tau')\delta\varphi(\tau)\Big)\,. \end{aligned} \quad (3.27)$$

The functional integral over the auxiliary-field displacements $\delta\varphi$ is just a Gaussian integral that we can perform, yielding

$$\begin{aligned} \mathcal{G}_{\rm m}[\xi_x,\xi_y,\xi_z] + {\rm cst.} = \frac{1}{2}\sum_{rs}\int_{\tau,\tau'}\xi_r(\tau)\Big(&\tilde{\chi}_{rs,0}(\tau-\tau') \\ -\int_{u,v}\tilde{\chi}_{rx,0}(\tau-u)NW(u-v)\tilde{\chi}_{xs,0}(u-\tau')\Big)&\xi_s(\tau')\,. \end{aligned} \quad (3.28)$$

With this

$$\begin{aligned} \chi_{rs}(\tau-\tau') &= \frac{\delta}{\delta\xi_r(\tau)}\frac{\delta}{\delta\xi_s(\tau')}\mathcal{G}_{\rm m}[\xi_x,\xi_y,\xi_z]\Big|_{\xi_r=0\;\forall r} \\ &= \tilde{\chi}_{rs,0}(\tau-\tau') - \int_{u,v}\tilde{\chi}_{rx,0}(\tau-u)NW(u-v)\tilde{\chi}_{xs,0}(u-\tau')\,, \end{aligned} \quad (3.29)$$

or in Matsubara frequency space

$$\chi_{rs}(\omega_m) = \tilde{\chi}_{rs,0}(\omega_m) - \tilde{\chi}_{rx,0}(\omega_m)NW(\omega_m)\tilde{\chi}_{xr,0}(\omega_m)\,. \quad (3.30)$$

Putting together Eqs. (3.17) and (3.30) we arrive at the relations

$$\chi_{xr}(\omega_m) = \frac{\tilde{\chi}_{xr,0}(\omega_m)}{1+V_{\rm ind}(\omega_m)\tilde{\chi}_{xx,0}(\omega_m)}\,, \quad (3.31)$$

$$\chi_{rx}(\omega_m) = \frac{\tilde{\chi}_{rx,0}(\omega_m)}{1+V_{\rm ind}(\omega_m)\tilde{\chi}_{xx,0}(\omega_m)}\,, \quad (3.32)$$

$$\chi_{rs}|_{r,s\neq x}(\omega_m) = \tilde{\chi}_{rs,0}(\omega_m) - \frac{\tilde{\chi}_{rx,0}(\omega_m)V_{\rm ind}(\omega_m)\tilde{\chi}_{xs,0}(\omega_m)}{1+V_{\rm ind}(\omega_m)\tilde{\chi}_{xx,0}(\omega_m)}\,, \quad (3.33)$$

which together with Eq. (3.22) give us the dependence of the photonic propagator and matter response functions on the free photon propagator and the response functions $\tilde{\chi}_{rs,0}$. Note from Eqs. (3.18) and (3.26) that $\tilde{\chi}_{rs,0}$ are simply the response functions of the mean-field effective matter Hamiltonian. Equations (3.31), (3.31) and (3.33) exhibit a structure similar to the response functions commonly derived using the random phase approximation (RPA). It is important to highlight that these equations remain valid for all parameter ranges and are applicable to both normal and superradiant phases.

3.2 Equations of motion for the retarded Green functions

An alternative way to compute retarded Green functions is by formulating their equations of motion and, under some assumptions, solving them. Defining $G^{\mathrm{r}}_{A,B}(t) \equiv G^{\mathrm{r}}_{A,B}(t,0)$ we have from Eq. (3.2) that

$$i\partial t G^{\mathrm{r}}_{A,B}(t) = \delta(t)\langle[A,B]\rangle - G^{\mathrm{r}}_{[H,A],B}(t) \tag{3.34}$$

or in frequency space

$$\omega_+ G^{\mathrm{r}}_{A,B}(\omega) = \langle[A,B]\rangle - G^{\mathrm{r}}_{[H,A],B}(\omega)\,, \tag{3.35}$$

with $\omega_+ = \omega + i0^+$.

3.2.1 Solving the equations of motion

Let $\{|\alpha\rangle\}$ be a basis of the Hilbert space of the matter subsystem and let us define the Hubbard operators $X^{\alpha\gamma} = |\alpha\rangle\langle\gamma|$. We start by computing the matter correlation function χ_{rs}. Note that

$$\chi_{rs} = -\frac{1}{N} G^{\mathrm{r}}_{C_r,C_s} = -\frac{1}{N}\sum_{\alpha,\gamma} C_r^{\alpha\gamma} G^{\mathrm{r}}_{X^{\alpha\gamma},C_s} \tag{3.36}$$

where $C_r^{\alpha\gamma} = \langle\alpha|C_r|\gamma\rangle$. Then

$$\begin{aligned}\omega_+ G^{\mathrm{r}}_{X^{\alpha\gamma},C_s}(\omega) &= \langle[X^{\alpha\gamma},C_s]\rangle - G^{\mathrm{r}}_{[H,X^{\alpha\gamma}],C_s}(\omega)\\ &= -\Gamma_s^{\alpha\gamma} - G^{\mathrm{r}}_{[H_{\mathrm{m}},X^{\alpha\gamma}],C_s}(\omega)\\ &\quad - g G^{\mathrm{r}}_{(a+a^\dagger)[C_x,X^{\alpha\gamma}],C_s}(\omega) - \zeta\frac{g^2}{\Omega} G^{\mathrm{r}}_{[C_x^2,X^{\alpha\gamma}],C_s}(\omega)\,.\end{aligned} \tag{3.37}$$

Here $\Gamma_s^{\alpha\gamma} = \langle[C_s,X^{\alpha\gamma}]\rangle = \sum_\mu (C_s^{\mu\alpha}\langle X^{\mu\gamma}\rangle - C_s^{\gamma\mu}\langle X^{\alpha\mu}\rangle)$. The last two terms of Eq. (3.37) correspond to three-point Green functions. One could now write

the equations of motion for such three-point Green functions, which would in turn depend on four-point Green functions, and so on and so forth. This infinite hierarchy of n-point correlators involves light-matter interactions, as discussed in the context of lasing physics [131, Chapter 9] or light emission [132]. At some point, the hierarchy needs to be truncated. The crudest approximation is to restrict the theory to two-point Green functions, assuming that $G^{\mathrm{r}}_{AB,C} \approx \langle A\rangle G^{\mathrm{r}}_{B,C} + \langle B\rangle G^{\mathrm{r}}_{A,C}$, which amounts to neglecting correlations of order higher than two for all terms stemming from light-matter interaction. In terms of fluctuations, this means that only linear fluctuations between the two systems are relevant, and that correlated fluctuations are largely suppressed. This approach is reminiscent of RPA or mean-field approximations, which need to be justified. This has indeed been discussed within the Dicke model, where the traditional educated guess that quantum fluctuations vanish in the $N \to \infty$ limit [131, Chapter 9] (Cf. with the equilibrium argument in [17]) has been rigorously demonstrated recently [133]. In that work, the proof was restricted to the Dicke model and within the Lindblad framework, i.e., adding dissipation in a Markovian manner. This result is relevant to us since LRT falls within the conditions of the theorem demonstrated in that reference, which requires the dynamics to start with an uncorrelated initial condition between light and matter. This can be safely assumed here since the response is independent of the excitation and can be obtained from excitation functions where the initial condition is assumed to be at equilibrium, which can be well approximated by uncorrelated light-matter states [76]. It is true, however, that in our case we are not considering dissipative Lindblad dynamics, and we include potential matter-matter interactions. Here we show that it is still exact, as it agrees with the exact saddle-point solution for $N \to \infty$ discussed in the previous section. This suggests that generalizing Ref. [133] might be possible in a future work. With this,

$$\begin{aligned}\omega_+ G^{\mathrm{r}}_{X^{\alpha\gamma},C_s}(\omega) &= -\Gamma_s^{\alpha\gamma} - G^{\mathrm{r}}_{[H_{\mathrm{m}},X^{\alpha\gamma}],C_s}(\omega) \\ &- g\langle a + a^\dagger\rangle G^{\mathrm{r}}_{[C_x,X^{\alpha\gamma}],C_s}(\omega) - \zeta\frac{2g^2}{\Omega}\langle C_x\rangle G^{\mathrm{r}}_{[C_x,X^{\alpha\gamma}],C_s}(\omega) \\ &- g\Gamma_x^{\alpha\gamma}\left(G^{\mathrm{r}}_{a,C_s}(\omega) + G^{\mathrm{r}}_{a^\dagger,C_s}(\omega)\right) - \zeta\frac{2g^2}{\Omega}\Gamma_x^{\alpha\gamma} G^{\mathrm{r}}_{C_x,C_s}(\omega)\,.\end{aligned} \tag{3.38}$$

We can put together the second, third and fourth elements in the right-hand side to build a mean field matter Hamiltonian

$$H_{\mathrm{m}}^{\mathrm{MF}} = H_{\mathrm{m}} + g\langle a + a^\dagger\rangle C_x + \zeta\frac{2g^2}{\Omega}\langle C_x\rangle C_x\,. \tag{3.39}$$

Note that the constant terms in this mean-field Hamiltonian are omitted here. We will show later that this Hamiltonian is equivalent to the mean-field effective Hamiltonian (2.35) obtained with the path integral approach under a mean-field

decoupling of the full light-matter Hamiltonian. At this point we can assume that the basis that we have been using $\{|\alpha\rangle\}$ is precisely the eigenbasis of $H_{\mathrm{m}}^{\mathrm{MF}}$, with eigenenergies $\{E_\alpha\}$, obtaining

$$\begin{aligned}\omega_+ G^{\mathrm{r}}_{X^{\alpha\gamma},C_s}(\omega) &= -\Gamma_s^{\alpha\gamma} - (E_\alpha - E_\gamma) G^{\mathrm{r}}_{X^{\alpha\gamma},C_s}(\omega) \\ &\quad - g\Gamma_x^{\alpha\gamma}\left(G^{\mathrm{r}}_{a,C_s}(\omega) + G^{\mathrm{r}}_{a^\dagger,C_s}(\omega)\right) - \zeta\frac{2g^2}{\Omega}\Gamma_x^{\alpha\gamma} G^{\mathrm{r}}_{C_x,C_s}(\omega)\,.\end{aligned} \tag{3.40}$$

We can compute the photon-matter Green functions that appear on the second line obtaining

$$(\omega_+ - \Omega) G^{\mathrm{r}}_{a,C_s}(\omega) = g G^{\mathrm{r}}_{C_x,C_s}(\omega)\,, \tag{3.41}$$

$$(\omega_+ + \Omega) G^{\mathrm{r}}_{a^\dagger,C_s}(\omega) = -g G^{\mathrm{r}}_{C_x,C_s}(\omega)\,. \tag{3.42}$$

Putting together Eqs. (3.40), (3.41) and (3.42) we get

$$(\omega_+ + E_\alpha - E_\gamma) G^{\mathrm{r}}_{X^{\alpha\gamma},C_s}(\omega) = -\Gamma_s^{\alpha\gamma} - \Gamma_x^{\alpha\gamma} V_{\mathrm{ind}}(\omega)\frac{1}{N} G^{\mathrm{r}}_{C_x,C_s}(\omega)\,, \tag{3.43}$$

with $V_{\mathrm{ind}}(\omega) = V_{\mathrm{ind}}(\omega_m)|_{i\omega_m\to\omega+i0^+}$. Together with Eq. (3.36) this gives

$$\begin{aligned}\chi_{rs}(\omega) &= \frac{1}{N}\sum_{\alpha\gamma} C_r^{\alpha\gamma}\frac{\Gamma_s^{\alpha\gamma}}{\omega_+ + E_\alpha - E_\gamma} \\ &\quad - \frac{1}{N}\sum_{\alpha\gamma} C_r^{\alpha\gamma}\frac{\Gamma_x^{\alpha\gamma}}{\omega_+ + E_\alpha - E_\gamma} V_{\mathrm{ind}}(\omega)\chi_{xs}(\omega)\,.\end{aligned} \tag{3.44}$$

From the definition of $\Gamma_s^{\alpha\gamma}$ and noting that $\langle X^{\alpha\gamma}\rangle = Z^{-1}\delta_{\alpha\gamma}\exp(-\beta E_\alpha)$ we find that

$$\frac{1}{N}\sum_{\alpha\gamma} C_r^{\alpha\gamma}\frac{\Gamma_s^{\alpha\gamma}}{\omega_+ + E_\alpha - E_\gamma} = \tilde{\chi}_{rs,0}(\omega)\,. \tag{3.45}$$

With this and Eq. (3.44), we finally obtain

$$\chi_{xr}(\omega) = \frac{\tilde{\chi}_{xr,0}(\omega)}{1 + V_{\mathrm{ind}}(\omega)\tilde{\chi}_{xx,0}(\omega)}\,, \tag{3.46}$$

$$\chi_{rx}(\omega) = \frac{\tilde{\chi}_{rx,0}(\omega)}{1 + V_{\mathrm{ind}}(\omega)\tilde{\chi}_{xx,0}(\omega)}\,, \tag{3.47}$$

$$\chi_{rs}|_{r,s\neq x}(\omega) = \tilde{\chi}_{rs,0}(\omega) - \frac{\tilde{\chi}_{rx,0}(\omega)V_{\mathrm{ind}}(\omega)\tilde{\chi}_{xs,0}(\omega)}{1 + V_{\mathrm{ind}}(\omega)\tilde{\chi}_{xx,0}(\omega)}\,, \tag{3.48}$$

which coincide with the analytic continuation of Eqs. (3.31), (3.32) and (3.33).

Proceeding similarly, we can now compute D and $D_+ = G^{\mathrm{r}}_{a^\dagger,a^\dagger}$. First we have

$$(\omega_+ - \Omega) D(\omega) = 1 + g G^{\mathrm{r}}_{C_x,a^\dagger}(\omega)\,, \tag{3.49}$$

$$(\omega_+ + \Omega) D_+(\omega) = -g G^{\mathrm{r}}_{C_x,a^\dagger}(\omega)\,. \tag{3.50}$$

Again we use the decomposition $G^{\mathrm{r}}_{C_x,a^\dagger} = \sum_{\alpha\gamma} C_x^{\alpha\gamma} G^{\mathrm{r}}_{X^{\alpha\gamma},a^\dagger}$ and compute

$$(\omega_+ + E_\alpha - E_\gamma) G^{\mathrm{r}}_{X^{\alpha\gamma},a^\dagger} = -g\Gamma_x^{\alpha\gamma}\left(D(\omega) + D_+(\omega)\right) - \zeta\frac{2g^2}{\Omega}\Gamma_x^{\alpha\gamma} G^{\mathrm{r}}_{C_x,a^\dagger}(\omega)\,, \tag{3.51}$$

such that

$$G^{\mathrm{r}}_{C_x,a^\dagger} = \frac{-Ng\tilde{\chi}_{xx,0}(\omega)}{1+\zeta\frac{2\lambda^2}{\Omega}\tilde{\chi}_{xx,0}(\omega)}\left(D(\omega) + D_+(\omega)\right)\,. \tag{3.52}$$

Plugging this into Eqs. (3.49) and (3.50) we get

$$(\omega-\Omega)D(\omega) = 1 - \frac{\lambda^2\tilde{\chi}_{xx,0}(\omega)}{1+\zeta\frac{2\lambda^2}{\Omega}\tilde{\chi}_{xx,0}(\omega)}\left(D(\omega) + D_+(\omega)\right)\,, \tag{3.53}$$

$$(\omega+\Omega)D_+(\omega) = \frac{\lambda^2\tilde{\chi}_{xx,0}(\omega)}{1+\zeta\frac{2\lambda^2}{\Omega}\tilde{\chi}_{xx,0}(\omega)}\left(D(\omega) + D_+(\omega)\right)\,. \tag{3.54}$$

We can now solve for D and D_+ to get

$$D(\omega) = \frac{\omega_+ + \Omega + \lambda^2\frac{2\zeta(\omega_+ + \Omega)-\Omega}{\Omega}\tilde{\chi}_{xx,0}(\omega)}{\omega_+^2 - \Omega^2 + 2\lambda^2\frac{\zeta(\omega_+^2-\Omega^2)+\Omega^2}{\Omega}\tilde{\chi}_{xx,0}(\omega)}\,, \tag{3.55}$$

$$D_+(\omega) = \frac{\lambda^2\tilde{\chi}_{xx,0}(\omega)}{\omega_+^2 - \Omega^2 + 2\lambda^2\frac{\zeta(\omega_+^2-\Omega^2)+\Omega^2}{\Omega}\tilde{\chi}_{xx,0}(\omega)}\,. \tag{3.56}$$

Although not immediately obvious, Eq. (3.55) is precisely the analytic continuation of Eq. (3.22). We prove this relation in App. D.

3.2.2 Mean-field decoupling of the light-matter Hamiltonian

Let us consider the Hamiltonian in Eq. (3.1) with a mean-field decoupling of the light-matter interaction and P^2 terms. We expand $C_x = \langle C_x\rangle + \delta C_x$ and $a+a^\dagger = \langle a+a^\dagger\rangle + \delta(a+a^\dagger)$ and neglect terms quadratic in fluctuations, obtaining two decoupled Hamiltonians and some constants: $H = H_{\mathrm{m}}^{\mathrm{MF}} + H_{\mathrm{ph}}^{\mathrm{MF}} + \mathrm{cst.}$ with

$$H_{\mathrm{m}}^{\mathrm{MF}} = H_{\mathrm{m}} + g\langle a+a^\dagger\rangle C_x + \zeta\frac{2g^2}{\Omega}\langle C_x\rangle C_x\,, \tag{3.57}$$

$$H_{\mathrm{ph}}^{\mathrm{MF}} = \Omega a^\dagger a + g(a+a^\dagger)\langle C_x\rangle\,, \tag{3.58}$$

$$\mathrm{cst.} = -g\langle a+a^\dagger\rangle\langle C_x\rangle - \zeta\frac{g^2}{\Omega}\langle C_x\rangle^2\,. \tag{3.59}$$

The mean-field photonic Hamiltonian $H_{\mathrm{ph}}^{\mathrm{MF}}$ can be diagonalized with a displacement, $a = b - g/\Omega\langle C_x\rangle$, yielding $H_{\mathrm{ph}}^{\mathrm{MF}} = \Omega b^\dagger b$, a new constant $-g^2/\Omega\langle C_x\rangle^2$ and the relation $\langle a+a^\dagger\rangle = -2g/\Omega\langle C_x\rangle$. Plucking this relation and all the constants gathered in the different steps into the mean-field matter Hamiltonian $H_{\mathrm{m}}^{\mathrm{MF}}$ yields precisely the mean-field effective Hamiltonian $H_{\mathrm{eff}}^{\mathrm{MF}}$ of Eq. (2.35). The constants are important for a potential variational solution.

3.3 Comparison of the two approaches

In this section we have shown the equivalence between two different approaches to address the linear response regime of cavity QED materials. Although seemingly very different, the path-integral in imaginary time and the equation of motion in real time provide exact analytical results in the thermodynamic limit, $N \to \infty$. The effect of the thermodynamic limit is clearly identified in the path integral approach when the saddle point method is invoked. Instead, with the equations-of-motion method it requires an analysis of the scaling of the correlated parts of higher-order correlation functions with N. On the other hand, the equations-of-motion approach does not require the auxiliary field of the Hubbard-Stratonovich transformation, which allows us to interpret the steps used to calculate its propagator W. We can see that the auxiliary field $\varphi_{\rm sp}$ plays the same role as the mean-field background in the equation of motion, which couples to the fluctuations.

The two approaches, in conjunction with the equilibrium theory of Chap. 2, cement the understanding that mean-field approaches are exact in the thermodynamic limit for Dicke-like models, even if matter interactions are considered. Together, they paint the following picture. One can construct a hierarchy of light-matter correlations: observables, response functions, three-point correlators, etc. Normally, this hierarchy is not closed, meaning that n-point correlators depend on $n+1$-point correlators, and so on, ad infinitum. This can be seen in our equations-of-motion approach. In contrast, for Dicke-like models of the form of Eq. (3.1) it seems that this hierarchy can be truncated at any order and still provide exact results for that order of the hierarchy. In this paper we have confirmed that this is the case for one- and two-point correlators. One-point correlators (expected values of a single light or matter observable) are computed from the effective mean-field Hamiltonian of Eq. (2.35). Note that at this level it seems like we are neglecting all light-matter correlations, even two-point correlations. Then, two-point correlations, which define linear-response theory, are given by Eqs. (3.22), (3.31), (3.32) and (3.33) and depend solely on bare two-point correlators, in particular on those of the mean-field effective Hamiltonian. From our path-integral approach, we see that this is simply a consequence of the fact that each order of correlations corresponds to a new term of the saddle point expansion, and as such is a factor $1/N$ less significant than the previous order [83]. In the thermodynamic limit every order is completely independent of all higher orders in the hierarchy.

As a caveat, note that this discussion only applies to light-matter correlations. The material subsystem will generally be an interacting many-body system on its own where correlations can not be computed exactly with the same

mean-field philosophy. As such, even though we have expressed the response functions of Dicke-like models in terms of the bare response functions of the cavity and the mean-field effective Hamiltonian, computing the latter will generally be a challenge itself. In Chaps. 4 and 5 we study some cases in which this can be done exactly as well.

This has been studied and exploited before at equilibrium [17, 76, 109], in the dynamics [133] and in Refs. [45, 59] and now here for the LRT. Beyond the LRT, the equations-of-motion approach opens the possibility of studying real-time dynamics. Indeed, in Chap. 6 we will explore the dynamics of magnetic cavity QED materials.

The comparison between the two approaches is not just an academic exercise. In many cases it can be interesting to go beyond the $N \to \infty$ limit. This would be the case in topological systems, where boundaries play an important role. In that case the two approaches offer complementary methods to incorporate finite-size corrections. In the path integral approach, corrections are computed by extending the saddle-point expansion to higher orders, and thus relaxing $W = W_0$ to the weaker $W^{-1} = W_0^{-1} + \Pi$, where Π can be computed with standard diagrammatic techniques in terms of fourth- and higher-order matter response functions [59]. In the equations-of-motion approach, corrections are introduced by expanding the theory from two- to three- and higher-order Green functions before invoking the mean-field factoring of the correlators.

Finally, it is also evident from the expressions derived along this chapter for two-point correlators that the LRT theory rests on the equilibrium solution of the model that we developed in Chap. 2. The bare matter correlators have to be computed from the mean-field effective Hamiltonian that determines the equilibrium properties of the model. Therefore, although we have presented them as independent units for the sake of clarity, the LRT builds on top of the equilibrium theory, and together they can be taken as a monolithic theory for the equilibrium of cavity QED materials and its perturbations.

Chapter 4

Applications to electronic systems

In this chapter we will apply the equilibrium and linear response theories to several electronic systems. First, in a general setting, we will discuss the phenomenon of equilibrium superradiance and propose a general critical condition for a superradiant phase transition obtained from our linear response theory (LRT). Then, we will discuss equilibrium superradiance specifically in the cases of localized emitters and electron liquids, using the previously derived critical condition as well as the effective Hamiltonian. In the former case the effective Hamiltonian itself provides a no-go theorem for electric dipoles, and we will discuss the consequences for more complex systems. In the latter case we will derive a no-go theorem for homogeneous cavity fields and a critical condition for non-homogeneous cavity fields. Finally, we will specifically compute the equilibrium and optical response properties of a two-dimensional (2D) electron gas coupled to a cavity. For the optical response, we will include a perpendicular classical magnetic field to study the cavity-modified integer quantum Hall effect.

This chapter is based on parts of Refs. [62, 63].

4.1 Equilibrium superradiance

Originally, equilibrium superradiance is defined as the phase transition of the Dicke model (See Sec. 1.3.1). More generally, it may refer to a phase transition in any GDM (1.39) stemming from the light-matter coupling and resulting in a non-zero expectation value of the matter coupling operators $\langle C_k \rangle \neq 0$ and a macroscopic photonic population in the cavity $\langle a_k^\dagger a_k \rangle \sim N$. So far, the understanding is as follows. If one adopts the correct gauge-invariant

description of a single uniform cavity mode, the phase transition is forbidden. This has been proven true even without the dipole approximation [76, 78, 81, 88]. This transition is often referred to as *equilibrium superradiance* or *photon condensation*, although some ambiguity still surrounds these terms [98]. Moreover, critical conditions have been obtained in the case of non-uniform cavity fields [77, 134, 135]. Subtleties arise from the fact that the separation between light and matter subsystems is manifestly gauge-dependent [81, 98]. For that reason, it is preferable to characterize the phase transition in terms of gauge invariant observables such as the transverse photon number. However, although theoretically valid, this choice suffers from the fact that not all observables, in particular the transverse photon number, are experimentally measurable, a handicap that challenges their validity as signatures of a phase transition. To avoid this pitfall, we propose to look at this issue from a different perspective: instead of arguing whether the phase transition has a "light" or a "matter" signature, we will simply compare the behavior of the material when it is placed outside a cavity, i.e., in a region of space with an unconfined electromagnetic field, against its behavior when it is placed inside a cavity, i.e., in a region of space where the electromagnetic field is confined. Note that this is *the experimentally relevant question*. In fact, alterations of matter and condensation of photons are two sides of the same coin.

Our formalism is particularly well suited to answer this question because it eliminates the cavity, reformulating the model in terms of the bare matter plus effective terms that reflect the interactions with the cavity. In the case of the effective Hamiltonian the effect of the cavity is reflected in the effective interactions. In the case of the LRT the effect of the cavity is reflected in the dressing of the bare matter propagators [Cf. Eq. (3.32)]. Whether a material behaves differently after placing it inside a cavity will be answered by studying the impact, or lack thereof, that the effective terms have in its behavior.

4.1.1 General critical condition for equilibrium superradiance

We can extract a general critical condition from our LRT. On the one hand, the response functions present poles at the resonant frequencies of the system and thus provide information about the spectrum. On the other hand, phase transitions are signaled by a closing of the energy gap between the ground and first excited states. Thus, a phase transition occurs when a response function presents a pole at zero frequency. The caveat is that each response function only displays poles at the frequencies of the transitions driven by the operators that compose it. For instance χ_{xx} will only display poles for the transitions driven by the matter coupling operator C_x. For the remainder of the argument we are going to assume that C_x can drive transitions between the ground and

first excited states and thus that a pole of χ_{xx} will correspond to the energy gap of the system. This is a safe assumption since we can always choose an appropriate response function and apply to it the argument that we will now develop. For reference, in Sec. 5.3 we study a counterexample, a case where χ_{xx} does not reveal the gap. From Eq. (3.32) we can see that the response function of the matter coupling operator χ_{xx} can have poles from two sources. First if the numerator $\chi_{xx,0}$ has a pole, which would indicate that the bare matter already presents a phase transition without coupling to a cavity. Note that we examine $\chi_{xx,0}$ and not $\tilde{\chi}_{xx,0}$ because we can always approach the phase transition from the normal phase, where the mean field is zero and the effective Hamiltonian matches the bare matter Hamiltonian. The second source of poles is the zeros of the denominator in Eq. (3.32), which yield the general critical condition

$$1 + V_{\text{ind}}(0)\chi_{xx,0}(0) = 0\,. \tag{4.1}$$

This is the critical condition for equilibrium superradiance, a light-induced phase transition in the material. No-go theorems for equilibrium superradiance will appear when the critical condition cannot be satisfied under certain circumstances.

4.1.2 Localized emitters

If we consider a system of localized emitters such as the one discussed in Sec. 1.2.2, the corresponding effective Hamiltonian reads

$$\begin{aligned} H_{\text{eff}} = H_{\text{m}} &+ \sum_{\kappa} \omega_{\boldsymbol{k}} \left| A_{\boldsymbol{k}} \sum_j \left(\boldsymbol{d}_j \cdot \boldsymbol{u}_\kappa(\boldsymbol{R}_j) - \frac{\omega_{\boldsymbol{k}}}{c} \text{Tr}(U_\kappa(\boldsymbol{R}_j) Q_j) \right) \right|^2 \\ &- \sum_{\kappa} \omega_{\boldsymbol{k}} \left| A_{\boldsymbol{k}} \sum_j \left(\frac{1}{c} \boldsymbol{m}_j \cdot \boldsymbol{u}_{\perp,\kappa}(\boldsymbol{R}_j) + i \boldsymbol{d}_j \cdot \boldsymbol{u}_\kappa(\boldsymbol{R}_j) - i \frac{\omega_{\boldsymbol{k}}}{c} \text{Tr}(U_\kappa(\boldsymbol{R}_j) Q_j) \right) \right|^2 , \end{aligned} \tag{4.2}$$

which simplifies to

$$H_{\text{eff}} = H_{\text{m}} - \sum_{ij} \boldsymbol{m}_i \cdot \Lambda^{\text{mm}}_{ij} \cdot \boldsymbol{m}_j - \sum_{ij} \boldsymbol{m}_i \cdot \Lambda^{\text{md}}_{ij} \cdot \boldsymbol{d}_j - \sum_{ij} \sum_{\alpha\beta\gamma} m_{i,\alpha} \Lambda^{\text{mq}}_{ij,\alpha\beta\gamma} Q_{j,\beta\gamma} \tag{4.3}$$

with

$$\Lambda_{ij}^{\mathrm{mm}} = \sum_{\kappa} \frac{\omega_{\boldsymbol{k}} A_{\boldsymbol{k}}^2}{c^2} \boldsymbol{u}_{\perp,\kappa}(\boldsymbol{R}_i) \otimes \boldsymbol{u}_{\perp,\kappa}^*(\boldsymbol{R}_j) \,, \tag{4.4}$$

$$\Lambda_{ij}^{\mathrm{md}} = \sum_{\kappa} \frac{2\omega_{\boldsymbol{k}} A_{\boldsymbol{k}}^2}{c} \mathrm{Im}\left[\boldsymbol{u}_{\perp,\kappa}(\boldsymbol{R}_i) \otimes \boldsymbol{u}_{\kappa}^*(\boldsymbol{R}_j)\right] \,, \tag{4.5}$$

$$\Lambda_{ij}^{\mathrm{mq}} = \sum_{\kappa} \frac{2\omega_{\boldsymbol{k}}^2 A_{\boldsymbol{k}}^2}{c^2} \mathrm{Im}\left[\boldsymbol{u}_{\perp,\kappa}(\boldsymbol{R}_i) \otimes U_{\kappa}^*(\boldsymbol{R}_j)\right] \,, \tag{4.6}$$

where $\otimes$ denotes the outer product.

We see in Eq. (4.3) that cavity-mediated electric dipole-dipole interactions, dipole-quadrupole interactions and quadrupole-quadrupole interactions are canceled by the P^2 term. This is the no-go theorem in the dipole gauge: if the electromagnetic field is considered homogeneous enough that the multipolar expansion can be truncated at the level of the electric dipole, then the resulting effective Hamiltonian is equal to the bare matter Hamiltonian, there are no cavity-mediated effects. Note that in the case of working with electric dipoles in the dipole gauge, $V_{\mathrm{ind}}(0) = 0$ [Cf. Eqs. (3.1) and (3.9)], making the critical condition of Eq. (4.1) trivially unsatisfiable. With this, the effective Hamiltonian and the LRT provide the same no-go theorem. In essence, they are both manifestations of the fact that $V_{\mathrm{ind}}(0) = 0$ in this system, at different points of the theory.

The no-go theorem tells us that in order to have any cavity-mediated effect, the electromagnetic field has to be inhomogeneous enough that the magnetic dipole starts playing a role. In that case, the effective Hamiltonian is the bare matter Hamiltonian plus additional cavity-mediated terms corresponding to magnetic dipole-dipole interactions, magnetic-dipole-electric-dipole interactions and magnetic-dipole-electric-quadrupole interactions. Magnetic dipole-dipole and magnetic-dipole-electric-quadrupole interactions are weaker than magnetic-dipole-electric-dipole interactions by a factor $\omega_{\boldsymbol{k}}|\boldsymbol{r}_j|/c$ with c the speed of light [104]. Additionally, the bare matter Hamiltonian H_{m} may still contain the electrostatic Coulomb interactions between electric dipoles, which are themselves a factor $\omega_{\boldsymbol{k}}|\boldsymbol{r}_j|/c$ stronger that the magnetic-dipole-electric-dipole interactions. Therefore, the cavity-mediated interactions are expected to only be significant in materials with negligible electrostatic dipole-dipole interactions. This is the case in non-polarizable materials such as crystals of molecular nanomagnets, which we will explore in Sec. 5.2.2. Alternatively, one may investigate the effects arising from effective magnetic-dipole-electric-dipole interactions in materials with permanent electric dipoles but negligible intrinsic electric dipole-dipole interactions. However, these magnetoelectric interactions can be shown to be identically zero in reciprocal media in the fast-cavity limit

if the full electromagnetic spectrum is considered [61]. It would be interesting to consider scenarios outside this regime.

4.1.3 Electron liquids

Let us consider an electron liquid and for simplicity disregard the Zeeman term (See Sec. 1.2.1). Accordingly, we have a generalized Dicke model (GDM) with

$$H_{\mathrm{m}} = H'_{\mathrm{m}} = \sum_j \frac{\boldsymbol{p}_j^2}{2m} + V'_{\mathrm{C}} + V\,, \tag{4.7}$$

$$g_{\boldsymbol{k}} = \sqrt{\frac{\omega_{\boldsymbol{k}}}{\tilde{\omega}_{\boldsymbol{k}}}} g^{\mathrm{e}}_{\boldsymbol{k}}\,, \tag{4.8}$$

$$C_\kappa = \sum_j \sqrt{\frac{1}{2m\omega_{\mathrm{p}}}} \boldsymbol{p}_j \cdot \boldsymbol{u}_\kappa(\boldsymbol{r}_j)\,. \tag{4.9}$$

Then, in the thermodynamic limit, the effective matter Hamiltonian, according to Eq. 2.35, is

$$H_{\mathrm{eff}} = H'_{\mathrm{m}} - \sum_\kappa \frac{\omega_{\mathrm{p}}^2}{\omega_{\boldsymbol{k}}^2 + \omega_{\mathrm{p}}^2} \frac{1}{N} \sum_{ij} \frac{1}{2m} (\boldsymbol{p}_i \cdot \boldsymbol{u}_\kappa(\boldsymbol{r}_i))(\boldsymbol{p}_j \cdot \boldsymbol{u}^*_\kappa(\boldsymbol{r}_j)) \tag{4.10}$$

Recall that $\kappa \equiv (\boldsymbol{k}, \sigma)$ with σ the polarization index. We have an effective all-to-all coupling between the electrons' momenta. The strength of the coupling between a pair of electrons depends on their positions.

Unlike in the case of localized emitters that we treated in the multipolar gauge, a no-go theorem is not evident from the effective Hamiltonian in the case of the electron liquid treated in the Coulomb gauge. This is because no-go theorems stem from the A^2 in the Coulomb gauge and P^2 term in the multipolar gauge [90]. Whereas the P^2 is a matter-only term that appears explicitly in the effective Hamiltonian, the A^2 term is incorporated as a renormalization of the cavity frequencies and the light-matter coupling. As a result, the A^2 term results in a renormalization of the cavity-mediated matter-matter coupling. In contrast, the P^2 term results in the exact cancelation of the cavity-mediated matter-matter coupling. Thus, in the case of the electron liquid, we will rely solely on the critical condition for superradiance of Eq. (4.1).

No-go theorem for uniform cavity fields

If we make the approximation to a setup with a single uniform mode $\boldsymbol{k} \to 0$, $\sigma = 1$, in terms of the LRT we have

$$\Omega = \tilde{\omega}_0 \,, \tag{4.11}$$

$$\lambda = \sqrt{\frac{\omega_\mathrm{p}}{\tilde{\omega}_0}}\omega_\mathrm{p} \,, \tag{4.12}$$

$$C_x = \sqrt{\frac{1}{2m\omega_\mathrm{p}}} \sum_j \boldsymbol{e}_1 \cdot \boldsymbol{p}_j \,, \tag{4.13}$$

with $\tilde{\omega}_0^2 = \omega_0^2 + \omega_\mathrm{p}^2$. Accordingly, we have

$$V_\mathrm{ind}(0) = -\frac{2\omega_\mathrm{p}^3}{\tilde{\omega}_0^2} \,, \tag{4.14}$$

$$\chi_{xx,0}(0) = -\frac{1}{2m\omega_\mathrm{p}} \frac{1}{N} G^r_{\sum_j \boldsymbol{e}_1\cdot\boldsymbol{p}_j, \sum_j \boldsymbol{e}_1\cdot\boldsymbol{p}_j}(0) \,. \tag{4.15}$$

With this, the critical condition for superradiance reads

$$1 = -\frac{\omega_\mathrm{p}^2}{\omega_\mathrm{p}^2 + \omega_0^2} \frac{1}{Nm} G^r_{\sum_j \boldsymbol{e}_1\cdot\boldsymbol{p}_j, \sum_j \boldsymbol{e}_1\cdot\boldsymbol{p}_j}(0) \,. \tag{4.16}$$

Note that $-G^r_{\sum_j \boldsymbol{e}_1\cdot\boldsymbol{p}_j, \sum_j \boldsymbol{e}_1\cdot\boldsymbol{p}_j} > 0$ is proportional to the paramagnetic current-current response function for the electron gas. The electron system cannot respond to a uniform and time-independent vector potential $\boldsymbol{A}$, so the physical current-current response function, which is the sum of the paramagnetic and diamagnetic responses, must be zero. This is known as the diamagnetic sum rule [113, Chap. 3]. As a result, the paramagnetic current-current response function must be equal and opposite to the diamagnetic current-current response function, and thus it obeys

$$-G^r_{\sum_j \boldsymbol{e}_1\cdot\boldsymbol{p}_j, \sum_j \boldsymbol{e}_1\cdot\boldsymbol{p}_j}(0) = Nm \tag{4.17}$$

which, upon substitution in Eq. (4.16) renders the critical condition unsatisfiable

$$1 \neq \frac{\omega_\mathrm{p}^2}{\omega_\mathrm{p}^2 + \omega_0^2} \,, \tag{4.18}$$

for finite ω_p and non-zero ω_0. This is the no-go theorem for equilibrium superradiance of the electron liquid with homogeneous cavity fields. Consequently, we find that $H_\mathrm{eff} = H'_M$, thus the equilibrium effect of the transverse cavity fields on the matter system is non-existent. If there is a phase transition, its

origin lies within H'_M. Meaning that it is either caused by intrinsic interactions in the material or induced by electrostatic effects arising from the interaction between real charges and image charges.

To reinforce this result, let us compare it with the case in which the diamagnetic term is omitted in the light-matter interaction, breaking gauge invariance. This equates to setting $\tilde{\omega}_0 = \omega_0$ in Eqs. (4.11) and (4.12). Then, the critical condition becomes

$$\frac{\omega_\mathrm{p}}{\omega_0} = 1\,, \tag{4.19}$$

which can be satisfied if the plasma frequency ω_p and thus the light-matter coupling λ is large enough. We have thus not only arrived to a no-go theorem for uniform cavity fields, but we are also able to explain the appearance of critical behavior when the diamagnetic term is ignored.

Critical condition for non-uniform cavity fields

Extending the critical condition for superradiance to the multimode case requires the (multimode) generalization of the LRT that we develop in App. C. Then, assuming that momentum is conserved in the matter subsystem, i.e., that $\chi_{\kappa\kappa',0} = \delta_{\kappa\kappa'}\chi_{\kappa\kappa,0}$ with $\chi_{\kappa\kappa,0} = -N^{-1}G^\mathrm{r}_{C_{\boldsymbol{k},\sigma},C_{-\boldsymbol{k},\sigma}}$ the response function of the matter coupling operators to the cavity modes $(\boldsymbol{k},\sigma)$ and $(-\boldsymbol{k},\sigma)$, we obtain for each mode a critical condition analogous to the one we obtain in the case of a single uniform mode

$$1 + V_{\mathrm{ind},\kappa}(0)\chi_{\kappa\kappa,0}(0) = 0\,. \tag{4.20}$$

This already tells us that equilibrium superradiance will occur in a per-mode basis. Those modes that satisfy the critical condition will develop a finite population of photons accompanied by a proportional non-zero expectation value of the corresponding matter coupling operator C_k. Likewise, $V_{\mathrm{ind},k}(0)$ and C_k are also straightforward generalizations of the single-mode case

$$V_{\mathrm{ind},\kappa}(0) = -\frac{2\omega_\mathrm{p}^3}{\tilde{\omega}_{\boldsymbol{k}}^2}\,, \tag{4.21}$$

$$\chi_{\kappa\kappa,0}(0) = -\frac{1}{2m\omega_\mathrm{p}}\frac{1}{N}G^r_{\sum_j \boldsymbol{u}_{\boldsymbol{k},\sigma}(\boldsymbol{r}_j)\cdot\boldsymbol{p}_j,\sum_j \boldsymbol{u}_{-\boldsymbol{k},\sigma}(\boldsymbol{r}_j)\cdot\boldsymbol{p}_j}(0)\,. \tag{4.22}$$

The resulting critical condition for each mode reads

$$1 = -\frac{\omega_\mathrm{p}^2}{\omega_\mathrm{p}^2+\omega_\kappa^2}\frac{1}{Nm}G^r_{\sum_j \boldsymbol{u}_{\boldsymbol{k},\sigma}(\boldsymbol{r}_j)\cdot\boldsymbol{p}_j,\sum_j \boldsymbol{u}_{-\boldsymbol{k},\sigma}(\boldsymbol{r}_j)\cdot\boldsymbol{p}_j}(0)\,. \tag{4.23}$$

Unlike in the single uniform mode case, here the value of

$$-G^r_{\sum_j \boldsymbol{u}_{\boldsymbol{k},\sigma}(\boldsymbol{r}_j)\cdot\boldsymbol{p}_j,\sum_j \boldsymbol{u}_{-\boldsymbol{k},\sigma}(\boldsymbol{r}_j)\cdot\boldsymbol{p}_j}(0) > 0\,, \tag{4.24}$$

is not restricted by a diamagnetic sum rule. Accordingly, it could be large enough in certain conditions to satisfy the critical condition, allowing for equilibrium superradiance. A detailed discussion of the physical implications of this result and its extension to include the Zeeman coupling of the electronic spin to the cavity's magnetic field can be found in Ref. [77].

The application of the LRT developed in Chap. 3 to the problem of equilibrium superradiance has allowed us to unify and generalize, on rigorous grounds, several results pertaining to no-go theorems and critical conditions in electron liquids [76–78], like the one explained in Sec. 1.3.2.

4.2 2D electron gas in a cavity: equilibrium properties

The electron gas is a paradigmatic model in condensed matter physics. It was originally formulated by Sommerfeld [136] for the study of the thermal and electronic properties of materials, and it later became the building block of the Fermi liquid theory, developed by Landau [137, 138]. Its interacting generalization, known as the homogeneous electron gas or jellium model, is the basis for advanced computational techniques such as density functional theory (DFT) and the local density approximation (LDA) [139, 140]. Lowering the dimensionality, 2D electron gases can be found in semiconductor devices in solid state physics [141]. They also describe the integer quantum Hall effect when subjected to strong magnetic fields and low temperature [142, 143]. Having established that the electron gas is an interesting model exhibiting rich phenomenology, it seems suggestive to explore the extent to which its behavior can be altered by coupling it to a cavity. The first steps in this direction have already experimentally confirmed the breakdown of topological protection by cavity vacuum fields [19], and predicted the existence of a polaritonic Hofstadter butterfly and modified integer Hall conductance [51, 52] and cavity-mediated hopping [53] in the integer quantum Hall effect [144, 145].

Ref. [50] is dedicated to the exact analytical solution of the 2D free electron gas in a cavity. To adhere to the same assumptions as the authors, we will consider a multimode description of the cavity fields, but with the peculiarity that the wavelength of every mode be large enough that the electrons see the mode as uniform. In that case we have $\boldsymbol{u}_\kappa(\boldsymbol{r}_j) \equiv \boldsymbol{e}_\sigma$ where $\boldsymbol{e}_\sigma$ is the polarization vector of the mode, but we retain the summation in κ when summing over modes. In addition, the mode-mode interactions arising from the diamagnetic term are completely disregarded. On the matter side, free electrons are simply described by the kinetic term in Eq. (4.7), without intrinsic interactions. The 2D nature of the system is reflected in the fact that the momenta are confined to a plane: $\boldsymbol{p}_j = (p_{j,x}, p_{j,y})$. Adapting the effective Hamiltonian that we derived

for the electron liquid in Eq. (4.10) to these particularities yields

$$H_{\text{eff}} = \frac{1}{2m}\left[\sum_j \boldsymbol{p}_j^2 - \left(\sum_{\boldsymbol{k}} \frac{\omega_{\text{p}}^2}{\omega_{\boldsymbol{k}}^2 + \omega_{\text{p}}^2}\right)\frac{1}{N}\sum_\sigma \left(\sum_i \boldsymbol{p}_i \cdot \boldsymbol{e}_\sigma\right)^2\right] \tag{4.25}$$

This Hamiltonian corresponds precisely to the ground-state energy obtained in [50]. We find the added benefit that the Hamiltonian offers more flexibility in the amount of calculations that can be done from here. For instance finite temperature calculations, in contrast to the ground-state energy, which is limited in that regard.

4.3 Integer quantum Hall effect in a cavity

Having studied the equilibrium properties of the 2D electron gas coupled to a cavity in the previous section, here we look into its response properties, in particular its optical conductivity in the presence of a perpendicular magnetic field. In other words, we will apply the LRT theory developed in Chap. 3 to study the modification of the integer quantum Hall effect.

4.3.1 The Hamiltonian

The matter system under consideration is a two-dimensional electron gas subject to a perpendicular classical magnetic field. The Hamiltonian of the electron gas coupled to a single-mode cavity reads

$$H = \sum_j \frac{(\boldsymbol{p}_j - e\boldsymbol{A}_{\text{ext}}(\boldsymbol{r}_j) - e\boldsymbol{A}_0(b + b^\dagger))^2}{2m} + \omega_0 b^\dagger b\,. \tag{4.26}$$

Both the external classical vector potential and the cavity's vector potential point along the x-direction: $\boldsymbol{A}_{\text{ext}}(\boldsymbol{r}_j) = -By_j\boldsymbol{e}_x$ and $\boldsymbol{A}_0 = \sqrt{1/(2\epsilon_0 V\omega_0)}\boldsymbol{e}_x$. After some manipulations, we can write the Hamiltonian as

$$\begin{aligned} H = H_{\text{m}} - \frac{\omega_{\text{p}}}{\sqrt{N}}\left(\sqrt{\frac{\omega_{\text{p}}}{\omega_0}}\bar{p}_x + \sqrt{\frac{\omega_{\text{c}}}{\omega_0}}\bar{y}\right)\left(b + b^\dagger\right) \\ + \omega_0 b^\dagger b + \frac{\omega_{\text{p}}^2}{4\omega_0}\left(b + b^\dagger\right)^2\,, \end{aligned} \tag{4.27}$$

where H_{m} is the bare (without cavity) electron gas Hamiltonian

$$H_{\text{m}} = \sum_j \frac{(\boldsymbol{p}_j - e\boldsymbol{A}_{\text{ext}}(\boldsymbol{r}_j))^2}{2m} \tag{4.28}$$

and $\bar{p}_x$ and $\bar{y}$ are adimensionalized collective operators

$$\bar{p}_x = \frac{1}{\sqrt{2m\omega_\mathrm{p}}} \sum_j p_{x,j} \,, \tag{4.29}$$

$$\bar{y} = \sqrt{\frac{m\omega_\mathrm{c}}{2}} \sum_j y_j \,. \tag{4.30}$$

$\omega_\mathrm{p} = \sqrt{e^2 N/(m\epsilon_0 V)}$ is the plasma frequency, and we have defined the cyclotron frequency $\omega_\mathrm{c} = eB/m$. The photonic terms of the Hamiltonian can be diagonalized with a Bogoliubov transformation, which yields

$$H = H_\mathrm{m} - \frac{\omega_\mathrm{p}}{\sqrt{N}} \left(\sqrt{\frac{\omega_\mathrm{p}}{\tilde{\omega}}} \bar{p}_x + \sqrt{\frac{\omega_\mathrm{c}}{\tilde{\omega}}} \bar{y} \right) \left(a + a^\dagger \right) + \tilde{\omega} a^\dagger a \,, \tag{4.31}$$

with $\tilde{\omega}^2 = \omega_0^2 + \omega_\mathrm{p}^2$. By identifying $g = -\omega_\mathrm{p}/\sqrt{N}$ and $C_x = \sqrt{\omega_\mathrm{p}/\tilde{\omega}}\bar{p}_x + \sqrt{\omega_\mathrm{c}/\tilde{\omega}}\bar{y}$ the Hamiltonian takes the form of Eq. (3.1). Note that in this case there is no P^2 term, i.e., $\zeta = 0$, as we are working in the Coulomb gauge. In exchange, the elimination of the A^2 term through the Bogoliubov transform renormalizes the cavity frequency and light-matter coupling.

4.3.2 Current and optical conductivity

In the quantum Hall effect [144, 145], one is typically interested in computing the longitudinal and transverse conductivities. The optical conductivity tensor can be computed with the Kubo formalism in terms of the current response functions

$$\sigma_{rs}(\omega) = \frac{i}{\omega_+} \left[\frac{e^2 \rho_\mathrm{2D}}{m} \delta_{rs} + \frac{G^\mathrm{r}_{J_r,J_s}(\omega)}{A} \right] \,, \tag{4.32}$$

where $\omega_+ = \omega + i\delta$, A and ρ_2D are the area and surface density of the two-dimensional electron gas, δ is the broadening parameter, δ_{rs} is the Kronecker delta and $J_{a,b}$ are the current operators in the a and b directions, with $a, b \in \{x, y\}$ [113, 146]. We will now compute $G^\mathrm{r}_{J_r,J_s}$ using the theory outlined in Chap. 3, i.e., we will express $G^\mathrm{r}_{J_r,J_s}$ in terms of the response functions of the bare electron gas $G^{r0}_{J_r,J_s}$.

The current operator is given by

$$\begin{aligned} \boldsymbol{J} &= e \sum_j \boldsymbol{v}_j \\ &= \frac{e}{m} \sum_j \left(\boldsymbol{p}_j - e\boldsymbol{A}_\mathrm{ext}(\boldsymbol{r}_j) - e\boldsymbol{A}_0 (b + b^\dagger) \right) \,. \end{aligned} \tag{4.33}$$

Then, after some manipulation, we can express

$$J_x = \sqrt{\frac{2e^2\tilde{\omega}}{m}}\left(C_x + \gamma(a+a^\dagger)\right), \tag{4.34}$$

$$J_y = \sqrt{\frac{2e^2\tilde{\omega}}{m}}C_y, \tag{4.35}$$

with $\gamma = -\sqrt{N}\omega_\mathrm{p}/(2\tilde{\omega})$ and $C_y = \sqrt{\omega_\mathrm{p}/\tilde{\omega}}\bar{p}_y$. Here $\sqrt{2m\omega_\mathrm{p}}\bar{p}_y = \sum_j p_{y,j}$. Meaning that we need to compute

$$G^\mathrm{r}_{J_x,J_x} = \frac{2e^2\tilde{\omega}}{m}G^\mathrm{r}_{C_x+\gamma(a+a^\dagger),C_x+\gamma(a+a^\dagger)}, \tag{4.36}$$

$$G^\mathrm{r}_{J_x,J_y} = \frac{2e^2\tilde{\omega}}{m}G^\mathrm{r}_{C_x+\gamma(a+a^\dagger),C_y}, \tag{4.37}$$

$$G^\mathrm{r}_{J_y,J_y} = \frac{2e^2\tilde{\omega}}{m}G^\mathrm{r}_{C_y,C_y}. \tag{4.38}$$

Following App. E, these are given by

$$G^\mathrm{r}_{J_x,J_y}(\omega) = \left(1+\left(\frac{\omega_\mathrm{p}}{\tilde{\omega}}\right)^2\frac{\tilde{\omega}}{2}D^\mathrm{s}_0(\omega)\right)\frac{G^{\mathrm{r},0}_{J_x,J_y}(\omega)}{1-V_\mathrm{ind}(\omega)\frac{m}{2e^2\tilde{\omega}N}G^{\mathrm{r},0}_{J_x,J_x}(\omega)}, \tag{4.39}$$

$$\begin{aligned}G^\mathrm{r}_{J_x,J_x}(\omega) = \left(1+\left(\frac{\omega_\mathrm{p}}{\tilde{\omega}}\right)^2\frac{\tilde{\omega}}{2}D^\mathrm{s}_0(\omega)\right)^2\frac{G^{\mathrm{r},0}_{J_x,J_x}(\omega)}{1-V_\mathrm{ind}(\omega)\frac{m}{2e^2\tilde{\omega}N}G^{\mathrm{r},0}_{J_x,J_x}(\omega)}\\ + \frac{Ne^2}{m}\left(\frac{\omega_\mathrm{p}}{\tilde{\omega}}\right)^2\frac{\tilde{\omega}}{2}D^\mathrm{s}_0(\omega),\end{aligned} \tag{4.40}$$

$$\begin{aligned}G^\mathrm{r}_{J_y,J_y}(\omega) = \frac{1}{1-V_\mathrm{ind}(\omega)\frac{m}{2e^2\tilde{\omega}N}G^{\mathrm{r},0}_{J_x,J_x(\omega)}}\Bigg(G^{\mathrm{r},0}_{J_y,J_y}(\omega)\\ + V_\mathrm{ind}(\omega)\frac{m}{2e^2\tilde{\omega}N}\left(G^{\mathrm{r},0}_{J_x,J_y}(\omega)G^{\mathrm{r},0}_{J_y,J_x}(\omega) - G^{\mathrm{r},0}_{J_x,J_x}(\omega)G^{\mathrm{r},0}_{J_y,J_y}(\omega)\right)\Bigg).\end{aligned} \tag{4.41}$$

Obtaining explicit expressions for the current response functions is now just a matter of computing the current response functions of the bare electron gas $G^{\mathrm{r},0}_{J_r,J_s}$. We refer to the latter as bare current response functions, and we compute them in the next section.

4.3.3 Computing the bare current response functions

To study the bare 2D electron gas we lean on the reasoning laid out in Ref. [52]. There, they study the same 2D electron gas subject to a perpendicular classical magnetic field and coupled to a cavity (4.26). They show that the cavity only couples to the center-of-mass coordinates. Furthermore, they show

that the center-of-mass and relative coordinate sectors of the Hamiltonian commute. This essentially splits the problem into two, the problem of the relative coordinates unmodified by the cavity, and the problem of the center or mass coupled to the cavity. Note from Eqs. (4.34) and (4.35) that the currents also only depend on center-of-mass coordinates. In summary, the full problem of a 2D electron gas coupled to a cavity can be broken into the problem of the relative coordinates, decoupled from the cavity, and the problem of an independent center of mass coordinate, which couples to the cavity and is solely responsible for the conduction properties of the electron gas. Consequently, in order to compute bare current response functions, we only need to study the center-of-mass sector of the matter Hamiltonian

$$H_{\mathrm{m}}^{\mathrm{cm}} = \frac{\left(\boldsymbol{P} - e\boldsymbol{A}_{\mathrm{ext}}(\boldsymbol{R})\right)^2}{2m}\,, \tag{4.42}$$

with $\sqrt{N}\boldsymbol{R} = \sum_j \boldsymbol{r}_j$ and $\sqrt{N}\boldsymbol{P} = \sum_j \boldsymbol{p}_j$ the center-of-mass position and momentum operators. This is just the Hamiltonian of a single electron under a classical magnetic field, the prototypical example of Landau quantization [147, Chap. 1]. The eigenstates of the system are separable, into plane waves in the X direction and eigenstates of a displaced harmonic oscillator of frequency ω_{c} along the Y direction

$$\begin{aligned} H_{\mathrm{m}}^{\mathrm{cm}}|K_X, n\rangle &= \omega_{\mathrm{c}}\left(c^\dagger c + \frac{1}{2}\right)|K_X, n\rangle \\ &= \omega_{\mathrm{c}}\left(n + \frac{1}{2}\right)|K_X, n\rangle\,, \end{aligned} \tag{4.43}$$

With $P_X|K_X, n\rangle = K_X|K_X, n\rangle$. Here

$$V = \sqrt{\frac{1}{2\omega_{\mathrm{c}}}}\left(c + c^\dagger\right)\,, \tag{4.44}$$

$$P_V = i\sqrt{\frac{\omega_{\mathrm{c}}}{2}}\left(c^\dagger - c\right)\,, \tag{4.45}$$

and $V = \sqrt{m}(Y + K_X l_c^2)$, $P_V = P_Y/\sqrt{m}$, with $l_c = \sqrt{1/(eB)}$.

From the definition in Eq. (4.33) (ignoring the contribution from the cavity to get the bare current) we can see that the current only depends on center-of-mass coordinates

$$\boldsymbol{J} = \sqrt{N}\frac{e}{m}\left(\boldsymbol{P} - e\boldsymbol{A}_{\mathrm{ext}}(\boldsymbol{R})\right)\,. \tag{4.46}$$

After some manipulation, we can express

$$J_x = \frac{e\omega_{\mathrm{c}}}{\sqrt{2m}}\left(\frac{1}{\omega_{\mathrm{c}}\sqrt{m}}(P_X - K_X) + \frac{1}{\sqrt{\omega_{\mathrm{c}}}}(c + c^\dagger)\right)\,, \tag{4.47}$$

$$J_y = i\frac{e\sqrt{\omega_{\mathrm{c}}}}{\sqrt{2m}}\left(c^\dagger - c\right)\,, \tag{4.48}$$

and the matrix elements

$$\langle K'_X, n|J_x|K_X, m\rangle = \delta_{K_X,K'_X}\frac{e\sqrt{\omega_c}}{\sqrt{2m}}(\sqrt{m+1}\delta_{n,m+1} + \sqrt{m}\delta_{n,m-1})\,, \tag{4.49}$$

$$\langle K'_X, n|J_y|K_X, m\rangle = \delta_{K_X,K'_X}\, i\frac{e\sqrt{\omega_c}}{\sqrt{2m}}(\sqrt{m+1}\delta_{n,m+1} - \sqrt{m}\delta_{n,m-1})\,. \tag{4.50}$$

This shows that the current operators are diagonal with respect to the plane waves along the X direction, such that the spectral decomposition of the current response functions can be written simply as a sum over eigenstates of the harmonic oscillator along the Y direction. At zero temperature, this reads

$$G^{\mathrm{r},0}_{J_r,J_s}(\omega) = \sum_n \left(\frac{\langle 0|J_r|n\rangle\langle n|J_s|0\rangle}{\omega_+ + E_0 - E_n} - \frac{\langle n|J_r|0\rangle\langle 0|J_s|n\rangle}{\omega_+ + E_n - E_0}\right). \tag{4.51}$$

From Eqs. (4.49), (4.50) and (4.51) we obtain the bare current response functions

$$G^{\mathrm{r},0}_{J_x,J_x}(\omega) = G^{\mathrm{r},0}_{J_y,J_y}(\omega) = -\frac{Ne^2\omega_c}{m}\frac{1}{2}\left(\frac{1}{\omega_+ + \omega_c} - \frac{1}{\omega_+ - \omega_c}\right), \tag{4.52}$$

$$G^{\mathrm{r},0}_{J_x,J_y}(\omega) = \frac{Ne^2\omega_c}{m}\frac{i}{2}\left(\frac{1}{\omega_+ + \omega_c} + \frac{1}{\omega_+ - \omega_c}\right), \tag{4.53}$$

$$G^{\mathrm{r},0}_{J_y,J_x}(\omega) = -\frac{Ne^2\omega_c}{m}\frac{i}{2}\left(\frac{1}{\omega_+ + \omega_c} + \frac{1}{\omega_+ - \omega_c}\right). \tag{4.54}$$

4.3.4 Closed expressions for the current response functions

Substituting Eqs. (4.52), (4.53), (4.54) and $V_{\mathrm{ind}}(\omega) = \omega_p^2 D_0^s(\omega)$, with $D_0^s(\omega)$ the analytic continuation of $D_0^s(\omega_m)|_{i\omega_m\to\omega_+}$ (E.5), into Eqs. (E.11), (E.12) and (E.13) yields, after some manipulation,

$$G^{\mathrm{r}}_{J_x,J_y}(\omega) = i\frac{Ne^2}{m}\frac{\omega_c\omega_+\left(\omega_+^2 - \omega_0^2\right)}{\left(\omega_+^2 - \tilde{\omega}^2\right)\left(\omega_+^2 - \omega_c^2\right) - \omega_p^2\omega_c^2}\,, \tag{4.55}$$

$$G^{\mathrm{r}}_{J_x,J_x}(\omega) = \frac{Ne^2}{m}\frac{\left(\omega_c^2 + \omega_p^2\right)\left(\omega_+^2 - \frac{\omega_0^2\omega_c^2}{\omega_c^2+\omega_p^2}\right)}{\left(\omega_+^2 - \tilde{\omega}^2\right)\left(\omega_+^2 - \omega_c^2\right) - \omega_p^2\omega_c^2}\,, \tag{4.56}$$

$$G^{\mathrm{r}}_{J_y,J_y}(\omega) = \frac{Ne^2}{m}\frac{\omega_c^2\left(\omega_+^2 - \omega_0^2\right)}{\left(\omega_+^2 - \tilde{\omega}^2\right)\left(\omega_+^2 - \omega_c^2\right) - \omega_p^2\omega_c^2}\,. \tag{4.57}$$

These current response functions have poles at $\omega_+ = \pm\Omega_\pm$, with $\Omega_\pm$ the frequencies of the Landau polaritons

$$2\Omega_\pm = \tilde{\omega}^2 + \omega_c^2 \pm \sqrt{(\tilde{\omega}^2 - \omega_c^2)^2 + 4\omega_c^2\omega_p^2}\,. \tag{4.58}$$

This is all in agreement with the Landau polaritons and current response functions computed in Ref. [52]. There, they solve the system exactly, computing the energies and wavefunctions and subsequently the current response functions from the spectral decomposition formula. We also recover the dc conductivities in the long-wavelength limit $\omega_0 \to 0$, $\delta \to 0$ of Ref. [51].

For completeness, let us write down the dc ($\omega \to 0$) conductivities, which are typically of interest when considering the quantum Hall effect,

$$\sigma_{xy} = \frac{e^2\nu}{h}\frac{\omega_c^2\omega_0^2 + \omega_c^2\delta^2}{(\Omega_-^2+\delta^2)(\Omega_+^2+\delta^2)}\,, \tag{4.59}$$

$$\sigma_{xx} = \sigma_D\left(1 - \frac{\omega_c^2\omega_0^2 + \omega_c^2\delta^2 + \omega_p^2\delta^2}{(\Omega_-^2+\delta^2)(\Omega_+^2+\delta^2)}\right)\,, \tag{4.60}$$

$$\sigma_{yy} = \sigma_D\left(1 - \frac{\omega_c^2\omega_0^2 + \omega_c^2\delta^2}{(\Omega_-^2+\delta^2)(\Omega_+^2+\delta^2)}\right)\,. \tag{4.61}$$

Note that $\sigma_D = e^2\rho_{2D}/(m\delta)$ is the Drude dc conductivity and that in σ_{xy} we have introduced the Landau-level filling factor $\nu = \rho_{2D}h/(eB)$. These indicate a modification of the transverse conductivity from its quantized value in the absence of the cavity. However, this effect vanishes in the limit of no dissipation

$$\lim_{\delta\to 0}\sigma_{xy} = \frac{e^2\nu}{h}\,. \tag{4.62}$$

We show in Fig. 4.1(a) the dependence of σ_{xy} on the plasma frequency ω_p for a finite but small broadening parameter, $\delta/\omega_c \ll 1$ and $\delta/\omega_0 \ll 1$. One can see from Eq. (4.59) that in this regime

$$\sigma_{xy} \approx \frac{e^2\nu}{h}\left(1 - \frac{\delta^2}{\omega_c}\left(1 + \frac{\omega_p^2}{\omega_0^2}\right)\right)\,. \tag{4.63}$$

To clarify these effects on the conductivity, it is convenient to compute the resistivity matrix, $\rho = \sigma^{-1}$,

$$\rho_{xy} = \frac{h}{e^2\nu}\,, \tag{4.64}$$

$$\rho_{xx} = \sigma_D^{-1}\frac{\omega_0^2 + \omega_p^2 + \delta^2}{\omega_0^2 + \delta^2}\,, \tag{4.65}$$

$$\rho_{yy} = \sigma_D^{-1}\,. \tag{4.66}$$

We see now that the modifications of all the conductivity components arise solely from a modification to the longitudinal resistivity ρ_{xx}. Figure 4.1(b) shows the dependence of ρ_{xx} on the plasma frequency ω_p. The Hall resistivity

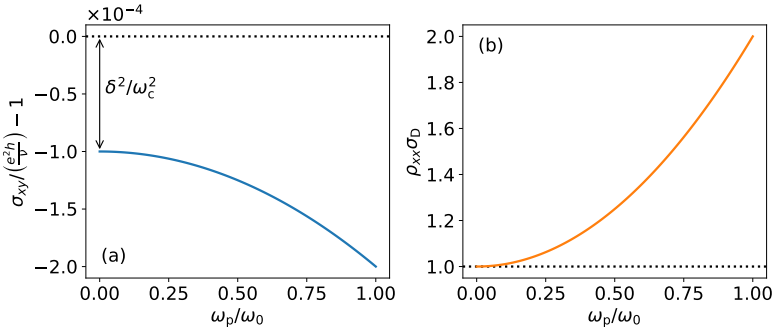

Figure 4.1: (a) Transverse conductivity σ_{xy} as a function of the plasma frequency ω_p for $\omega_\mathrm{c} = \omega_0$ and $\delta = 10^{-2}\omega_0$. (b) Longitudinal resistivity, plotted as $\rho_{xx}\sigma_\mathrm{D}$, as a function of the plasma frequency ω_p in the limit of vanishing broadening parameter $\delta \to 0$.

ρ_{xy}, which is the experimental hallmark of the quantum Hall effect, is not modified by the cavity. To see how a change solely to ρ_{xx} can affect all the conductivity components, it is clarifying to look at the relation between the conductivity matrix elements and the resistivity matrix elements

$$\begin{pmatrix} \sigma_{xx} & \sigma_{xy} \\ -\sigma_{xy} & \sigma_{yy} \end{pmatrix} = \frac{1}{\rho_{xx}\rho_{yy} + \rho_{xy}^2} \begin{pmatrix} \rho_{yy} & -\rho_{xy} \\ \rho_{xy} & \rho_{xx} \end{pmatrix} . \tag{4.67}$$

Additionally, we note that for a vanishing broadening parameter $\delta = 0$, the Drude resistivity is zero $\sigma_\mathrm{D}^{-1} = 0$, and thus so are the longitudinal resistivities $\rho_{xx} = \rho_{yy} = 0$ independently of the light-matter coupling ω_p. This explains why the cavity effects on the conductivity vanish for $\delta = 0$.

It is also interesting to consider the limit of vanishing classical magnetic field $\omega_\mathrm{c} \to 0$, where the system is just the bare electron gas coupled to a cavity [50]. In this case, we can see from Eqs. (4.55), (4.56) and (4.57) that only $G^\mathrm{r}_{J_x,J_x}$ is non-zero. This stems from the fact that all the bare current response functions vanish in this limit, Cf. Eqs (4.52), (4.53) and (4.54). Despite this, $G^\mathrm{r}_{J_x,J_x}$ does not vanish because it contains a term that depends solely on the cavity, i.e., the cavity acts as a current channel in the direction of the light-matter coupling independent of whether the material is a conductor or not. This is evidenced by Eq. (E.9) where the last term solely depends on the free photonic propagator. With this, the optical conductivity reads

$$\sigma_{xx}(\omega) = \sigma_\mathrm{D} \frac{i\delta}{\omega_+} \left(1 + \frac{\omega_\mathrm{p}^2}{\omega_+^2 - \tilde{\omega}^2} \right) . \tag{4.68}$$

Note that the dc limit ($\omega_+ \to i\delta$) of this expression is the inverse of the longitudinal resistivity ρ_{xx} of Eq. (4.65). This indicates that the presence of

a classical perpendicular magnetic field does not fundamentally change how the cavity affects the electron gas. In both cases it does so by modifying its longitudinal resistivity in the direction of the cavity's vector potential ρ_{xx} by the same amount. The presence of a classical magnetic field only determines how this change in longitudinal resistivity affects the different conductivity components. In the absence of a classical magnetic field, the off-diagonal components of the resistivity matrix are zero, and we only see a modification of the longitudinal conductivity, which is the inverse of the longitudinal resistivity. In the presence of a classical magnetic field, the off-diagonal components of the resistivity matrix become non-zero. Accordingly, all the components of the conductivity matrix depend on ρ_{xx}, which is modified by the cavity.

In summary, in this model, the modifications to the integer quantum Hall effect arise solely from a modification of the (longitudinal) resistivity of the underlying electron gas. The only effect of the classical field is to induce the typical Hall physics that give rise to non-zero transverse resistivities and conductivities. There are no additional effects from the simultaneous presence of the classical magnetic field and the cavity field. Most importantly, the transverse resistivity is not modified by the cavity, and therefore this model [51, 52] cannot be used to explain the recently observed breakdown of the topological protection of the integer quantum Hall effect due to cavity vacuum fluctuations [19]. A description of the cavity-modified transverse conductivity probably requires the consideration of disorder and edge effects in a finite system [53], a topological analysis of the bulk band structure, leaning on the bulk-edge correspondence (provided that it is preserved in the presence of the cavity, which has been shown not to be the case in certain topological models coupled to a cavity [33]), or at least the consideration of non-uniform cavity fields.

Chapter 5

Applications to spin models

In Secs. 4.1.2 and 4.1.3 we showed, using our theory, that electron liquids subject to homogeneous cavity field and electric dipoles suffer from no-go theorems that prevent the modification of equilibrium material properties (and the number of cavity photons) by the coupling to a cavity. This is in agreement with previous results in the literature. At the same time, we learned that magnetic effects, triggered by inhomogeneous cavity fields or by directly considering magnetic dipoles, offer a way to circumvent these no-go theorems. In this chapter we explore the latter avenue: magnetic dipoles.

Along this chapter we will apply our equilibrium and linear response theories (LRTs) to a number of spin models. These will be particularizations of the generalized Dicke model (GDM) as defined in Eq. (3.1). We will warm up on the simplest case: the Dicke model. We presented it in Sec. (1.2.3) and solved numerically in Sec. (2.5) as a means to test our equilibrium theory, now we will solve the mean-field effective Hamiltonian and compute its response functions using out LRT. Then, we will consider the Dicke-LMG model, which we will argue can describe dipolar magnets coupled to a cavity. Based on this model, we will propose an experimental implementation consisting of a crystal of molecular nanomagnets coupled to an on-chip microwave cavity that can display cavity-enhanced ferromagnetism. Next, we will consider the Dicke-Ising model, which is an example of a solvable model with non-collective intrinsic interactions. We will show that the cavity binds Ising magnon pairs into localized bound states. Finally, we will consider a Heisenberg ferromagnet.

In the particular case of the Dicke model, for the sake of completeness, we will compare the cases with and without the P^2 term, $\zeta = 0, 1$, since it was historically proposed to describe electric dipoles [15], in which case the P^2 term is necessary to ensure gauge-invariance [106, 107]. Thus, with the P^2 term, the Dicke model describes electric dipoles and without it, it describes magnetic

dipoles. Then, we will proceed to consider the rest of the models without the P^2 term, assuming that they describe magnetic dipoles.

This chapter is based on parts of Refs. [26, 64].

5.1 Dicke model

We apply now our equilibrium and linear response theories to the paradigmatic Dicke model [15], for which $H_{\rm m} = \frac{\omega_z}{2}\sum_j \sigma_j^z$ and $C_x = \sum_j \sigma_j^x$. Here the matter subsystem is just a collection of independent emitters and the only interactions are those mediated by the cavity. Accordingly,

$$H_{\rm eff}^{\rm MF} = \frac{\omega_z}{2}\sum_j \sigma_j^z + \frac{2\lambda^2(\zeta-1)}{\Omega} m_x \sum_j \sigma_j^x - \frac{N\lambda^2(\zeta-1)}{\Omega} m_x^2 \tag{5.1}$$

with $m_x = N^{-1}\langle \sum_j \sigma_j^x \rangle$. Note that for $\zeta = 1$, i.e., in the presence of a P^2 term, the effective term vanishes and $H_{\rm eff}^{\rm MF} = H_{\rm m}$. In this case there is no phase transition, as the effective Hamiltonian describes free spins, and $m_x = 0$. For $\zeta = 0$, Hamiltonian (5.1) is non-trivial and can be solved variationally with respect to m_x (See App. F for details) obtaining, at zero temperature,

$$m_x = \begin{cases} 0 & \text{if} \quad \lambda \leq \lambda_{\rm c}\,, \\ \sqrt{1-\left(\frac{\lambda_{\rm c}}{\lambda}\right)^4} & \text{if} \quad \lambda > \lambda_{\rm c}\,, \end{cases} \tag{5.2}$$

with $\lambda_{\rm c} = \sqrt{\omega_z \Omega}/2$. We see that for $\zeta = 0$ the model exhibits a phase transition between a paramagnetic phase with $m_x = 0$ and a ferromagnetic phase (also termed superradiant when the emphasis is put on the cavity) with $m_x \neq 0$. In any case, the response function reads

$$\tilde{\chi}_{xx,0}(\omega) = -\frac{\omega_z^2}{\varepsilon^2}\frac{2\varepsilon}{\omega_+^2 - \varepsilon^2}\,, \tag{5.3}$$

with $\varepsilon^2 = \omega_z^2 + \left(\frac{4\lambda^2(1-\zeta)}{\Omega} m_x\right)^2$. It depends on the value of m_x and thus on the phase.

The photonic propagator $D(\omega)$ which exhibits poles at the resonant frequencies of the hybrid system, is shown in Fig. 5.1. In Fig. 5.1(a) we see that for $\zeta = 0$ there is a complete softening of the lower polariton at the critical coupling, signaling the phase transition. In contrast, in Fig. 5.1(b) we see that for $\zeta = 1$ the softening is partial and no phase transition occurs.

In Fig. 5.1 we also overlay the polaritons that can be obtained with a bosonization of the Dicke model in the thermodynamic limit (See App. G for

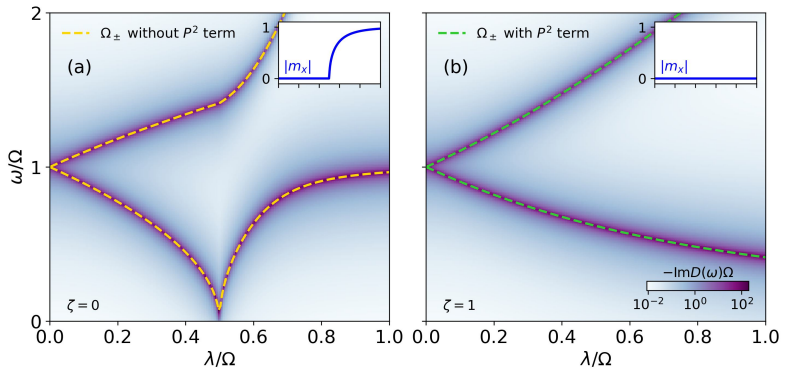

Figure 5.1: Cavity response D of the Dicke model as a function of the collective coupling λ without the P^2 term, $\zeta = 0$, (a) and with the P^2 term, $\zeta = 1$, (b). The dashed lines correspond to the polaritons computed via bosonization. The spins and cavity are resonant, $\omega_z = \Omega$.

details), which is known to give exact results (See Sec. 1.3.1). In the case of $\zeta = 0$, which corresponds to the standard Dicke model, these read [148]

$$2\Omega_{\pm}^2 = \begin{cases} \omega_z^2 + \Omega^2 \pm \sqrt{(\omega_z^2 - \Omega^2)^2 + 16\lambda^2\omega_z\Omega} & \text{if} \quad \lambda \leq \lambda_c\,, \\ \omega_z^2/\mu^2 + \Omega^2 \pm \sqrt{(\omega_z^2/\mu^2 - \Omega^2)^2 + 4\omega_z^2\Omega^2} & \text{if} \quad \lambda > \lambda_c\,, \end{cases} \tag{5.4}$$

with $\mu = \lambda_c^2/\lambda^2$. In the case of $\zeta = 1$, the same analysis is possible, except in this case there is only a paramagnetic phase due to the presence of the P^2 term. In the bosonization, the P^2 term affecting the spin becomes an A^2 term of the corresponding boson. It can be eliminated with a Bogoliubov transform, yielding a renormalized frequency $\tilde{\omega}_z^2 = \omega_z(\omega_z + 4\lambda^2/\Omega)$ and coupling $\tilde{\lambda} = \lambda\left(1 + 4\lambda^2/(\omega_z\Omega)\right)^{-1/4}$. Then, the polaritons are just those of the standard Dicke model in the normal phase (top case of Eq. (5.4)), with the substitution $\omega_z \to \tilde{\omega}_z$ and $\lambda \to \tilde{\lambda}$.

5.2 Dicke-LMG model: a model for dipolar magnets in a cavity

Dipolar interactions in three-dimensional molecular magnets, as an instance of long-range interactions, are well described by mean-field theory [149, 150]. The most extreme case of long-range interactions are homogeneous all-to-all interactions, which the Lipskin-Meshkov-Glick (LMG) model considers. These assume that every spin interacts with the same strength with every other spin. Provided that the interaction term is adequately normalized, there is

no difference in the mean-field solution of models with different interaction ranges. It follows that the LMG model is a good toy model for dipolar magnets and, thus, that the Dicke-Ising model, which considers LMG spins coupled to a cavity, is a good toy model for dipolar magnets in a cavity.

5.2.1 Longitudinal Dicke-LMG model

We consider now the Lipskin-Meshkov-Glick (LMG) model with longitudinal coupling to the cavity as a marginal generalization of the Dicke model. In contrast with the Dicke model, this one incorporates intrinsic all-to-all interactions in the matter subsystem [151, 152].

The full Hamiltonian reads

$$H = \frac{\omega_z}{2}\sum_j \sigma_j^z - \frac{J}{N}\sum_{ij}\sigma_i^x\sigma_j^x + \Omega a^\dagger a + g(a+a^\dagger)\sum_j \sigma_j^x \,. \tag{5.5}$$

Interestingly, the collective nature of the intrinsic interaction allows two alternative treatments within the linear response theory. The first option is to treat it like we would any other intrinsic interaction: bundle it together with the field term to form the matter Hamiltonian, $H_{\rm m} = \frac{\omega_z}{2}\sum_j \sigma_j^z - \frac{J}{N}\sum_{ij}\sigma_i^x\sigma_j^x$, and then follow the linear response theory as described in Chap. 3. The second option exploits the collective nature of the intrinsic interaction and treats this term not within $H_{\rm m}$ but explicitly within the linear response theory, analogously to the P^2 term, as it is, in fact, just a negative P^2 term [Cf. Eqs. (3.1) and (5.5)]. We will follow this second option for its simplicity, since, as we show below, the resulting $H_{\rm eff}^{\rm MF}$ corresponds to free spins and is identical in structure to the one from the Dicke model (5.1). Accordingly, we have

$$V_{\rm ind}(\omega) = \frac{2\lambda^2}{\Omega}\frac{\Omega^2}{\omega^2-\Omega^2} - 2J \,, \tag{5.6}$$

and

$$H_{\rm eff}^{\rm MF} = \frac{\omega_z}{2}\sum_j \sigma_j^z - 2J_{\rm eff} m_x \sum_j \sigma_j^x + N J_{\rm eff} m_x^2 \,, \tag{5.7}$$

with $m_x = N^{-1}\langle\sum_j \sigma_j^x\rangle$ and $J_{\rm eff} = \lambda^2/\Omega + J$. Solving the Hamiltonian variationally with respect to m_x (See App. F for details) yields, at zero temperature,

$$m_x = \begin{cases} 0 & \text{if} \quad \omega_z \geq 4J_{\rm eff} \,, \\ \sqrt{1-\left(\frac{\omega_z}{4J_{\rm eff}}\right)^2} & \text{if} \quad \omega_z < 4J_{\rm eff} \,. \end{cases} \tag{5.8}$$

Like the Dicke model (for $\zeta = 0$), the LMG model exhibits a phase transition between a paramagnetic phase with $m_x = 0$ and a ferromagnetic phase with

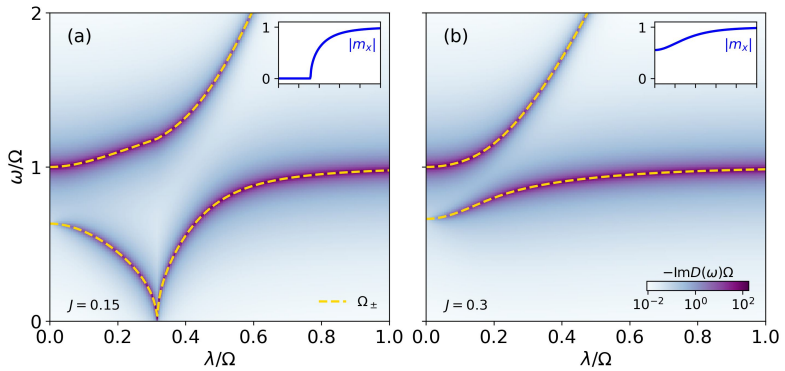

Figure 5.2: Cavity response D of the longitudinal LMG model as a function of the collective coupling λ for different values of the intrinsic interaction J. The dashed lines correspond to the polaritons computed via bosonization. The top right insets show the magnetization. The transverse field is set to $\omega_z = \Omega$.

$m_x \neq 0$. The response function reads [59]

$$\tilde{\chi}_{xx,0}(\omega) = -\frac{\omega_z^2}{\varepsilon^2}\frac{2\varepsilon}{\omega_+^2 - \varepsilon^2}\,, \tag{5.9}$$

with $\varepsilon^2 = \omega_z^2 + (4J_{\text{eff}}m_x)^2$. It depends on the value of m_x and thus on the phase.

In Fig. 5.2 we show the photonic propagator $D(\omega)$ which exhibits poles at the resonant frequencies of the hybrid system, as a function of the collective coupling. In Fig. 5.2(a), for $J < \omega_z/4$, the lower mode goes to zero at finite coupling, signaling the phase transition. The critical point is displaced to a lower coupling λ with respect to the Dicke model due to the synergy between the intrinsic and effective interactions. In Fig. 5.2(b), for$J > \omega_z/4$, the system is always in the ordered phase independently of the value of λ. In both cases there is a splitting at zero coupling, $\lambda = 0$, due to the intrinsic interactions.

In Fig. 5.2 we also overlay the polaritons obtained with a bosonization of the longitudinal Dicke-LMG model in the thermodynamic limit. It is a generalization of the bosonization of the Dicke model, developed in Ref. [148], to account for the interaction term (See App. G for details). It is also a particular case of the polaritons obtained in Ref. [152] for the anisotropic Dicke model with collective matter interactions. The resulting polaritons are

$$2\Omega_\pm^2 = \begin{cases} \tilde{\omega}_z^2 + \Omega^2 \pm \sqrt{\left(\tilde{\omega}_z^2 - \Omega^2\right)^2 + 16\tilde{\lambda}^2\omega_z\Omega} & \text{if} \quad \omega_z \geq 4J_{\text{eff}}\,, \\ \omega_z^2/\tilde{\mu}^2 - 4\tilde{\mu}J\omega_z + \Omega^2 & \\ \pm \sqrt{\left(\omega_z^2/\tilde{\mu}^2 - 4\tilde{\mu}J\omega_z + \Omega^2\right)^2 + 16\lambda^2\tilde{\mu}\omega_z\Omega} & \text{if} \quad \omega_z < 4J_{\text{eff}}\,, \end{cases} \tag{5.10}$$

with $\tilde{\omega}_z^2 = \omega_z(\omega_z - 4J)$, $\tilde{\lambda} = \lambda(1 - 4J/\omega_z)^{-1/4}$ and $\tilde{\mu} = \omega_z/(4J_{\text{eff}})$. The polaritons obtained via bosonization match the LRT results.

This model describes recent experiments in rare earth quantum Ising systems, such as $LiHoF_4$ [115, 130]. These experiments aim to observe how the lowest excitation mode softens as it approaches the ferromagnetic transition. We can understand that Eq. (5.5) is equivalent to a Dicke model where λ becomes $\sqrt{\lambda^2 + J\Omega}$. Therefore, the softening of the mode can be viewed as the behavior of the lower polariton in the Dicke model.

5.2.2 Molecular nanomagnets as a platform for cavity-modified magnetism and equilibrium superradiance

We just described how the ordered phase can be enhanced in a spin model with intrinsic ferromagnetic interactions parallel to the cavity field, since the cavity-mediated and intrinsic interactions are synergistic. Additionally, we know from Eq. (2.50) that the expectation value of the cavity field is proportional to the matter coupling operator. This implies that the ferromagnetic phase is also superradiant. Here we argue that such a model can be realized experimentally by coupling magnetic molecules to superconducting microwave resonators via the Zeeman interaction [153]. Hybrid platforms coupling electron [154] and, particularly, spin [155, 156] ensembles to superconducting resonators or cavities complement circuit QED.

The platform

Artificial magnetic molecules [157, 158], designed and synthesized by chemical methods, consist of a high-spin cluster core surrounded and stabilized by a cloud of organic molecular ligands. The ability to chemically tune their relevant properties, such as the ground state spin, magnetic anisotropy and mutual interactions, combined with their stability as isolated molecular units, confer them a potential interest as magnetic memories in spintronic devices [159] and as qubits for scalable quantum information schemes [160–162]. Besides, they tend to organize forming crystals, which makes them model systems to study pure magnetic dipolar order and quantum phase transitions [149, 163–166]. To realize a Dicke-LMG model and observe enhanced magnetism, setups hosting molecular crystals offer the crucial advantage of coupling a macroscopic number of identical and perfectly organized spins to a single cavity mode.

A vast majority of molecular nanomagnets are both neutral and exhibit a close to zero electric dipole. The diamagnetic response, which arises mainly from the molecular ligands surrounding the magnetic core, is much smaller that

the paramagnetic one and can be safely neglected, especially at sufficiently low temperatures. Therefore, following Sec. 1.2.2, their interaction with the cavity is described by the coupling of their magnetic dipole to the cavity's magnetic field. In fact, their coupling to any magnetic field, be it the cavity's or an external classical field, is described by Zeeman coupling. Their magnetic dipole is described by a "giant" spin often subject to magnetic anisotropy.

The Hamiltonian that describes the coupling of these molecules to a superconducting cavity reads

$$H = H_{\mathrm{m}} + \hbar\Omega a^\dagger a + \sum_j \hbar \boldsymbol{g}_j \cdot \boldsymbol{S}_j (a^\dagger + a)\,, \tag{5.11}$$

with

$$\boldsymbol{g}_j = \frac{g_e \mu_B}{\hbar} \boldsymbol{B}_{\mathrm{rms}}(\boldsymbol{r}_j)\,. \tag{5.12}$$

Here $[S_i, S_j] = i\epsilon_{ijk} S_k$ are dimensionless spin S operators. The local quantized magnetic field generated by the superconducting currents can be written as $\boldsymbol{B}_{\mathrm{mw}}(\boldsymbol{r}) = \boldsymbol{B}_{\mathrm{rms}}(\boldsymbol{r})(a^\dagger + a)$, with $B^2_{\mathrm{rms}}(\boldsymbol{r}) = \langle 0|B^2_{\mathrm{mw}}(\boldsymbol{r})|0\rangle$ its zero-point fluctuations.

Critical condition

Following Sec. 4.1, we can provide a critical condition for such an ensemble of molecules to display equilibrium superradiance. The critical condition in the thermodynamic limit is given by the pole condition for the response functions at vanishing frequency, which signal the softening of the lower polariton of the hybrid system. Within our LRT [Cf. Eq. (3.1)], we identify $gC_x = \sum_j \hbar \boldsymbol{g}_j \cdot \boldsymbol{S}_j$, and we obtain the critical condition

$$\chi_{xx,0}(0) = \frac{\hbar\Omega}{2}\,. \tag{5.13}$$

Here, $\chi_{xx,0}(0)$ is the static response function of the bare molecular ensemble, which can be obtained from its spectral decomposition in terms of the eigenvalues and eigenvectors of the bare matter Hamiltonian describing the molecular ensemble

$$\chi_{xx,0}(0) = \frac{\sum_{m,n} e^{-\beta\epsilon_m} |\langle\psi_m| \sum_j \hbar \boldsymbol{g}_j \cdot \boldsymbol{S}_j |\psi_n\rangle|^2 \frac{e^{\beta\Delta_{mn}} - 1}{\Delta_{mn}}}{\sum_m e^{-\beta\epsilon_m}}\,, \tag{5.14}$$

with $|\psi_m\rangle$, ϵ_m the eigenstates and eigenenergies of H_{m} and $\Delta_{mn} = \epsilon_m - \epsilon_n$.

A candidate molecular crystal: Fe_8

Next, we consider a particular model. It corresponds to a specific molecular material, a crystal of Fe_8 clusters with $S = 10$, which shows a ferromagnetic phase transition purely induced by dipolar interactions below a critical temperature $T_c(B_\perp = 0) \cong 0.6$ K and a zero-temperature critical magnetic field $B_{\perp,c} \simeq 2.65$ T [149]. The magnetic phase diagram measured for a magnetic field perpendicular to the magnetic anisotropy axis is shown in Fig. 5.3. As expected for a system dominated by long-range dipolar interactions, it agrees very well with the predictions of a mean-field Hamiltonian

$$H_m = -DS_x^2 + E\left(S_z^2 - S_y^2\right) - g_e\mu_B \boldsymbol{B}\cdot\boldsymbol{S} - 2J\langle S_x\rangle S_x + J\langle S_x\rangle^2 \tag{5.15}$$

with parameters given in Fig. 5.3. The combination of high spin, thus high susceptibility, and negligible exchange interactions, which lead to a quite low T_c even for a densely concentrated spin lattice, makes this material well suited to obtain and measure equilibrium superradiance.

As reflected in Eq. (5.11), the magnetic field generated by a superconducting resonator is inhomogeneous over the volume occupied by the molecular crystal. To simplify the calculations, we consider a uniform coupling equal to the root-mean-square coupling, $\lambda_{rms}^2 = \sum_j |\boldsymbol{g}_j|^2$, which for a dense uniform crystal can be approximated by the integral

$$\lambda_{rms}^2 = \frac{N}{V_{sample}} \int_{V_{sample}} |\boldsymbol{g}(\boldsymbol{r})|^2 dV = \frac{g_e^2\mu_B^2\mu_0}{2\hbar}\rho\nu\Omega\,, \tag{5.16}$$

where V_{sample} is the cavity volume occupied by spins and $\rho = N/V_{sample}$ is the density of spins. In the second equality, we have used Eq. (5.12) and the Virial theorem and introduced the filling factor $\nu = I(V_{sample})/I(V_{total})$ with $I(V) = \int_V |\boldsymbol{B}_{rms}(\boldsymbol{r})|^2 dV$. Therefore, the root-mean-square coupling is essentially determined by the density of spins ρ and the filling factor ν which in combination measure how well the spins cover the volume of space where the cavity's magnetic field is significant. The use of λ_{rms} is not an arbitrary simplification, it can be shown that λ_{rms} gives the critical condition in a Dicke model with inhomogeneous couplings.

Figure 5.3 shows the effects that a uniform cavity field parallel to the intrinsic interaction can have on an Fe_8 crystal. The light-matter interaction has a remarkable effect on the equilibrium phase diagram, enhancing both $B_{\perp,c}$ and T_c, the latter by almost as much as a factor six, depending on the filling factor of the cavity. This can be understood by noting that the effective Hamiltonian is given by Eq. (5.15) but with the coupling J replaced by $J_{eff} = J + \hbar\lambda_{rms}^2/\Omega = J + \eta\rho\nu$, with $\eta/k_B \cong 1.566 \cdot 10^{-29}\,\mathrm{m^3K}$. This enhancement evidences that the cavity

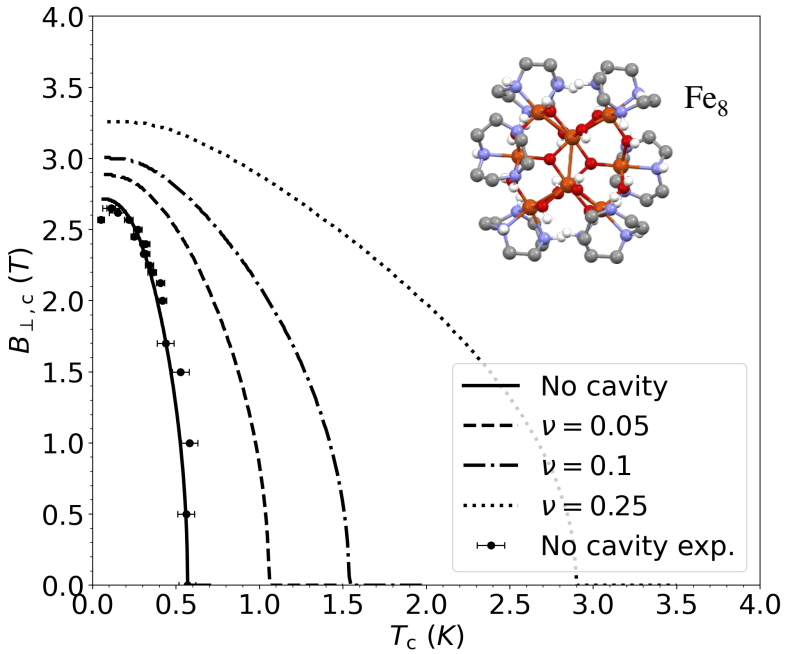

Figure 5.3: $B_{\perp,c} - T_c$ phase boundary. The solid line corresponds to the bare spin model (5.15) and is verified against experimental data (dots) obtained for a crystal of Fe_8 molecular clusters [149], whose structure [167] is shown in the inset. The external field $\boldsymbol{B}$ is applied perpendicular to the easy magnetization axis x: $\boldsymbol{B} = B_\perp (0, \sin\phi, -\cos\phi)$ with $\phi = 68°$. The magnetic anisotropy parameters are $D/k_B = 0.294$ K and $E/k_B = 0.046$ K, and the coupling $J/k_B = 2.85 \times 10^{-3}$ K. The remaining lines are obtained with the same method taking into account the coupling to a microwave cavity for a range of filling factors ν. The parameters used are $\rho = 5.1 \cdot 10^{20}$ cm^{-3}, taken from the crystal lattice of Fe_8 and $\Omega = 1.4 \times 10^9$ s^{-1}.

induces quite strong ferromagnetic correlations which in this case co-operate with the intrinsic interactions between the spins in the crystal. Achieving filling factors above 0.1 seems reasonable provided that one achieves a sufficiently good interface between the chip and the magnetic material.

Transmission experiment

Finally, we discuss how to measure a signature of the cavity-modified phase transition. A direct route would be to measure the order temperature of the magnetic material *inside* and *outside* the cavity. However, conventional methods to measure T_c (or B_c), based on magnetic susceptibility or neutron diffraction [149], do not lend themselves easily to include a superconducting cavity. Besides, they require very large crystals, often much larger than the typical cavity volumes. Therefore, we envision here a more accessible way: a transmission

experiment, where the cavity is coupled to a microwave transmission line. An input signal, sent through it, interacts with the cavity-spins system and the transmitted signal is recorded. We assume that the transmission, the ratio between the transmitted and input signals, will be proportional to the cavity's spectral function $t \propto \mathrm{Im}\, D(\omega)$ where $D(\omega)$ is the photon propagator [168].

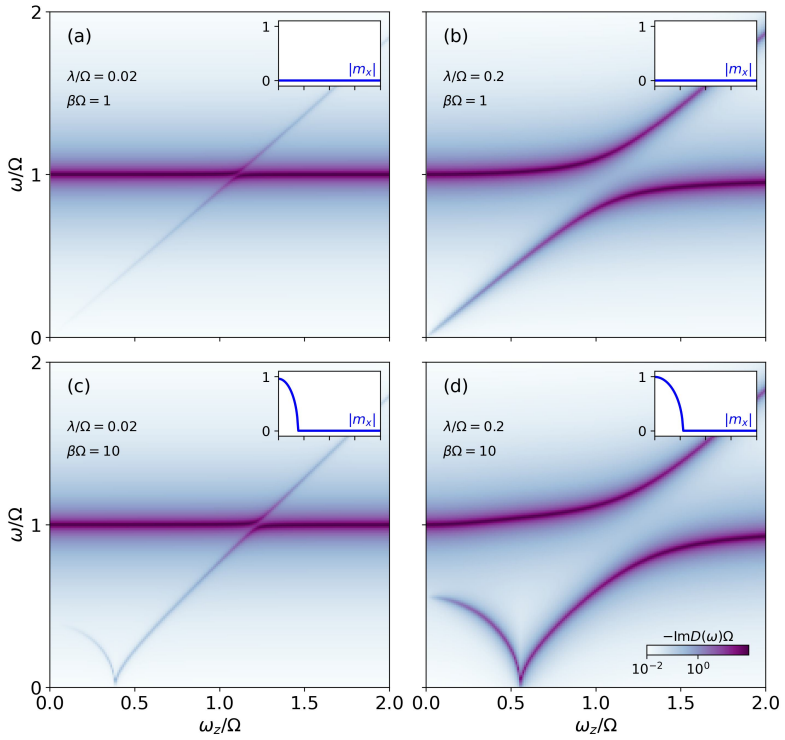

Figure 5.4: Cavity response D of the longitudinal Dicke-LMG model as a function of the transverse field ω_z for different values of the collective coupling λ and inverse temperature β. The top right insets show the magnetization. The intrinsic interaction is set to $J = 0.1\Omega$.

For simplicity, let us consider the longitudinal Dicke-LMG model studied in Sec. 5.2 as toy model for a crystal of magnetic molecules such as Fe_8, assuming that the molecules behave effectively as a spin 1/2 with a mean-field interaction along the easy axis and with the coupling of the cavity also parallel to the easy axis. We have studied the photon propagator in the longitudinal Dicke-LMG model in Fig. 5.2 and we know that the phase transition of the model is signaled by a softening of the lower polariton to zero frequency at the critical point. We also know that the effect of the cavity-mediated interactions and intrinsic interactions is synergistic, so the critical point is shifted with respect to the bare material. In Fig. 5.4 we show the transmission spectrum above and below the critical temperature for small and large couplings. The effect

of the cavity can be seen as a shift of the critical field at which the lower polariton softens below the critical temperature. Although not shown, we know from Fig. 5.3, that the critical temperature is also increased by the cavity. Therefore, the effect of the cavity could also be detected from the crossover point from high-temperature transmission features, shown in panels (a) and (b), and low-temperature transmission features, shown in panels (c) and (d).

In summary, we propose that the superradiant phase transition, manifesting as cavity-enhanced dipolar ferromagnetism in molecular magnets, can be detected in a standard temperature-dependent transmission experiment, provided that the spin-photon coupling is large enough.

5.2.3 Transverse Dicke-LMG model

Thus far we have only considered models where the intrinsic and cavity-mediated interactions are synergistic, here we consider the (transverse) Dicke-LMG model: an LMG model with transverse coupling to the cavity [151, 152], named in analogy to the Dicke-Ising model that we will study in the next section. The full Hamiltonian reads

$$H = \frac{\omega_x}{2}\sum_j \sigma_j^x + \frac{\omega_z}{2}\sum_j \sigma_j^z - \frac{J}{N}\sum_{ij}\sigma_i^z\sigma_j^z + \Omega a^\dagger a + g\left(a + a^\dagger\right)\sum_j \sigma_j^x \,. \quad (5.17)$$

For vanishing longitudinal and transverse fields the transverse Dicke-LMG model has a $\mathbb{Z}_2 \times \mathbb{Z}_2$ symmetry. The first symmetry corresponds to a spin flip, $\sigma_j^z \to -\sigma_j^z$, and in the bare LMG model it is spontaneously broken in a second order phase transition from a paramagnetic to a ferromagnetic phase. The second symmetry corresponds to a simultaneous cavity-field and spin flip, $a \to -a$ and $\sigma_j^x \to -\sigma_j^x$, and in the bare Dicke model it is spontaneously broken in a second order phase transition from a normal to a superradiant phase. As we show in the following, we find that the combination of the two symmetries gives rise to a first-order phase transition in the Dicke-LMG model between two symmetry-broken phases: a z-ferromagnetic normal (zFMN) phase for large J and an x-ferromagnetic (xFMS) superradiant phase for large λ^2/Ω, this is akin to what occurs in the Dicke-Ising model (See Sec. 5.3). Switching on one of the external fields has the effect of explicitly breaking the corresponding symmetry, preventing the spontaneous symmetry breaking that characterizes a phase transition. We find that if only one external field is switched on, the phase transition is demoted from first to second order. If the two external fields are switched on, the phase transition is eliminated completely.

In order to solve the model, we will consider the intrinsic collective interactions explicitly within the linear response theory. However, unlike in the

case of the LMG model with longitudinal coupling to the cavity, in this case the cavity-mediated and intrinsic interactions act on different axes, i.e., they couple different collective operators: $C_x = \sum_j \sigma_j^x$ and $C_z = \sum_j \sigma_j^z$ respectively. Accordingly, a slight generalization of the linear response theory presented in Chap. 3 is required as there are now two induced interaction terms within the effective action

$$V_{\mathrm{ind},x}(\omega) = \frac{2\lambda^2}{\Omega}\frac{\Omega^2}{\omega_+^2 - \Omega^2}\,, \tag{5.18}$$

$$V_{\mathrm{ind},z}(\omega) = -2J\,. \tag{5.19}$$

The system can be solved with the multimode generalization of the linear response theory developed in App. C, since from Eq. (C.2) onward it is irrelevant whether the different induced interaction terms all stem from actual cavity modes or if some stem from cavity modes and others from intrinsic collective interactions. The expression for the photonic propagator remains unchanged, see Eq. 3.22, as it is solely determined by the operator that couples to the cavity. In contrast, matter correlators have new contributions afforded by the new interaction channel $V_{\mathrm{ind},z}$. We find

$$\chi_{xx} = \frac{\tilde{\chi}_{xx,0} + V_{\mathrm{ind},z}\det(\tilde{\chi}_0)}{1 + V_{\mathrm{ind},x}\tilde{\chi}_{xx,0} + V_{\mathrm{ind},z}\tilde{\chi}_{zz,0} + V_{\mathrm{ind},x}V_{\mathrm{ind},z}\det(\tilde{\chi}_0)}\,, \tag{5.20}$$

with $(\tilde{\chi}_0)_{ab} = \tilde{\chi}_{ab,0}$. The mean-field effective Hamiltonian reads

$$H_{\mathrm{eff}}^{\mathrm{MF}} = \frac{\tilde{\omega}_x}{2}\sum_j \sigma_j^x + \frac{\tilde{\omega}_z}{2}\sum_j \sigma_j^z + \frac{N\lambda^2}{\Omega}m_x^2 + NJm_z^2\,, \tag{5.21}$$

with $\tilde{\omega}_x = \omega_x - 4\lambda^2/\Omega m_x$ and $\tilde{\omega}_z = \omega_z - 4Jm_z$. Solving variationally with respect to m_x and m_z (See App. F for details) allows us to compute the equilibrium values of m_x and m_z numerically and subsequently the response functions $\tilde{\chi}_{xx,0}$, $\tilde{\chi}_{xz,0}$, $\tilde{\chi}_{zx,0}$ and $\tilde{\chi}_{zz,0}$, which depend on the values of m_x and m_z.

In Fig. 5.5 we show the photonic propagator $D(\omega)$ the matter response function $\chi_{zz}(\omega)$ (left inset) and the magnetizations, m_x and m_z, (right inset) as functions of the collective coupling λ in four different scenarios of external fields values. The intrinsic interaction is set so that at zero coupling the cavity and the spins are resonant: $4J = \Omega$. In the case of vanishing ω_x and ω_z, Fig. 5.5(a), we observe a first order phase transition, evidenced by the discontinuous behavior in the order parameters of the two ordered phases. The photonic propagator has a pole that goes to zero at the critical point, signaling the gap closing. We include χ_{zz} in the left inset for completeness because the photonic propagator depends on χ_{xx} [Cf. Eq. (3.22)] and the system becomes unresponsive to

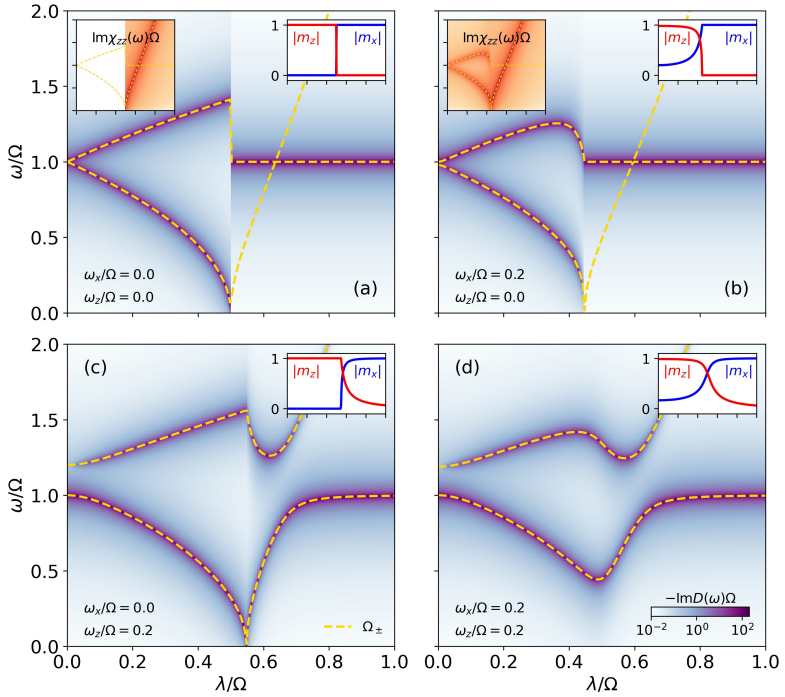

Figure 5.5: Cavity response D of the transverse Dicke-LMG model as a function of the collective coupling λ for different values of the longitudinal and transverse fields, ω_z and ω_x respectively. The top left insets show the matter response χ_{zz}. The dashed lines correspond to the polaritons computed via bosonization. The top right insets show the magnetizations. The intrinsic interaction is set to $4J = \Omega$.

probing along the x direction in the superradiant phase. This is caused by the fact that the intrinsic interaction is the only term in the Hamiltonian containing σ^z operators. Due to its collective nature, its effect is switched off (mean-field behavior) in the superradiant phase where $m_z = 0$ [Cf. Eq. (5.21)]. The system is then fully ordered along x and with no off-diagonal terms it becomes unresponsive to probing with σ^x. Accordingly, in the superradiant phase the photonic propagator only shows a pole at the cavity frequency. To witness the other excitation of the system we look at χ_{zz} which shows a pole that emerges from zero at the critical point, signaling the gap reopening. The combination of D and χ_{zz} provides a complete picture of the excitations of the system. In Fig. 5.5(b) we see that switching on the transverse field ω_x eliminates the superradiant symmetry. The phase transition becomes of second order, with m_z the sole order parameter. Like in the previous case, the absence of non mean-field terms containing σ^z in the Hamiltonian makes the system unresponsive to σ_x in the superradiant phase. Thus, we also include χ_{zz} to witness the gap reopening. Alternatively, in Fig. 5.5(c) we see that switching

on the longitudinal field ω_z eliminates the ferromagnetic symmetry. The phase transition becomes of second order, with m_x as the sole order parameter. In this case, the presence of the longitudinal field endows the photonic propagator with visibility of all the excitations, showcasing the full gap closing and reopening at the critical point. Finally, in Fig. 5.5(d) we switch on both the longitudinal and transverse fields. All symmetries are now explicitly broken, and the phase transition gives way to a smooth crossover of m_z and m_x dominant regimes for small and large λ respectively. The gap remains finite at all times.

In Fig. 5.5 we also overlay the polaritons obtained with a bosonization of the transverse Dicke-LMG model in the thermodynamic limit. It is a generalization of the bosonization in Refs. [148, 152] (See App. G for details). In contrast with previous examples, the resulting polaritons do not have a closed expression for $\omega_x \neq 0$ because the superradiant symmetry is explicitly broken in this case. The polaritons computed via bosonization match the LRT results.

5.3 (Transverse) Dicke-Ising model

Thus far we have only considered models with collective intrinsic interactions, such that despite being intrinsic, these collective interactions were handled on a par with the light-matter interactions using the LRT. As a result, the mean-field effective Hamiltonian corresponded to free spins and was trivially solved. Here we consider the (transverse) Dicke-Ising model: an Ising model with nearest-neighbor intrinsic interactions and a transverse coupling to the cavity [109, 169–172]. Alternatively, the linear response theory of the Ising chain with longitudinal coupling to the cavity (the longitudinal Dicke-Ising model) has been studied in Ref. [115].

5.3.1 Phase diagram and linear response theory

The full Hamiltonian reads

$$H = \frac{\omega_x}{2}\sum_j \sigma_j^x - J\sum_j \sigma_j^z\sigma_{j+1}^z + \Omega a^\dagger a + g\left(a + a^\dagger\right)\sum_j \sigma_j^x \,. \tag{5.22}$$

Like the transverse Dicke-LMG model, and for the same reasons (See Sec. 5.2.3), for vanishing transverse field the Dicke-Ising model has a $\mathbb{Z}_2 \times \mathbb{Z}_2$ symmetry that gives rise to a first-order phase transition between two symmetry-broken phases: a z-ferromagnetic normal (zFMN) phase for large J and an x-ferromagnetic superradiant (xFMS) phase for large λ^2/Ω. However, unlike in the Dicke-LMG model, the phase transition remains of first order after switching on the transverse field that explicitly breaks the superradiant symmetry. We attribute

this robustness to the fact that the intrinsic interactions are not collective in this case. As we will see below, we do not consider a longitudinal field because the resulting mean-field effective Hamiltonian would not be analytically solvable.

The corresponding mean-field effective Hamiltonian is that of an Ising chain in transverse field

$$H_{\text{eff}}^{\text{MF}} = \frac{\tilde{\omega}_x}{2}\sum_j \sigma_j^x - J\sum_j \sigma_j^z\sigma_{j+1}^z + \frac{N\lambda^2}{\Omega}m_x^2\,, \tag{5.23}$$

with $\tilde{\omega}_x = \omega_x - 4\lambda^2/\Omega m_x$ and $m_x = N^{-1}\sum_j\langle\sigma_j^x\rangle$. The transverse field is a combination of the external field and the mean-field cavity-induced interaction. It is clear now that adding a longitudinal field would make $H_{\text{eff}}^{\text{MF}}$ analytically intractable, as it would yield an Ising model with both longitudinal and transverse fields. In the thermodynamic limit, $N\to\infty$, the ground-state energy per spin is given by

$$e_0(m_x) = \frac{\lambda^2}{\Omega}m_x^2 - \frac{1}{2}\int_{-\pi}^{\pi}\frac{dk}{2\pi}\epsilon_k\,, \tag{5.24}$$

with

$$\epsilon_k = \sqrt{(2J)^2 + \tilde{\omega}_x^2 - 4J\tilde{\omega}_x\cos k}\,. \tag{5.25}$$

Solving variationally allows us to compute the equilibrium value of m_x numerically and subsequently the longitudinal magnetization as [173]

$$m_z = \begin{cases} \left(1-\left(\frac{\tilde{\omega}_x}{2J}\right)^2\right)^{\frac{1}{8}} & \text{if} \quad 0\le\frac{\tilde{\omega}_x}{2J}\le 1\,, \\ 0 & \text{if} \quad 1<\frac{\tilde{\omega}_x}{2J}\,, \end{cases} \tag{5.26}$$

the number of photons per spin, from Eq. (2.52),

$$n_{\text{ph}} = \frac{\lambda^2}{\Omega^2}m_x^2\,, \tag{5.27}$$

and the response function $\tilde{\chi}_{xx,0}$. The zero-temperature phase diagram is presented in Fig. 5.6. For $\omega_x = 0$ the longitudinal magnetization acts as an order parameter for the superradiant phase. An analysis of $e_0(m_x)$ in this case reveals that the system undergoes a first-order phase transition at $\lambda^2/(\Omega J)\approx 0.837$. In the opposite case of vanishing light-matter coupling, $\lambda = 0$, the Ising chain in transverse field is known to undergo a second order phase transition at $\omega_x/J = 2$. In previous solutions of the Dicke-Ising model the transverse field is set in a direction perpendicular to both the intrinsic interaction and the cavity field, which would be the y direction in our case [109, 169]. Although this difference is subtle, in implies that m_x is always an order parameter. Then, a Landau analysis of the ground-state energy in terms of its series expansion in powers of m_x reveals the existence of a tricritical point

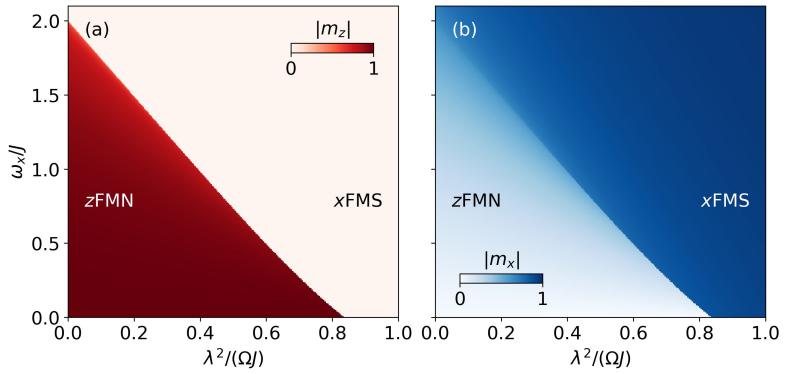

Figure 5.6: Phase diagram of the (transverse) Dicke-Ising model in the $(\lambda^2/\Omega, \omega_x)$ plane. (a) Longitudinal magnetization m_z, which is the order parameter of the z-ferromagnetic normal (zFMN) phase. (b) Transverse magnetization m_x, which is an order parameter of the xFMS phase for $\omega_x = 0$.

splitting the critical line into a regime of second-order criticality for large ω_x and small λ and a regime of first-order criticality for small ω_x and large λ [169]. In the present case, where the classical transverse field and the cavity fields are aligned, the Landau analysis is not possible. Nevertheless, a visual inspection of the landscape of energy minima of $e_0(m_x)$ still reveals the existence of a tricritical point at $\lambda^2/(\Omega J) \approx 0.225$ and $\omega_x/J = 1.427$.

At zero temperature and in the continuum limit, $\tilde{\chi}_{xx,0}$ is given by (See App. H for details)

$$\tilde{\chi}_{xx,0}(\omega) = -32J^2 \int_{-\pi}^{\pi} \frac{dk}{2\pi} \frac{\sin^2 k}{\epsilon_k(\omega^2 - 4\epsilon_k^2)} \,. \tag{5.28}$$

Interestingly, we find that $\tilde{\chi}_{xx,0}$ has poles at $\pm 2\epsilon_k$. This stems from the fact that the coupling operator C_x creates and destroys excitations in pairs of opposite momentum

$$C_x = \sum_j \sigma_j^x = N - 2\sum_k \left(v_k^2 + (u_k^2 - v_k^2)\gamma_k^\dagger \gamma_k + i u_k v_k (\gamma_k^\dagger \gamma_{-k}^\dagger - \gamma_{-k}\gamma_k)\right) , \tag{5.29}$$

where γ_k and $\gamma_k^\dagger$ are the annihilation and creation operators of the Bogoliuvov fermions that constitute the elementary excitations of the Ising model after a Jordan-Wigner fermionization, with u_k and v_k the Bogoliubov coefficients [174, Chap. 10]. Here $u_k = \cos(\theta_k/2)$ and $v_k = \sin(\theta_k/2)$ are the Bogoliubov coefficients, with

$$\tan\theta_k = \frac{\sin k}{\frac{\tilde{\omega}_x}{2J} - \cos k} \,. \tag{5.30}$$

Thus, χ_{xx} and D will reflect how the zero-momentum sector of the two-excitation band (a double-energy replica of the single-excitation band) of the Ising model

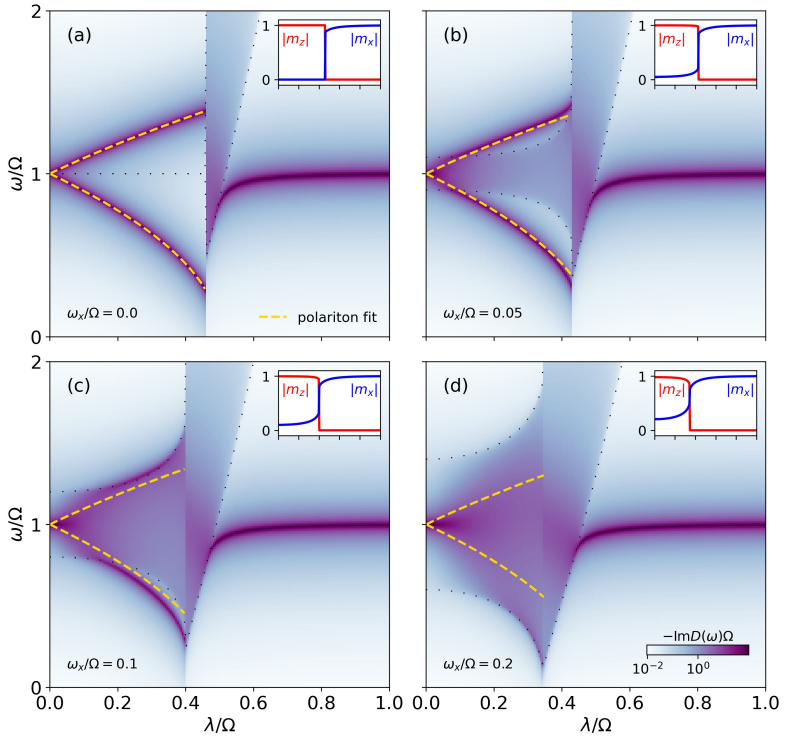

Figure 5.7: Cavity response D of the Dicke model as a function of the collective coupling λ for different values of the classical transverse field ω_x. The yellow dashed lines correspond to a fit of the polaritons with a two-oscillator model [See Eq. (5.31)]. The top right insets show the magnetization. The dotted lines mark the edges of the band of the mean-field effective Hamiltonian (5.23). The Ising interaction is set to $4J = \Omega$.

hybridizes with the cavity photon. The fact that the excitations are created in pairs of opposite momenta allows one to probe the full band, despite the collective nature of C_x.

This feature brings novel phenomenology that we summarize in Fig. 5.7, where the cavity response (3.22) is plotted for different scenarios. In all panels, we set $4J = \Omega$, such that the two-excitation band is in resonance with the cavity frequency. Figure 5.7(a) shows the case of vanishing classical field, $\omega_x = 0$. In this case, the model is non-dispersive in the normal phase, as the only source of transverse field is the effective mean field. Instead of a band, the model has a collection of degenerate excitations with energy $2J$: domain walls. Accordingly, the zero-momentum sector of the two-excitation band is a degenerate collection of the domain-wall pairs that correspond to single-spin flips. This is a typical situation where the cavity is coupled to a collective mode hybridizing with the cavity photon, forming polaritons whose energy can be fitted by a model of two

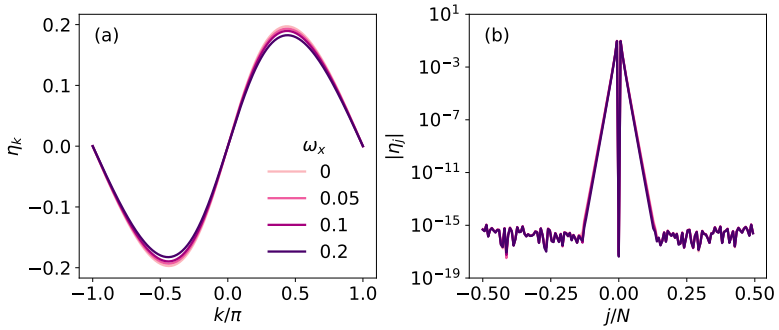

Figure 5.8: (a) Coupling of the Bogoliubov fermions η_k and (b) its Fourier transform, $\eta_j = \mathcal{F}\{\eta_k\}$, for different values of the classical transverse field ω_x. The Ising interaction is set to $4J = \Omega$ and the light-matter coupling to $\lambda = 0.2\Omega$. A finite size of $N = 150$ was used for the Fourier transform.

coupled quantum harmonic oscillators of frequencies Ω and $4J$:

$$2\Omega_{\pm}^2 = 4J^2 + \Omega^2 \pm \sqrt{(4J^2 - \Omega^2)^2 + 32\lambda^2 J\Omega}\,. \tag{5.31}$$

At the first-order phase transition, the effective mean field acquires a non-zero value, opening the band. The lower polariton hardens to become the cavity photon in the deep superradiant regime.

Figures 5.7(b), (c) and (d) show the case of non-zero classical field, $\omega_x \neq 0$. Then, the Ising band (5.25) is already open in the normal phase, and we can understand the model as an impurity model, where it is the cavity that plays the impurity role. The original collective coupling of the spins to the cavity translates into a momentum-dependent coupling of the Bogoliubov fermions that diagonalize the effective Ising model to the cavity [Cf. Eq. (5.29)]. In Fig. 5.8 we show that the coupling

$$\eta_k = 2u_k v_k = 2J \sin k/\epsilon_k \tag{5.32}$$

has an exponentially localized profile in real space. Thus, the analogy with the impurity is complete. Moreover, the equation for the poles of $D(\omega)$ can be shown to be

$$F(\omega) = \omega_+^2 - \Omega^2 - 4\lambda^2\Omega \int_{-\pi}^{\pi} \frac{dk}{2\pi} \eta_k^2 \frac{4\epsilon_k}{\omega_+^2 - 4\epsilon_k^2} = 0\,, \tag{5.33}$$

which can be compared with the equation for the eigenvalues of a discrete system coupled to a continuum with a finite bandwidth [175], in our case the band of the Ising model given by (5.25).

5.3.2 Existence of bound polariton states

By simple inspection, we observe in Figure 5.7 that $D(\omega)$ has poles outside the band given by $2\epsilon_k$ in Eq. (5.25). We refer to these states as *bound polariton states*. While we could simply use the term bound states, we retain the term polaritons since we are within the field of cavity QED materials. Additionally, this highlights their complementarity to the usual bound states in quantum optics, where matter localizes photons around an impurity. Here, it is the cavity that localizes spin excitations.

The possibility of bound states emerging is well known [175–177]. These states belong to the discrete spectrum and are solutions to $F(\omega) = 0$ for ω outside the band. Much is known about bound states, particularly that their existence is primarily determined by the bandwidth, the coupling, and the position of the impurity [178, 179], which in our case is the cavity.

We consider it important to emphasize that these states emerge from a non-trivial system, which, despite being exactly solvable, is a strongly correlated model of matter non-perturbatively coupled to a cavity field. The fact that it can be solved highlights how useful the thermodynamic limit is in cavity QED materials when performing calculations at any value of the light-matter coupling. Similar existence conditions should be obtained in other scenarios, such as intersubband polaritons [180, 181] or lattice fermion models like the SSH model or similar [32, 86]. The existence of bound states in those cases can be discussed, and should depend on the band limits and the density of states of the matter coupled to the cavity near those band limits.

In Fig. 5.7, we see how tuning the bandwidth with ω_x results in the detachment of bound states from the band edges. Furthermore, we understand their increased visibility (with respect to the band) when they appear, as it is well known that the contribution of the impurity (the cavity) is finite in the bound states. Additionally, the localized nature of bound states explains why the polariton formula (5.31) accounts well for their energy.

5.3.3 Finite-size effects

Finally, we present a comparison between our LRT and finite-size exact-diagonalization results in Fig. 5.9. This allows us to discuss how quickly finite-size effects are washed out as we increase the system size and provides another check of our formulas in this non-trivial case. We compare our LRT in Figs. 5.9(a), (c) and (e), valid in the thermodynamic limit, with exact-diagonalization results for system sizes up to $N = 14$ in Figs. 5.9(b), (d) and (f). Let us begin by comparing Figs. 5.9 (a) and (b), which correspond to

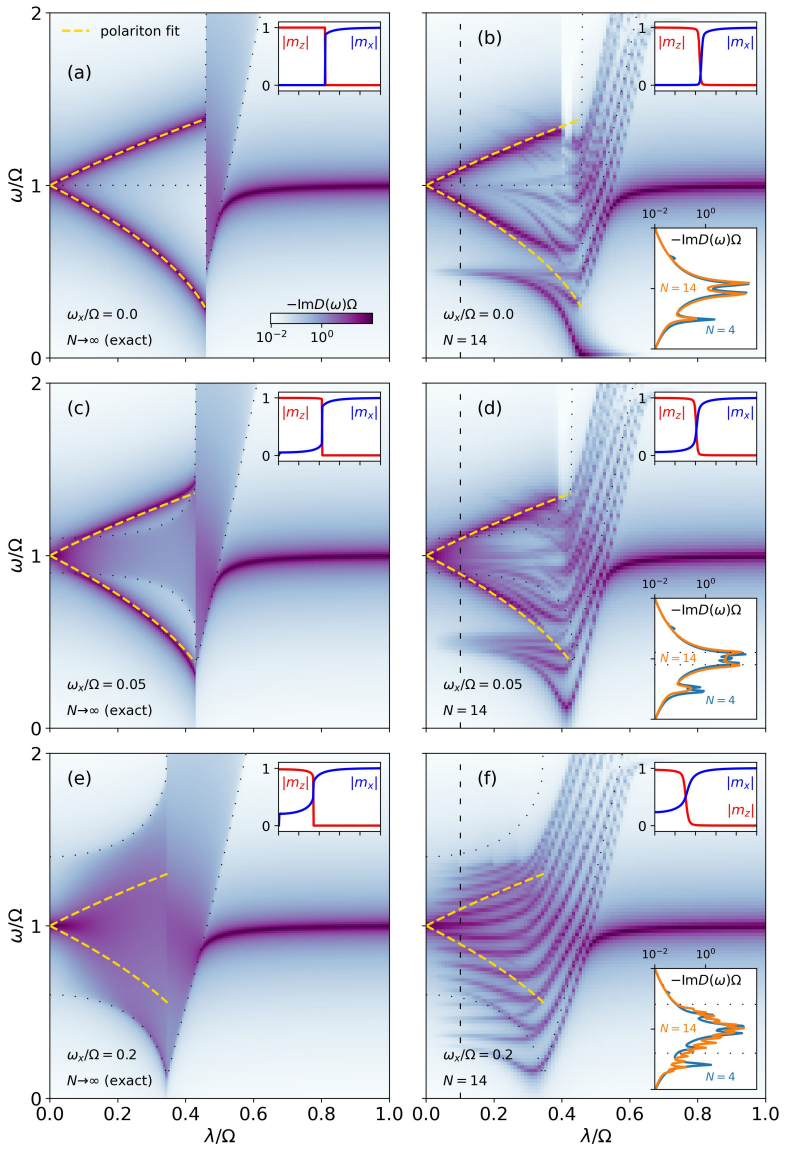

Figure 5.9: Cavity response D of the Dicke-Ising model as a function of the collective coupling λ computed analytically in the thermodynamic limit, $N \to \infty$, (left) and with exact diagonalization, $N = 14$, (right) for different values of the classical field ω_x. The yellow dashed lines correspond to a fit of the polaritons with a two-oscillator model [See Eq. (5.31)]. The top right insets show the magnetizations. The bottom right inset in the right plots shows a vertical cut at the black dashed line for two finite sizes, $N = 4$ and $N = 14$. The dotted lines mark the edges of the band of the mean-field effective Hamiltonian (5.23). The parameters are $\omega_x = 0$ and $4J = \Omega$. In the exact-diagonalization results, the Fock basis for the photonic Hilbert space is truncated at 40 photons.

the case of vanishing classical field. In this case we observe the formation of polaritons in the zFMN phase and the opening of the two-excitation band and the hardening of the lower polariton in the xFMS phase in Fig. 5.9(a). The same features are observed in Fig. 5.9(b), although the two-excitation band is not fully formed, and instead we can distinguish a collection of discrete levels. Additionally, there are some finite-size effects. Most prominently, there is a pole corresponding to the single-excitation band in the zFMN phase, at $\omega = 2J = \Omega/2$ for $\lambda \to 0$. This is explained by noting that the coupling operator, C_x (5.29) can create domain walls at the edges of the chain, something which is impossible in the thermodynamic limit and thus an effect that becomes negligible as $N \to \infty$. This interpretation is confirmed by the bottom right inset in Fig. 5.9(b), which shows that the intensity of this pole decreases with size, unlike the poles corresponding to the polaritons. Figures 5.9(c), (d), (e) and (f) feature a finite classical field ω_x and thus a finite bandwidth in the normal phase. In Fig. 5.9(c) the narrow bandwidth allows the formation of bound polariton states (BPS) with well-defined energies below and above the band. This is validated in Fig. 5.9(d). Again, we observe additional features that we attribute to finite size-effects. In particular the single-excitation band, at $\omega = 2J = \Omega/2$ for $\lambda \to 0$. Its visibility is shown to decrease with size in the bottom right inset of Fig. 5.9(d). In Fig. 5.9(e) the large bandwidth prevents the formation for BPS. This is confirmed in Fig. 5.9(f) where we observe a collection of closely packed levels of equal visibility that are expected to form the band in the thermodynamic limit. There are not any two levels that stand out as polaritons, in agreement with our LRT. The levels that fall outside the would-be band are shown to be finite-size artifacts in the bottom right inset of Fig. 5.9(f).

5.4 Heisenberg ferromagnet coupled to a cavity

We finish the chapter by commenting on the paradigmatic Heisenberg model. In particular, we consider a ferromagnetic Heisenberg model on a $3D$ lattice, such that the model is ordered below a critical temperature,

$$H_{\mathrm{m}} = -J \sum_{\langle ij \rangle} \boldsymbol{\sigma}_i \cdot \boldsymbol{\sigma}_j + \frac{\omega_z}{2} \sum_j \sigma_j^z \,. \tag{5.34}$$

The ground state of the model corresponds to a symmetry broken ferromagnetic state. For vanishing field, $\omega_z = 0$, the spins will be magnetized in a random direction of space, spontaneously breaking the $SO(3)$ symmetry of the model. The addition of a field demotes the symmetry to $SO(2)$ in the plane perpendicular to the field, setting the magnetization direction along the field. It also opens a gap between the spin-wave band and the ground state, such that the zero

momentum spin-wave has an energy gap with respect to the ground state of ω_z. The coupling to a cavity in a direction perpendicular to the classical field will demote the remaining $SO(2)$ symmetry to $\mathbb{Z}_2$ in the cavity field direction. The cavity coupling, $C_x = \sum_j \sigma_j^x$, will compete with the classical field in setting the magnetization direction. The corresponding effective Hamiltonian reads

$$H_{\text{eff}}^{\text{MF}} = \frac{\omega_z}{2}\sum_j \sigma_j^z - J\sum_{\langle ij\rangle} \boldsymbol{\sigma}_i \cdot \boldsymbol{\sigma}_j - \frac{2\lambda^2}{\Omega} m_x \sum_j \sigma_j^x + \frac{\lambda^2}{\Omega} m_x^2 \tag{5.35}$$

If we assume that the model is ordered, the interaction term contributes an energy $-Jz$ with z the coordination number, independently of the value of m_x. Thus, the variational Hamiltonian is equivalent to that of a Dicke model (Cf. Sec. 5.1). The behavior of the magnetization m_x is also inherited from the Dicke model. For a subcritical coupling, $\lambda < \sqrt{\omega_z \Omega}/2$, the model is ordered along z. When the coupling reaches the critical point, the magnetization starts to turn towards the x axis in a second order phase transition.

The response function $\tilde{\chi}_{xx,0}$ corresponds to the excitation of the zero-momentum magnon, with a pole at $\omega^2 = \omega_z^2 + (4\lambda^2 m_x/\Omega)^2$. Therefore, our LRT predicts the formation of polaritons of this zero-momentum magnon with frequencies given by Eq. 5.4, following the physics of the Dicke model.

Chapter 6

Dynamics of a magnetic material coupled to a cavity

In Chap. 3 we laid out the equations of motion for the two-point correlators of the generalized Dicke model. We were able to relate them to the bare photonic propagator and matter response functions. While this is a powerful formalism that was exploited in Chaps. 4 and 5 to study some paradigmatic solvable models, it relies on being able to compute the bare matter response functions. This is in general a very complex problem that constitutes the essence of traditional condensed matter physics. In most cases, this challenge will have to be tackled using approximate methods or numerical techniques. We also discussed that light-matter correlations form a closed hierarchy that can be treated at any order. In particular, light-matter correlations can be disregarded completely.

These two ideas find application in the fields of magnonics and micromagnetic simulation. Magnetic materials are routinely described within a mean-field description that neglects correlations entirely. The combination of this mean-field decoupling with a phenomenological dissipation term yields the Landau-Lifshitz-Gilbert (LLG) equation. It is a classical differential equation for the magnetization that can be solved analytically in some cases and most often numerically. The magnetization evolves subject to a torque that depends on a time- and space-dependent effective field that is the mean-field aggregate of the different effects at play in the material, such as exchange interactions or magneto-crystalline anisotropy [182]. Remarkably, this is sufficient to describe non-trivial states in magnetic materials, such as vortices and skyrmions. It seems reasonable then to consider magnetic materials coupled to a cavity and study their time evolution under a complete mean-field decoupling. The light-matter decoupling is justified by our theory of Chaps. 2 and 3 and the

matter-matter decoupling that leads to the LLG equation is justified by its demonstrated success in the field of micromagnetic simulations.

Thus, in this chapter we will present the LLG equation and discuss how it is modified when the magnetic material is coupled to a cavity. Following the spirit of the thesis, we will show that the cavity can be eliminated from the dynamical description and its effect incorporated as a new contribution to the mean field that induces the precession of the spins in the LLG equation. Then, we will introduce the micromagnetic simulation software Mumax3 and explain how we have modified its open-source code to implement the effect of the cavity. We have shipped the resulting software as Mumax3-cQED. Finally, we will benchmark Mumax3-cQED on the Dicke model, and we will present two simulations of realistic ferromagnets that highlight the potential of Mumax3-cQED to reproduce experiments in which magnetic field or magnetization inhomogeneities play a fundamental role.

This chapter is based on Ref. [66].

6.1 The Landau-Lifshitz-Gilbert equation

Typically, one considers a finite-difference discretization of space, dividing the magnetic material into orthorombic cells and associating a reduced magnetization vector, $\boldsymbol{m}_j$ (a unit vector), to the center of each cell. The evolution of the reduced magnetization is computed by numerically solving the LLG equation

$$\dot{\boldsymbol{m}}_j \equiv \frac{\partial \boldsymbol{m}_j}{\partial t} = -\gamma \frac{1}{1+\alpha^2} \left(\boldsymbol{m}_j \times \boldsymbol{B}_{\text{eff}}(\boldsymbol{r}_j) + \alpha \boldsymbol{m}_j \times (\boldsymbol{m}_j \times \boldsymbol{B}_{\text{eff}}(\boldsymbol{r}_j)) \right) , \quad (6.1)$$

with $\gamma > 0$ the gyromagnetic ratio, α a dimensionless damping parameter and $\boldsymbol{B}_{\text{eff}}$ the effective field. The effective field can have the several contributions, such as external $\boldsymbol{B}_{\text{ext}}$, demagnetization $\boldsymbol{B}_{\text{demag}}$, exchange $\boldsymbol{B}_{\text{exch}}$, Dzyaloshinskii-Moriya $\boldsymbol{B}_{\text{dm}}$, magneto-crystalline anisotropy $\boldsymbol{B}_{\text{anis}}$ and thermal $\boldsymbol{B}_{\text{therm}}$ fields [183]. In the following, we will show that the effect of the cavity can be incorporated as an additional contribution to $\boldsymbol{B}_{\text{eff}}$: the cavity field $\boldsymbol{B}_{\text{cav}}$.

The first term on the right-hand side of Eq. (6.1) represents the precession of a spin around the effective magnetic field $\boldsymbol{B}_{\text{eff}}$ within a classical and mean-field approximation. This equation corresponds to the large spin limit of the Heisenberg equation for the spin operator, expressed as

$$\dot{\boldsymbol{S}}_j = \frac{i}{\hbar}[H, \boldsymbol{S}_j] , \quad (6.2)$$

where the dimensionfull spin operators satisfy

$$[S_j^\alpha, S_j^\beta] = i\hbar \epsilon_{\alpha\beta\gamma} S_j^\gamma , \quad (6.3)$$

with $\epsilon_{\alpha\beta\gamma}$ denoting the Levi-Civita symbol. In Eq. (6.2), H is the total Hamiltonian that accounts for all interactions and fields through $\boldsymbol{B}_{\text{eff}}$. Within the mean-field treatment it is simply $H = \gamma \sum_j \boldsymbol{S}_j \cdot \boldsymbol{B}_{\text{eff}}(\boldsymbol{r}_j)$. In the large spin limit, the spin operator can be approximated as a classical vector, $\boldsymbol{S}_j \to \boldsymbol{S}_j = \langle \boldsymbol{S}_j \rangle$, with a magnitude of $\hbar S_j$. The magnetic dipole moment is defined as $\boldsymbol{\mu}_j = -\gamma \boldsymbol{S}_j$, and the magnetization as $\boldsymbol{M}_j = \boldsymbol{\mu}_j / V_{\text{c}}$, where V_{c} is the cell volume. The reduced magnetization is then $\boldsymbol{m}_j = \boldsymbol{M}_j / M_{\text{s},j}$, with the saturation magnetization given by $M_{\text{s},j} = \hbar\gamma S_j / V_{\text{c}}$. Consequently, the equation of motion for the magnetization is

$$\dot{\boldsymbol{m}}_j = -\gamma \boldsymbol{m}_j \times \boldsymbol{B}_{\text{eff}}(\boldsymbol{r}_j)\,, \tag{6.4}$$

consistent with the first term on the right-hand side of the LLG equation (6.1). The second term is the so-called phenomenological Gilbert damping. It induces a decay of the magnetization vector toward the precession axis determined by $\boldsymbol{B}_{\text{eff}}$.

We will focus on the modification of the first term by the cavity, and, once we establish how $\boldsymbol{B}_{\text{eff}}$ is modified there, we will include this modification also in the $\boldsymbol{B}_{\text{eff}}$ that appears on the second term, à la Gilbert.

6.2 LLG equation for a magnet coupled to a cavity

We will consider a single mode cavity, in that case the Hamiltonian is (See Sec. (1.2.2))

$$H = \gamma \sum_j \boldsymbol{S}_j \cdot \boldsymbol{B}_{\text{eff}}(\boldsymbol{r}_j) + \gamma \sum_j \boldsymbol{S}_j \cdot \boldsymbol{B}_{\text{rms}}(\boldsymbol{r}_j) \left(a + a^\dagger\right) + \hbar\Omega a^\dagger a\,. \tag{6.5}$$

Here the spins are subject to both an effective field $\boldsymbol{B}_{\text{eff}}$ and the average cavity magnetic field $\boldsymbol{B}_{\text{rms}} \left(a + a^\dagger\right)$, with a, $a^\dagger$ the bosonic annihilation and creation operators obeying canonical commutation relations $[a, a^\dagger] = 1$ and Ω the cavity frequency. The corresponding Heisenberg equations of motion are

$$\dot{\boldsymbol{S}}_j = -\gamma \boldsymbol{S}_j \times \boldsymbol{B}_{\text{eff}}(\boldsymbol{r}_j) - \gamma \left(\boldsymbol{S}_j \times \boldsymbol{B}_{\text{rms}}(\boldsymbol{r}_j)\right) \left(a + a^\dagger\right)\,, \tag{6.6}$$

$$\dot{a} = -i\omega_c a - i\frac{\gamma}{\hbar} \sum_j \boldsymbol{S}_j \cdot \boldsymbol{B}_{\text{rms}}(\boldsymbol{r}_j)\,. \tag{6.7}$$

Hamiltonian (6.5) is essentially the Dicke model (See Sec. 6.4). Its equations of motion [Eqs. (6.6) and (6.7)] are fully quantum (within the mean-field approximation for spin-spin interactions). Consequently, the light-matter interaction generates spin-photon correlations. However, in the large S limit, which is the focus here, these correlations can be disregarded if one only seeks a description

of one-point correlators, i.e., observables (See the discussion in Sec. 3.3) [133]. This is consistent with the classical uncorrelated limit assumed for the spin dynamics in the LLG equation and corresponds to treating light-matter and matter-matter quantum correlations on the same footing: neglecting both completely. Armed with this information, if we take expected values in Eqs. (6.6) and (6.7), we can simplify

$$\langle (\boldsymbol{S}_j \times \boldsymbol{B}_{\mathrm{rms}}(\boldsymbol{r}_j)) \left(a + a^\dagger\right) \rangle \to \langle \boldsymbol{S}_j \rangle \times \boldsymbol{B}_{\mathrm{rms}}(\boldsymbol{r}_j) \langle a + a^\dagger \rangle \,, \tag{6.8}$$

and arrive to classical equations of motion for the expected values of the spin and cavity degrees of freedom. This corresponds to a zeroth-order mean-field decoupling of light and matter that is exact if the initial states of the evolution are uncorrelated. The same mean-field decoupling at the level of the equations of motion but carried out to first order was used to compute two-point correlators in Chap. 3. Defining $\alpha = \langle a \rangle$ and $\alpha^* = \langle a^\dagger \rangle$ we can write the equations of motion as

$$\dot{\boldsymbol{S}}_j = -\gamma \boldsymbol{S}_j \times \boldsymbol{B}'_{\mathrm{eff}}(\boldsymbol{r}_j) \,, \tag{6.9}$$

$$\dot{\alpha} = -i\Omega\alpha - i\frac{\gamma}{\hbar} \sum_j \boldsymbol{S}_j \cdot \boldsymbol{B}_{\mathrm{rms}}(\boldsymbol{r}_j) \,, \tag{6.10}$$

with $\boldsymbol{B}'_{\mathrm{eff}}(\boldsymbol{r}_j) = \boldsymbol{B}_{\mathrm{eff}}(\boldsymbol{r}_j) + \boldsymbol{B}_{\mathrm{rms}}(\boldsymbol{r}_j)(\alpha + \alpha^*)$ and $\boldsymbol{S}_j$ a classical vector now. As explained in Sec. 6.1, Equation (6.9) is the LLG equation with a modified effective field that depends on two additional cavity degrees of freedom. The system dynamics could be obtained by explicitly solving Eqs. (6.9) and (6.10). However, following the spirit of the thesis, let us integrate out the cavity degrees of freedom and arrive to an effective description that depends only on the magnetization. This will prove useful in a moment, when we discuss how to implement these cavity modified dynamics into the micromagnetic simulation software Mumax3. The cavity is eliminated by explicitly solving its equations of motion, which yields (See App. I for details)

$$\dot{\boldsymbol{m}}_j = -\gamma \boldsymbol{m}_j \times \boldsymbol{B}'_{\mathrm{eff}}(\boldsymbol{r}_j) \,, \tag{6.11}$$

with $\boldsymbol{B}'_{\mathrm{eff}}(\boldsymbol{r}_j) = \boldsymbol{B}_{\mathrm{eff}}(\boldsymbol{r}_j) + \boldsymbol{B}_{\mathrm{cav}}(\boldsymbol{r}_j)$ and

$$\boldsymbol{B}_{\mathrm{cav}}(\boldsymbol{r}_j) = \boldsymbol{B}_{\mathrm{rms}}(\boldsymbol{r}_j)\Gamma(t) \,, \tag{6.12}$$

where

$$\begin{aligned} \Gamma(t) &= 2e^{-\kappa t}\, \mathrm{Re}\left(\alpha_0 e^{-i\Omega t}\right) \\ &\quad - \frac{2V_{\mathrm{c}}}{\hbar} \int_0^t d\tau e^{-\kappa(\tau - t)} \sin(\Omega(\tau - t)) \sum_j M_{\mathrm{s},j} \boldsymbol{m}_j(\tau) \cdot \boldsymbol{B}_{\mathrm{rms}}(\boldsymbol{r}_j) \,. \end{aligned} \tag{6.13}$$

With this, the effect of the cavity can be incorporated in the standard LLG equation as a new contribution to the effective field: $\boldsymbol{B}_{\text{eff}} \to \boldsymbol{B}'_{\text{eff}} = \boldsymbol{B}_{\text{eff}} + \boldsymbol{B}_{\text{cav}}$. This new cavity field $\boldsymbol{B}_{\text{cav}}$ (6.12) is the average magnetic field of the cavity $\boldsymbol{B}_{\text{rms}}$ times a memory factor Γ. In turn, the differential equation that is the LLG equation has become an integro-differential equation (IDE) by the appearance of the memory term $\Gamma(t)$, which depends on the full magnetization history. We can understand this as the mathematical reflection of the fact that we have eliminated the cavity from our dynamical description and, as a consequence, a cavity-mediated retarded interaction between the spins appears. Much like dissipation is introduced phenomenologically in the LLG equation with the Gilbert term, we have introduced dissipation in the cavity by promoting $\Omega \to \Omega - i\kappa$ in Eq. (6.7). This corresponds to local dissipation at the level of a Linblad master equation for the cavity.

Despite having eliminated α and α^* as dynamical variables, one might be interested in their values. For instance, $|\alpha|^2 = \langle a^\dagger a \rangle$ is the number of photons in the cavity. These can be computed a posteriori from the magnetization $\boldsymbol{m}(t)$, obtained from a simulation of the cavity-modified LLG equation. They are given by (See App. I for details)

$$\alpha = \alpha_0 e^{-\kappa t} e^{-i\Omega t} + i\frac{V_c}{\hbar}\int_0^t d\tau e^{\kappa(\tau-t)} e^{i\Omega(\tau-t)} \sum_j M_{s,j} \boldsymbol{m}_j(\tau) \cdot \boldsymbol{B}_{\text{rms}}(\boldsymbol{r}_j)\,, \quad (6.14)$$

6.3 Modifying Mumax3 to include the effect of the cavity

Mumax3 is an open-source GPU-accelerated micromagnetic simulation software designed to efficiently solve the LLG equation (6.1) for arbitrary geometries and materials. In this section, we describe how we have modified the source code to implement the cavity field $\boldsymbol{B}_{\text{cav}}$. The resulting software, which we have released under the name Mumax3-cQED, can now be used by the scientific community to simulate magnon-polaritons in realistic magnetic materials and nanostructures and design magnon-cavity experiments under two conditions: that the dynamics of the ferromagnet can be reliably reproduced with Mumax3, and that the spatial distribution of magnetic fields created by the cavity can be simulated (using another software). See App. App. J for more details on the API and source code of Mumax3-cQED.

The design principle that we have followed is to implement the cavity contribution to the effective field, $\boldsymbol{B}_{\text{cav}}$ (6.12), into Mumax3-cQED without making any modification to the existing ordinary differential equation (ODE) integrator in Mumax3. This also motivates the elimination of the cavity degrees

of freedom, since Mumax3 is designed to handle only the magnetization. First, it is convenient to decouple the time dependence on t, the current time, and τ, the past time, in the integral of Eq. (6.13), such that

$$\Gamma(t) = 2e^{-\kappa t}\,\mathrm{Re}\left(\alpha_0 e^{-i\omega_c t}\right) - \frac{2V_c}{\hbar}e^{-\kappa t}\left(\cos(\omega_c t)S(t) - \sin(\omega_c t)C(t)\right)\,, \quad (6.15)$$

with

$$S(t) = \int_0^t d\tau e^{\kappa\tau}\sin(\omega_c\tau)\sum_j M_{s,j}\boldsymbol{m}_j(\tau)\cdot\boldsymbol{B}_{\mathrm{rms}}(\boldsymbol{r}_j)\,, \quad (6.16)$$

$$C(t) = \int_0^t d\tau e^{\kappa\tau}\cos(\omega_c\tau)\sum_j M_{s,j}\boldsymbol{m}_j(\tau)\cdot\boldsymbol{B}_{\mathrm{rms}}(\boldsymbol{r}_j)\,. \quad (6.17)$$

Note that here the integrands no longer depend on the current time t. So far we have dealt with time as a continuous variable, but in Mumax3, time is discretized. Expressing $S(t)$ and $C(t)$ in terms of discrete time, $t \to t_n = n\Delta t$ yields

$$S_n = S(t_n) = S_{n-1} + e^{\kappa t_n}\sin(\omega_c t_n)\sum_j M_{s,j}\boldsymbol{m}_j(t_n)\cdot\boldsymbol{B}_{\mathrm{rms}}(\boldsymbol{r}_j)\Delta t\,, \quad (6.18)$$

$$C_n = C(t_n) = C_{n-1} + e^{\kappa t_n}\cos(\omega_c t_n)\sum_j M_{s,j}\boldsymbol{m}_j(t_n)\cdot\boldsymbol{B}_{\mathrm{rms}}(\boldsymbol{r}_j)\Delta t\,. \quad (6.19)$$

with $S_0 = S(0) = C_0 = C(0) = 0$. This recursive definition is the key to efficiently implementing $\boldsymbol{B}_{\mathrm{cav}}$ within Mumax3. By storing S_n and C_n as persistent variables across consecutive calls to the integrator we avoid storing the full history of magnetizations, saving memory, and avoid resumming the full history at each time step, optimizing run speed.

Finally, to avoid handling complex variables in Mumax3 we express the term $\mathrm{Re}\left(\alpha_0 e^{-i\omega_c t}\right)$ in terms of the real and imaginary parts of α_0, which yields

$$\Gamma(t_n) = e^{-\kappa t_n}\cos(\omega_c t_n)\left(x_0 - \frac{2V_c}{\hbar}S_n\right) - e^{-\kappa t_n}\sin(\omega_c t_n)\left(p_0 - \frac{2V_c}{\hbar}C_n\right)\,, \quad (6.20)$$

with $x_0 = \alpha_0 + \alpha_0^* = 2\,\mathrm{Re}(\alpha)$ and $p_0 = \alpha_0 - \alpha_0^* = -2\,\mathrm{Im}(\alpha)$.

6.4 Benchmark on the Dicke model

Our testbed will be the Dicke model. We choose the Dicke model for two reasons. First, it can be implemented in Mumax3-cQED using one single cell, i.e., it does not benefit from the GPU-reliant parallelization. Therefore, its evolution can also be numerically simulated in Python (or any other programming language)

with reasonable CPU runtimes. This is done by simply integrating the joint LLG equation and equations of motion for the cavity degrees of freedom associated to Eqs. (6.9) and (6.10) with the default integrators included in Python's Scipy. This unsophisticated implementation in Python provides the transparency that the highly optimized Mumax3 code lacks. It also allows us to check to what degree the implicit integration (with the magnetization as sole degree of freedom) that we implement in Mumax3-cQED is equivalent to an explicit integration of the original equations of motion. Second, the Dicke model can be solved exactly at equilibrium, as discussed in Sec. 1.3.1, providing the equilibrium value of the magnetization (5.2), to which we can expect the dynamics to converge at large times, as well as the frequencies of the polaritons (5.4), against which we can compare the Fourier spectrum of the time evolution obtained with Mumax3.

As explained in Sec. 1.3.1, the ground-state sector of the Dicke Hamiltonian can be described in terms of spin $S = N/2$ operators. Comparing Eqs. 1.53 and Eq. (6.5) we see that we can implement the Dicke model in Mumax3-cQED by identifying

$$\boldsymbol{B}_{\text{eff}} = \boldsymbol{B}_{\text{ext}} = \left(0, 0, \frac{\omega_z}{\gamma}\right) , \tag{6.21}$$

$$\boldsymbol{B}_{\text{rms}} = \left(\sqrt{\frac{2}{S}}\frac{\lambda}{\gamma}, 0, 0\right) . \tag{6.22}$$

This corresponds to a single cell, i.e., a single magnetization vector, under the effect of an external field and the cavity field: $\boldsymbol{B}_{\text{eff}} = \boldsymbol{B}_{\text{ext}} + \boldsymbol{B}_{\text{cav}}$.

Fig. 6.1(a) shows an example of a time evolution of m_x computed with Mumax3-cQED within the normal paramagnetic phase, $\lambda < \lambda_c$. It matches the evolution computed with Python. The magnetization converges to zero at large times, consistent with the equilibrium value [Cf. Eq. (5.2)]. Figs. 6.1(b) and (c) show the Fourier transform of two time evolutions, like the one shown in Fig. 6.1(a). The Fourier spectra present peaks at the polaritonic frequencies of the Dicke model, at $\omega = \omega_z = \Omega$ for $\lambda = 0$ and at $\omega = \Omega_\pm$ (5.4) for non-zero λ.

The dynamics within the superradiant ferromagnetic phase serve to explicitly demonstrate the numerical differences between the IDE integration in MuMax and the ODE approach in our custom Python code. In the broken-symmetry phase, the two possible equilibrium solutions $\pm\sqrt{1-\mu^2}$ act as attractors or fixed points of the system. Consequently, even minor differences may lead the system to converge to different attractors. However, this divergence has no physical consequences. As shown in Figure 6.2, small numerical variations result in the system reaching distinct attractors, but both solutions converge to the correct equilibrium values. This consistency emphasizes that dissipation

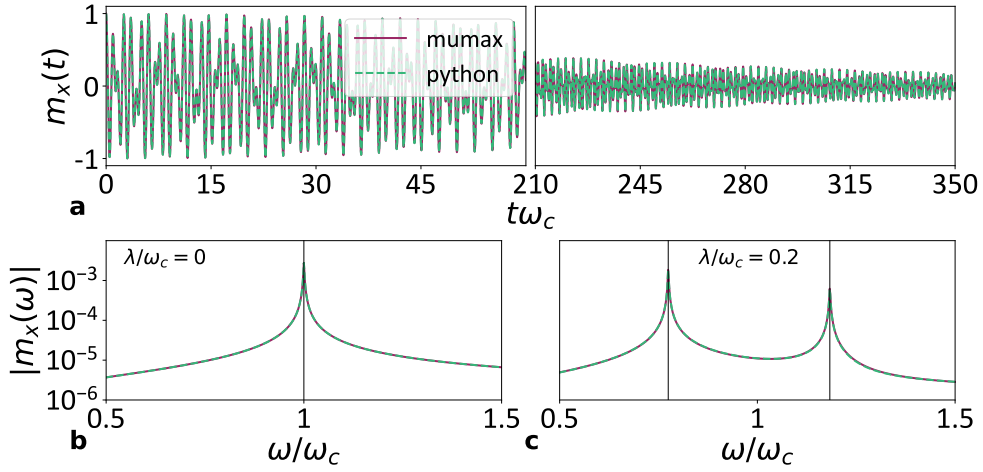

Figure 6.1: Time evolution of the Dicke model in the normal paramagnetic phase, $\lambda < \lambda_c$, for $\omega_z = \Omega$. a: Magnetization as a function of time, for small and large times. b and c: Fourier spectra of the magnetization for zero (b) and non-zero (c) coupling. The vertical black lines mark the frequencies of the polaritons computed analytically.

is introduced in a thermodynamically consistent manner.

We have conducted tests analogous to the ones presented in Figs. 6.1 and 6.2 in the full range of values of Ω, ω_z and λ with similar results. The differences between the Mumax3-cQED and Python evolutions grow with increasing coupling λ and are only significant well into the ultra-strong coupling regime. In any case, Mumax3-cQED always produces one of the correct equilibrium values for the different observables, indicating that this formalism is capable of describing proper thermalization, and Fourier spectra peaked at the correct polaritonic frequencies. We take this as confirmation that Mumax3-cQED works as intended. It correctly captures the hybridization of light and spins, even in non-trivial ordered phases and ultra-strong coupling regimes, and it enables the study of non-equilibrium dynamics in magnonic QED.

6.5 Ferromagnetic materials in a cavity

We finally show the potential of Mumax3-cQED applied to two relevant non-analytical problems. The first focuses on a saturated ferromagnet coupled to a realistic resonator which generates strongly non-homogeneous magnetic field modes. In the second example, we will calculate the response of a spin texture interacting with cavity photons. Understanding magnon-photon interactions in highly non-homogeneous ferromagnets and cavities is of enormous technological and conceptual interest [184–194].

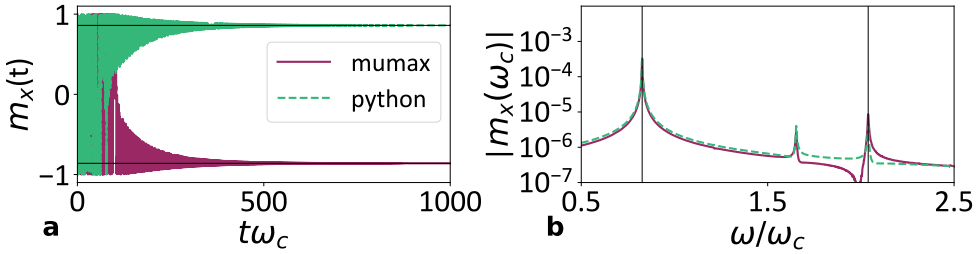

Figure 6.2: Time evolution of the Dicke model in the superradiant ferromagnetic phase, $\lambda/\lambda_c = 1.4$, for $\omega_z = \Omega$. a: Magnetization as a function of time. The horizontal black lines mark the possible equilibrium values of the magnetization computed analytically. b: Corresponding Fourier spectra of the magnetization. The vertical black lines mark the frequencies of the polaritons computed analytically.

6.5.1 Effects of the parity of the magnetic mode

We first consider a three-dimensional cavity with a "re-entrant" element, i.e., a metallic post or rod that extends into the cavity from one side. This element modifies the electromagnetic field distribution, concentrating the magnetic field near the bottom part of the post. On the other hand, an antinode of the electric field is created at the gap, between the post and the top of the cavity [195]. Using two posts results in two non-degenerate modes with antiparallel and parallel currents. These currents produce even and odd field distributions between the two posts, referred to as bright and dark modes, respectively (see Fig. 6.3a and b). Here, we will reproduce the results obtained by Goryachev *et al.* [196] using an yttrium iron garnet (YIG) sphere (radius of 0.4 mm) located between the two posts of a re-entrant cavity (internal radius of 5 mm, height 1.4 mm, post radius of 0.4 mm, post gap of 73 μm, and distance between the posts 1.5 mm) with dark and bright modes at frequencies $f_{\uparrow\downarrow} = 20.8$ GHz and $f_{\uparrow\uparrow} = 13.2$ GHz, respectively.

To obtain reasonable simulation times we scale down the whole system by a factor of 800 resulting into a YIG sphere with radius 500 nm ($\gg \lambda_{ex} \sim 14$ nm, the exchange length of YIG). As demonstrated in Refs. [197] and [198], the coupling strength is $g \propto B_{\mathrm{rms}}\sqrt{V_m}$, with V_m the volume of the magnet. Therefore, to compensate the reduced volume of the system, and yield a coupling g equivalent to the experiment, we also need to scale up B_{rms} by a factor of $\sim (800)^{3/2}$. The spatial-dependence of $\boldsymbol{B}_{\mathrm{rms}}(\boldsymbol{r}_j)$ created by the bright and dark modes are simulated with the software COMSOL as described in J.2. For the bright mode, two antiparallel currents yield an even, quasi homogeneous distribution of zero-point magnetic field fluctuations (see Fig. 6.3c). For the dark mode, two parallel identical currents result in an odd, highly non-homogeneous distribution (see Fig. 6.3d).

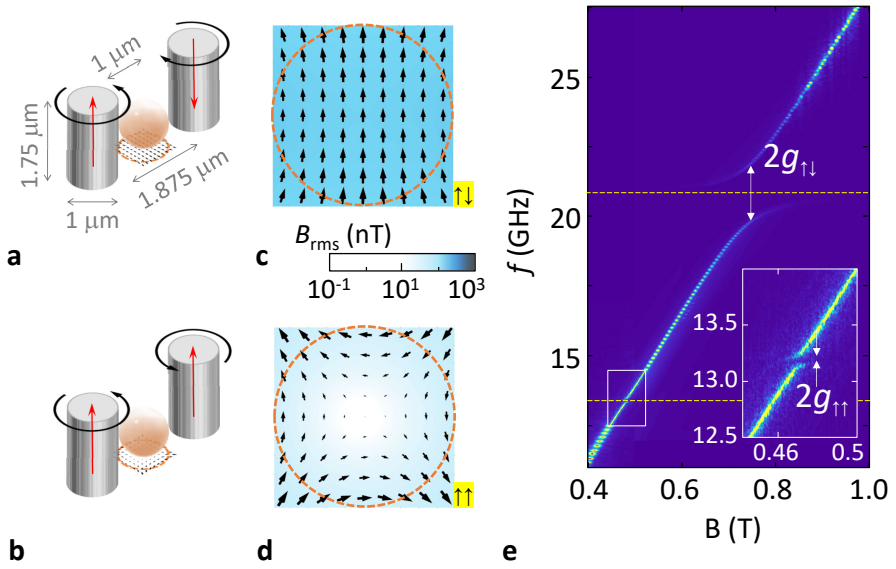

Figure 6.3: Two-post re-entrant cavity with electric currents (red arrows) flowing antiparallel (a: bright mode) or parallel (b: dark mode). Resulting magnetic field lines are represented by black arrows. Spatial distribution of B_{rms} for the bright (c) and dark (d) modes with the YIG sphere position highlighted in dashed orange. e: Response of the YIG sphere, inset: region of coupling to the dark mode. Dashed yellow lines highlight the frequencies of the bright and dark modes.

Polariton dynamics are then calculated using Mumax3-cQED (see J.3) and shown in Fig. 6.3e. Due to symmetry reasons, the bright mode can excite and couples strongly to the Kittel mode in the YIG sphere, yielding a coupling energy of $g_{\uparrow\downarrow}/2\pi \sim 1$ GHz, as reported by Goryachev *et al.* On the other hand, the odd-symmetric dark mode couples very weakly to the Kittel precession, leading to a much weaker $g_{\uparrow\uparrow}/2\pi \sim 30$ MHz. We note that the excitation of additional (experimentally visible) magnetostatic modes cannot be reproduced. These modes are neither visible in simulations performed with the unmodified Mumax3, probably due to the strong reduction of the sphere radius (factor of 800).

In its current state, Mumax3-cQED considers a single-mode cavity field. However, our simulations demonstrate that results for multimode cavities can also be reproduced by simulating each mode individually. This is true as long as the cavity frequencies are well-separated, at least as much as the coupling strength. In any case, extending Mumax3-cQED to handle multimode cavities is straightforward and will be included in future releases.

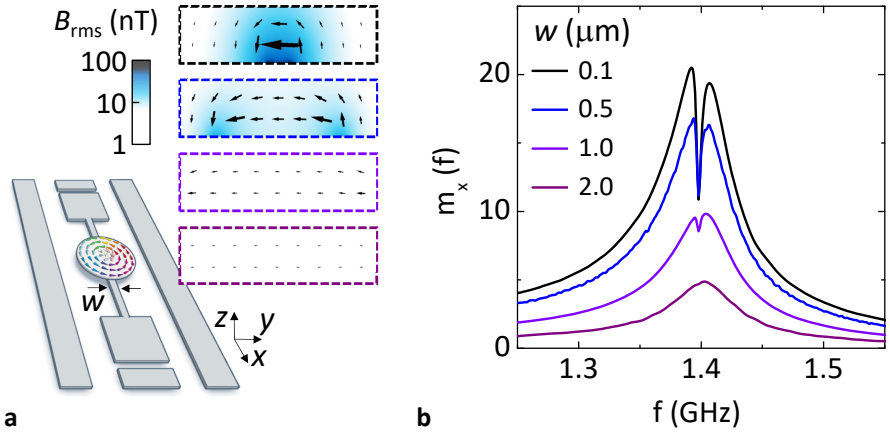

Figure 6.4: a: Py disc located at the magnetic antinode of a cpw distributed resonator of width w. The non-homogeneous distribution of zero-point field fluctuations at the disc position (yz plane, dashed rectangles) is shown for different values of w (from top to bottom, 0.1, 0.5, 1 and 2 μm). b: Response of the Py disc vs. frequency for different values of w (in μm). Decreasing w allows going from the weak to the strong coupling regime.

6.5.2 Spin textures

Finally, we will simulate magnon-polariton dynamics in magnetic vortices. Spin textures such as domain walls, vortices and skyrmions are topological solitons that can be created, annihilated and displaced with minimal distortion, offering attractive possibilities for classical and quantum information processing [199]. Quantum states encoded in spin textures can be initialized, entangled and read out using superconducting or magnonic cavities [185, 186, 188, 190, 191]. Vortices are also appealing for implementing nanoscopic cavities, with the potential to readout individual spins[184] or to mediate strong interactions between spin qubits and superconducting microcircuits[198]. Magnetic vortices are easily stabilized in mesoscopic magnetic thin-film discs with lateral sizes between a few 100 nm up to several μm [200, 201]. Minimization of the magnetostatic energy yields an in-plane spiral distribution of spins with an out-of-plane vortex core. Cylindrical symmetry yields a number of magnetostatic (azimuthal and radial) modes whereas the central soliton-like vortex exhibits a peculiar translation mode [202]. This is the distinctive mode in which the vortex core gyrates around its equilibrium position. The sense of gyration is determined solely by the vortex's polarity, while the frequency is determined by the radius-to-thickness ratio. The experimental observation of strong coupling between cavity photons and the gyrotropic mode in magnetic vortices is still awaiting.

We chose a Py disc of radius 400 nm and thickness 150 nm in which a magnetic vortex is naturally stabilized resulting in a gyrotropic frequency of $f = 1.4$ GHz. The disc is coupled to the magnetic antinode of a cpw resonator, with central conductor cross-section of thickness 50 nm and width w. The corresponding distribution of $\boldsymbol{B}_{\mathrm{rms}}(\boldsymbol{r}_j)$ is calculated as described in J.2 and shown in the inset of Fig. 6.4a. Decreasing w has the effect of reducing the mode volume of the cavity. Consequently, the intensity of B_{rms} increases for the smallest linewidth of the central transmission line (upper panel in Fig. 6.4a). Figure 6.4b shows the response of the Py disc in frequency domain calculated using Mumax3-cQED (see J.3). Decreasing w allows reaching the strong vortex-photon regime as demonstrated by the opening of an anti-crossing for the minimum $w = 100$ nm, yielding a splitting of $2g/2\pi = 15$ MHz.

Chapter 7

Solving quantum strong long-range models

In Chap. 2 we showed that a model with a finite number of collective interactions can be described exactly by mean-field theory. We used this fact to show the equivalence between the generalized Dicke model (GDM) and an effective matter-only Hamiltonian, by showing that they were both equivalent to the same mean-field effective Hamiltonian. We have thus far only exploited this fact in the forward direction, to study the properties of different models of cavity QED materials by analyzing their corresponding effective Hamiltonians or solving the associated mean-field effective Hamiltonian (See Fig. 2.1). However, the equivalence works also in reverse and the implication is obvious: models with interactions that can be cast as finite sum of collective interactions can be solved through their equivalent mean-field effective Hamiltonian, provided that the corresponding variational problem is tractable.

In this chapter we will do precisely that, as the last application of the large-N theories developed in this thesis. We will start by introducing and defining long-range models, and we will identify several regimes of long-range interactions, among which are strong long-range interactions. Then, we will show that only certain strong long-range interactions can be expressed as a finite sum of collective interactions and thus solved. We will exploit this fact to formulate the general solution of those quantum strong-long range models as a variational problem and discuss its tractability in the different cases. Finally, we particularize the solution for Ising chains, and we will use it to study the ferromagnetic and unfrustrated antiferromagnetic Ising chains. As we will show, we use it to explore the effect that long-range and staggered interactions have on the order of quantum phase transitions and the appearance of tricritical points.

This chapter is based on Refs. [203, 204].

7.1 What are long-range systems?

Long-range systems are those in which two-body interactions decay as a power-law at large distances. They are ubiquitous in nature, with some examples given by dipolar, Coulomb or Wan-der-Walls interactions. Recent experimental advances in atomic, molecular and optical systems have lead to a resurgence of interest in long-range models [205–208]. In these experiments, the effective interactions between spins are often long-ranged and tunable, renewing the need for a comprehensive understanding of long-range systems. Although less studied than their short-ranged counterparts, there are already some rigorous and numerical results available [209–213]. Some equilibrium and dynamical properties have been discussed in comparison with short-range systems. Notable examples are the spontaneous breaking of continuous symmetries in one dimension [214], the existence of an area law of entanglement [215–218], the existence of Majorana modes [219], the spreading of correlations [220] and topological properties [221, 222].

In these examples, the phenomenology can be understood within a classification in terms of the range of interactions they exhibit. To fix notation and ideas, let us introduce this classification with the models considered in this chapter: quantum models in an N-site lattice with a Hamiltonian of the form

$$H = H_0 - \sum_{ij}^{N} J_{ij} C_i C_j \,, \tag{7.1}$$

where C_i is a local hermitian operator acting on site i. We consider a power-law decaying interactions $J_{ij} = \Gamma \tilde{J}(\mathbf{r}_{ij})/\tilde{N}$,

$$\tilde{J}(\mathbf{r}_{ij}) = \begin{cases} b & \text{if} \quad \mathbf{r}_{ij} = 0 \\ |\mathbf{r}_{ij}|^{-\alpha} & \text{otherwise} \end{cases} \tag{7.2}$$

and periodic boundary conditions (PBC). The distance between sites $\mathbf{r}_{ij}$ is then given by the nearest image convention. We will focus on the case of attractive or ferromagnetic interaction, so the interaction strength is $\Gamma > 0$. The extension to antiferromagnetic or repulsive models will be discussed later. b is a parameter that can be tuned to shift the spectrum of J. The decay rate α sets the range of the interactions. For $\alpha < d$, where d is the dimensionality of the lattice, the interactions decay slowly enough that the sum in the coupling term (7.1) depends superlinearly on N, breaking the extensivity of the model (See App.

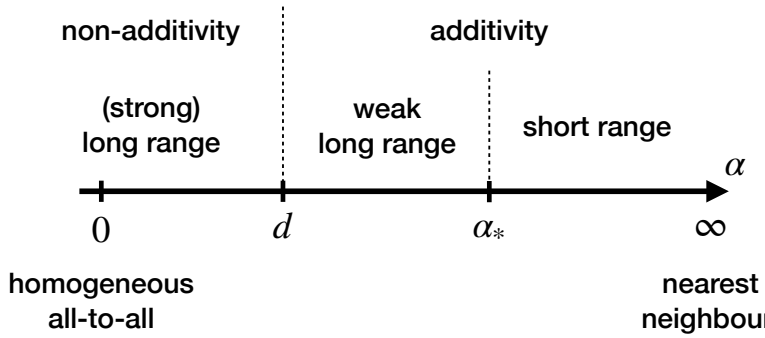

Figure 7.1: Classification of long-range models following reviews [209] and [212] valid for both the classical and quantum models.

K.1). Kac's renormalization factor $1/\tilde{N}$ restores extensivity, ensuring a well-defined thermodynamic limit. Here $\tilde{N} = \sum_i \tilde{J}_{ij}$, note that PBC make the model translation invariant and thus $\sum_i \tilde{J}_{ij}$ is independent of j. Regardless, the model remains non-additive in this regime. Non-additivity brings about particular statistical and dynamical phenomena that differ from the commonly studied short-range models, such as ensemble inequivalence, negative specific heat and quasistationary states [212]. Accordingly, the regime $\alpha < d$ is identified as *(strong) long-range*. In the regime $\alpha > d$, the model is naturally extensive, and Kac's renomarlization factor amounts to a rescaling of the interaction strength. Within the regime $\alpha > d$ two further subregimes can be identified: for $\alpha > \alpha_*$ the critical exponents of the model match those of the nearest-neighbours model ($\alpha \to \infty$), this is the *short-range regime*; for $d < \alpha < \alpha_*$ the model presents critical exponents that differ from the short-range ones, the effects of long-range interactions are felt but the model is additive, this is the *weak long-range regime* [209, 212]. For convenience, we summarize this classification in Fig. 7.1.

Strong long-range models are commonly disregarded in many analytical and numerical studies on the grounds of the ill-defined thermodynamic limit brought about by the non-extensivity. Kac's rescaling eliminates this barrier, making their study possible. For quantum models, seminal numerical studies solving the transverse-field Ising model in the strong long-range regime are found in Refs. [223, 224]. They confirm that in this regime the model is within the mean-field universality class. This is in agreement with the claim that mean field is exact for quantum spin models in the strong long-range regime [150] that generalizes similar findings in classical systems [225–228]. These works are crucial for the rigorous understanding of the physics of long-range systems. On the one hand, they provide an exact way to solve them, on the other hand, they provide a starting point for approximations that tackle the weak long-range regime.

This chapter provides a recipe to analytically solve, in the canonical ensemble, quantum strong long-range models. Therefore, it complements the work of Mori [150] by confirming that *in the strong long-range regime mean field is exact*. Besides, it extends the work of Campa and coworkers for classical strong long-range models to the quantum case [229].

7.2 General solution

7.2.1 Mapping strong long-range interactions to collective interactions

We showed in Sec. 2.3 that in the thermodynamic limit the equilibrium properties of a Hamiltonian with a finite number of collective interactions are exactly described by self-consistently trating each collective interaction as a mean-field [Cf. Eqs. (2.35) and (2.34)]. Here, we ellucidate in which cases an interaction of the form of Eq. (7.1) can be cast as a finite number of collective interactions:

$$-\sum_{ij}^{N} J_{ij} C_i C_j \xrightarrow{?} -\sum_{k}^{M} \frac{D_k}{N} \left(\sum_i \lambda_{ik} C_i \right)^2 , \tag{7.3}$$

with $\lim_{N\to\infty} M/N = 0$. We could further define $g_k C_k = N^{-1/2} \sum_i \lambda_{ik} C_i$ and $\Omega_k = 1/D_k$ to recover the effective Hamiltonian of Eq. (2.35).

If we start from an arbitrary extensive [1] model of the form of Eq. (7.1), the first step is to diagonalize the interaction matrix $J = \Lambda D \Lambda^T$, where D is a diagonal matrix, $D_{kp} \equiv D_k \delta_{kp}$. Note that Λ is orthogonal because J is symmetric. The matrix elements are then given by

$$J_{ij} = \sum_{k=0}^{N-1} \Lambda_{ik} D_k \Lambda_{jk} \tag{7.4}$$

Assuming that $J_{ij} > 0$, the smallest eigenvalue of J can always be set to zero by adjusting its diagonal elements, which we denote b. Fixing $b \neq 0$ introduces, generally, non-trivial diagonal terms of the form $\Gamma b/\tilde{N} C_i^2$. These can be shown to be negligible in the thermodynamic limit, so the freedom to set b remains (See App. K.2). For a general interaction matrix the number of non zero eigenvalues M scales with the size of the matrix N. Conveniently, it can be shown that for a model with power-law decaying interactions and PBC, such as the one considered here (7.1), the number of non-zero modes in the

[1] Meaning that Kac's prescription is used to ensure extensivity if the model is strong-long-ranged

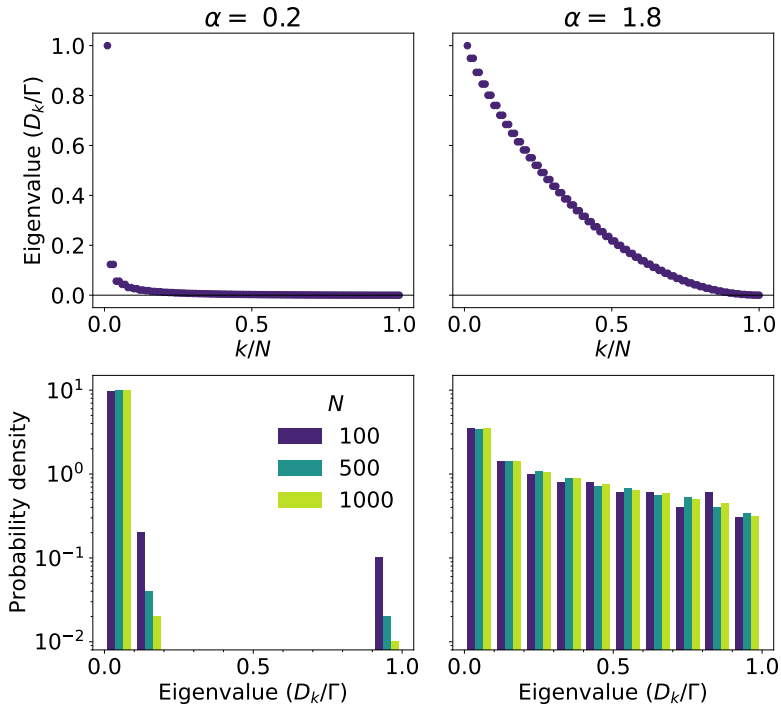

Figure 7.2: Analysis of the eigenvalues of the coupling matrix J (7.1) for $d = 1$. Left: For $\alpha = 0.2 < 1$, a plot of the eigenvalues for $N = 100$ on top and a histogram of the eigenvalues as a function of N on the bottom. Right: Same but for $\alpha = 1.8 > 1$.

thermodynamic limit ($N \to \infty$) depends on the decay rate of the interaction [229]. For a model in the strong long-range regime $\alpha < d$ only a small number of modes have a non zero eigenvalue, such that $\lim_{N\to\infty} M/N = 0$. This can be seen analytically in models with a translation-invariant interaction matrix, which can be diagonalized in Fourier space, obtaining a closed expression for its eigenvalues:

$$D(\mathbf{q}) = \frac{\Gamma}{\tilde{N}} \sum_{\mathbf{r}} \tilde{J}(\mathbf{r}) \exp[-i\mathbf{q}\mathbf{r}]\,. \tag{7.5}$$

Here $\mathbf{q}$ denotes any of the N reciprocal-space vectors in the first Brillouin zone and the sum runs over all lattice points. The large-N behaviour of $D(\mathbf{q})$ can then be estimated by replacing the sum with an integral [229].

Complementarily, we provide in Fig. 7.2 a graphical analysis of this phenomenon by showing the typical distribution of eigenvalues depending on α for $d = 1$ (the same behaviour is observed in other dimensions, not shown). This graphical analysis can be useful for models without translation invariance. In Fig. 7.2 we show that for a strong long-range model the eigenvalues bunch around zero as N increases, whereas they remain more uniformly distributed in

the weak long-range regime. This can be condensed into a criterion for determining whether arbitrary models are tractable: knowing that the eigenvalues of J are non-negative and bounded by construction, if only a vanishingly small fraction M/N are non-zero for $N \to \infty$, then their average will tend to zero and vice versa. Thus, for an arbitrary interaction matrix J, if

$$\lim_{N\to\infty} \frac{1}{N} \sum_{k=0}^{M-1} D_k = \lim_{N\to\infty} \frac{1}{N} \mathrm{Tr}(J) = 0 \tag{7.6}$$

the model is tractable, i.e., the number M of non-zero eigenvalues scales as $\lim_{N\to\infty} M/N = 0$. If we apply this criterion to translation invariant models we find $\lim_{N\to\infty} 1/N \sum_k D_k = \lim_{N\to\infty} \Gamma b/\tilde{N}$, which is zero for $\alpha < 1$ and non-zero otherwise (See Apps K).

Once it is established that a given model has a sufficiently small number of non-zero eigenvalues, one can sort them by decreasing value and truncate the sum in Eq. (7.4) to consider only the first M terms for which $D_k \neq 0$. This, together with the rescaled elements of the change of basis matrix, $\lambda_{ik} = \sqrt{N}\Lambda_{ik}$, completes the mapping of Eq. (7.3). Following Chap. 2, this reveals a duality between quantum strong long-range models described by Eq. (7.1) and a GDM with $H_\mathrm{m} = H_0$.

We have thus far defaulted to considering only ferromagnetic (attractive) models, as per the definition of the power-law decaying interactions of Eq. (7.2). However, now that the requisites for the mapping of Eq. (7.3) are clear, let us discuss its applicability to antiferromagnetic (repulsive) models [230, 231]. Frustrated antiferromagnetic long-range models cannot be tackled with our method. To see why, it suffices to look at Fig. 7.2, frustrated antiferromagnetic models arise from changing the global sign of the interaction in Eq. (7.1), which in turn results in a change of sign of the eigenvalues of the interaction matrix. For a general model, a shift to render the smallest eigenvalue equal to zero is not possible as it would require a b of the order of $\tilde{N}$, leading to non-vanishing diagonal elements even in the $N \to \infty$ limit. For a model in which $C_i^2 = 1$, the shift is possible, but after a shift to render the smallest eigenvalue equal to zero, we find that the majority of the eigenvalues are non-zero, regardless of the range of interactions α. In contrast, it is possible to define unfrustrated long-range antiferromagnetic models, $J_{ij} = \Gamma(-1)^{i+j}\tilde{J}(\boldsymbol{r}_{ij})/\tilde{N}$, as an extension of unfrustrated nearest-neighbour antiferromagnetic interactions [222, 232–240]. Here, the sign change is alternating, rather than global, effectively defining two sublattices in a square lattice. The interaction matrix defined this way shares the eigenvalues of its ferromagnetic counterpart and the corresponding model can thus be tackled with our method. This is clear by noting that such a model can be mapped to a ferromanetic model with a staggered longitudinal field by

a rotation of the spins corresponding to even (or odd) lattice sites. We study the long-range unfrustrated antiferromagnetic Ising chain in Sec. 7.4.

7.2.2 Free energy of the corresponding model with collective interactions

We have shown that a ferromagnetic strong long-range interaction is equivalent to a finite number of collective interactions. We will solve the resulting model following following Sec. 2.3, by solving the equivalent mean-field Hamiltonian

$$H^{\mathrm{MF}} = H_0 - \sum_{k=0}^{M-1} \frac{2\lambda_k^2}{N\Omega_k} \langle C_k \rangle C_k + \sum_{k=0}^{M-1} \frac{\lambda_k^2}{N\Omega_k} \langle C_k \rangle^2 \,, \tag{7.7}$$

with $\lambda_k C_k = \sum_i \lambda_{ik} C_i$. For convenience, we can reexpress the Hamiltonian in terms of the intensive variational variables $u_k = \lambda_k \langle C_k \rangle / (N\Omega_k)$, yielding

$$H^{\mathrm{MF}} = H_0 - \sum_{k=0}^{M-1} 2\lambda_k u_k C_k + \sum_{k=0}^{M-1} \Omega_k u_k^2 \,, \tag{7.8}$$

Defining $f_0[u_k] = -(N\beta)^{-1} \log Z_0[u_k]$ and

$$Z_0[u_k] = \mathrm{Tr}\left[e^{-\beta(H_0 - \sum_{ki} 2u_k \lambda_{ik} C_i)} \right] \,, \tag{7.9}$$

we obtain the variational free energy for the quantum strong long-range model as

$$f[u_k] = \sum_{k=0}^{M-1} \Omega_k u_k^2 + f_0[u_k] \,, \tag{7.10}$$

and we denote the true free energy as $f[\bar{u}_k] = \min_{\{u_k\}} f[u_k]$.

Computing the equilibrium properties of a quantum strong long-range model is thus reduced to a multivariate maximization problem. In the presence of several maxima, one has to find the global maximum. Finding global extrema of a multivariate scalar function is normally a complex task, without guarantee or provability of success, but in we show in Sec. 7.3, using the particular example of the ferromagnetic Ising chain, that this task is greatly facilitate for homogeneous or near-homogeneous systems.

In the next sections and in order to give concrete formulas, we particularize for the case of the ferromagnetic and unfrustrated antiferromagnetic Ising chains. However, the ideas presented here can be applied to other models. For instance, the Fermi-Hubbard model with long-range interactions could also be treated with our method. Here $H_0 = \sum_{ij} t_{ij} c_i^\dagger c_j$ and $C_i = c_i^\dagger c_i$ with

$\{c_i, c_j^\dagger\} = \delta_{ij}$ fermionic operators. Finally, we could consider for H_0 any model such that $H_0 + \sum_i \xi_i C_i$ is solvable, where the ξ_i are constants. In doing so, we could combine short-range models (as the one-dimensional short-range Ising model in transverse field, the XY model, and so on) with strong long-range interactions. This is because our method requires knowledge of the eigenstates of $H_0 + \sum_{k,i} 2\lambda_{ik} u_k C_i$, Cf. Eq. (7.9).

7.3 The ferromagnetic Ising chain

To showcase the effectiveness of the formalism presented in the previous sections, we particularize now to an Ising chain. First, we will obtain an expression for the free energy. This expression is valid both in the ferromagnetic and unfrustrated antiferromagnetic cases. Their difference will be encoded in the eigenvectors of the interaction matrix $\{\lambda_{ik}\}$. Then, we will particularize to the ferromagnetic case in the remainder of the seccion, computing the ground state phase diagram and correlations, before moving on to the more nuanced unfrustrated antiferromagnetic case in Sec. 7.4.

7.3.1 Free energy of a strong-long range Ising chain

The Ising chain Hamiltonian reads

$$H = -\omega_z \sum_i S_i^z - \omega_x \sum_i S_i^x - \sum_{ij} J_{ij} S_i^x S_j^x \,, \tag{7.11}$$

where ω_z and ω_x are, respectively, transverse and longitudinal fields and S_i^α are adimensionalized spin s operators obeying $[S_i^\alpha, S_j^\beta] = i\delta_{ij}\epsilon_{\alpha\beta\gamma} S_i^\gamma$ with $\epsilon_{\alpha\beta\gamma}$ the Levi-Civita symbol. Accordingly, we have

$$H_0 = -\omega_z \sum_i S_i^z - \omega_x \sum_i S_i^x \,, \tag{7.12}$$

$$C_i = S_i^x \,, \tag{7.13}$$

and so

$$Z_0[u_k] = \prod_i^N \mathrm{Tr}_i \left[e^{-\beta H_i} \right] \,, \tag{7.14}$$

with

$$H_i = -\omega_z S_i^z - (\omega_x + 2 \sum_{k=0}^{M-1} \lambda_{ik} u_k) S_i^x \,. \tag{7.15}$$

This Hamiltonian can be diagonalized with a rotation of the spins to yield $H_i = 2\varepsilon_i S_i^{z\prime}$ with

$$2\varepsilon_i = \sqrt{\omega_z^2 + \left(\omega_x + 2\sum_{k=0}^{M-1} \lambda_{ik} u_k\right)^2}\,, \tag{7.16}$$

and the partition function

$$Z_0[u_k] = \prod_i^N \sum_{m=-s}^{s} e^{-\beta 2\varepsilon_i m} = \prod_i^N \frac{\sinh((2s+1)\beta\varepsilon_i)}{\sinh(\beta\varepsilon_i)}\,. \tag{7.17}$$

With this, in order to solve the model, we have to minimize the variational free energy

$$f[u_k] = \sum_{k=0}^{M-1} \Omega_k u_k^2 - \frac{1}{N\beta}\sum_i^N \ln\left[\frac{\sinh((2s+1)\beta\varepsilon_i)}{\sinh(\beta\varepsilon_i)}\right]. \tag{7.18}$$

The condition of vanishing gradient results in the self consistent condition

$$\Omega_k \bar{u}_k = \frac{s}{N}\sum_i^N \frac{\lambda_{ik}\left(\omega_x + 2\sum_{k=0}^{M-1}\lambda_{ik}\bar{u}_k\right)}{2\bar{\varepsilon}_i} B_s(2s\beta\bar{\varepsilon}_i)\,, \tag{7.19}$$

for the extrema $\{u_k\}$, with $\bar{\varepsilon}_i = \varepsilon_i[\bar{u}_k]$, and where $B_s(x)$ are the Brillouin functions [241, Chap. 11]. For reference, note that $B_{1/2}(x) = \tanh(x)$ and that rest of the family of functions present a qualitatively similar behaviour, being odd functions and having the limit $\lim_{x\to\infty} B_s(x) = 1$.

7.3.2 Phase diagram

The remainder of the section is specific to the ferromagnetic case, since we will use the particular form of the eigenvectors $\{\lambda_{ik}\}$ of the interaction matrix J to obtain our results. Additionally, we consider here only the case of zero longitudinal field, $\omega_x = 0$. Otherwise, the spin-flip symmetry of the model is explicitely broken and no quantum phase transition occurs.

In the case of a homogeneous H_0, as is the case for the Ising chain, we show in Apps. L that the global minimum is homogeneous in the lattice. In terms of the minimization variables, homogeneity implies that $u_0 = u \neq 0$ and $u_{k\neq 0} = 0$, see App. L. This means that only the zero mode, which is constant on the lattice for ferromagnetic interactions, $\lambda_{i0} = 1\ \forall i$, is relevant in determining the thermodynamic properties of the model. In turn, one finds that the critical properties of the model are independent of the decay rate of interactions α, since the latter only determines the degree to which higher-frequency modes

($k > 0$) have to be considered in the diagonalization of J. In more intuitive terms, homogeneity is revealed in the fact that $2\epsilon_i = 2\epsilon = \sqrt{\omega_z^2 + 4u^2}$, $\forall i$. In any case, the multivariate maximization problem simplifies to a single variable maximization problem $\min_u f(u)$, with

$$f(u) = \frac{u^2}{\Gamma} - \frac{1}{\beta} \ln \left[\frac{\sinh((2s+1)\beta\varepsilon)}{\sinh(\beta\varepsilon)} \right] . \tag{7.20}$$

Note that $\Omega_0 = 1/\Gamma$. Taking the derivative of f with respect to u yields the condition

$$\bar{u}\bar{\epsilon} = s\Gamma\bar{u}B_s\left(2s\beta\bar{\varepsilon}\right) , \tag{7.21}$$

which is manifestly α-independent. Note that $\bar{\epsilon} = \epsilon(\bar{u})$. For $\Gamma < \omega_z/(2s)$, $\bar{u} = 0$ is the only solution. For $\Gamma > \omega_z/(2s)$, the solution depends on β, for $\beta > \beta_c$, with β_c given by

$$\omega_z = 2s\Gamma B_s\left(s\beta_c\omega_z\right) , \tag{7.22}$$

there is another solution to Eq. (7.21) given by

$$\bar{\epsilon} = s\Gamma B_s\left(2s\beta\bar{\varepsilon}\right) . \tag{7.23}$$

The solution $\bar{u} = 0$ corresponds to a maximum in the regime where it is the only solution and becomes a minimum for $\beta > \beta_c$ with the maximum given by the other solution [17]. This marks the paramagnetic-ferromagnetic transition point. This is the well-known mean-field critical behaviour of the standard (single-mode homogeneous coupling) Dicke model [17, 112], which is shared by the Lipkin-Meshkov-Glick (LMG) model (all-to-all homogeneous Ising) [242, 243] and, as we just showed, is also universal to all strong-long-range Ising models and their associated GDMs, i.e., we have demonstrated that the critical point is independent of α. This can be visualized in Fig. 7.3 where the vertical line marks the phase transition, located at the maximum for the susceptibility (see below), and is independent of α. Besides, in Fig. 7.4 we compute the critical line, in red, in the $(\Gamma, 1/\beta)$-plane and compare it against the simulations in Ref. [224]. We find excellent agreement with their numerical results and showcase that the critical point is independent of α and coincides with the mean-field value.

In terms of observables, we focus now on the calculation of the magnetization. In order to do so from the partition function, we introduce a perturbative longitudinal field to the Hamiltonian, such that $H \to H - \sum_i h_i S_i^x$. Then one can compute the order parameter $\beta\langle S_i^x\rangle = \partial \ln Z/\partial h_i$ and the susceptibilities [2]

$$\chi_{ij} = \lim_{\{h_n\}\to 0} \frac{\partial\langle S_i^x\rangle}{\partial h_j} . \tag{7.24}$$

[2]The magnetization must be kept $\{h_n\}$-dependent in order to compute the susceptibility, the magnetization of the $\{h_n\}$-independent model is defined as $\beta\langle S_i^x\rangle = \lim_{\{h_n\}\to 0} \partial \ln Z/\partial h_i$

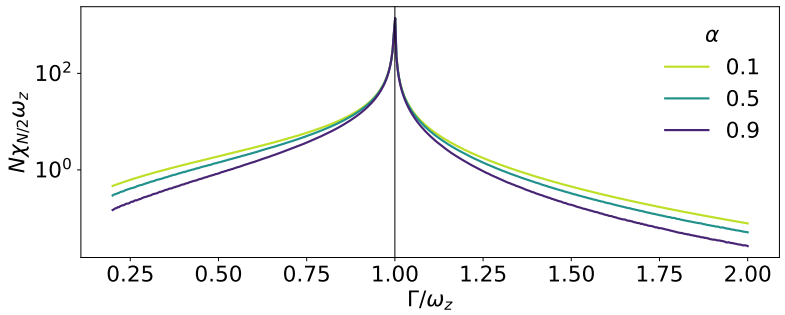

Figure 7.3: Susceptibility for maximally separated spins $\chi_{N/2}$, for the strong long-range ferromagnetic Ising chain in transverse field, as a function of the interaction strength Γ. The parameters used were $\omega_z = 1$, $\beta\omega_z = 10$, $s = 1/2$, and $N = 100$.

The introduction of longitudinal fields leads to the substitution $2\sum_k \lambda_{ik} u_k \to 2\sum_k \lambda_{ik} u_k + h_i$ in Eq. (7.15). The magnetization is then

$$\langle S_i^x \rangle = sB_s\left(2s\beta\bar{\varepsilon}\right) \frac{2\sum_{k=0}^{M-1} \lambda_{ik}\bar{u}_k + h_i}{2\epsilon_i[\bar{u}_k]} \,. \tag{7.25}$$

Here, the magnetization appears as a function of the maximization variables $\{\bar{u}_k\}$. However, it is possible to show that $\sum_k \lambda_{ik}\bar{u}_k = \sum_j J_{ij}\langle S_j^x\rangle$, rewriting Eq. (7.25) as a self-consistent equation on $\{\langle\sigma_i^x\rangle\}$ which is precisely the self-consistent equation that arises in a standard mean-field solution of the original model of Eq. (7.11). Our exact analytical method is thus equivalent to standard mean-field theory. Recall that our method is based on the equilibrium theory of Chap. 2 where we showed that a finite number of collective interactions can be treated exactly with a mean-field theory of each collective interaction. Following that, in this chapter we have expressed strong long-range interactions as a finite sum of collective interactions and solved those via their equivalent mean-field Hamiltonian. In contrast, standard mean field theory would ammout to applying a mean-field decoupling directly to Eq. (7.11). Anecdotally, our theory evidences that the self-consistent solution from standard mean-field theory is redundant, in the sense that the solution involves a transcendental equation of N variables (the magnetizations $\{\langle S_i^x\rangle\}$), whereas the same problem can be rewritten in terms of M variables (the $\{u_k\}$), with $\lim_{N\to\infty} M/N = 0$.

7.3.3 Correlations

Our next result concerns the decay of correlations. In weak long-range and short-range systems correlations decay exponentially at long distances. Only at the critical point do these systems exhibit power law decay of correlations [244–246]. Conversely, strong long-range systems exhibit power law decay of

correlations at all distances. In the absence of exponential decay, the concept of correlation length cannot be straightforwardly defined, although there have been some attempts [247]. Here we study the susceptibility χ_{ij} (7.24) as a measure of correlations between spins, as it is proportional to the Kubo correlator [248, Chap. 4]

$$\chi_{ij} = \beta \left(\frac{1}{Z} \int_0^\beta \mathrm{Tr} \left(e^{-(\beta-s)H} S_i^x e^{-sH} S_j^x \right) - \langle S_i^x \rangle \langle S_j^x \rangle \right) . \tag{7.26}$$

The susceptibility can be computed analytically from Eq. (7.24) [249, Chap. 6] or numerically otherwise. First, from Eqs. (7.19) and (7.25) we have

$$\Omega_k \bar{u}_k = \frac{1}{N} \sum_i^N \langle S_i^x \rangle \lambda_{ik} \tag{7.27}$$

and thus

$$\frac{\partial \bar{u}_k}{\partial h_i} = \frac{1}{N} \sum_i^N \chi_{ij} \frac{\lambda_{ik}}{\Omega_k} \tag{7.28}$$

Then from Eq. (7.24) we have

$$\chi_{ij} = Y_i \left(\delta_{ij} + 2 \sum_{k=0}^{M-1} \lambda_{ik} \frac{\partial \bar{u}_k}{\partial h_j} \right) , \tag{7.29}$$

with

$$\begin{aligned} Y_i = \frac{s}{2\bar{\varepsilon}_i^2} \Bigg[& \bar{\varepsilon}_i B_s(2s\beta\bar{\varepsilon}) \\ & + \left(2 \sum_{k=0}^{M-1} \lambda_{ik} \bar{u}_k + h_i + \omega_x \right)^2 \left(\frac{s\beta}{2} B_s'(2s\beta\bar{\varepsilon}) - \frac{1}{4\bar{\varepsilon}_i} B_s(2s\beta\bar{\varepsilon}) \right) \Bigg] . \end{aligned} \tag{7.30}$$

From Eqs. (7.28) and (7.29) and after some manipulation and taking the limit $\{h_i\} \to 0$, we get

$$\chi_{ij} = Y_i \left(\delta_{ij} + 2 \sum_r^N J_{ir} \chi_{rj} \right) , \tag{7.31}$$

where Y_i now stands for the $\{h_i\} \to 0$ limit of Eq. (7.30). In fact, as we proved that in the ferromagnetic Ising chain the global minimum is homogeneous, $Y_i = Y$ also is. Accordingly, Eq. (7.31) can be solved with a Fourier transformation. Defining

$$\chi_{ij} = \frac{1}{N} \sum_{k=0}^{N-1} \lambda_{ik} \chi_k \lambda_{jk} \tag{7.32}$$

we find

$$\chi_k = \frac{\Omega_k Y}{\Omega_k - 2Y}\,, \tag{7.33}$$

and finally

$$\chi_{ij} = Y\delta_{ij} + \frac{1}{N}\sum_{k=0}^{M-1} \lambda_{ij}\,(\chi_k - Y)\,\lambda_{jk}\,, \tag{7.34}$$

This expression evidences that $\chi_{i\neq j}$ goes to zero in the thermodynamic limit with a speed that is determined by the ratio M/N and thus ultimately by α (by its relation to d).

For a numerical calculation, the introduction of a site-dependent field h_i breaks the homogeneity of the model and the multivariate minimization of f is carried out numerically, $\langle S_i^x \rangle$ is then computed according to Eq. (7.25) and χ_{ij} is computed as a finite difference. We have verified that both methods yield the same results for the current model. This is noteworthy because the numerical calculation relies on a multivariate optimization which could, a priori, converge to an incorrect result corresponding to a local maxima. We believe the success is due to the fact that the only deviation from homogeneity stems from the introduction of a perturbative field and is thus small. Hence, although the optimization is strictly multivariate, the landscape does not differ much from the univariate case.

Despite the fact that the analytical results have been obtained under the assumption that we worked in the thermodynamic limit $N \to \infty$. The computation of the susceptibility, whether numerically or according to Eq. (7.34), requires us to fix a finite value of N and M. For each value of α and N, we increase the value of M until convergence is reached while enforcing the constraint that $\lim_{N\to\infty} M(N)/N = 0$.

Because the model is translation invariant, the susceptibility is only a function of distance, allowing us to define $\chi_{ii+r} \equiv \chi_r$. In Fig. 7.3 we study the susceptibility at a fixed distance: we plot the half-chain susceptibility $\chi_{N/2}$ as a function of the interaction strength Γ for different decay rates $\alpha < 1$ at zero temperature $\beta \to \infty$. The half-chain susceptibility displays α-independent divergence at the critical point and some dependence on α away from it. Intuitively, the correlations remain larger for longer-ranged models. We now turn to the spatial dependence of the susceptibility. In the absence of a correlation length, we study the susceptibility decay rate α_χ defined from the relation $\chi_r = A \cdot r^{-\alpha_\chi}$. Interestingly, one finds that α_χ depends linearly on α, $\alpha_\chi = a\alpha + b$. In Fig. 7.4 we plot the slope a as a function of interaction strength Γ and inverse temperature $1/\beta$. Close to the critical line, the susceptibility decay rate α_χ becomes independent of the interaction decay rate α, in agreement with Fig. 7.3. As one moves further from the critical line, $a \to 1$, varying

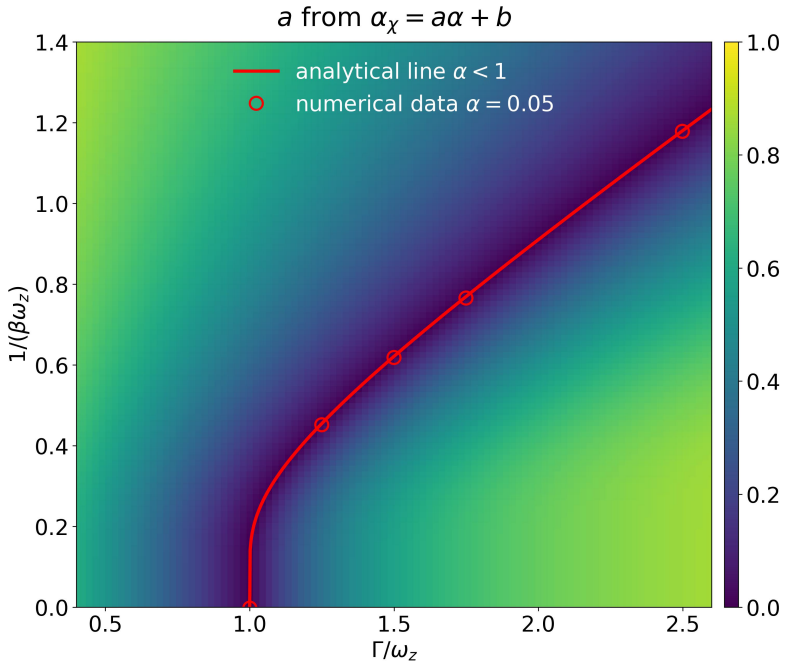

Figure 7.4: Phase diagram of the strong long-range Ising chain in transverse field. The red line corresponds to the universal critical line for $\alpha < 1$. The numerical data is taken from Ref. [224]. The colormap shows the slope of the linear dependence $\alpha_\chi = a\alpha + b$, where α_χ is susceptibility decay rate and α is the rate of decay of interactions, computed with parameters $\omega_z = 1$ and $N = 100$.

continuously from 0 to 1 in intermediate regions. In all cases we find $b \approx 0$. Similar algebraic decays have been described previously for the connected correlator $\langle S_1^x S_r^x \rangle - \langle S_1^x \rangle \langle S_r^x \rangle$ in the paramagnetic phase [244]. There, a linear relation between α_χ and α is also reported. Here we extend those findings to the full phase diagram.

7.4 The unfrustrated antiferromagnetic Ising chain

Long-range interactions have been shown to induce first-order phase transitions in classical dipolar gases [250] and (quantum) Bose-Hubbard [251, 252] and XX [253] models. To elucidate the effect of long-range interactions on the order of phase transitions, it is convenient to construct a minimal model. The trivial long-range generalization of the TFIC is known to feature only a second-order phase transition [223, 254, 255], as we showed in our own analytical study of the ferromagnetic case in Sec. 7.3. In fact, there is no phase transition at all for antiferromagnetic interactions at extremely long

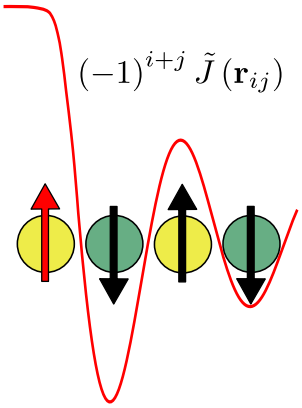

Figure 7.5: Sketch of long-range unfrustrated antiferromagnetic interactions between a given spin (in red) and its first three neighboring spins. The interactions are ferromagnetic between spins belonging to the same sublattice and antiferromagnetic between spins belonging to different sublattices.

ranges. At the same time, it has been shown that the Ising model with antiferromagnetic nearest-neighbor interactions and ferromagnetic next-nearest-neighbor interactions presents a tricritical point (TP) where the critical line changes from first to second order [256]. To shed more light on this issue, in this section we generalize the antiferromagnetic Ising chain to feature tunable-range *unfrustrated* antiferromagnetic interactions and study its ground-state phase diagram analytically in the strong long-range regime using the technique that we have presented in this chapter and then in the full range of interactions using a variational quantum Monte Carlo method.

Again, we consider the Hamiltonian of the Ising chain (7.11), but now with $J_{ij} = (-1)^{i+j}\,\Gamma\tilde{J}(\mathbf{r}_{ij})/\tilde{N}$, with $\tilde{J}(\mathbf{r}_{ij})$ still given by Eq. (7.2). The alternating sign makes the interactions antiferromagnetic when spins are separated by an odd number of lattice parameters and ferromagnetic when spins are separated by an even number of parameters, see Fig. 7.5. In the limit $\alpha \to \infty$, the model corresponds to the nearest-neighbor Ising chain with transverse and longitudinal fields. The tunable-range staggered interactions that we consider here are a generalization of the antiferromagnetic nearest-neighbor interactions in unfrustrated lattices. The alternating sign prevents frustration and allows for the formation of two sublattices, as sketched in Fig. 7.5. For vanishing fields, the ground state is the antiferromagnetic configuration, with the spins fully polarized along the x axis in alternating directions for even and odd spins. Staggered tunable-range interactions have been studied previously for the Heisenberg model [222, 232–240].

7.4.1 Ground-state phase diagram

The free energy of the model is still given by Eq. (7.18). The difference with the ferromagnetic case lies in the $\{\lambda_{ik}\}$ and it manifests itself in the fact that the global minimum is no longer homogeneous in the lattice. It is instead antihomogeneous, or staggered. Nevertheless, just like homogeneity implied a univariate, and thus tractable, free energy in the ferromangetic case so does antihomogeneity in the antiferromagnetic case. For $\alpha = 0$ (homogeneous all-to-all couplings which are ferromagnetic or antiferromagnetic depending on the distance between the spins) the problem naturally becomes univariate, as there is only one non-zero eigenvalue of the interaction matrix J, so $M = 1$. This is equivalent to setting $u_{k\neq 0} = 0$, with u_0 corresponding to the largest eigenvalue: $D_0 = \max\{D_k\} = \Gamma$ and $\lambda_{i0} = (-1)^i$. Additionally, we find that this solution with $u_{k\neq 0} = 0$ is the global minimum also for $0 \neq \alpha < 1$. This can be shown analytically for $\omega_x = 0$ (See. Appendix L) and has been verified numerically otherwise. In more intuitive terms, antihomogeneity is revealed in the fact that $2\epsilon_i = 2\epsilon_{(-1)^i}$ with

$$2\varepsilon_\pm = \sqrt{\omega_z^2 + (\omega_x \pm 2u)^2}\,. \tag{7.35}$$

With this, computing the canonical partition function has been reduced to a univariate minimization of

$$f(u) = \frac{u^2}{\Gamma} - \frac{1}{2\beta}\ln\left[\frac{\sinh((2s+1)\beta\varepsilon_+)}{\sinh(\beta\varepsilon_+)}\right] - \frac{1}{2\beta}\ln\left[\frac{\sinh((2s+1)\beta\varepsilon_-)}{\sinh(\beta\varepsilon_-)}\right] \tag{7.36}$$

in terms of $u \equiv u_0$ for all $\alpha < 1$, which can be tackled analytically or numerically.

To reduce the number of free parameters of the model, we work in the zero temperature limit. We define the variational ground-state energy as the zero-temperature limit of the variational free energy $e_0(u) = \lim_{\beta\to\infty} f(u)$, such that

$$e_0(u) = \frac{u^2}{\Gamma} - s\left(\varepsilon_+(u) + \varepsilon_-(u)\right)\,. \tag{7.37}$$

Following the same procedure that we used to obtain Eq. (7.25) in the ferromagnetic case, it can be shown that now the global minimum $\bar{u}$ is proportional to the staggered magnetization

$$\bar{m}_\mathrm{s} = \frac{1}{N}\sum_{i=1}^{N}(-1)^i\langle S_i^x\rangle = \frac{\bar{u}}{\Gamma}\,. \tag{7.38}$$

The staggered magnetization is the order parameter of unfrustrated antiferromagnetic models. It is zero in the paramagnetic phase and it measures how close the ground state is to a perfect antiferromagnetic configuration in the antiferromagnetic phase. Figure 7.6(a) shows the phase diagram of the model.

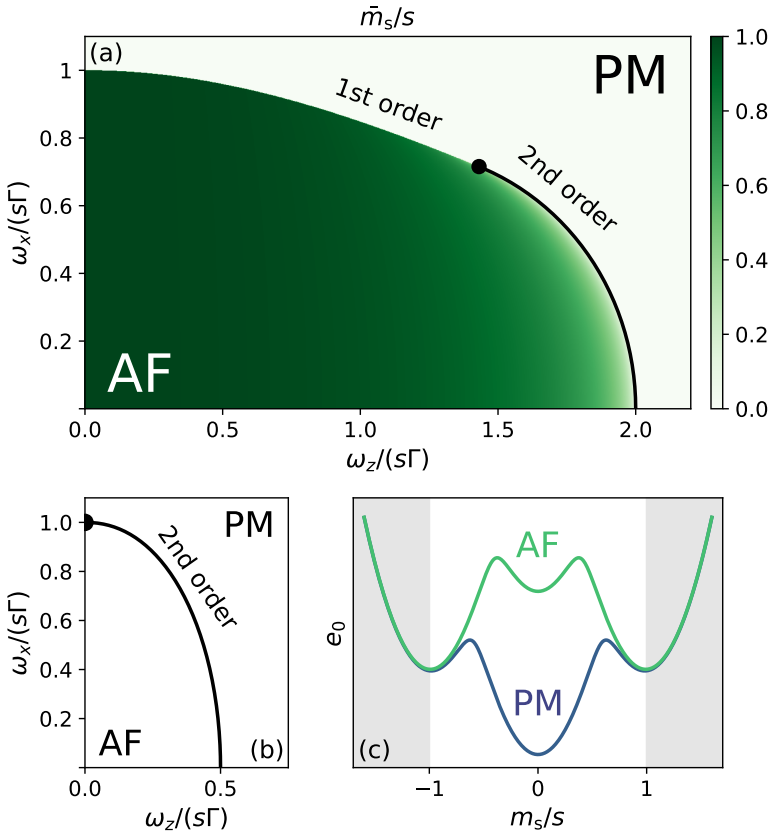

Figure 7.6: (a) Ground-state phase diagram of the strong long-range unfrustratrated antiferromagnetic Ising chain for $\alpha < 1$ as a function of the longitudinal ω_x and transverse ω_z fields. The black line marks the second order portion of the critical line. The black dot marks the tricritical point. (b) Sketch of the ground-state phase diagram of the nearest-neighbors antiferromagnetic Ising chain. (c) Variational free energy (7.37) in the antiferromagnetic, $(\omega_x, \omega_z) = (0.8, 0.2)s\Gamma$, and paramagnetic, $(\omega_x, \omega_z) = (1.2, 0.2)s\Gamma$, phases. Grey shaded areas are not valid values of the staggered magnetization, but are included for improved visualization of the energy landscape.

The staggered magnetization is obtained from $\bar{u}$, by minimizing e_0, and plotted as a function of the longitudinal and transverse fields. The model exhibits a quantum phase transition (QPT) between an antiferromagnetic phase and a paramagnetic phase. The nature of the phase transition changes along the critical line from a second- to a first-order QPT. The change can be described analytically by applying the Landau theory of phase transitions to a series expansion of $e_0(m_s)$, with $m_s = u/\Gamma$ the variational staggered magnetization. By studying the change of sign of the expansion coefficients we obtain the

tricritical point

$$\omega_{x,\mathrm{tp}} = s\Gamma\frac{8}{5\sqrt{5}}\,, \tag{7.39}$$

$$\omega_{z,\mathrm{tp}} = s\Gamma\frac{16}{5\sqrt{5}}\,, \tag{7.40}$$

and the equation for the second-order portion of the critical line

$$4s^2\Gamma^2\omega_z^4 = \left(\omega_z^2+\omega_x^2\right)^3\,, \tag{7.41}$$

when $|\omega_z| > 2|\omega_x|$. The first-order critical condition cannot be obtained from this analysis because the global minima corresponding to the antiferromagnetic configuration fall outside of the radius of analyticity of the series expansion of $e_0(m_\mathrm{s})$. Nevertheless, having identified the second-order portion, the rest of the critical line is of first order by exclusion. We verify this graphically in Fig. 7.6(c) where we show the landscape of minima of e_0 for different values of ω_x when $\omega_z/(s\Gamma) = 0.2$. For $\omega_x/(s\Gamma) = 0.8$ there exists a local minimum at $m_\mathrm{s} = 0$, corresponding to the paramagnetic state, and two degenerate global minima at $m_\mathrm{s} \approx \pm 1$, corresponding to the symmetric antiferromagnetic ground states. For $\omega_x/(s\Gamma) = 1.2$, the minimum at $m_\mathrm{s} = 0$ has become the global minimum, following a first-order phase transition between the antiferromagnetic and paramagnetic phases. The same behavior is observed for any $\omega_z < \omega_{z,\mathrm{tp}}$.

We have thus found the existence of a first-order QPT on a finite portion of the critical line. We emphasize that this is valid for all strong-long range models, $\alpha < 1$. This constitutes a qualitative difference with respect to the nearest-neighbor limit, $\alpha \to \infty$, of the model, in which the QPT is second-order along the full critical line except for the point where $\omega_z = 0$, when the model is classical [230, 257]. This is sketched in Fig. 7.6(b) for comparison. It is worth noting that there is some evidence that the phase transition could be of mixed order [258, 259] around the classical point in the nearest-neighbor limit, but not purely of first order like we have just described for the strong long-range regime [260].

For $\alpha = 0$ it is possible to do a classical analysis of the model that predicts the same phase diagram that we just described, with distinct finite regions of first and second order phase transitions. See App. M for more details. This illustrates that a classical analysis can serve as a prospecting tool for spin models with all-to-all interactions. It offers an alternative perspective on the phase transition based on the magnetizations of each sublattice rather than the order parameter (the staggered magnetization in this case). In any case, it is not a replacement for an exact solution due to the fact that its application is limited to $\alpha = 0$ and that it does not allow for the computation of susceptibilities.

7.4.2 Correlations

Correlations can be computed as in the ferromagnetic case up until Eq. (7.31). However, now, in the unfrustrated antiferromagnetic case, $Y_i = Y_{(-1)^i}$ is antihomogeneous. Thus, we cannot solve the system of equations that defines the real space correlations in Eq. (7.31) with a Fourier transform. Instead, we can write a matrix equation,

$$\sum_{r=1}^{N} \left(\delta_{ir} - 2Y_i J_{ir}\right) \chi_{rj} = Y_i \delta_{ij} \,, \tag{7.42}$$

which allows us to obtain the susceptibilities as

$$\chi_{ij} = (A^{-1})_{ij} Y_j \,, \tag{7.43}$$

where the matrix is defined by $A_{ij} = \delta_{ij} - 2Y_i J_{ij}$ and $Y_i = s\omega_z^2/(8\bar{\varepsilon}_i)$ with $\bar{\varepsilon}_i = \varepsilon_{(-1)^i}$ as defined in Eq. (7.35).

In Figs. 7.7(a) and (b) we show the behavior of the susceptibility matrix χ_{ij} for $\alpha = 0$ in the two phases of the model. Although Eq. (7.43) has been obtained in the thermodynamic limit ($N \to \infty$), evaluating it requires that we fix a finite value of N. We set $N = 8$ and mask out the diagonal elements to better display the structure of the correlation matrix. For $\alpha = 0$, in the antiferromagnetic phase the correlations show an alternating pattern with intrasublattice correlations being positive and intersublattice correlations being negative. In addition, the intrasublattice correlations of the sublattice that is ordered with the longitudinal field (even sites) are weaker than the intrasublattice correlations of the sublattice that is ordered against the field (odd sites). This effect accentuates with increasing longitudinal field, to the point that the correlations almost vanish for the sublattice ordered with the field for large longitudinal field. The spins of the sublattice that is ordered with the longitudinal field behave increasingly as paramagnetic free spins despite the model still being in an antiferromagnetic state. In the paramagnetic phase the two sublattices become equally magnetized along the combined external field and the correlation matrix recovers a perfectly alternating pattern that matches the staggered interactions, with intra- and intersublattice correlations being of equal magnitude and opposite sign.

Setting $\alpha \neq 0$ introduces spatial dependence in the correlations in both phases. The structure of the correlation matrix remains the same but the elements are modulated by the distance between the corresponding spins. The correlations exhibit a power-law decay with distance within each of the possible families: intersublattice, even intrasublattice and odd intrasublattice. This is the case regardless of the proximity to the critical point. This behaviour

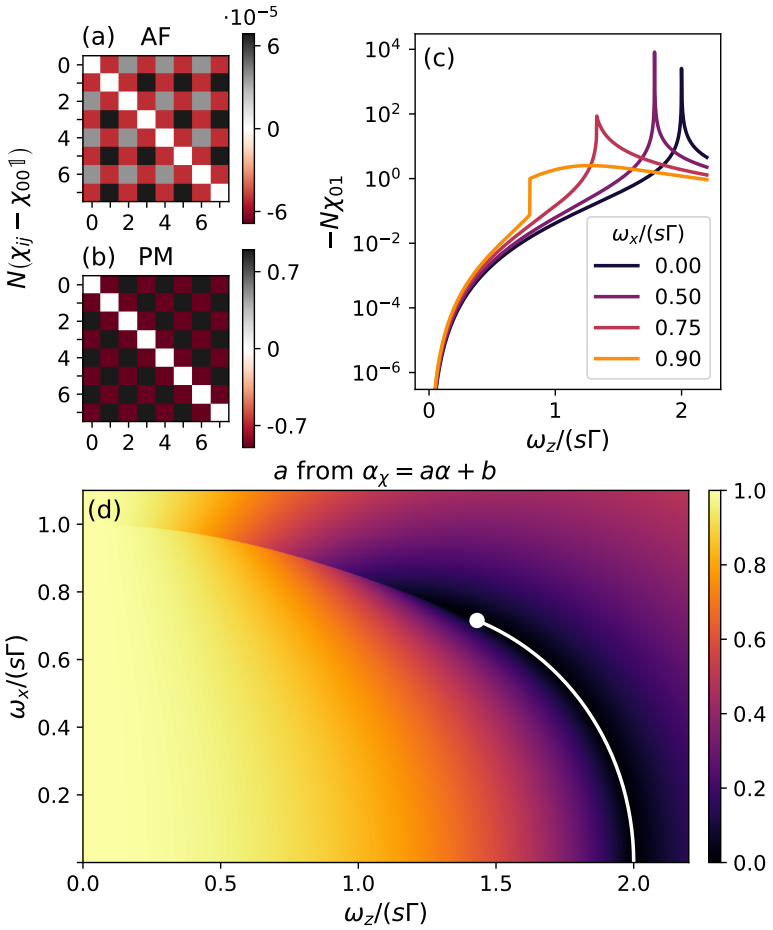

Figure 7.7: (a) Susceptibility matrix for $\alpha = 0$ in the antiferromagnetic phase, $(\omega_x, \omega_z) = (0.1, 0.2)s\Gamma$. (b) Susceptibility matrix for $\alpha = 0$ in the paramagnetic phase, $(\omega_x, \omega_z) = (1, 2)s\Gamma$. Both have been obtained for $N = 8$ and autocorrelations have not been depicted. (c) Evolution of intersublattice correlations across the phase diagram, computed using $N = 100$ and $\alpha = 0$. (d) Slope of the linear relation $\alpha_\chi = a\alpha + b$, computed using $N = 100$. It is independent of the element from the susceptibility matrix used. The white line marks the second order portion of the critical line. The white dot marks the tricritical point.

is typical of strong long-range systems and contrasts with weak long-range and short range systems where power-law decay is only present at the critical point [244–246], it was also present in the ferromagnetic case studied in Sec. 7.3. Since the model is translation invariant, we can define $\chi_{r,01} \equiv \chi_{0\,2r+1}$, $\chi_{r,00} \equiv \chi_{0\,2r}$ and $\chi_{r,11} \equiv \chi_{1\,2r+1}$ for the intersublattice, even intrasublattice and odd intrasublattice correlations, they all follow a power-law decay: $\chi_r \propto r^{-\alpha_\chi}$ with the same exponent α_χ. In the paramagnetic phase $\chi_{r,00} = \chi_{r,11}$. The rate

of decay of correlations depends linearly on the rate of decay of interactions, i.e., $\alpha_\chi = a\alpha + b$. Fig. 7.7 (b) shows the slope a across the phase diagram. The numerical fit of the relation also shows that $b \approx 0$ in all cases, which is consistent with the fact that the model must become distance independent for $\alpha = 0$. Close to the second order critical line α_χ becomes independent of α with $a = 0$. This is consistent with the behavior described in Sec. 7.3 for the strong long-range ferromagnetic Ising model. In contrast, the first order phase transition is marked by a discontinuity in the slope of the linear dependence, between two non-zero values.

The effect of the first and second order phase transitions is also apparent in the behavior of single correlation matrix elements across the phase diagram. Figure 7.7(c) shows the value of a correlation matrix element as a function of the longitudinal and transverse fields, for $\alpha = 0$. They exhibit a divergence at the second-order phase transition and a finite discontinuity at the first-order phase transition. The behavior is analogous for any matrix element and any value of α.

7.4.3 Numerical simulations: bridging the gap to the nearest-neighbor limit

Having established a significant difference between the phase diagram of the strong long-range and nearest-neighbors models, it is natural to wonder how this difference is interpolated for arbitrary values of the range of interactions α. Since only the strong long-range regime is analytically tractable, in this section we resort to zero-temperature variational quantum Monte Carlo (qMC) [261] simulations with a visual transformer (ViT) [262–264] ansatz for finite system sizes to study the model in the full range of interactions. In this section we show the results obtained for spins with $s = 1/2$ using the latter architecture, given its recent success in describing spin-1/2 chains with long-range interactions [255]. Details on the particular implementation used here can be found in Ref. [204].

Using this technique we obtain the ground state of finite size chains with periodic boundary conditions along the whole parameter space (ω_x ω_z α). In order to study how the phase transition evolves with α, we choose as order parameter the squared staggered magnetization m_s^2 [cf. Eq. (7.38)]. This choice is justified by the fact that, in finite size chains, the symmetry of the ground state is not broken and the staggered magnetization is zero throughout the whole parameter space. The squared magnetization, on the contrary, exhibits all the features related to first and second order phase transitions and allows us to carry out this numerical characterization.

In Fig. 7.8 we observe how $\langle m_s^2 \rangle$ behaves for different slices of the phase diagram (cf. Fig. 7.6) as a function of different values of α for a fixed chain size of $N = 50$. In panels (a), (b) and (c), which correspond to vertical slices (fixed transverse field), we see that for certain values of α the nature of the phase transition evolves from first order to second order as the transverse field ω_z increases. Panel (a), corresponding to $\omega_z/(s\Gamma) = 0.2$, merits special attention. It shows that the discontinuity characteristic of first order phase transitions is clearly present up to $\alpha = 2.5$ (See Ref. [204] for further confirmation). In panels (b) and (c) we see how this transition becomes of second order, with a continuous change of the order parameter at the critical point. If instead of comparing a given value of α across panels we focus on any given panel, (a), (b) or (c), we observe that the transition develops a discontinuity as α is lowered. In all cases the transition is clearly discontinuous for $\alpha \leq 1$, in agreement with the analytical predictions.

It is interesting to note that analytical results of Sec. 7.4.1 predict that for any $\alpha \leq 1$, the critical behavior should be universal. In contrast, the numerical results do exhibit a dependence of the critical point and the value of the order parameter on α, we attribute this to finite-size effects. The relatively small size considered here allows us to witness dependencies on α that are washed away in the thermodynamic limit. Additionally, we observe that the ansatz encounters difficulties in obtaining the correct ground state near the critical point for $\alpha \leq 1$. One would expect the critical point to recede toward smaller values of ω_x as α increases. However, for $\alpha \leq 1$ the opposite trend is observed. Since in that region the states corresponding to the ordered and paramagnetic phases are practically degenerate in energy, it seems that the ViT falls into the paramagnetic local minimum prematurely.

In Fig. 7.8(d) we show a horizontal slice of the phase diagram (fixed longitudinal field). The phase transition is of second order for all values of α, as expected from the analytical results of Sec. 7.4.1. Following Figs. 7.6(a) and (b) we expected a decrease of the second order critical point as α increases. This is confirmed by the numerical results. The critical point tends to the predicted values of $\omega_z/(s\Gamma) = 2$ for $\alpha \leq 1$ (strong long-range regime) and $\omega_z/(s\Gamma) = 0.5$ in the limit of $\alpha \to \infty$ (nearest-neighbors regime). We observe that from $\alpha \gtrsim 7$ the curves collapse and thus it can be considered as the numerical limit from which the model is the nearest-neighbors regime. On the other hand, the numerical instabilities now appear at a point where the model is classical (no transverse field).

To better certify the order of the different phase transitions, beyond a visual analysis of the discontinuities (or lack there of) of the order parameter, we perform a finite-size scaling analysis. In Fig. 7.8 we show this analysis for

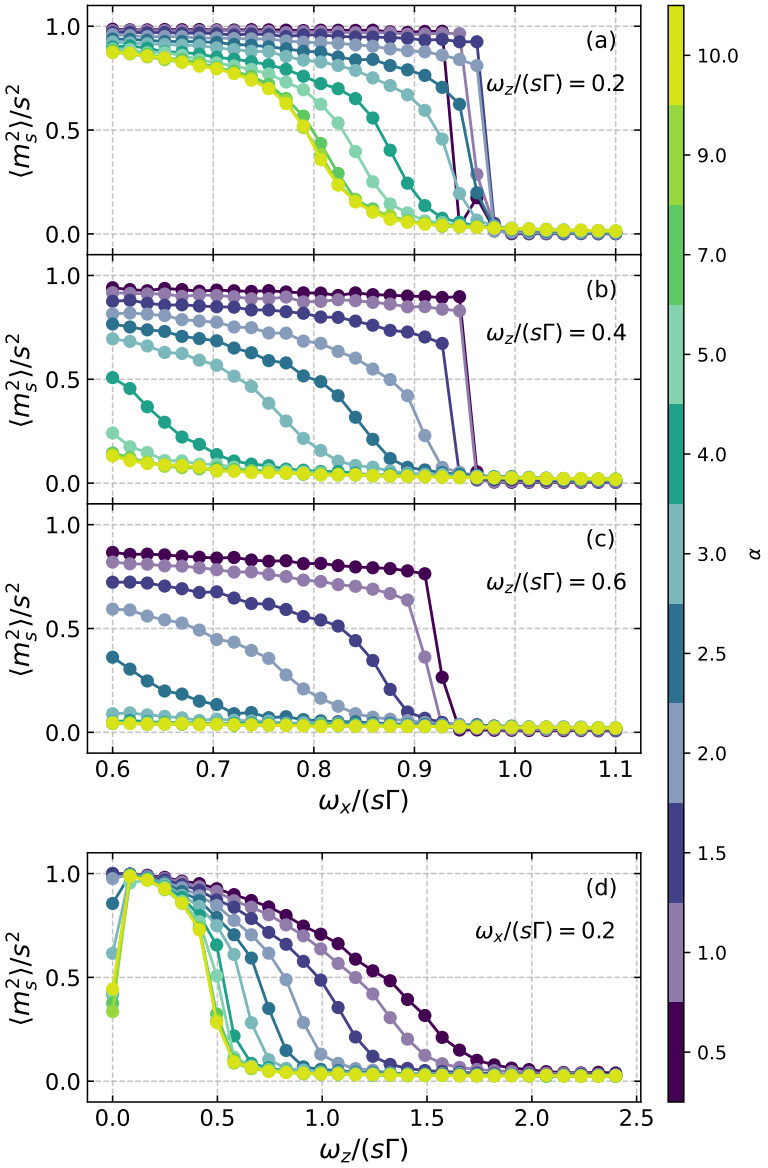

Figure 7.8: Characterization of the parameter space through vertical slices (panels a,b,c) and horizontal slices (panel d) of the phase diagram for the squared staggered magnetization. Each slice represents a different α value and all simulations have been carried out for a chain size of $N = 50$.

$\alpha = 2$ (See Ref. [204] for other values of α). As it can seen from panel (a), all the curves corresponding to $N = 50, 70, 100$ coincide, showing an independence with size characteristic of first-order transitions, in addition to the discontinuity in the order parameter. In contrast, in panel (c), the curves exhibit the typical

size dependence of second-order phase transitions. The continuous change of the order parameter becomes increasingly non-analytical as the size increases. The crossover point marks the second-order critical point expected in the thermodynamic limit.

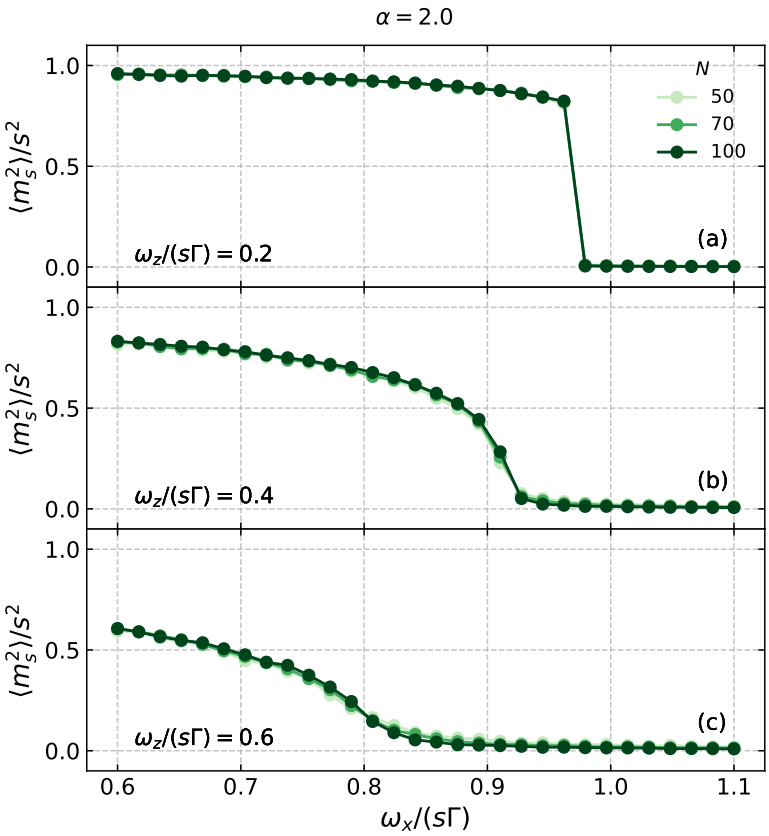

Figure 7.9: Squared staggered magnetization behavior for three different vertical slices of the phase diagram and $\alpha = 2.5$. The first order transition transforms into a second order phase transition as the transverse field is increased. Lightest colors indicate smaller sizes, being $N = 50$ the smallest, $N = 100$ the largest and $N = 70$ the intermediate size.

Figure 7.10 summarizes the numerical results discussed in this section, along with additional results that can be found in Ref. [204]. We sketch the critical line for different values of α, highlighting the regions where it is of first and second order. We have established that the first order phase transition at finite transverse field is present for $\alpha \leq 2.5$. The portion of the critical line that is of first order decreases progressively with increasing α until for $\alpha \gtrsim 3$ the full critical line is of second order. This is remarkable because it indicates that the first order phase transition is present not only in the strong long-range

regime but also beyond the mean-field threshold and presumably (see the next paragraph) in the full weak long-range regime. Although the precise boundaries α_{MF} and α^* between the regime in which the model exhibits mean-field critical exponents and the weak long-range regime and between the weak long-range and short-range regimes, have not been established for the antiferromagnetic model under consideration, it is know that for the analogous ferromagnetic model they lie at $\alpha_{\mathrm{MF}} = 5/3 \approx 1.66$ and $\alpha^* = 3$ [212]. Additionally, we have witnessed the shrinking of the antiferromagnetic phase as the model approaches the short range regime, driven by a decrease of the critical transverse field at zero longitudinal field from $\omega_z/(s\Gamma) = 2$ for $\alpha > 1$ to $\omega_z/(s\Gamma) = 0.5$ for $\alpha \gtrsim 7$.

It is worth noting that the first order phase transition is very sensitive to finite size effects. This is evident from the curve corresponding to $\alpha = 0.5$. We know from our analytical results that the tricritical point where the transition changes from first to second order occurs at $\omega_z/(s\Gamma) = 16/(5\sqrt{5}) \approx 1.43$. However, from our numerical results with $N = 100$ we are only able to certify a first-order phase transition up to $\omega_z/(s\Gamma) = 0.8$. This leads us to believe that our numerical results are also underestimating the region where the critical line is of first order for all the other values of α, and therefore also for how low a value of α the first order phase transition survives.

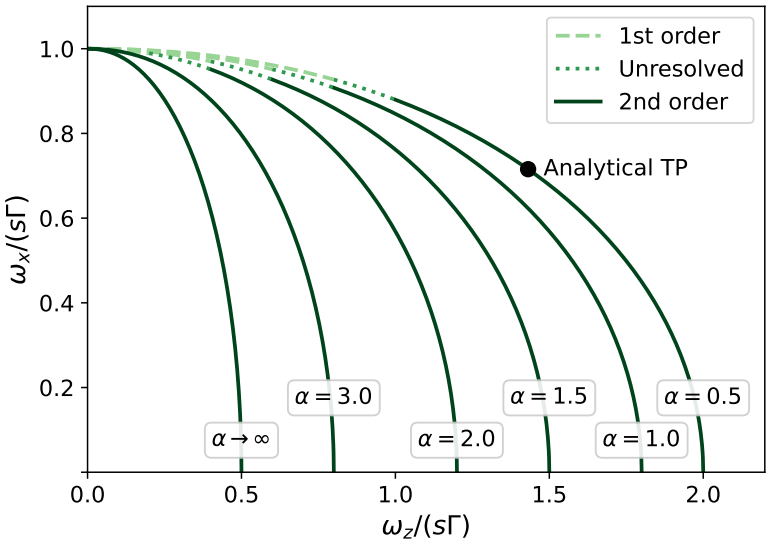

Figure 7.10: Summary of the numerical results for the order of the quantum phase transition. For reference, the black dot marks the analytical tricritical point in the strong long-range regime [Eqs. (7.39) and (7.40)].

7.4.4 The effect of long-range interactions on the order of phase transitions

The motivation to consider the tunable-range unfrustrated antiferromagnetic Ising chain was to ellucidate the role of the interaction range on the order of quantum phase transitions. We have shown analitically that the unfrustrated antiferromagnetic Ising chain in the strong long-range regime presents a tricritical point in the phase diagram where the critical line changes from first to second order. This is in contrast with the nearest-neighbours limit, where the critical line was known to be always second order but for the point of vanishing transverse field, where the model is classical. Then, we have shown numerically that the first-order phase transition is present beyond the strong long-range regime, apparently in the full weak long-range regime, only disappearing when the model enters the short-range regime beyond $\alpha \approx 3$. This confirms that the range of interactions can influence the nature of phase transitions in a model.

The fact that similar behaviour has been observed in a model with only antiferromagnetic nearest-neighbor and ferromagnetic next-nearest-neighbor interactions [256] suggests that the key ingredient that stabilizes a first-order phase transition is the presence of intrasublattice ferromagnetic interactions, in contrast with models with only intersublattice antiferromagnetic interactions. To verify this hypothesis we can also consider the unfrustrated antiferromagnetic chain but without intrasublattice ferromagnetic interactions, i.e., with $J_{ij} = 0$ for $i + j$ even. This model is not tractable with the analytical method used throughout this chapter, so an exact solution in the strong long-range regime is not possible. Nevertheless, a classical analysis of the $\alpha = 0$ limit, analogous to the one described in App. M, shows that the phase transition is always second order, except for the point of vanishing transverse field, $\omega_z = 0$, where the model is classical. Thus, we can conclude that intrasublattice ferromagnetic interactions (on top of intersublattice antiferromagnetic interactions) are the key ingredient to generate a first-order phase transition. In that sense, in the tunable-range unfrustrated antiferromagnetic Ising model, α acts as a tuning knob to change the ratio between inter- and intrasublattice interactions. For low enough α, intrasublattice ferromagnetic interactions become large enough to stabilize a first-order phase transition. The same mechanism might explain the first-order phase transitions reported in other quantum long-range models with staggered interactions [251–253].

Finally, the appearance of a first-order phase transition at zero temperature suggests that the strong long-range unfrustrated antiferromagnetic Ising chain may exhibit ensemble inequivalence at finite temperature, i.e., different properities across thermodynamic ensembles. Ensemble inequivalence has been reported to appear in the strong long-range regime in both classical [265, 266]

and quantum models featuring a first-order phase transition [267, 268].

Conclusions

This thesis is dedicated to the study of cavity QED materials by means of the large-N expansion typically used in quantum field theory. We have identified the main microscopic models used to describe cavity QED materials and unified them under the umbrella of the generalized Dicke model (GDM). In the GDM, the parameter N is the number of material degrees of freedom and thus, the large-N limit is the thermodynamic limit. Then, we have applied the large-N expansion to the GDM with the following results.

Large-N expansion and mean-field theory

Using a path integral formulation for the partition function, we have constructed an effective action for the matter subsystem with an effective interaction constant scaling as $1/N$. Then, we have decoupled it by introducing -with a Hubbard-Stratonovich transformation- an auxiliary field for each collective interaction channel. The resulting action for the auxiliary fields is explicitly extensive, i.e., it can be written as $S = \beta N f$ with f a functional independent of N in the thermodynamic limit $N \to \infty$. Here, the large-N expansion can be performed, and we have shown that it can be exactly truncated at any order, provided that the number of matter degrees of freedom N and the number of collective interaction channels M obey the limit $\lim_{N\to\infty} M/N = 0$. When truncated at order zero, the large-N expansion provides an equilibrium theory in terms of a mean-field effective Hamiltonian, which can be promoted to a full Hamiltonian. When truncated at second order around a saddle-point, the large-N expansion provides a linear response theory in terms of the response functions of the bare cavity and the mean-field effective Hamiltonian. The linear response theory can also be derived from a standard mean-field theory of the equations of motion for the retarded Green functions, cut off at the order of two-point correlations.

Together, these results clarify the validity of mean-field theory for cavity QED materials, via their proxy the GDM, and more generally for models with a finite number M of collective interaction channels, $\lim_{N\to\infty} M/N = 0$.

In the thermodynamic limit, the equilibrium and linear response properties of the GDM are given in terms of a mean-field effective Hamiltonian for the matter. The equilibrium properties are obtained by solving the mean-field effective Hamiltonian and the linear response properties are given as a function of the response functions of the bare cavity and the mean-field effective Hamiltonian. It is important to note that the mean-field decoupling afforded by the thermodynamic limit only applies to the light-matter coupling, the bare material will in general be highly correlated in and of itself and thus the solution of the mean-field effective Hamiltonian will require approximate analytical techniques or numerical calculations. Corrections to the thermodynamic limit can be computed systematically with the path integral formulation, but in the Dicke and Dicke-Ising models we observe fast convergence to the thermodynamic-limit results.

Equilibrium superradiance

The field of cavity QED materials answers the broad question of what interesting phenomena can be realized by coupling a material to a cavity. We know that at least some modifications are possible because the formation of hybrid light-matter excitations (polaritons) is well understood. In this regard it is a matter of deepening our understanding of polaritonic effects, searching for interesting and useful examples and realizing them in experiments. A more concrete question is the possibility of equilibrium superradiance, whether the cavity and the material can affect each other to the extent of inducing a quantum phase transition to a state where the material is polarized and the cavity develops a macroscopic population of photons.

We have studied equilibrium superradiance from the lens of the linear response theory developed in this thesis. We have defined a general critical condition for equilibrium superradiance by looking for zero-frequency poles of the response functions that originate from light-matter interaction. These would indicate a gap closing, and thus the superradiant phase transition. With this tool, we have unified and generalized previous results regarding equilibrium superradiance. In particular, several no-go theorems that rule out equilibrium superradiance for electric dipoles and the electron liquid subject to homogeneous cavity fields. At the same time, these results indicate that equilibrium superradiance is in principle possible if the cavity fields are inhomogeneous and if the material's paramagnetic susceptibility is large enough.

Magnetic materials in a cavity

Following the expertise of our group and the promising results regarding equilibrium superradiance, we have focused on the study of magnetic materials. We have proposed to use molecular nanomagnets coupled to an on-chip microwave cavity to realize equilibrium superradiance and cavity-enhanced ferrogmanetism. This should be possible in dense crystals of dipolar ferromagnets such as Fe_8 featuring a Curie temperature on the order of the kelvin, which is comparable with the cavity-induced shift in Curie temperature, even for modest filling factors. The modifications to the Curie temperature and critical field could be observed with a temperature-dependent transmission measurement.

We have identified interesting phenomenology in the excitation spectrum of the Dicke-Ising model. The cavity couples inhomogeneously to the zero-momentum sector of the two-excitation band of the Ising model. As a result, the cavity, despite coupling homogeneously to the real-space spins of the Ising chain, acts as an impurity for the momentum-space Bogoliubov fermions that are the elementary excitations of the Ising model. The result is that the cavity acts as an impurity that can localize magnon-pairs into bound polariton states outside the band. We have provided the condition for the existence of the bound polariton states, which could also appear in other systems where the cavity couples to a band of material excitations.

Applying the understanding gained about the validity of a mean-field decoupling, we have studied the dynamics of ferromagnetic materials coupled to a cavity by computing the modification of the Landau-Lifshitz-Gilbert (LLG) equation. We have implemented this cavity-modified LLG equation into the micromagnetic simulation software Mumax3 and released the new software as Mumax3-cQED.

Solving strong long-range models

Ultimately, the large-N expansion relies on the fact that the action has a finite number M of collective interaction channels. In the GDM, these collective interactions are cavity-mediated, but is also possible to consider cases in which these collective interactions are intrinsic. A hybrid case is afforded by the Dicke-LMG model, which combines cavity-mediated and intrinsic collective interactions. Beyond the Dicke-LMG model, we have studied this issue more systematically in pure matter models. We have shown that in the thermodynamic limit strong long-range interactions can be cast as a sum of M collective interactions, with $\lim_{N\to\infty} M/N = 0$. Thus, these models can be solved exactly in the same

way as the GDM. We have applied this to the ferromagnetic and unfrustrated antiferromagnetic Ising chains. We have shown that, in the strong long-range regime, the latter presents a tricritical point separating second- and first-order regions of the critical line. Using quantum Monte Carlo simulations, we have studied the behavior of the tricritical point across the full interaction range, showing that it is present in most, if not all, of the weak long-range regime. Our results indicate that the mechanism that induces a first-order phase transition and a tricritical point in models with antiferromagnetic intersublattice interactions is the addition of ferromagnetic intrasublattice interactions of comparable strength. In tunable-range models, the range of interactions is the tuning knob for the ratio between intra- and intersublattice interactions, which explains why the tricritical point is present in the long-range regimes and not in the short-range regime.

Conclusiones

Esta tesis está dedicada al estudio de *cavity QED materials* mediante la expansión de N grande típicamente utilizada en teoría cuántica de campos. Hemos identificado los principales modelos microscópicos utilizados para describir *cavity QED materials* y los hemos unificado bajo el paraguas del modelo de Dicke generalizado (GDM, por sus siglas en inglés). En el GDM, el parámetro N es el número de grados de libertad de la materia, por lo que el límite de N grande es el límite termodinámico. Luego hemos aplicado la expansión de N grande al GDM con los siguientes resultados.

Expansion de N grande y teoría de campo medio

Usando una formulación de integral de camino para la función de partición, hemos construido una acción efectiva para el subsistema de materia con una constante de interacción efectiva que escala como $1/N$. Luego, la hemos desacoplado introduciendo, mediante una transformación de Hubbard-Stratonovich, un campo auxiliar para cada canal de interacción colectiva. La acción resultante para los campos auxiliares es explícitamente extensiva, es decir, puede escribirse como $S = \beta N f$, donde f es un funcional independiente de N en el límite termodinámico $N \to \infty$. Aquí, se puede realizar la expansión de N grande, y hemos demostrado que puede truncarse exactamente a cualquier orden, siempre que el número de grados de libertad de la materia N y el número de canales de interacción colectiva M cumplan con el límite $\lim_{N\to\infty} M/N = 0$. Cuando se trunca a orden cero, la expansión de N grande proporciona una teoría de equilibrio en términos de un Hamiltoniano efectivo de campo medio, el cual puede ser promovido a un Hamiltoniano completo. Cuando se trunca a segundo orden alrededor de un punto de silla, la expansión de N grande proporciona una teoría de respuesta lineal en términos de las funciones de respuesta de la cavidad desnuda y el Hamiltoniano efectivo de campo medio. La teoría de respuesta lineal también puede derivarse de una teoría estándar de campo medio de las ecuaciones de movimiento para las funciones de Green retardadas,

truncada para considerar solo correlaciones de dos puntos.

En conjunto, estos resultados clarifican la validez de la teoría de campo medio para *cavity QED materials*, a través de su sustituto el GDM, y más generalmente para modelos con un número finito M de canales de interacción colectiva, $\lim_{N\to\infty} M/N = 0$. En el límite termodinámico, las propiedades de equilibrio y de respuesta lineal del GDM se dan en términos de un Hamiltoniano efectivo de campo medio para la materia. Las propiedades de equilibrio se obtienen resolviendo el Hamiltoniano efectivo de campo medio y las propiedades de respuesta lineal se dan como una función de las funciones de respuesta de la cavidad desnuda y el Hamiltoniano efectivo de campo medio. Es importante señalar que el desacoplamiento de campo medio que se obtiene en el límite termodinámico solo se aplica al acoplamiento luz-materia, el material desnudo en general será altamente correlacionado en sí mismo, por lo que la solución del Hamiltoniano efectivo de campo medio requerirá técnicas analíticas aproximadas o cálculos numéricos. Las correcciones al límite termodinámico pueden calcularse sistemáticamente con la formulación de integral de camino, pero en los modelos de Dicke y Dicke-Ising observamos una rápida convergencia hacia los resultados en el límite termodinámico.

Superradiancia de equilibrio

El campo de *cavity QED materials* responde a la amplia pregunta de qué fenómenos interesantes pueden realizarse al acoplar un material a una cavidad. Sabemos que al menos algunas modificaciones son posibles porque la formación de excitaciones híbridas luz-materia (polaritones) está bien entendida. En este sentido, se trata de profundizar en la comprensión de los efectos polaritónicos, buscar ejemplos interesantes y útiles, y realizarlos en experimentos. Una pregunta más concreta es la posibilidad de superradiancia en equilibrio, es decir, si la cavidad y el material pueden afectarse mutuamente hasta el punto de inducir una transición de fase cuántica hacia un estado en el que el material esté polarizado y la cavidad desarrolle una población macroscópica de fotones.

Hemos estudiado la superradiancia en equilibrio desde la perspectiva de la teoría de respuesta lineal desarrollada en esta tesis. Hemos definido una condición crítica general para la superradiancia en equilibrio buscando polos de frecuencia cero en las funciones de respuesta que provienen de la interacción luz-materia. Estos polos indicarían que la energía de excitación mínima se hace cero, y por lo tanto, la transición de fase superradiante. Con esta herramienta, hemos unificado y generalizado resultados previos sobre la superradiancia en equilibrio. En particular, varios teoremas de imposibilidad para la superradiancia en equilibrio para dipolos eléctricos y para un líquido de electrones sometido a

campos de cavidad homogéneos. Al mismo tiempo, estos resultados indican que la superradiancia en equilibrio es posible en principio si los campos de la cavidad son no homogéneos y si la susceptibilidad paramagnética del material es lo suficientemente grande.

Materiales magnéticos en una cavidad

Siguiendo la experiencia de nuestro grupo y los prometedores resultados sobre la superradiancia en equilibrio, nos hemos centrado en el estudio de materiales magnéticos. Hemos propuesto utilizar nanoimanes moleculares acoplados a una cavidad de microondas para realizar superradiancia en equilibrio y ferromagnetismo potenciado por la cavidad. Esto debería ser posible en cristales densos de ferromagnetos dipolares como el Fe_8, que presentan una temperatura de Curie del orden del kelvin, lo cual es comparable con el cambio inducido por la cavidad en la temperatura de Curie, incluso para factores de llenado modestos. Las modificaciones en la temperatura de Curie y el campo crítico podrían observarse mediante una medición de transmisión dependiente de la temperatura.

Hemos identificado una fenomenología interesante en el espectro de excitación del modelo Dicke-Ising. La cavidad se acopla de forma no homogénea al sector de momento cero de la banda de dos excitaciones del modelo de Ising. Como resultado, la cavidad, a pesar de acoplarse homogéneamente a los espines en el espacio real de la cadena de Ising, actúa como una impureza para los fermiones de Bogoliubov en el espacio de momento, que son las excitaciones elementales del modelo de Ising. El resultado es que la cavidad actúa como una impureza que puede localizar pares de magnones en estados ligados de polaritones fuera de la banda. Hemos proporcionado la condición para la existencia de estos estados ligados de polaritones, que también podrían aparecer en otros sistemas donde la cavidad se acopla a una banda de excitaciones del material.

Aplicando lo entendido sobre la validez del desacoplamiento de campo medio, hemos estudiado la dinámica de materiales ferromagnéticos acoplados a una cavidad mediante el cálculo de la modificación de la ecuación de Landau-Lifshitz-Gilbert (LLG). Hemos implementado esta ecuación LLG modificada por la cavidad en el software de simulación micromagnética Mumax3 y hemos publicado el nuevo software como Mumax3-cQED.

Resolviendo modelos de largo alcance fuerte

En última instancia, la expansión de N grande se basa en el hecho de que la acción tiene un número finito M de canales de interacción colectiva. En el GDM, estas interacciones colectivas son mediadas por la cavidad, pero también es posible considerar casos en los que estas interacciones colectivas son intrínsecas. Un caso híbrido es proporcionado por el modelo Dicke-LMG, que combina interacciones colectivas mediadas por cavidad e intrínsecas. Más allá del modelo Dicke-LMG, hemos estudiado esta cuestión de manera más sistemática en modelos puramente de materia. Hemos mostrado que, en el límite termodinámico, las fuertes interacciones a largo alcance pueden expresarse como una suma de M interacciones colectivas, con $\lim_{N\to\infty} M/N = 0$. Por lo tanto, estos modelos pueden resolverse exactamente de la misma manera que el GDM. Hemos aplicado esto a las cadenas de Ising ferromagnéticas y antiferromagnéticas no frustradas. Hemos demostrado que, en el régimen de interacciones de largo alcance fuerte, la última presenta un punto tricrítico que separa las regiones de segundo y primer orden de la línea crítica. Usando simulaciones de Monte Carlo cuántico, hemos estudiado el comportamiento del punto tricrítico a través de todo el rango de interacciones, mostrando que está presente en la mayoría, si no en todos, los regímenes de interacciones de largo alcance débil. Nuestros resultados indican que el mecanismo que induce una transición de fase de primer orden y un punto tricrítico en modelos con interacciones antiferromagnéticas entre subredes es la adición de interacciones ferromagnéticas dentro de la subred de intensidad comparable. En modelos de rango ajustable, el rango de interacciones es el parámetro que modifica el ratio entre interacciones intra e intersubredes, lo que explica por qué el punto tricrítico está presente en los regímenes de largo alcance y no en el régimen de corto alcance.

Appendix A

Neutral atoms in the Coulomb gauge

Under the long-wavelength approximation $\boldsymbol{R}_j + \boldsymbol{r}_j \approx \boldsymbol{R}_j$, the light-matter Hamiltonian for a system of neutral single-electron atoms reads

$$H = \sum_j \frac{\big(\boldsymbol{p}_j + e\boldsymbol{A}(\boldsymbol{R}_j)\big)^2}{2m} + V_{\mathrm{C}} + V + H_{\mathrm{em}} + \frac{g_{\mathrm{e}}\mu_{\mathrm{B}}}{2}\sum_j \boldsymbol{\sigma}_j \cdot \boldsymbol{B}(\boldsymbol{R}_j)\,, \quad \text{(A.1)}$$

The main difference with the description of the electron liquid is that now the electromagnetic fields are operators acting solely on the Hilbert space of the light. The mode functions that describe their spatial dependence are not promoted to operators since they depend on the fixed positions $\{\boldsymbol{R}_j\}$. After expanding the kinetic term and substituting the explicit forms of the vector potential and the magnetic field, we obtain

$$\begin{aligned} H = H_{\mathrm{m}} &+ \sum_\kappa \omega_{\boldsymbol{k}} a_\kappa^\dagger a_\kappa + \sum_j \sum_\kappa \frac{e}{m} A_{\boldsymbol{k}} \boldsymbol{p}_j \cdot (\boldsymbol{u}_\kappa(\boldsymbol{R}_j) a_\kappa + \text{h.c.}) \\ &+ \sum_j \frac{e^2}{2m} \sum_{\kappa,\kappa'} A_{\boldsymbol{k}} A_{\boldsymbol{k}'} \, (\boldsymbol{u}_\kappa(\boldsymbol{R}_j) a_\kappa + \text{h.c.}) \cdot (\boldsymbol{u}_{\kappa'}(\boldsymbol{R}_j) a_{\kappa'} + \text{h.c.}) \\ &+ \frac{g_{\mathrm{e}}\mu_{\mathrm{B}}}{2} \sum_\kappa \sum_j B_{\boldsymbol{k}} \boldsymbol{\sigma}_j \cdot (\boldsymbol{u}_{\perp,\kappa}(\boldsymbol{R}_j) a_\kappa + \text{h.c.})\,. \end{aligned} \quad \text{(A.2)}$$

To condense the notation, we define the quantities

$$U_{\kappa,\kappa'} = N^{-1} \sum_j \boldsymbol{u}_\kappa(\boldsymbol{R}_j) \cdot \boldsymbol{u}_{\kappa'}(\boldsymbol{R}_j)\,, \quad \text{(A.3)}$$

$$\bar{U}_{\kappa,\kappa'} = N^{-1} \sum_j \boldsymbol{u}_\kappa(\boldsymbol{R}_j) \cdot \boldsymbol{u}^*_{\kappa'}(\boldsymbol{R}_j)\,. \quad \text{(A.4)}$$

With these, we write the terms that depend quadratically on the bosonic operators as

$$H_{\text{ph}} = \sum_{\kappa} \omega_{\boldsymbol{k}} a_{\kappa}^{\dagger} a_{\kappa} + \sum_{\kappa,\kappa'} \Delta_{\boldsymbol{k},\boldsymbol{k}'} \left(U_{\kappa,\kappa'} a_{\kappa} a_{\kappa'} + \bar{U}_{\kappa,\kappa'} a_{\kappa} a_{\kappa'}^{\dagger} + \text{h.c.} \right) . \tag{A.5}$$

Whereas in the case of the electron liquid the photonic Hamiltonian could not be diagonalized in the general case, the fact that the coefficients of the quadratic terms are now c-numbers allows us to exactly diagonalize the photonic terms by means of a Bogoliubov transform. First, we define $\Psi^t = (a_{\kappa_1}^{\dagger}, \ldots, a_{\kappa_M}^{\dagger}, a_{\kappa_1}, \ldots, a_{\kappa_M})$, which allows us to write the Hamiltonian as

$$H_{\text{ph}} = \frac{1}{2} \Psi^{\dagger} \mathbb{H} \Psi \,, \qquad \text{with} \qquad \mathbb{M} = \begin{pmatrix} \mathbb{H}_1 & \mathbb{H}_2 \\ \mathbb{H}_2^{\dagger} & \mathbb{H}_1^{*} \end{pmatrix} , \tag{A.6}$$

where the $M \times M$ blocks $\mathbb{H}_1$ and $\mathbb{H}_2$ are defined in terms of their matrix elements

$$(\mathbb{H}_1)_{\kappa,\kappa'} = 2\Delta_{\kappa,\kappa'} \bar{U}_{\kappa,\kappa'} + \delta_{\kappa\kappa'} \omega_{\boldsymbol{k}} \,, \tag{A.7}$$

$$(\mathbb{H}_2)_{\kappa,\kappa'} = 2\Delta_{\kappa,\kappa'} U_{\kappa,\kappa'} \,. \tag{A.8}$$

The Bogoliubov transform is determined by a transformation matrix $\mathbb{T}$, obeying the pseudounitarity condition $\mathbb{T}^{\dagger} \mathbb{I}_{-} \mathbb{T} = \mathbb{I}_{-}$, which defines a new set of bosonic operators $\Phi = \mathbb{T}^{-1} \Psi = (b_{\kappa_1}^{\dagger}, \ldots, b_{\kappa_M}^{\dagger}, b_{\kappa_1}, \ldots, b_{\kappa_M})$ and a new Hamiltonian matrix $\tilde{\mathbb{H}} = \mathbb{T}^{\dagger} \mathbb{H} \mathbb{T}$ such that $\tilde{\mathbb{H}}$ is diagonal [116]. The resulting Hamiltonian can be written as

$$H_{\text{ph}} = \sum_{\kappa} \tilde{\omega}_{\boldsymbol{k}} b_{\kappa}^{\dagger} b_{\kappa} \,. \tag{A.9}$$

The pseudounitarity of $\mathbb{T}$ ensures that the new bosonic operators obey the canonical commutation relations. The $\mathbb{I}_{-}$ block matrix is defined as

$$\mathbb{I}_{-} = \begin{pmatrix} \mathbb{I}_M & 0 \\ 0 & -\mathbb{I}_M \end{pmatrix} , \tag{A.10}$$

with $\mathbb{I}_M$ the identity matrix of dimension M. The old bosonic operators can be written in terms of the new ones as

$$a_{\kappa} = \sum_{\kappa'} (\alpha_{\kappa,\kappa'} b_{\kappa'} + \beta_{\kappa,\kappa'} b_{\kappa'}^{\dagger}) \,. \tag{A.11}$$

With this, and defining

$$\tilde{A}_{\boldsymbol{k}} \tilde{\boldsymbol{u}}_{\kappa}(\boldsymbol{R}_j) = \sum_{\kappa'} A_{\boldsymbol{k}'} \left(\boldsymbol{u}_{\kappa'}(\boldsymbol{R}_j) \alpha_{\kappa,\kappa'} + \boldsymbol{u}_{\kappa'}^{*}(\boldsymbol{R}_j) \beta_{\kappa,\kappa'}^{*} \right) , \tag{A.12}$$

$$\tilde{B}_{\boldsymbol{k}} \tilde{\boldsymbol{u}}_{\perp,\kappa}(\boldsymbol{R}_j) = \sum_{\kappa'} B_{\boldsymbol{k}'} \left(\boldsymbol{u}_{\perp,\kappa'}(\boldsymbol{R}_j) \alpha_{\kappa,\kappa'} + \boldsymbol{u}_{\perp,\kappa'}^{*}(\boldsymbol{R}_j) \beta_{\kappa,\kappa'}^{*} \right) , \tag{A.13}$$

and the constants

$$\tilde{g}^e_{\boldsymbol{k}} = e\tilde{A}_{\boldsymbol{k}}\sqrt{\frac{2\omega_\mathrm{p}}{m}}\,, \tag{A.14}$$

$$\tilde{g}^m_{\boldsymbol{k}} = \mu_B \tilde{B}_{\boldsymbol{k}}\,, \tag{A.15}$$

we can conveniently write the total Hamiltonian as

$$\begin{aligned} H = H_\mathrm{m} + \sum_\kappa \tilde{\omega}_{\boldsymbol{k}} b^\dagger_\kappa b_\kappa + \sum_\kappa \sum_j \tilde{g}^m_{\boldsymbol{k}} \frac{g_\mathrm{e}}{2} \boldsymbol{\sigma}_j \cdot (\tilde{\boldsymbol{u}}_{\perp,\kappa}(\boldsymbol{R}_j) b_\kappa + \mathrm{h.c.}) \\ + \sum_\kappa \sum_j \tilde{g}^e_{\boldsymbol{k}} \sqrt{\frac{1}{2m\omega_\mathrm{p}}} \boldsymbol{p}_j \cdot (\tilde{\boldsymbol{u}}_\kappa(\boldsymbol{R}_j) b_\kappa + \mathrm{h.c.})\,. \end{aligned} \tag{A.16}$$

Defining the coupling operator

$$g_{\boldsymbol{k}} C_\kappa = \sum_j \left(\tilde{g}^e_{\boldsymbol{k}} \sqrt{\frac{1}{2m\omega_\mathrm{p}}} \boldsymbol{p}_j \cdot \tilde{\boldsymbol{u}}_\kappa(\boldsymbol{R}_j) + \tilde{g}^m_{\boldsymbol{k}} \frac{g_\mathrm{e}}{2} \boldsymbol{\sigma}_j \cdot \tilde{\boldsymbol{u}}_{\perp,\kappa}(\boldsymbol{R}_j) \right)\,, \tag{A.17}$$

we can finally write the Hamiltonian as

$$H = H_\mathrm{m} + \sum_\kappa \tilde{\omega}_{\boldsymbol{k}} b^\dagger_\kappa b_\kappa + \sum_\kappa g_{\boldsymbol{k}} \left(C_\kappa b_\kappa + \mathrm{h.c.} \right)\,. \tag{A.18}$$

Which is formally identical to Hamiltonian (1.17), the only difference lies in how $\tilde{\omega}_{\boldsymbol{k}}$, $g_{\boldsymbol{k}}$, C_κ and b_κ are defined in this case.

Appendix B

Validity of the saddle-point approximation

Functional integrals, and more specifically the functional determinants that Gaussian functional integrals give rise to, are generally infinite. Nevertheless, for physical purposes, such as the computation of expectation values, one encounters ratios of functional integrals that are well defined.

It is apparent from the definition of Z_φ in Eq. (2.18) that Z_φ is proportional to $Z_{\rm ph}$ with the proportionality factor being N^∞. This infinite factor is precisely canceled by a factor $(1/N)^\infty$ produced by the Gaussian integral of the second order saddle-point expansion of $f[\varphi_k, \bar\varphi_k]$, as a result we have

$$Z = e^{-N\beta f[\varphi_{k,\rm sp},\bar\varphi_{k,\rm sp}]} \prod_k^M \det\left(H_f[\varphi_k,\bar\varphi_k]\right)^{-1} , \tag{B.1}$$

with $H_f[\varphi_k,\bar\varphi_k]$ the functional Hessian of $f[\varphi_k,\bar\varphi_k]$ and M the number of complex auxiliary fields φ_k and $\bar\varphi_k$. We can see now that the free energy per particle is

$$f = -\frac{1}{\beta N}\ln Z = f[\varphi_{k,\rm sp},\bar\varphi_{k,\rm sp}] + \frac{1}{\beta N}\sum_k^M \ln\left[\det\left(H_f[\varphi_k,\bar\varphi_k]\right)\right] . \tag{B.2}$$

The second term scales as M/N and thus it is negligible in the thermodynamic limit provided that $\lim_{N\to\infty} M/N = 0$. With this, we see that the choice of name for $f[\varphi_k,\bar\varphi_k]$ is not arbitrary, as it plays the role of a variational free energy per site, with $f[\varphi_{k,\rm sp},\bar\varphi_{k,\rm sp}]$ the true equilibrium free energy in the thermodynamic limit, $N\to\infty$.

The same argument applies to the case of a matter-only model with collective interactions studied in Sec. 2.3.

Appendix C

Linear response theory for a multimode cavity

We consider the multimode generalization of Eq. (3.1)

$$H = H_{\rm m} + \sum_k \Omega_k a_k^\dagger a_k + \sum_k g_k \left(a_k + a_k^\dagger\right) C_k + \zeta \sum_k \frac{g_k^2}{\Omega_k} C_k^2 \,. \tag{C.1}$$

The corresponding induced action reads

$$S_{\rm ind} = \frac{1}{2} \sum_k \int_{\tau,\tau'} C_k(\tau) \frac{1}{N} V_{\rm ind,k}(\tau - \tau') C_k(\tau') \,, \tag{C.2}$$

with

$$V_{\rm ind,k}(\omega_m) = 2\lambda_k^2 \frac{\Omega_k^2(\zeta - 1) + \zeta\omega_m^2}{\Omega_k(\omega_m^2 + \Omega_k^2)} \,. \tag{C.3}$$

The induced interaction can be decoupled with a Hubbard-Stratonovich transformation that introduces an auxiliary scalar field for each mode, φ_k:

$$e^{-S_{\rm ind}} = \frac{1}{Z_\varphi} \oint_\varphi e^{-\frac{1}{2}N \sum_k \int_{\tau,\tau'} \varphi_k(\tau) V^{-1}_{{\rm ind},k}(\tau-\tau')\varphi_k(\tau') - i\sum_k \int_\tau \varphi_k(\tau) C_k(\tau)} \,. \tag{C.4}$$

We define the propagator of the auxiliary fields as

$$W_{kp}(\tau) = \langle \varphi_k(\tau)\varphi_p(0)\rangle^{\rm c} \,. \tag{C.5}$$

The generating functional for bare connected correlation functions of the matter coupling operators C_k is $\mathcal{G}^0_{\rm m}[\xi_k] = -N^{-1}\log Z_{\rm m}[\xi_k]$ with

$$Z_{\rm m}[\xi_k] = \oint_c e^{-(S_{\rm m} + i\sum_k \int_\tau \xi_k(\tau) C_k(\tau))} \,, \tag{C.6}$$

such that

$$\frac{\delta}{\delta\xi_{k_1}(\tau_1)}\cdots\frac{\delta}{\delta\xi_{k_n}(\tau_n)}\mathcal{G}^0_{\mathrm{m}}[\xi_k]\Big|_{\xi_k=0} = -\frac{(-i)^n}{N}\langle C_{k_1}(\tau_1)\cdots C_{k_n}(\tau_n)\rangle^{\mathrm{c}}_{\mathrm{m}} \equiv \chi^{(n)}_{k_1\ldots k_n,0}(\tau_1,\ldots,\tau_n)\,. \tag{C.7}$$

In the following we will denote $\chi^{(2)}_{kp,0} \equiv \chi_{kp,0}$. With this, after partial integration over the matter degrees of freedom, we can write

$$Z = \oint_{\varphi_k} e^{-N\beta f[\varphi_k]}\,, \tag{C.8}$$

with

$$f[\varphi_k] = \frac{1}{2\beta}\sum_k \int_{\tau,\tau'} \varphi_k(\tau)V^{-1}_{\mathrm{ind},k}(\tau-\tau')\varphi_k(\tau') + \mathcal{G}^0_{\mathrm{m}}[\varphi_k]\,. \tag{C.9}$$

Like in the single-mode case, we apply a saddle-point approximation for large N. This requires that the number of modes M be finite, i.e., that $\lim_{N\to\infty} M/N \to 0$. Otherwise higher order terms in the saddle-point expansion might not actually be negligible. The constant solutions to the saddle-point equations are

$$\varphi_{k,\mathrm{sp}} = -\frac{i}{N}V_{\mathrm{ind,k}}(\omega_m=0)\langle C_k\rangle_{\varphi_{k,\mathrm{sp}}}\,. \tag{C.10}$$

This tells us that $\varphi_{k,\mathrm{sp}}$ is self-consistently proportional to $\langle C_x\rangle_{\varphi_{k,\mathrm{sp}}}$, i.e., to the expectation value of C_k for the bare matter subject to fields $i\varphi_{k,\mathrm{sp}} = \frac{1}{N}V_{\mathrm{ind,k}}(\omega_m=0)\langle C_k\rangle$. This is precisely the self-consistent condition that arises from computing $\langle C_k\rangle$ from the mean-field Hamiltonian

$$\begin{aligned} H^{\mathrm{MF}}_{\mathrm{eff}} =& H_{\mathrm{m}} + \sum_k \frac{2\lambda_k^2(\zeta-1)}{N\Omega_k}\langle C_k\rangle C_k \\ &- \sum_k \frac{\lambda_k^2(\zeta-1)}{N\Omega_k}\langle C_k\rangle^2\,. \end{aligned} \tag{C.11}$$

Expanding f around the saddle-point yields

$$(NW_0)^{-1}_{kp} = \delta_{kp}V^{-1}_{\mathrm{ind,k}} + \tilde{\chi}_{kp,0}\,, \tag{C.12}$$

with

$$\tilde{\chi}_{kp,0}(\tau_1,\tau_2) = \frac{\delta}{\delta\varphi_{k,\mathrm{sp}}(\tau_1)}\frac{\delta}{\delta\varphi_{p,\mathrm{sp}}(\tau_2)}\mathcal{G}^0_{\mathrm{m}} = \frac{1}{N}\langle C_k(\tau)C_p(\tau')\rangle^{\mathrm{c}}_{\mathrm{eff}}\,. \tag{C.13}$$

For $N\to\infty$ one can safely truncate the saddle-point expansion to second order, which implies that $W = W_0$.

We can now obtain relations between the auxiliary field propagator W_{kp} the photonic propagator D_k and matter response functions. Let us define the generating functional for photonic connected correlators by introducing complex fields in the action: $\mathcal{G}_{\rm ph}[\eta_k, \bar{\eta}_k] = -\log Z[\eta_k, \bar{\eta}_k]$, with

$$Z[\eta_k, \bar{\eta}_k] = \oint_{a_k, \bar{a}_k, c} e^{-(S + \sum_k \int_\tau (a_k(\tau)\bar{\eta}_k(\tau) + \bar{a}_k(\tau)\eta_k(\tau))}\,. \tag{C.14}$$

After partial integration of the cavity fields, this yields

$$\begin{aligned} Z[\eta_k, \bar{\eta}_k] = \oint_c \exp -\Bigg(& S_{\rm m} + \zeta \sum_k \frac{g_k^2}{\Omega_k} \int_\tau C_k^2(\tau) \\ & + \sum_k \int_{\tau,\tau'} \bar{m}_k(\tau) D_k(\tau - \tau') m_k(\tau) \Bigg)\,, \end{aligned} \tag{C.15}$$

with $m_k(\tau) = \eta_k(\tau) + g_k C_k(\tau)$. With this

$$D_k(\omega_m) = D_{k,0}(\omega_m) - \lambda_k^2 D_{k,0}(\omega_m)\chi_{kk}(\omega_m) D_{k,0}(\omega_m)\,. \tag{C.16}$$

Likewise, we can define the generating functional for matter connected correlators: $\mathcal{G}_{\rm m}[\xi_k] = -N^{-1} \log Z[\xi_k]$ with

$$Z[\xi_k] = \oint_{c, \varphi_k} e^{-(S_{\rm eff} + i \sum_k \int_\tau \xi_k(\tau) C_k(\tau))}\,. \tag{C.17}$$

After partial integration over the cavity fields, this yields

$$Z[\xi_k] = \oint_{\varphi_k} e^{-N f[\varphi_k, \xi_k]}\,, \tag{C.18}$$

with

$$f[\varphi_k, \xi_k] = \frac{1}{2} \sum_k \int_{\tau,\tau'} \varphi_k(\tau) V^{-1}_{{\rm ind},k}(\tau - \tau') \varphi_k(\tau') + \mathcal{G}^0_{\rm m}[\varphi_k + \xi_k]\,. \tag{C.19}$$

Then, a second order expansion of $f[\varphi_k, \xi_k]$ around the saddle point yields

$$\begin{aligned} f[\varphi_k, \xi_k] - f[\varphi_{k,{\rm sp}}, 0] = \frac{1}{2} \sum_{k,p} \int_{\tau,\tau'} \Big(& \delta\varphi_k(\tau)(NW)^{-1}_{kp}(\tau - \tau')\delta\varphi_p(\tau') \\ & + \xi_k(\tau)\tilde{\chi}_{kp,0}(\tau - \tau')\xi_p(\tau') \\ & + \delta\varphi_k(\tau)\tilde{\chi}_{kp,0}(\tau - \tau')\xi_p(\tau') \\ & + \xi_k(\tau)\tilde{\chi}_{kp,0}(\tau - \tau')\delta\varphi_p(\tau) \Big)\,. \end{aligned} \tag{C.20}$$

The functional integral over the auxiliary-field displacements $\delta\varphi_k$ is just an M-dimensional Gaussian integral that we can perform, yielding

$$G_{\mathrm{m}}[\xi_k] + \mathrm{cst.} = \frac{1}{2}\sum_{k,p}\int_{\tau,\tau'}\xi_k(\tau)\Bigg(\tilde{\chi}_{kp,0}(\tau-\tau') - \sum_{k',p'}\int_{u,v}\tilde{\chi}_{kk',0}(\tau-u)NW_{k'p'}(u-v)\tilde{\chi}_{p'p,0}(v-\tau')\Bigg)\xi_p(\tau')\,. \tag{C.21}$$

With this

$$\chi_{kp}(\omega_m) = \tilde{\chi}_{kp,0}(\omega_m) - \sum_{k',p'}\tilde{\chi}_{kk',0}(\omega_m)NW_{k'p'}(\omega_m)\tilde{\chi}_{p'p,0}(\omega_m)\,. \tag{C.22}$$

Note that obtaining final expressions for $\chi_{kp}(\omega_m)$ requires inverting the matrix $(NW)^{-1}$ that is defined in Eq. (C.12).

Appendix D

Equivalence between the two approaches to LRT

In the equations-of-motion formulation, the photonic propagator is given by Eq. (3.55). Here, we show that after some manipulations, this expression is equivalent to Eqs. (3.22) and (3.31) obtained from the path-integral formulation.

First we rewrite Eq. (3.55) as

$$D(\omega) = \frac{D_0(\omega) + \lambda^2 \frac{2\zeta(\omega_+ + \Omega) - \Omega}{\Omega(\omega_+^2 - \Omega^2)} \tilde{\chi}_{xx,0}(\omega)}{1 + 2\lambda^2 \frac{\zeta(\omega_+^2 - \Omega^2) + \Omega^2}{\Omega(\omega_+^2 - \Omega^2)} \tilde{\chi}_{xx,0}(\omega)} \tag{D.1}$$

Then, we note that

$$2\lambda^2 \frac{\zeta(\omega_+^2 - \Omega^2) + \Omega^2}{\Omega} = V_{\text{ind}}(\omega)\,, \tag{D.2}$$

and similarly

$$\lambda^2 \frac{2\zeta(\omega_+ + \Omega) - \Omega}{\Omega} = D_0(\omega)\left(V_{\text{ind}}(\omega) - \lambda^2 D_0(\omega)\right)\,. \tag{D.3}$$

With this

$$\begin{aligned} D(\omega) &= \frac{D_0(\omega) + D_0(\omega)\left(V_{\text{ind}}(\omega) - \lambda^2 D_0(\omega)\right)\tilde{\chi}_{xx,0}(\omega)}{1 + V_{\text{ind}}(\omega)\tilde{\chi}_{xx,0}} \\ &= \frac{D_0(\omega)\left(1 + V_{\text{ind}}(\omega)\tilde{\chi}_{xx,0}(\omega)\right) - \lambda^2 D_0^2(\omega)}{1 + V_{\text{ind}}(\omega)\tilde{\chi}_{xx,0}} \\ &= D_0(\omega) - \lambda^2 D_0(\omega)\frac{\tilde{\chi}_{xx,0}(\omega)}{1 + V_{\text{ind}}(\omega)\tilde{\chi}_{xx,0}(\omega)} D_0(\omega)\,, \end{aligned} \tag{D.4}$$

which is precisely the analytic continuation $i\omega_m \to \omega_+$ of the combination of Eqs. (3.22) and (3.31).

Appendix E

Current response functions in the quantum Hall effect

To compute these alternative Green functions following Chap. 3, we formulate the following generating functional for mixed connected correlators: $\mathcal{G}_{\mathrm{mix}}[\eta,\xi_x,\xi_y] = -\log Z[\eta,\xi_x,\xi_y]$, with

$$Z[\eta,\xi_x,\xi_y] = \oint_{a,\bar{a},c} \exp\left[-\Big(S + \int_\tau \eta(\tau)(a(\tau)+\bar{a}(\tau)) + \sum_r \int_\tau \xi_r(\tau) C_r(\tau)\Big)\right]. \tag{E.1}$$

After partial integration of the cavity fields, this yields

$$Z[\eta,\xi_x,\xi_y] = \oint_{c} \exp\left[-\Big(S_{\mathrm{m}} + \int_{\tau,\tau'} m(\tau) D_0(\tau-\tau') m(\tau) + \sum_r \int_\tau \xi_r(\tau) C_r(\tau)\Big)\right], \tag{E.2}$$

with $m(\tau) = \eta(\tau) + gC_x(\tau)$. With this

$$\begin{aligned} G^{\mathrm{t}}_{\gamma(a+a^\dagger),C_r}(\tau-\tau') &= -\gamma \frac{\delta}{\delta\eta(\tau)} \frac{\delta}{\delta\xi_r(\tau')} \mathcal{G}_{\mathrm{mix}}[\eta,\xi_x,\xi_y] \\ &= \gamma \int_u D^{\mathrm{s}}_0(\tau-u) N g \chi_{xr}(u-\tau')\,, \end{aligned} \tag{E.3}$$

or in Matsubara frequency space

$$G^{\mathrm{t}}_{\gamma(a+a^\dagger),C_r}(\omega_m) = -\gamma D^{\mathrm{s}}_0(\omega_m) N g \chi_{xr}(\omega_m)\,. \tag{E.4}$$

Here $D^s_0(\tau) = D_0(\tau) + D_0(-\tau)$ is the symmetrized free photon propagator

$$D^{\mathrm{s}}_0(\omega_m) = \frac{1}{i\omega_m - \tilde{\omega}} - \frac{1}{i\omega_m + \tilde{\omega}}\,. \tag{E.5}$$

Likewise

$$G^{\mathrm{t}}_{C_x,\gamma(a+a^\dagger)}(\omega_m) = -\gamma D_0^{\mathrm{s}}(\omega_m) N g \chi_{xx}(\omega_m) \tag{E.6}$$

and

$$G^{\mathrm{t}}_{\gamma(a+a^\dagger),\gamma(a+a^\dagger)}(\omega_m) = \gamma^2 D_0^{\mathrm{s}}(\omega_m) - \gamma^2 D_0^{\mathrm{s}}(\omega_m)\lambda^2 \chi_{xx}(\omega_m) D_0^{\mathrm{s}}(\omega_m)\,. \tag{E.7}$$

With these we obtain, after analytic continuation $i\omega_m \to \omega_+$,

$$\begin{aligned} G^{\mathrm{r}}_{J_x,J_y}(\omega) &= -N\frac{2e^2\tilde{\omega}}{m}\left(1+\gamma g D_0^{\mathrm{s}}(\omega)\right)\chi_{xy}(\omega)\,, \\ &= -N\frac{2e^2\tilde{\omega}}{m}\left(1+\left(\frac{\omega_{\mathrm{p}}}{\tilde{\omega}}\right)^2\frac{\tilde{\omega}}{2}D_0^{\mathrm{s}}(\omega)\right)\chi_{xy}(\omega)\,, \end{aligned} \tag{E.8}$$

and similarly

$$\begin{aligned} G^{\mathrm{r}}_{J_x,J_x}(\omega) = -N\frac{2e^2\tilde{\omega}}{m}\Bigg(&\left(1+\left(\frac{\omega_{\mathrm{p}}}{\tilde{\omega}}\right)^2\frac{\tilde{\omega}}{2}D_0^{\mathrm{s}}(\omega)\right)^2\chi_{xx}(\omega) \\ &-\frac{1}{2\tilde{\omega}}\left(\frac{\omega_{\mathrm{p}}}{\tilde{\omega}}\right)^2\frac{\tilde{\omega}}{2}D_0^{\mathrm{s}}(\omega)\Bigg)\,, \end{aligned} \tag{E.9}$$

$$G^{\mathrm{r}}_{J_y,J_y}(\omega) = -N\frac{2e^2\tilde{\omega}}{m}\chi_{yy}(\omega)\,. \tag{E.10}$$

We can relate χ_{xx}, χ_{xy} and χ_{yy} to $\tilde{\chi}_{xx,0}$, $\tilde{\chi}_{xy,0}$ and $\tilde{\chi}_{yy,0}$ through Eqs. (3.31) and (3.33), obtaining

$$G^{\mathrm{r}}_{J_x,J_y}(\omega) = \left(1+\left(\frac{\omega_{\mathrm{p}}}{\tilde{\omega}}\right)^2\frac{\tilde{\omega}}{2}D_0^{\mathrm{s}}(\omega)\right)\frac{\tilde{G}^{\mathrm{r},0}_{J_x,J_y}(\omega)}{1-V_{\mathrm{ind}}(\omega)\frac{m}{2e^2\tilde{\omega}N}\tilde{G}^{\mathrm{r},0}_{J_x,J_x}(\omega)}\,, \tag{E.11}$$

with $\tilde{G}^{\mathrm{r},0}_{J_r,J_s} = -N\tilde{\chi}_{rs,0}$. Likewise

$$\begin{aligned} G^{\mathrm{r}}_{J_x,J_x}(\omega) = &\left(1+\left(\frac{\omega_{\mathrm{p}}}{\tilde{\omega}}\right)^2\frac{\tilde{\omega}}{2}D_0^{\mathrm{s}}(\omega)\right)^2\frac{\tilde{G}^{\mathrm{r},0}_{J_x,J_x}(\omega)}{1-V_{\mathrm{ind}}(\omega)\frac{m}{2e^2\tilde{\omega}N}\tilde{G}^{\mathrm{r},0}_{J_x,J_x}(\omega)} \\ &+\frac{Ne^2}{m}\left(\frac{\omega_{\mathrm{p}}}{\tilde{\omega}}\right)^2\frac{\tilde{\omega}}{2}D_0^{\mathrm{s}}(\omega)\,, \end{aligned} \tag{E.12}$$

$$\begin{aligned} G^{\mathrm{r}}_{J_y,J_y}(\omega) = &\frac{1}{1-V_{\mathrm{ind}}(\omega)\frac{m}{2e^2\tilde{\omega}N}\tilde{G}^{\mathrm{r},0}_{J_x,J_x(\omega)}}\Bigg(\tilde{G}^{\mathrm{r},0}_{J_y,J_y}(\omega) \\ &+V_{\mathrm{ind}}(\omega)\frac{m}{2e^2\tilde{\omega}N}\left(\tilde{G}^{\mathrm{r},0}_{J_x,J_y}(\omega)\tilde{G}^{\mathrm{r},0}_{J_y,J_x}(\omega)-\tilde{G}^{\mathrm{r},0}_{J_x,J_x}(\omega)\tilde{G}^{\mathrm{r},0}_{J_y,J_y}(\omega)\right)\Bigg)\,. \end{aligned} \tag{E.13}$$

That $\tilde{\chi}_{rs,0} = \chi_{rs,0}$ and thus $\tilde{G}^{\mathrm{r},0}_{J_r,J_s} = G^{\mathrm{r},0}_{J_r,J_s}$ follows from the no-go theorem discussed in Sec. 4.1.3, which can be straightforwardly extended to this case.

With this, Equations (E.11), (E.12) and (E.13) turn into Eqs. (4.39), (4.40) and (4.41) and provide us with an implicit expression of the current response functions of the electron gas coupled to a cavity in terms of the current response functions of the bare electron gas. This culminates the application of our linear response theory.

Appendix F

A spin subject to variational fields

F.1 Spectrum and response functions of a free spin

Let us consider the following free spin model

$$H = \frac{\omega_x}{2}\sigma_x + \frac{\omega_z}{2}\sigma_z \,. \tag{F.1}$$

It is diagonalized by a rotation that defines spin operators along new directions

$$\sigma'_z = \frac{\omega_z}{\epsilon}\sigma_z - \frac{\omega_x}{\epsilon}\sigma_x \,, \tag{F.2}$$

$$\sigma'_x = \frac{\omega_x}{\epsilon}\sigma_z + \frac{\omega_z}{\epsilon}\sigma_x \,, \tag{F.3}$$

where $\epsilon^2 = \omega_x^2 + \omega_z^2$. With these, the Hamiltonian reads

$$H = \frac{\epsilon}{2}\sigma'_z \,, \tag{F.4}$$

with ground-state energy $E_0 = -\epsilon/2$.

We compute the response functions from their spectral decomposition, which, at zero temperature, reads

$$\chi_{ab}(\omega) = -\left(\frac{\langle 0|\sigma_a|1\rangle\langle 1|\sigma_b|0\rangle}{\omega^+ + E_0 - E_1} - \frac{\langle 1|\sigma_a|0\rangle\langle 0|\sigma_b|1\rangle}{\omega^+ + E_1 - E_0}\right) , \tag{F.5}$$

where the sum is over the eigenstates of the system. With the matrix elements being

$$\langle 1|\sigma_x|0\rangle = -\frac{\omega_x}{\epsilon} \,, \tag{F.6}$$

$$\langle 1|\sigma_z|0\rangle = \frac{\omega_z}{\epsilon} \,, \tag{F.7}$$

we obtain

$$\chi_{xx}(\omega) = -\frac{\omega_z^2}{\epsilon^2}\frac{2\epsilon}{\omega_+^2 - \epsilon^2}\,, \tag{F.8}$$

$$\chi_{xz}(\omega) = \chi_{zx}(\omega) = -\frac{\omega_x\omega_z}{\epsilon^2}\frac{2\epsilon}{\omega_+^2 - \epsilon^2}\,, \tag{F.9}$$

$$\chi_{zz}(\omega) = -\frac{\omega_x^2}{\epsilon^2}\frac{2\epsilon}{\omega_+^2 - \epsilon^2}\,. \tag{F.10}$$

F.2 Considering variational fields

There will be situations in which we arrive to a free spin model like the one defined in Eq. (F.1) from a mean field approximation. As a result we will have a Hamiltonian of the form

$$H(m_x, m_z) = \frac{\tilde{\omega}_x}{2}\sigma_x + \frac{\tilde{\omega}_z}{2}\sigma_z + \Delta(m_x, m_z)\,, \tag{F.11}$$

where now the fields, $\tilde{\omega}_x$ and $\tilde{\omega}_z$ depend on mean-field parameters $m_{a\in\{x,z\}} = \langle\sigma_a\rangle$ and there is a constant energy term that also depends on the variational parameters. The Hamiltonian can be diagonalized as explained in the previous section, and the ground state energy and response functions are now functions of m_x and m_z. In particular, $E_0(m_x, m_z) = -\epsilon(m_x, m_z)/2 + \Delta(m_x, m_z)$, with $\epsilon^2 = \tilde{\omega}_x^2 + \tilde{\omega}_z^2$. The values of m_x and m_z are determined variationaly from a minimization of $E_0(m_x, m_z)$. Depending on the particular problem, this can be done analytically or numerically.

Appendix G

Bosonization of Dicke-LMG models

In Ref. [148] the ground-state sector of the Dicke model is solved exactly in the thermodynamic limit. A Holstein-Primakov transformation is used to bosonize the collective spin representing the N two-level atoms of the Dicke model. The resulting model is that of two coupled quantum harmonic oscillators and can be diagonalized with a Bogoliubov transformation to obtain the normal modes of the system. These are the polaritons of the Dicke model. To describe the superradiant (symmetry-broken) phase of the Dicke model, a displacement is introduced in the two oscillators prior to invoking the thermodynamic limit, to account for their finite occupation at equilibrium. Here we extend this technique to the longitudinal and transverse Dicke-LMG models considered in Sec. 5.2. Similar extensions have been developed in Ref. [152].

G.1 Longitudinal Dicke-LMG model

The ground-state sector of the Hamiltonian of the longitudinal Dicke-LMG model [See Eq. (5.5)] can be written in terms of maximum-total-spin operators as

$$H = \omega_z S_z - \frac{J}{N}\left(S_+ + S_-\right)^2 + \Omega a^\dagger a + \frac{\lambda}{\sqrt{N}}\left(S_+ + S_-\right)\left(a + a^\dagger\right), \qquad \text{(G.1)}$$

with S_z, S_+, S_- spin $S = N/2$ operators. The Holstein-Primakov transformation provides a mapping between bosonic annihilation and creation operators

and spin operators

$$S_z = b^\dagger b - N\,, \tag{G.2}$$

$$S_+ = \sqrt{N} b^\dagger \sqrt{1 - \frac{b^\dagger b}{N}}\,, \tag{G.3}$$

$$S_- = \sqrt{N} \sqrt{1 - \frac{b^\dagger b}{N}} b\,, \tag{G.4}$$

with $[b, b^\dagger] = 1$. Ignoring constants, the resulting bosonic Hamiltonian reads

$$\begin{aligned} H = \omega_z b^\dagger b - J \left(b^\dagger \sqrt{1 - \frac{b^\dagger b}{N}} + \sqrt{1 - \frac{b^\dagger b}{N}} b \right)^2 \\ + \Omega a^\dagger a + \lambda \left(b^\dagger \sqrt{1 - \frac{b^\dagger b}{N}} + \sqrt{1 - \frac{b^\dagger b}{N}} b \right) \left(a + a^\dagger \right)\,. \end{aligned} \tag{G.5}$$

To allow for the description of both a normal and a symmetry-broken phase, in which the bosonic degrees of freedom acquire macroscopic occupations, we displace the bosonic operators as

$$a^\dagger \to c^\dagger + \sqrt{\alpha}\,, \tag{G.6}$$

$$b^\dagger \to d^\dagger - \sqrt{\beta}\,. \tag{G.7}$$

with α and β real parameters whose value we will determine later but which are assumed to scale as N. This is equivalent to assuming that in the symmetry broken phases the two modes acquire a macroscopic occupation. With these displacements and ignoring constants, the Hamiltonian becomes

$$\begin{aligned} H = \omega_z \left(d^\dagger d - \sqrt{\beta}(d + d^\dagger) \right) - J \frac{k}{N} \left(d^\dagger \sqrt{\xi} + \sqrt{\xi} d - 2\sqrt{\beta}\sqrt{\xi} \right)^2 \\ + \Omega \left(c^\dagger c + \sqrt{\alpha}(c + c^\dagger) \right) \\ + \lambda \sqrt{\frac{k}{N}} \left(d^\dagger \sqrt{\xi} + \sqrt{\xi} d - 2\sqrt{\beta}\sqrt{\xi} \right) \left(c + d^\dagger + 2\sqrt{\alpha} \right)\,, \end{aligned} \tag{G.8}$$

with

$$\sqrt{\xi} = \sqrt{1 - \frac{d^\dagger d - \sqrt{\beta}(d + d^\dagger)}{k}}\,, \tag{G.9}$$

and $k = N - \beta$. Taking the thermodynamic limit by expanding the square root $\sqrt{\xi}$ and setting terms with overall powers of N in the denominator to zero we

obtain

$$\begin{aligned} H = &\left\{\omega_z + \frac{2\lambda}{k}\sqrt{\frac{\alpha\beta k}{2j}} + 4J\frac{\beta}{N}\right\} d^\dagger d \\ &+ \left\{\frac{\lambda}{2k^2}\sqrt{\frac{\alpha\beta k}{N}}(2k+\beta) + J\frac{k}{N}\left(\frac{4\beta}{k} - 1\right)\right\}\left(d + d^\dagger\right)^2 \\ &+ \Omega c^\dagger c + \frac{2\lambda}{k}\sqrt{\frac{k}{N}}\left(\frac{N}{2} - \beta\right)\left(d + d^\dagger\right)\left(c + c^\dagger\right) \\ &+ \left\{\frac{4\lambda}{k}\sqrt{\frac{\alpha k}{N}}\left(\frac{N}{2} - \beta\right) - \omega_z\sqrt{\beta} + \frac{8J\sqrt{\beta}}{N}\left(\frac{N}{2} - \beta\right)\right\}\left(d + d^\dagger\right) \\ &+ \left\{2\lambda\sqrt{\frac{\beta k}{N}} - \Omega\sqrt{\alpha}\right\}\left(c + c^\dagger\right) \end{aligned} \tag{G.10}$$

To eliminate the linear terms we impose

$$2\lambda\sqrt{\frac{\beta k}{N}} - \Omega\sqrt{\alpha} = 0\,, \tag{G.11}$$

$$\frac{4\lambda}{k}\sqrt{\frac{\alpha k}{N}}\left(\frac{N}{2} - \beta\right) - \omega_z\sqrt{\beta} + \frac{8J}{N}\left(\frac{N}{2} - \beta\right)\sqrt{\beta}\,. \tag{G.12}$$

These equations admit a trivial solution $\sqrt{\alpha} = \sqrt{\beta} = 0$, which corresponds to the normal phase, and a non-trivial solution for $\omega_z < J_{\text{eff}}$

$$\sqrt{\alpha} = \frac{\lambda}{\Omega}\sqrt{N(1-\tilde{\mu}^2)}\,, \tag{G.13}$$

$$\sqrt{\beta} = \sqrt{\frac{N}{2}(1-\tilde{\mu})}\,, \tag{G.14}$$

with $\tilde{\mu} = \omega_z/(4J_{\text{eff}})$ and $J_{\text{eff}} = J + \lambda^2/\Omega$, which corresponds to the symmetry-broken phase. Accordingly, the Hamiltonian in the normal phase reads

$$H = \omega_z d^\dagger d - J\left(d + d^\dagger\right)^2 + \Omega c^\dagger c + \lambda\left(d + d^\dagger\right)\left(c + c^\dagger\right)\,, \tag{G.15}$$

and in the symmetry-broken phase

$$\begin{aligned} H = &\frac{\omega_z}{2\tilde{\mu}}(1+\tilde{\mu})d^\dagger d + \Omega c^\dagger c + \lambda\tilde{\mu}\sqrt{\frac{2}{1+\tilde{\mu}}}\left(d + d^\dagger\right)\left(c + c^\dagger\right) \\ &+ \left\{\omega_z\frac{(1-\tilde{\mu})(3+\tilde{\mu})}{8\tilde{\mu}(1+\tilde{\mu})} - 2J\frac{\tilde{\mu}^2}{1+\tilde{\mu}}\right\}\left(d + d^\dagger\right)^2\,. \end{aligned} \tag{G.16}$$

These can be diagonalized with a Bogoliubov transformation to obtain the polaritons of Eq. (5.10).

G.2 Transverse Dicke-LMG model

Here we will apply the same method to obtain the polaritons of the transverse Dicke-LMG model. To avoid repetition, we will present the main equations and we will discuss only the differences between the two models.

The ground-state sector of the Hamiltonian of the transverse Dicke-LMG model [See Eq. (5.5)] can be written in terms of maximum-total-spin operators as

$$H = \omega_z S_z + \frac{\omega_x}{2}\left(S_+ + S_-\right) - \frac{4J}{N}S_z^2 + \Omega a^\dagger a + \frac{\lambda}{\sqrt{N}}\left(S_+ + S_-\right)\left(a + a^\dagger\right) , \tag{G.17}$$

After the Holstein-Primakov trasnformation, the Hamiltonian reads

$$\begin{aligned} H = \omega_z b^\dagger b + \frac{\omega_x\sqrt{N}}{2}\left(b^\dagger\sqrt{1-\frac{b^\dagger b}{N}} + \sqrt{1-\frac{b^\dagger b}{N}}\,b\right) - \frac{4J}{N}\left(b^\dagger b - \frac{N}{2}\right)^2 \\ + \Omega a^\dagger a + \lambda\left(b^\dagger\sqrt{1-\frac{b^\dagger b}{N}} + \sqrt{1-\frac{b^\dagger b}{N}}\,b\right)\left(a + a^\dagger\right) . \end{aligned} \tag{G.18}$$

Once again, we introduce the displacements of Eqs. (G.6) and (G.7), which yield

$$\begin{aligned} H = \omega_z\left(d^\dagger d - \sqrt{\beta}(d + d^\dagger)\right) + \frac{\omega_x}{2}\sqrt{k}\left(d^\dagger\sqrt{\xi} + \sqrt{\xi}d - 2\sqrt{\beta}\sqrt{\xi}\right) \\ - \frac{4J}{N}\left(d^\dagger d - \sqrt{\beta}(d + d^\dagger) + \beta - \frac{N}{2}\right)^2 + \Omega\left(c^\dagger c + \sqrt{\alpha}(c + c^\dagger)\right) \\ + \lambda\sqrt{\frac{k}{N}}\left(d^\dagger\sqrt{\xi} + \sqrt{\xi}d - 2\sqrt{\beta}\sqrt{\xi}\right)\left(c + d^\dagger + 2\sqrt{\alpha}\right) . \end{aligned} \tag{G.19}$$

Here we take the thermodynamic limit by expanding the square root $\sqrt{\xi}$ and the square in the first term of the second line and neglecting terms with overall

powers of N in the denominator, obtaining

$$\begin{aligned} H = &\left\{\omega_z + \frac{2\lambda}{k}\sqrt{\frac{\alpha\beta k}{2j}} + \frac{8J}{N}\left(\frac{N}{2}-\beta\right)\right\} d^\dagger d \\ &+ \left\{\frac{\lambda}{2k^2}\sqrt{\frac{\alpha\beta k}{N}}(2k+\beta) - 4J\frac{\beta}{N}\right\}\left(d+d^\dagger\right)^2 \\ &+ \Omega c^\dagger c + \frac{2\lambda}{k}\sqrt{\frac{k}{N}}\left(\frac{N}{2}-\beta\right)\left(d+d^\dagger\right)\left(c+c^\dagger\right) \\ &+ \left\{\frac{4\lambda}{k}\sqrt{\frac{\alpha k}{N}}\left(\frac{N}{2}-\beta\right) - \omega_z\sqrt{\beta} - \frac{8J\sqrt{\beta}}{N}\left(\frac{N}{2}-\beta\right)\right. \\ &\left. + \frac{\omega_x}{\sqrt{k}}\left(\frac{N}{2}-\beta\right)\right\}\left(d+d^\dagger\right) + \left\{2\lambda\sqrt{\frac{\beta k}{N}} - \Omega\sqrt{\alpha}\right\}\left(c+c^\dagger\right) \end{aligned} \tag{G.20}$$

To eliminate the linear terms we impose

$$2\lambda\sqrt{\frac{\beta k}{N}} - \Omega\sqrt{\alpha} = 0\,, \tag{G.21}$$

$$\frac{4\lambda}{k}\sqrt{\frac{\alpha k}{N}}\left(\frac{N}{2}-\beta\right) - \omega_z\sqrt{\beta} - \frac{8J\sqrt{\beta}}{N}\left(\frac{N}{2}-\beta\right) + \frac{\omega_x}{\sqrt{k}}\left(\frac{N}{2}-\beta\right) = 0\,. \tag{G.22}$$

In this case, since we are considering a finite longitudinal field ω_x the symmetry is always explicitly broken, so there is no spontaneous symmetry breaking. Accordingly, there is no trivial solution, and in general Eqs. (G.21) and (G.22) do not have an analytical solution. Nevertheless, they can be solved numerically, and the resulting Hamiltonian can be diagonalized with a Bogoliubov transform to obtain the polaritons that we show in Fig. 5.5.

For the sake of completeness, let us solve analytically the case of $\omega_x = 0$. In this case, Eqs. (G.21) and (G.22) admit a trivial solution $\sqrt{\alpha} = \sqrt{\beta} = 0$, which corresponds to the normal phase, and a non-trivial solution for $\omega_z < 4(\lambda^2/\Omega - J)$ with the same expression for $\sqrt{\alpha}$ and $\sqrt{\beta}$ as in Eqs. (G.13) and (G.14) but now with

$$\tilde{\mu} = \frac{\omega_z}{4\left(\frac{\lambda^2}{\Omega} - J\right)}\,, \tag{G.23}$$

which corresponds to the symmetry-broken phase. The difference in the value of $\tilde{\mu}$ between this (transverse) case and the longitudinal case showcases the fact that in the longitudinal case there is a synergy between the intrinsic and cavity-mediated interactions whereas in this (transverse) case there is a competition. Accordingly, the Hamiltonian in the normal phase reads

$$H = \tilde{\omega}_z d^\dagger d + \Omega c^\dagger c + \lambda\left(d+d^\dagger\right)\left(c+c^\dagger\right)\,, \tag{G.24}$$

with $\tilde{\omega}_z = \omega_z + 4J$, and in the symmetry-broken phase

$$H = (1+\tilde{\mu})\left(\frac{\omega_z}{2\tilde{\mu}} + 2J\right) d^\dagger d + \Omega c^\dagger c + \lambda\tilde{\mu}\sqrt{\frac{2}{1+\tilde{\mu}}}\left(d+d^\dagger\right)\left(c+c^\dagger\right) + \left\{\omega_z \frac{(1-\tilde{\mu})(3+\tilde{\mu})}{8\tilde{\mu}(1+\tilde{\mu})} - J\frac{(1-\tilde{\mu})(1+3\tilde{\mu})}{2(1+\tilde{\mu})}\right\}\left(d+d^\dagger\right)^2 . \tag{G.25}$$

These can be diagonalized with a Bogoliubov transformation to obtain the polaritons. In the normal phase, the Hamiltonian is that of a Dicke model with a bare spin energy $\tilde{\omega}_z$. Thus, the polaritons are the same as for the normal phase in Eq. (5.4) with the substitution $\omega_z \to \tilde{\omega}_z$. In the symmetry-broken phase, the polaritons can be written formally as

$$2\Omega_\pm^2 = \omega_\mathrm{A}^2 + 4\omega_\mathrm{A}\omega_\mathrm{B} + \Omega^2 \pm \sqrt{\left(\omega_\mathrm{A}^2 + 4\omega_\mathrm{A}\omega_\mathrm{B} - \Omega^2\right)^2 + 16\omega_\mathrm{A}\omega_\mathrm{C}^2\Omega}\,, \tag{G.26}$$

with

$$\omega_\mathrm{A} = (1+\tilde{\mu})\left(\frac{\omega_z}{2\tilde{\mu}} + 2J\right), \tag{G.27}$$

$$\omega_\mathrm{B} = \omega_z\frac{(1-\tilde{\mu})(3+\tilde{\mu})}{8\tilde{\mu}(1+\tilde{\mu})} - J\frac{(1-\tilde{\mu})(1+3\tilde{\mu})}{2(1+\tilde{\mu})}, \tag{G.28}$$

$$\omega_\mathrm{C} = \lambda\tilde{\mu}\sqrt{\frac{2}{1+\tilde{\mu}}}\,. \tag{G.29}$$

Appendix H

Transverse response function of the Ising chain in transverse field

The spectral decomposition of $\tilde{\chi}_{xx,0}$ reads

$$\tilde{\chi}_{xx,0} = -\frac{1}{N}\sum_n |\langle n|C_x|0\rangle|^2 \frac{2(E_n - E_0)}{\omega_+^2 - (E_n - E_0)^2}\,, \tag{H.1}$$

where $|n\rangle$ is the eigenstate of $H_{\text{eff}}^{\text{MF}}$ (5.23) with eigenvalue E_n. From Eq. (5.29) we see that

$$\langle n|C_x|0\rangle = \delta_{n0}\left(N + \sum_k v_k^2\right) - 2i\sum_k u_k v_k \langle n|\gamma_k^\dagger \gamma_{-k}^\dagger|0\rangle\,, \tag{H.2}$$

with [174, Chap. 10]

$$u_k = \sin(\theta_k/2)\,, \tag{H.3}$$
$$v_k = \cos(\theta_k/2)\,, \tag{H.4}$$
$$\tan\theta_k = \frac{\sin k}{\frac{\tilde{\omega}_x}{2J} - \cos k}\,. \tag{H.5}$$

With this, we find

$$\tilde{\chi}_{xx,0} = -\frac{16J^2}{N}\sum_k \frac{\sin^2 k}{\epsilon_k(\omega_+^2 - 4\epsilon_k^2)} \tag{H.6}$$

and in the thermodynamic limit, $\lim_{N\to\infty} N^{-1}\sum_k f_k = \int_{-\pi}^{\pi} dk/(2\pi) f_k$, we obtain Eq. (5.28).

Appendix I

Solving the equation of motion of the cavity degrees of freedom

We use a change of variables to a "rotating frame": $\bar{\alpha} = \alpha e^{i\omega_c t}$, $\bar{\boldsymbol{S}} = \boldsymbol{S} e^{i\omega_c t}$. Using these rotating variables, Eq. (6.7) becomes

$$\dot{\bar{\alpha}} = -i\frac{\gamma}{\hbar}\sum_i \bar{\boldsymbol{S}}_i \cdot \boldsymbol{B}_{\mathrm{rms}}(\boldsymbol{r}_i)\,, \tag{I.1}$$

which is solved by

$$\bar{\alpha} = \alpha_0 - i\frac{\gamma}{\hbar}\int_0^t d\tau \sum_i \bar{\boldsymbol{S}}_i(\tau) \cdot \boldsymbol{B}_{\mathrm{rms}}(\boldsymbol{r}_i)\,. \tag{I.2}$$

Here, $\alpha_0 = \bar{\alpha}_0 = \alpha(t=0)$. Reversing the change of variable yields

$$\alpha = \alpha_0 e^{-i\omega_c t} - i\frac{\gamma}{\hbar}\int_0^t d\tau e^{i\omega_c(\tau - t)} \sum_i \boldsymbol{S}_i(\tau) \cdot \boldsymbol{B}_{\mathrm{rms}}(\boldsymbol{r}_i)\,. \tag{I.3}$$

Now, by noting that $\boldsymbol{S}_i^* = \boldsymbol{S}_i$, summing $\alpha + \alpha^*$ yields

$$\alpha(t) + \alpha^*(t) = 2\,\mathrm{Re}\left(\alpha_0 e^{-i\omega_c t}\right) + \frac{2\gamma}{\hbar}\int_0^t d\tau \sin(\omega_c(\tau - t)) \sum_i \boldsymbol{S}_i(\tau) \cdot \boldsymbol{B}_{\mathrm{rms}}(\boldsymbol{r}_i)\,, \tag{I.4}$$

with $\alpha_0 = \alpha(t=0)$ the initial condition of α. Substituting Eq. (I.4) into Eq. (6.6) yields $\dot{\boldsymbol{S}}_i = -\gamma \boldsymbol{S}_i \times \boldsymbol{B}'_{\mathrm{eff}}(\boldsymbol{r}_i)$, with $\boldsymbol{B}'_{\mathrm{eff}}(\boldsymbol{r}_i) = \boldsymbol{B}_{\mathrm{eff}}(\boldsymbol{r}_i) + \boldsymbol{B}_{\mathrm{cav}}(\boldsymbol{r}_i)$, $\boldsymbol{B}_{\mathrm{cav}}(\boldsymbol{r}_i) = \boldsymbol{B}_{\mathrm{rms}}(\boldsymbol{r}_i)\Gamma(t)$ and

$$\Gamma(t) = 2\,\mathrm{Re}\left(\alpha_0 e^{-i\omega_c t}\right) + \frac{2\gamma}{\hbar}\int_0^t d\tau \sin(\omega_c(\tau - t)) \sum_i \boldsymbol{S}_i(\tau) \cdot \boldsymbol{B}_{\mathrm{rms}}(\boldsymbol{r}_i)\,. \tag{I.5}$$

We introduce dissipation in the cavity by promoting $\omega_c \to \omega_c - i\kappa$ in Eq. (6.7). This corresponds to local dissipation at the level of a Linblad master equation for the cavity. As a result, Eq. (I.5) becomes

$$\begin{aligned}\Gamma(t) &= 2e^{-\kappa t}\,\mathrm{Re}\left(\alpha_0 e^{-i\omega_c t}\right) \\ &+ \frac{2\gamma}{\hbar}\int_0^t d\tau e^{-\kappa(\tau-t)}\sin(\omega_c(\tau-t))\sum_i \boldsymbol{S}_i(\tau)\cdot\boldsymbol{B}_{\mathrm{rms}}(\boldsymbol{r}_i)\,.\end{aligned} \tag{I.6}$$

Finally, we can express $\Gamma(t)$ in terms of the reduced magnetization, which is Mumax3's natural variable, to yield Eq. (6.13).

Appendix J

Workflow in Mumax3-cQED

J.1 API of Mumax3-cQED

Mumax3-cQED has been implemented as a fork of Mumax3[1]. The source code, including detailed installation intructions for UNIX and Windows systems, is hosted in a Git repository[2]. A summary of the source code changes implemented in Mumax3-cQED is provided in [66]. The new Mumax3-cQED source code has been tested in Windows 10 with *go 1.9* and *CUDA 10.2* and in *Debian 12 Bookworm* with *go 1.9* and *CUDA 12.0*. In both cases a GPU *NVIDIA RTX A4000* has been used.

After installation, Mumax3-cQED follows a script-based workflow inherited from Mumax3. Mumax3-cQED accepts an input script that defines the parameters and initial conditions of the micromagnetic simulation and returns output data representing the results of the simulation. We have introduced a new set of built-in instructions for the scripting language that extend the existing API of Mumax3:

- B_rms (type `vector`): Zero-point magnetic field (vacuum field) of the cavity [See Eq. (6.5)]. This is a three-component vector, it can take a single homogeneous value or it can take spatially-dependent values loaded from an OVF file (units T).
- Wc (type `float64`): Resonant frequency of the cavity [See Eq. (6.5)] (units rad$\cdot$ s^{-1}).
- Kappa (type `float64`): Cavity dissipation rate [See Eq. (6.13)] (units rad$\cdot$ s^{-1}).

[1] https://github.com/mumax/3
[2] https://github.com/Mumax3-cQED/mumax3-cqed

- X0 (type `float64`): Initial value of $x_0 = 2\,\mathrm{Re}(\alpha)$ [See Eq. (6.20)] (default value 0).

- P0 (type `float64`): Initial value of $p_0 = -2\,\mathrm{Im}(\alpha)$ [See Eq. (6.20)] (default value 0).

- HBAR (type `float64`): Reduced Planck constant (default value 1.05457182e−34 `J · s`).

- ResetMemoryTerm() (type `func`): Function to reset the memory term Γ [See Eq. (6.20)]. Resetting the memory term amounts to establishing the current state of the simulation as corresponding to the initial time, $t = 0$, at which the cavity and the magnet couple. This allows to chain different simulations in the same script.

- CavityFeatureStatus (type `int`): Read-only variable to check whether the cavity feature is active or not, it can be invoked from the print as `print(CavityFeatureStatus)`. It offers a sanity check, it returns 1 if B_rms has been set (cavity enabled) and 0 otherwise (cavity disabled).

In J.2 we discuss how the cavity $\boldsymbol{B}_{\mathrm{rms}}$ can be computed with other software and in J.3 we provide an example script showing how it can be loaded into Mumax3-cQED and used in a simulation. This and other example scripts are included in the source code. In addition to these variables that set the cavity parameters, we have also introduced some control instructions to provide the user with detailed information about the simulation:

- ShowSimulationSummary (type `boolean`): Whether to show a summary of the simulation after calling the `run()` function in the script. The summary is printed to the console and to the log file (default value `true`).

- PrintScriptExecutionTime() (type `func`): Function to time the script execution or a portion of it, depending on the value of StartCheckPoint. It prints the start and end times and their difference to the console and to the log file.

- StartCheckPoint (type `date`): Variable to set the start time for the timing of the script execution. In principle, it must be set to `StartCheckPoint = now()` anywhere in the code to time the script execution from that point onwards (default value `now()` called at the beginning of the script execution).

J.2 Simulations of $\boldsymbol{B}_{\mathrm{rms}}$

The spatial distribution of zero-point field fluctuations created by the resonator at the sample's position is calculated numerically. This is typically done by assuming a *constant* zero-point current i_{rms} that creates $\boldsymbol{B}_{\mathrm{rms}}(\boldsymbol{r}_i)$ at the field anti-node. Notice that i_{rms} is also assumed to be constant in time since time-dependence is given by the photon operators a and $a^\dagger$ in the Hamiltonian of Eq. 6.5.

In the case of the three-dimensional re-entrant cavity, we use COMSOL. The magnitude of B_{rms} is chosen so to reproduce the results by Goryachev *et al.* [196]. For the bright mode ($f_{\uparrow\downarrow} = 20.8$ GHz), we set two antiparallel equal currents of $i_{\mathrm{rms}} = 785$ nA and calculate the resulting spatial distribution of $\boldsymbol{B}_{\mathrm{rms}}(\boldsymbol{r}_i)$ (see Fig. 6.3c). We recall that the latter will be larger than the actual field produced by the cavity by a factor of $(800)^{3/2}$. This accounts for the fact that the sphere's radius in the simulation is 800 times smaller than in the experiment. Inserting the resulting $\boldsymbol{B}_{\mathrm{rms}}(\boldsymbol{r}_i)$ into mumax3-cQED (as explained below) we obtain a peak splitting at resonance equal to $2g_{\uparrow\downarrow}/2\pi \sim 2$ GHz. For the dark mode, we scale down the intensity of zero-point current fluctuations by a factor proportional to the resonance frequency $f_{\uparrow\uparrow} = 13.2$ GHz. This results into two parallel equal currents of $i_{\mathrm{rms}} = 498$ nA that yield the spatial distribution of $\boldsymbol{B}_{\mathrm{rms}}(\boldsymbol{r}_i)$ shown in Fig. 6.3d.

In the case of the superconducting cpw resonator, we use the software 3D-MLSI. This code solves the London equations to calculate the space-dependent distribution of magnetic fields created by the resulting supercurrents [269]. One can estimate the zero-point current at the field antinode from the mode frequency ω_0 and the impedance of the circuit Z_0 using the formula derived in Ref. [153]:

$$i_{\mathrm{rms}} = \omega_0 \sqrt{\frac{\hbar\pi}{4Z_0}}\,, \tag{J.1}$$

We use $\omega_0/2\pi = 1.4$ GHz and $Z_0 = 50\ \Omega$ yielding $i_{\mathrm{rms}} = 11.3$ nA. This produces zero-point field fluctuations that strongly depend on the line-width of the central transmission line w as shown in the inset of Fig. 6.4a.

Once the spatial distribution of $\boldsymbol{B}_{\mathrm{rms}}(\boldsymbol{r}_i)$ is obtained, we convert it to OVF format (`brmsfile.ovf`) and pass it to the script.

J.3 Micromagnetic simulations with Mumax3-cQED

Simulations presented here are based on two materials widely used in cavity magnonics. YIG is a ferrimagnet famous for its record low Gilbert damping

parameter $\alpha \sim 10^{-3} - 10^{-5}$ [270]. We set the saturation magnetization to $M_{\text{sat}} = 0.14 \times 10^6$ A/m, the exchange stiffness $A = 0.37 \times 10^{-11}$ J/m and $\alpha = 10^{-4}$. On the other hand, Permalloy yields shorter spin wave lifetime but has the advantage of being easy to evaporate on different substrates. In the simulations we set $M_{\text{sat}} = 0.86 \times 10^6$ A/m, $A = 1.3 \times 10^{-11}$ J/m and $\alpha = 1 \times 10^{-2}$.

The action of the cavity is contained in the previously calculated distribution of $\boldsymbol{B}_{\text{rms}}(\boldsymbol{r}_i)$ given in the file brmsfile.ovf. On the other hand, to calculate the polariton dynamics we apply a space- and time-dependent excitation magnetic field. A drawback of the current implementation of Mumax3-cQED is that one cannot excite the system by driving the cavity, since the latter is eliminated as a dynamical degree of freedom. This prevents us from directly computing the cavity transmission. To mitigate this effect, we drive the ferromagnet with an excitation field that mimics the one created by the cavity. For this purpose, we use the same OVF file (brmsfile.ovf) multiplied by a proportionality factor that accounts for the intensity of the excitation magnetic field (much larger than the zero-point field fluctuations). Finally, we multiply it by the time-dependent function $\text{sinc}(\omega_{\text{cutoff}} t)$. This is equivalent to exciting all spin-waves at frequencies below ω_{cutoff}. The broadband dynamic response of the ferromagnet is finally obtained by calculating the numerical Fourier transform of the resulting time-dependent spatially-averaged magnetization along the relevant direction ($\mathbf{x}$ or $\mathbf{y}$ in the previous example).

Appendix K

Properties of the long-range interaction matrix

K.1 Loss of extensivity

In Fig. K.1 we illustrate the extensivity (or lack thereof) of a model with power-law decaying interactions in $d = 1$. We compute $\tilde{N} = \sum_j \tilde{J}_{ij}$ as a measure of the coupling energy per spin. In the absence of Kac's rescaling, this quantity must not scale with the number of spins N to keep the total coupling energy extensive. Fig. K.1 shows that this is not the case for $\alpha < 1$. The threshold case $\alpha = 1$ is highlighted for clarity and corresponds to a logarithmic dependence of $\tilde{N}$ on N. For $\alpha > 1$ the dependence is sublogarithmic, i.e., $\tilde{N}$ becomes independent of N at large N. As discussed in the main text, loss of extensivity is prevented with Kac's rescaling, which we can now understand as a renormalization of the total coupling energy by the energy per spin.

In fact, for $d = 1$ and $N \to \infty$ the scaling of $\tilde{N}$ can be computed analytically, since

$$\tilde{N} = \sum_{i}^{N} \tilde{J}_{ij} = b + 2 \sum_{r=1}^{\infty} r^{-\alpha} \,. \tag{K.1}$$

As b converges to a constant value when $N \to \infty$ (will be shown in App. K.2), the convergence of $\tilde{N}$ will be ruled by the convergence of the infinite series. For $\alpha > 1$ the series is convergent, so $\tilde{N}$ becomes independent of N at large N. For $\alpha \leq 1$ the series diverges.

K.2 Diagonal terms can be neglected in strong-long range models

Setting $b \neq 0$ introduces a new diagonal term in the Hamiltonian

$$-\sum_{i}^{N} \Gamma b/\tilde{N} \mathcal{C}_i^2 \,. \tag{K.2}$$

Importantly, this term contains a factor $b/\tilde{N}$. We know from App. K.1 that $\lim_{N\to\infty} \tilde{N} = \infty$ for $\alpha < d$. So if b is independent of N for $N \to \infty$, the diagonal term vanishes in the thermodynamic limit.

It can be shown analytically that this is the case for $d = 1$ and $\alpha > 0$. From Eq. (7.5) we see that the smallest eigenvalue of J when $N \to \infty$ is given by

$$D_{\min} = \frac{\Gamma}{\tilde{N}} \sum_{\mathbf{r}} \tilde{J}\left(\mathbf{r}\right) (-1)^r = \frac{\Gamma}{\tilde{N}} \left(b + 2 \sum_{r=1}^{\infty} (-1)^r \, r^{-\alpha} \right) . \tag{K.3}$$

Here $r = |\mathbf{r}|$. Hence, setting $D_{\min} = 0$ fixes

$$b = -2 \sum_{r=1}^{\infty} (-1)^r r^{-\alpha} \,. \tag{K.4}$$

The convergence of this series is proven by means of the alternating series test, since the absolute value of its terms monotonically decrease to 0. For $\alpha = 0$ and finite N, as $\tilde{J}_{i\neq j} = 1$, b must be fixed to 1 to ensure that the smallest eigenvalue of $\tilde{J}$ is zero. This is manifestly independent of N.

In other dimensions or other models, this test can be done graphically. In Fig. K.1 we show the value of b, for a model with power-law decaying interactions in $d = 1$, computed numerically for different values of N when b is chosen so that the smallest eigenvalue of J is zero. One can see that in this case the numerical results converge to the analytical prediction. The same behaviour is observed in other dimensions.

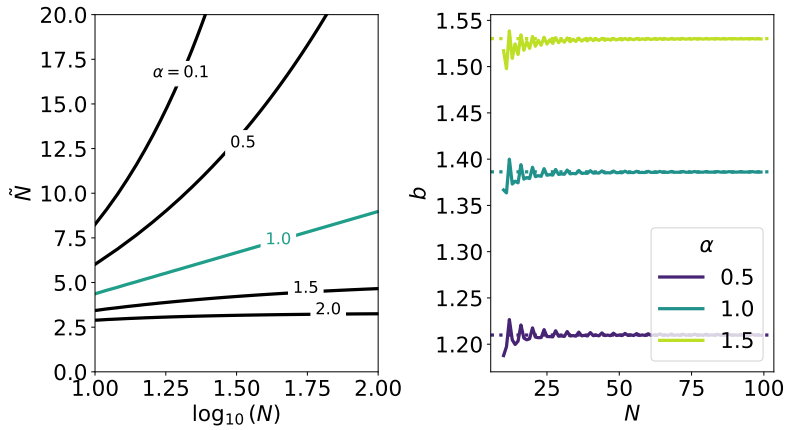

Figure K.1: Scaling of $\tilde{N} = \sum_j^N \tilde{J}_{ij}$ (left) and b (right) for a one dimensional model ($d = 1$) with power-law decaying interactions [See Eq. (7.2)]. Here b is fixed such that the smallest eigenvalue of $\tilde{J}$ is zero. The dotted lines indicate the analytical asymptote.

Appendix L

The (anti)homogeneous extremum is the global minimum

Equation (7.19) defines the extrema of $f[u_k]$. From here, let us define $\mu_i = \sum_k \lambda_{ik} u_k$ as alternative optimization variables and express the extremum condition (7.19) in terms of them

$$\bar{\mu}_j = s \sum_i^N J_{ij} \frac{\bar{\mu}_i}{\bar{\epsilon}_i} B_s(2s\beta\bar{\varepsilon}_i)\,. \tag{L.1}$$

Let us express f in terms of the variables $\{\mu_i\}$

$$f[\mu_i] = \frac{1}{N}\sum_{ij}^N \mu_i J^+_{ij} \mu_j - \frac{1}{N\beta}\sum_i^N \ln\left[\frac{\sinh((2s+1)\beta\varepsilon_i)}{\sinh(\beta\varepsilon_i)}\right], \tag{L.2}$$

with $NJ^+_{ij} = \sum_k \lambda_{ik}\Omega_k\lambda_{jk}$ and

$$2\bar{\varepsilon}_i = \sqrt{\omega_z^2 + 4\mu_i^2}\,, \tag{L.3}$$

in the absence of longitudinal field, $\omega_x = 0$. Note that $JJ^+J = J$. Substituting Eq. (L.1) in Eq. (L.2) yields an expression for f at the extrema

$$\begin{aligned} f[\bar{\mu}_i] &= \frac{s}{N}\sum_i^N B_s(2s\beta\bar{\varepsilon}_i)\frac{\bar{\mu}_i^2}{\bar{\varepsilon}_i} - \frac{1}{N\beta}\sum_i^N \ln\left[\frac{\sinh((2s+1)\beta\bar{\varepsilon}_i)}{\sinh(\beta\bar{\varepsilon}_i)}\right] \\ &= \frac{1}{N}\sum_i^N \xi(\bar{\mu}_i^2)\,. \end{aligned} \tag{L.4}$$

Equation (L.4) means that among all the possible local minima, the global one must satisfy that $|\bar{\mu}_i| = \bar{\mu}$ for each lattice site, in order to minimize each of

the N terms $\xi(\bar{\mu}_i^2)$. Due to the structure of the matrix λ_{ik}, the only possible configuration that meets $|\bar{\mu}_i| = \bar{\mu}$ is the homogeneous solution

$$\bar{\mu}_i = \bar{\mu}\,, \tag{L.5}$$

in the ferromagnetic case, and the antihomogeneous solution

$$\bar{\mu}_i = (-1)^i \bar{\mu}\,. \tag{L.6}$$

in the unfrustrated antiferromagnetic case.

To see how this affects the variables $\{\bar{u}_k\}$ it is useful to invert the relation and write u_k in terms of the $\{\mu_i\}$, yielding

$$u_k = \frac{1}{N}\sum_i^N \lambda_{ik}\mu_i\,. \tag{L.7}$$

Since the $\{\lambda_{ik}\}$ are the Fourier modes resulting from the diagonalization of J, we have $\sum_i \lambda_{ik} = N\delta_{k0}$ in the ferromagnetic case and $\sum_i (-1)^i \lambda_{ik} = N\delta_{k0}$ in the unfrustrated antiferromagnetic case. Accordingly, we find $\bar{u}_{k\neq 0} = \bar{\mu}\delta_{k0}$ in both cases.

This proof can be extended to the case with longitudinal field $\omega_x \neq 0$ in the ferromagnetic case, as long as it is uniform in the chain, since doing so keeps the model homogeneous. However, the same is not possible in the antiferromagnetic case since even a uniform longitudinal field breaks the antihomogeneity in the model. This is because the two sublattices no longer experience equal and opposite fields and interactions in the presence of a uniform longitudinal field.

Appendix M

Classical analysis of the phase transition for $\alpha = 0$

M.1 Classical energy landscape

For $\alpha = 0$ the interaction is homogeneous and alternating in sign and we can express Hamiltonian (7.11) in terms of total spin operators for each of the sublattices, $J^\gamma_\Lambda = \sum_{i\in\mathcal{L}(\Lambda)} S^\gamma_i$, with $\Lambda = A, B$ the sublattice index and $\mathcal{L}(\Lambda)$ the corresponding sublattice,

$$H = -\omega_z \left(J^z_A + J^z_B\right) - \omega_x \left(J^x_A + J^x_B\right) - \frac{\Gamma}{N}\left(J^x_A - J^x_B\right)^2 . \tag{M.1}$$

This Hamiltonian commutes with the total spin operators, $J^2_\Lambda = (J^x_\Lambda)^2 + (J^y_\Lambda)^2 + (J^z_\Lambda)^2$. Consequently, it connects only states with the same total spins J^2_A and J^2_B. Using exact diagonalization for finite sizes, we show in Appendix M.2 that the ground state always lies on the subspace of maximum total spins. This implies that the ground state properties of the model are perfectly captured by a model of two spins of sizes, $j_A = j_B = sN/2$, interacting according to Eq. (M.1). In the thermodynamic limit, $N \to \infty$, the description is further simplified by the fact that these spins can be described exactly in their classical limit [112]. We can therefore study the energy resulting from replacing the spins with classical magnetizations $J^\gamma_\Lambda \to sN/2 m^\gamma_\Lambda$. The magnetizations are unit vectors that we can assume to lie on the x, z plane $\boldsymbol{m}_\Lambda = (\cos\theta_\Lambda, 0, \sin\theta_\Lambda)$.

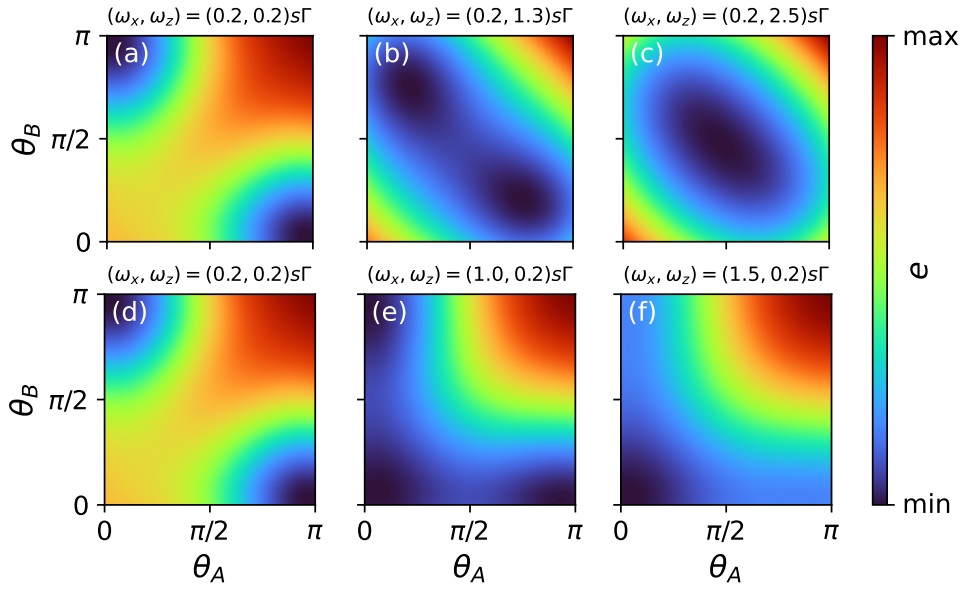

Figure M.1: Classical energy landscape [Eq. (M.2)] for different transverse ω_z and longitudinal ω_x fields.

With this, the energy per site reads

$$\begin{aligned} e(\theta_A, \theta_B) = &- \frac{s\omega_z}{2} (\sin\theta_A + \sin\theta_B) \\ &- \frac{s\omega_x}{2} (\cos\theta_A + \cos\theta_B) \\ &- \frac{s^2\Gamma}{4} (\cos\theta_A - \cos\theta_B)^2 \ . \end{aligned} \tag{M.2}$$

The ground state staggered magnetization is given by $m_s = s(\cos\bar{\theta}_A - \cos\bar{\theta}_B)/2$, with $\bar{\theta}_A$ and $\bar{\theta}_B$ the minimizers of $E(\theta_A, \theta_B)$.

In Fig. M.1 we show the energy landscape as a function of θ_A and θ_B for different values of ω_x and ω_z. For $\omega_x/(s\Gamma) \ll 1$ and $\omega_z/(s\Gamma) \ll 2$ there are two global minima at $(\bar{\theta}_A, \bar{\theta}_B) = (0, \pi)$ and $(\bar{\theta}_A, \bar{\theta}_B) = (\pi, 0)$ corresponding to the two symmetric antiferromagnetic configurations with $m_s = \pm s$. If ω_x is kept fixed and ω_z is increased until $\omega_z/(s\Gamma) > 2$, the two global minima merge into a single one at $(\bar{\theta}_A, \bar{\theta}_B) = (\pi/2, \pi/2)$ corresponding to a paramagnetic configuration with $m_s = 0$. The coalescence of minima is indicative of a second-order phase transition. Contrarily, if ω_z is kept fixed and ω_x is increased a new local minimum progressively develops at $(\theta_A, \theta_B) = (0, 0)$ until at $\omega_x/(s\Gamma) \geq 1$ it becomes the global minimum, corresponding to a paramagnetic configuration with $m_s = 0$. The former global minima become local minima. The formation of a new local minimum that grows until becoming the global minimum is

indicative of a first-order phase transition. In summary, Fig. M.1 shows that the energy landscape encoded in $E(\theta_A, \theta_B)$ displays the typical behavior associated with first- and second-order phase transitions.

We find that the phase diagram predicted by this simple classical model coincides with the phase diagram computed exactly and shown in Fig. 7.6. It is therefore an equivalent formulation of the minimization problem presented in Eq. (7.37), in terms of two variables θ_A, θ_B instead of the single minimization variable u. In this sense, we can understand that Eq. (7.37) provides the most concise formulation of the minimization problem, as a univariate function of the order parameter, that lends itself particularly well to the analysis in terms of the Landau theory of phase transitions that we performed in Sec. 7.4.1.

M.2 Verification using exact diagonalization

For $\alpha = 0$ there are two equivalent descriptions of the model in terms of either individual spins at each site, as in Hamiltonian (7.11), or in terms of total spin operators of each sublattice, as in Hamiltonian (M.1). As explained in App. M, the total spin of each sublattice J_Λ^2 is a conserved quantity and the Hamiltonian is block diagonal with blocks of fixed total spins. Here we diagonalize the subspace of maximum total spins, $j_A = j_B = sN/2$, and compare its low-energy spectrum to the low-energy spectrum of the full Hamiltonian (7.11). In Fig. M.2 we show that the ground-state energies of the two Hamiltonians coincide, with differences appearing in the multiplicity of excited states. We show this for $N = 10$ and $s = 1/2$ fixing $\omega_x/(s\Gamma) = 0.2$ and varying $\omega_z/(s\Gamma)$ and vice versa, but the same behavior is observed for any accessible system size N and spin size s and for any values of $\omega_x/(s\Gamma)$ and $\omega_z/(s\Gamma)$ of the phase diagram. This implies that the low energy physics are well captured by the subspace of maximum total spins, $j_A = j_B = sN/2$. This fact is exploited in App. M to provide a classical description of the ground state phase diagram.

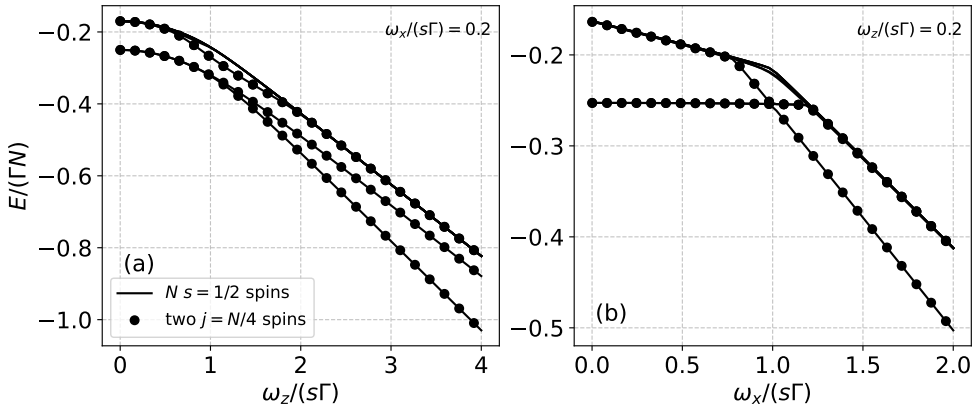

Figure M.2: Exact diagonalization spectra of Hamiltonian (M.1) for $N = 10$ and $s = 1/2$ as a function of ω_z with fixed $\omega_x/(s\Gamma) = 0.2$ on the top and as a function of ω_x with fixed $\omega_z/(s\Gamma) = 0.2$ on the bottom. The solid lines correspond to the first 15 energy levels of the full Hamiltonian, expressed as an ensemble of N $s = 1/2$ spins. The dots correspond to the first 5 energy levels of the subspace of maximum total spins, expressed as two spins of size $j_A = j_B = sN/2 = 5/2$ described by Hamiltonian (M.1).

List of publications

Publications included in this thesis:

- J. Román-Roche et al., "Photon condensation and enhanced magnetism in cavity qed", Phys. Rev. Lett. **127**, 167201 (2021)
- J. Román-Roche and D. Zueco, "Effective theory for matter in non-perturbative cavity QED", SciPost Phys. Lect. Notes, 50 (2022)
- J. Román-Roche et al., "Exact solution for quantum strong long-range models via a generalized hubbard-stratonovich transformation", Phys. Rev. B **108**, 165130 (2023)
- J. Román-Roche et al., "Bound polariton states in the dicke–ising model", Nanophotonics (2025)
- J. Román-Roche et al., "Linear response theory for cavity qed materials at arbitrary light-matter coupling strengths", Phys. Rev. B **111**, 035156 (2025)
- V. Herráiz-López et al., "First- and second-order quantum phase transitions in the long-range unfrustrated antiferromagnetic ising chain", Phys. Rev. B **111**, 014425 (2025)
- S. M.-L. del Rincón et al., *Mumax3-cqed: an extension of mumax3 to simulate magnon-photon interactions in cavity qed*, 2024

Bibliography

[1] T. Oka and S. Kitamura, "Floquet engineering of quantum materials", Annu. Rev. Condens. Matter Phys **10**, 387–408 (2019) (cit. on p. 5).

[2] F. J. Garcia-Vidal, C. Ciuti, and T. W. Ebbesen, "Manipulating matter by strong coupling to vacuum fields", Science **373**, eabd0336 (2021) (cit. on p. 6).

[3] F. Schlawin, D. M. Kennes, and M. A. Sentef, "Cavity quantum materials", Appl. Phys. Rev. **9**, 011312 (2022) (cit. on p. 6).

[4] J. Bloch, A. Cavalleri, V. Galitski, M. Hafezi, and A. Rubio, "Strongly correlated electron–photon systems", Nature **606**, 41–48 (2022) (cit. on p. 6).

[5] D. N. Basov, A. Asenjo-Garcia, P. J. Schuck, X. Zhu, and A. Rubio, "Polariton panorama", Nanophotonics **10**, 549–577 (2020) (cit. on p. 6).

[6] A. Thomas, J. George, A. Shalabney, M. Dryzhakov, S. J. Varma, J. Moran, T. Chervy, X. Zhong, E. Devaux, C. Genet, J. A. Hutchison, and T. W. Ebbesen, "Ground-state chemical reactivity under vibrational coupling to the vacuum electromagnetic field", Angew. Chem. Int. Ed. **55**, 11462–11466 (2016) (cit. on p. 6).

[7] A. Thomas, L. Lethuillier-Karl, K. Nagarajan, R. M. A. Vergauwe, J. George, T. Chervy, A. Shalabney, E. Devaux, C. Genet, J. Moran, and T. W. Ebbesen, "Tilting a ground-state reactivity landscape by vibrational strong coupling", Science **363**, 615–619 (2019) (cit. on p. 6).

[8] J. A. Hutchison, T. Schwartz, C. Genet, E. Devaux, and T. W. Ebbesen, "Modifying chemical landscapes by coupling to vacuum fields", Angew. Chem. - Int. Ed. **51**, 1592–1596 (2012) (cit. on p. 6).

[9] J. Feist, J. Galego, and F. J. Garcia-Vidal, "Polaritonic chemistry with organic molecules", ACS Photonics **5**, 205–216 (2017) (cit. on p. 6).

[10] J. Fregoni, F. J. Garcia-Vidal, and J. Feist, "Theoretical challenges in polaritonic chemistry", ACS Photonics **9**, 1096–1107 (2022) (cit. on p. 6).

[11] E. Orgiu, J. George, J. A. Hutchison, E. Devaux, J. F. Dayen, B. Doudin, F. Stellacci, C. Genet, J. Schachenmayer, C. Genes, G. Pupillo, P. Samorì, and T. W. Ebbesen, "Conductivity in organic semiconductors hybridized with the vacuum field", Nat. Mater. **14**, 1123–1129 (2015) (cit. on p. 6).

[12] G. G. Rozenman, K. Akulov, A. Golombek, and T. Schwartz, "Long-range transport of organic exciton-polaritons revealed by ultrafast microscopy", ACS Photonics **5**, 105–110 (2017) (cit. on p. 6).

[13] G. L. Paravicini-Bagliani, F. Appugliese, E. Richter, F. Valmorra, J. Keller, M. Beck, N. Bartolo, C. Rössler, T. Ihn, K. Ensslin, C. Ciuti, G. Scalari, and J. Faist, "Magneto-transport controlled by landau polariton states", Nat. Phys. **15**, 186–190 (2018) (cit. on p. 6).

[14] J. Keller, G. Scalari, F. Appugliese, S. Rajabali, M. Beck, J. Haase, C. A. Lehner, W. Wegscheider, M. Failla, M. Myronov, D. R. Leadley, J. Lloyd-Hughes, P. Nataf, and J. Faist, "Landau polaritons in highly nonparabolic two-dimensional gases in the ultrastrong coupling regime", Phys. Rev. B **101**, 075301 (2020) (cit. on p. 6).

[15] R. H. Dicke, "Coherence in spontaneous radiation processes", Phys. Rev **93**, 99–110 (1954) (cit. on pp. 6, 16, 69, 70).

[16] K. Hepp and E. H. Lieb, "Equilibrium statistical mechanics of matter interacting with the quantized radiation field", Phys. Rev. A **8**, 2517–2525 (1973) (cit. on pp. 6, 17, 19).

[17] Y. K. Wang and F. T. Hioe, "Phase transition in the dicke model of superradiance", Phys. Rev. A **7**, 831–836 (1973) (cit. on pp. 6, 17, 20, 48, 52, 112).

[18] P. Kirton, M. M. Roses, J. Keeling, and E. G. Dalla Torre, "Introduction to the dicke model: from equilibrium to nonequilibrium, and vice versa", Adv. Quantum Technol. **2**, 1800043 (2019) (cit. on p. 6).

[19] F. Appugliese, J. Enkner, G. L. Paravicini-Bagliani, M. Beck, C. Reichl, W. Wegscheider, G. Scalari, C. Ciuti, and J. Faist, "Breakdown of topological protection by cavity vacuum fields in the integer quantum hall effect", Science **375**, 1030–1034 (2022) (cit. on pp. 6, 60, 68).

[20] A. Thomas, E. Devaux, K. Nagarajan, T. Chervy, M. Seidel, G. Rogez, J. Robert, M. Drillon, T. T. Ruan, S. Schlittenhardt, M. Ruben, D. Hagenmüller, S. Schütz, J. Schachenmayer, C. Genet, G. Pupillo, and T. W. Ebbesen, "Exploring superconductivity under strong coupling with the vacuum electromagnetic field", J. Chem. Phys **162**, 134701 (2025) (cit. on p. 6).

[21] A. Thomas, E. Devaux, K. Nagarajan, G. Rogez, M. Seidel, F. Richard, C. Genet, M. Drillon, and T. W. Ebbesen, "Large enhancement of ferromagnetism under a collective strong coupling of ybco nanoparticles", Nano Lett. **21**, 4365–4370 (2021) (cit. on p. 6).

[22] G. Jarc, S. Y. Mathengattil, A. Montanaro, F. Giusti, E. M. Rigoni, R. Sergo, F. Fassioli, S. Winnerl, S. Dal Zilio, D. Mihailovic, P. Prelovšek, M. Eckstein, and D. Fausti, "Cavity-mediated thermal control of metal-to-insulator transition in 1t-tas2", Nature **622**, 487–492 (2023) (cit. on p. 7).

[23] F. Schlawin, A. Cavalleri, and D. Jaksch, "Cavity-mediated electron-photon superconductivity", Phys. Rev. Lett. **122**, 133602 (2019) (cit. on p. 7).

[24] M. A. Sentef, M. Ruggenthaler, and A. Rubio, "Cavity quantum- electrodynamical polaritonically enhanced electron-phonon coupling and its influence on superconductivity", Sci. Adv. **4**, eaau6969 (2018) (cit. on p. 7).

[25] M. Kiffner, J. R. Coulthard, F. Schlawin, A. Ardavan, and D. Jaksch, "Manipulating quantum materials with quantum light", Phys. Rev. B **99**, 085116 (2019) (cit. on p. 7).

[26] J. Román-Roche, F. Luis, and D. Zueco, "Photon condensation and enhanced magnetism in cavity qed", Phys. Rev. Lett. **127**, 167201 (2021) (cit. on pp. 7, 70, 181).

[27] K. Masuki and Y. Ashida, "Cavity moiré materials: controlling magnetic frustration with quantum light-matter interaction", Phys. Rev. B **109**, 195173 (2024) (cit. on p. 7).

[28] P. A. Pantazopoulos, J. Feist, F. J. García-Vidal, and A. Kamra, "Unconventional magnetism mediated by spin-phonon-photon coupling", Nat. Commun. **15**, 4000 (2024) (cit. on pp. 7, 18).

[29] J. Mochida and Y. Ashida, "Cavity-enhanced kondo effect", Phys. Rev. B **110**, 035158 (2024) (cit. on p. 7).

[30] O. Dmytruk, M. Trif, and P. Simon, "Cavity quantum electrodynamics with mesoscopic topological superconductors", Phys. Rev. B **92**, 245432 (2015) (cit. on p. 7).

[31] O. Dmytruk, M. Trif, and P. Simon, "Josephson effect in topological superconducting rings coupled to a microwave cavity", Phys. Rev. B **94**, 115423 (2016) (cit. on p. 7).

[32] O. Dmytruk and M. Schirò, "Controlling topological phases of matter with quantum light", Commun. Phys **5**, 271 (2022) (cit. on pp. 7, 24, 87).

[33] C. A. Downing, T. J. Sturges, G. Weick, M. Stobi ńska, and L. Martín-Moreno, "Topological phases of polaritons in a cavity waveguide", Phys. Rev. Lett. **123**, 217401 (2019) (cit. on pp. 7, 68).

[34] B. Pérez-González, Á. Gómez-León, and G. Platero, "Topology detection in cavity qed", Phys. Chem. Chem. Phys. **24**, 15860–15870 (2022) (cit. on p. 7).

[35] B. Pérez-González, G. Platero, and Á. Gomez-León, "Light-matter correlations in Quantum Floquet engineering of cavity quantum materials", Quantum **9**, 1633 (2025) (cit. on p. 7).

[36] O. Dmytruk and M. Schirò, "Hybrid light-matter states in topological superconductors coupled to cavity photons", Phys. Rev. B **110**, 075416 (2024) (cit. on pp. 7, 24).

[37] B. Pérez-González, G. Platero, and Á. Gómez-León, "Quantum origin of anomalous floquet phases in cavity-qed materials", Commun. Phys **7**, 419 (2024) (cit. on p. 7).

[38] C. B. Dag and V. Rokaj, "Engineering topology in graphene with chiral cavities", Phys. Rev. B **110**, L121101 (2024) (cit. on p. 7).

[39] Z. Bacciconi, G. M. Andolina, and C. Mora, "Topological protection of majorana polaritons in a cavity", Phys. Rev. B **109**, 165434 (2024) (cit. on p. 7).

[40] Á. Gómez-León, M. Schirò, and O. Dmytruk, *High-quality poor man's majorana bound states from cavity embedding*, 2024 (cit. on p. 7).

[41] M. Schuler, D. D. Bernardis, A. M. Läuchli, and P. Rabl, "The vacua of dipolar cavity quantum electrodynamics", SciPost Phys. **9**, 066 (2020) (cit. on p. 7).

[42] Y. Ashida, A. ç. İmamo ğlu, J. Faist, D. Jaksch, A. Cavalleri, and E. Demler, "Quantum electrodynamic control of matter: cavity-enhanced ferroelectric phase transition", Phys. Rev. X **10**, 041027 (2020) (cit. on pp. 7, 18).

[43] D. Shin, S. Latini, C. Schäfer, S. A. Sato, E. Baldini, U. De Giovannini, H. Hübener, and A. Rubio, "Simulating terahertz field-induced ferroelectricity in quantum paraelectric $SrTiO_3$", Phys. Rev. Lett. **129**, 167401 (2022) (cit. on p. 7).

[44] S. Latini, D. Shin, S. A. Sato, C. Schäfer, U. De Giovannini, H. Hübener, and A. Rubio, "The ferroelectric photo ground state of srtio 3 : cavity materials engineering", Proc. Natl. Acad. Sci. U.S.A. **118**, e2105618118 (2021) (cit. on p. 7).

[45] K. Lenk, J. Li, P. Werner, and M. Eckstein, "Dynamical mean-field study of a photon-mediated ferroelectric phase transition", Phys. Rev. B **106**, 245124 (2022) (cit. on pp. 7, 24, 29, 52).

[46] J. Feist and F. J. Garcia-Vidal, "Extraordinary exciton conductance induced by strong coupling", Phys. Rev. Lett. **114**, 196402 (2015) (cit. on p. 7).

[47] J. Schachenmayer, C. Genes, E. Tignone, and G. Pupillo, "Cavity-enhanced transport of excitons", Phys. Rev. Lett. **114**, 196403 (2015) (cit. on p. 7).

[48] G. Sandik, J. Feist, F. J. García-Vidal, and T. Schwartz, "Cavity-enhanced energy transport in molecular systems", Nat. Mater. **24**, 344–355 (2024) (cit. on p. 7).

[49] D. Hagenmüller, S. De Liberato, and C. Ciuti, "Ultrastrong coupling between a cavity resonator and the cyclotron transition of a two-dimensional electron gas in the case of an integer filling factor", Phys. Rev. B **81**, 235303 (2010) (cit. on p. 7).

[50] V. Rokaj, M. Ruggenthaler, F. G. Eich, and A. Rubio, "Free electron gas in cavity quantum electrodynamics", Phys. Rev. Res. **4**, 013012 (2022) (cit. on pp. 7, 30, 41, 60, 61, 67).

[51] V. Rokaj, M. Penz, M. A. Sentef, M. Ruggenthaler, and A. Rubio, "Polaritonic hofstadter butterfly and cavity control of the quantized hall conductance", Phys. Rev. B **105**, 205424 (2022) (cit. on pp. 7, 60, 66, 68).

[52] V. Rokaj, J. Wang, J. Sous, M. Penz, M. Ruggenthaler, and A. Rubio, "Weakened topological protection of the quantum hall effect in a cavity", Phys. Rev. Lett. **131**, 196602 (2023) (cit. on pp. 7, 60, 63, 66, 68).

[53] C. Ciuti, "Cavity-mediated electron hopping in disordered quantum hall systems", Phys. Rev. B **104**, 155307 (2021) (cit. on pp. 7, 60, 68).

[54] G. Arwas and C. Ciuti, "Quantum electron transport controlled by cavity vacuum fields", Phys. Rev. B **107**, 045425 (2023) (cit. on p. 7).

[55] D. Svintsov, G. Alymov, Z. Devizorova, and L. Martin-Moreno, "One-dimensional electron localization in semiconductors coupled to electromagnetic cavities", Phys. Rev. B **109**, 045432 (2024) (cit. on p. 7).

[56] G. E. Topp, C. J. Eckhardt, D. M. Kennes, M. A. Sentef, and P. Törmä, "Light-matter coupling and quantum geometry in moiré materials", Phys. Rev. B **104**, 064306 (2021) (cit. on p. 7).

[57] M. A. Sentef, J. Li, F. Künzel, and M. Eckstein, "Quantum to classical crossover of floquet engineering in correlated quantum systems", Phys. Rev. Res. **2**, 033033 (2020) (cit. on p. 7).

[58] K. Lenk and M. Eckstein, "Collective excitations of the $U(1)$-symmetric exciton insulator in a cavity", Phys. Rev. B **102**, 205129 (2020) (cit. on p. 7).

[59] K. Lenk, J. Li, P. Werner, and M. Eckstein, *Collective theory for an interacting solid in a single-mode cavity*, 2022 (cit. on pp. 7, 24, 29, 37, 52, 73).

[60] P.-A. Pantazopoulos, J. Feist, A. Kamra, and F. J. García-Vidal, "Electrostatic nature of cavity-mediated interactions between low-energy matter excitations", Phys. Rev. B **109**, L201408 (2024) (cit. on pp. 7, 8).

[61] C. J. Sánchez Martínez, F. Lindel, F. J. García-Vidal, and J. Feist, "General theory of cavity-mediated interactions between low-energy matter excitations", J. Chem. Phys. **161**, 194303 (2024) (cit. on pp. 7, 8, 57).

[62] J. Román-Roche and D. Zueco, "Effective theory for matter in nonperturbative cavity QED", SciPost Phys. Lect. Notes, 50 (2022) (cit. on pp. 7, 25, 53, 181).

[63] J. Román-Roche, Á. Gómez-León, F. Luis, and D. Zueco, "Linear response theory for cavity qed materials at arbitrary light-matter coupling strengths", Phys. Rev. B **111**, 035156 (2025) (cit. on pp. 7, 25, 42, 53, 181).

[64] J. Román-Roche, Á. Gómez-León, F. Luis, and D. Zueco, "Bound polariton states in the dicke–ising model", Nanophotonics (2025) (cit. on pp. 7, 70, 181).

[65] Y. Ashida, A. ç. İmamo ğlu, and E. Demler, "Cavity quantum electrodynamics at arbitrary light-matter coupling strengths", Phys. Rev. Lett. **126**, 153603 (2021) (cit. on p. 7).

[66] S. M.-L. del Rincón, J. Román-Roche, A. Martín-Megino, D. Zueco, and M. J. Martínez-Pérez, *Mumax3-cqed: an extension of mumax3 to simulate magnon-photon interactions in cavity qed*, 2024 (cit. on pp. 7, 92, 167, 181).

[67] Y. Ashida, A. ç. İmamo ğlu, and E. Demler, "Cavity quantum electrodynamics with hyperbolic van der waals materials", Phys. Rev. Lett. **130**, 216901 (2023) (cit. on p. 7).

[68] V. Rokaj, M. Penz, M. A. Sentef, M. Ruggenthaler, and A. Rubio, "Quantum electrodynamical bloch theory with homogeneous magnetic fields", Phys. Rev. Lett. **123**, 047202 (2019) (cit. on p. 7).

[69] V. Rokaj, S. I. Mistakidis, and H. R. Sadeghpour, "Cavity induced collective behavior in the polaritonic ground state", SciPost Phys. **14**, 167 (2023) (cit. on p. 7).

[70] D. M. Welakuh, V. Rokaj, M. Ruggenthaler, and A. Rubio, "Nonperturbative mass renormalization effects in nonrelativistic quantum electrodynamics", Phys. Rev. Res. **7**, 013093 (2025) (cit. on pp. 7, 30).

[71] M. Ruggenthaler, J. Flick, C. Pellegrini, H. Appel, I. V. Tokatly, and A. Rubio, "Quantum-electrodynamical density-functional theory: bridging quantum optics and electronic-structure theory", Phys. Rev. A **90**, 012508 (2014) (cit. on p. 7).

[72] J. Flick, M. Ruggenthaler, H. Appel, and A. Rubio, "Kohn–sham approach to quantum electrodynamical density-functional theory: exact time-dependent effective potentials in real space", Proc. Natl. Acad. Sci. U.S.A **112**, 15285–15290 (2015) (cit. on p. 7).

[73] I.-T. Lu, M. Ruggenthaler, N. Tancogne-Dejean, S. Latini, M. Penz, and A. Rubio, "Electron-photon exchange-correlation approximation for quantum-electrodynamical density-functional theory", Phys. Rev. A **109**, 052823 (2024) (cit. on p. 7).

[74] G. M. Andolina, A. De Pasquale, F. M. D. Pellegrino, I. Torre, F. H. L. Koppens, and M. Polini, "Amperean superconductivity cannot be induced by deep subwavelength cavities in a two-dimensional material", Phys. Rev. B **109**, 104513 (2024) (cit. on p. 7).

[75] Z. Bacciconi, H. B. Xavier, I. Carusotto, T. Chanda, and M. Dalmonte, "Theory of fractional quantum hall liquids coupled to quantum light and emergent graviton-polaritons", Phys. Rev. X **15**, 021027 (2025) (cit. on p. 7).

[76] G. M. Andolina, F. M. D. Pellegrino, V. Giovannetti, A. H. MacDonald, and M. Polini, "Cavity quantum electrodynamics of strongly correlated electron systems: a no-go theorem for photon condensation", Phys. Rev. B **100**, 121109 (2019) (cit. on pp. 7, 22, 41, 48, 52, 54, 60).

[77] G. M. Andolina, F. M. D. Pellegrino, V. Giovannetti, A. H. MacDonald, and M. Polini, "Theory of photon condensation in a spatially varying electromagnetic field", Phys. Rev. B **102**, 125137 (2020) (cit. on pp. 7, 11, 22, 24, 54, 60).

[78] G. M. Andolina, F. M. D. Pellegrino, A. Mercurio, O. Di Stefano, M. Polini, and S. Savasta, "A non-perturbative no-go theorem for photon condensation in approximate models", Eur. Phys. J. Plus **137**, 1348 (2022) (cit. on pp. 7, 24, 54, 60).

[79] P. Nataf and C. Ciuti, "No-go theorem for superradiant quantum phase transitions in cavity QED and counter-example in circuit QED", Nat. Commun. **1**, 72 (2010) (cit. on p. 7).

[80] G. Mazza and A. Georges, "Superradiant quantum materials", Phys. Rev. Lett. **122**, 017401 (2019) (cit. on pp. 7, 24).

[81] A. Stokes and A. Nazir, "Uniqueness of the phase transition in many-dipole cavity quantum electrodynamical systems", Phys. Rev. Lett. **125**, 143603 (2020) (cit. on pp. 7, 54).

[82] D. M. Rouse, A. Stokes, and A. Nazir, "Theory of photon condensation in an arbitrary-gauge condensed matter cavity model", Phys. Rev. B **107**, 205128 (2023) (cit. on p. 7).

[83] Z. Bacciconi, G. M. Andolina, T. Chanda, G. Chiriacò, M. Schirò, and M. Dalmonte, "First-order photon condensation in magnetic cavities: A two-leg ladder model", SciPost Phys. **15**, 113 (2023) (cit. on pp. 7, 51).

[84] D. Lamberto, O. Di Stefano, S. Hughes, F. Nori, and S. Savasta, "Quantum phase transitions in many-dipole light-matter systems", Phys. Rev. Res. **7**, 013271 (2025) (cit. on pp. 7, 8).

[85] A. Mercurio, G. M. Andolina, F. M. D. Pellegrino, O. Di Stefano, P. Jarillo-Herrero, C. Felser, F. H. L. Koppens, S. Savasta, and M. Polini, "Photon condensation, van vleck paramagnetism, and chiral cavities", Phys. Rev. Res. **6**, 013303 (2024) (cit. on p. 7).

[86] E. Vlasiuk, V. K. Kozin, J. Klinovaja, D. Loss, I. V. Iorsh, and I. V. Tokatly, "Cavity-induced charge transfer in periodic systems: length-gauge formalism", Phys. Rev. B **108**, 085410 (2023) (cit. on pp. 7, 24, 87).

[87] M. K. Svendsen, M. Ruggenthaler, H. Hübener, C. Schäfer, M. Eckstein, A. Rubio, and S. Latini, *Theory of quantum light-matter interaction in cavities: extended systems and the long wavelength approximation*, 2023 (cit. on p. 7).

[88] J. Keeling, "Coulomb interactions, gauge invariance, and phase transitions of the dicke model", J. Phys. Condens. Matter **19**, 295213 (2007) (cit. on pp. 8, 54).

[89] V. Rokaj, D. M. Welakuh, M. Ruggenthaler, and A. Rubio, "Light–matter interaction in the long-wavelength limit: no ground-state without dipole self-energy", J. Phys. B: At. Mol. Opt. Phys. **51**, 034005 (2018) (cit. on p. 8).

[90] C. Schäfer, M. Ruggenthaler, V. Rokaj, and A. Rubio, "Relevance of the quadratic diamagnetic and self-polarization terms in cavity quantum electrodynamics", ACS Photonics **7**, 975–990 (2020) (cit. on pp. 8, 57).

[91] D. D. Bernardis, P. Pilar, T. Jaako, S. D. Liberato, and P. Rabl, "Breakdown of gauge invariance in ultrastrong-coupling cavity qed", Phys. Rev. A **98**, 053819 (2018) (cit. on p. 8).

[92] O. D. Stefano, A. Settineri, V. Macrì, L. Garziano, R. Stassi, S. Savasta, and F. Nori, "Resolution of gauge ambiguities in ultrastrong-coupling cavity quantum electrodynamics", Nat. Phys. **15**, 803–808 (2019) (cit. on p. 8).

[93] L. Garziano, A. Settineri, O. D. Stefano, S. Savasta, and F. Nori, "Gauge invariance of the dicke and hopfield models", Phys. Rev. A **102**, 023718 (2020) (cit. on p. 8).

[94] J. Li, D. Golez, G. Mazza, A. J. Millis, A. Georges, and M. Eckstein, "Electromagnetic coupling in tight-binding models for strongly correlated light and matter", Phys. Rev. B **101**, 205140 (2020) (cit. on p. 8).

[95] S. Savasta, O. Di Stefano, A. Settineri, D. Zueco, S. Hughes, and F. Nori, "Gauge principle and gauge invariance in two-level systems", Phys. Rev. A **103**, 053703 (2021) (cit. on p. 8).

[96] O. Dmytruk and M. Schiró, "Gauge fixing for strongly correlated electrons coupled to quantum light", Phys. Rev. B **103**, 075131 (2021) (cit. on pp. 8, 24).

[97] A. Settineri, O. Di Stefano, D. Zueco, S. Hughes, S. Savasta, and F. Nori, "Gauge freedom, quantum measurements, and time-dependent interactions in cavity qed", Phys. Rev. Res. **3**, 023079 (2021) (cit. on p. 8).

[98] A. Stokes and A. Nazir, "Implications of gauge freedom for nonrelativistic quantum electrodynamics", Rev. Mod. Phys. **94**, 045003 (2022) (cit. on pp. 8, 16, 54).

[99] A. Stokes, H. Riley, and A. Nazir, "The gauge-relativity of quantum light, matter, and information", Open Syst. Inf. Dyn. **30**, 2350016 (2023) (cit. on p. 8).

[100] R. Sáez-Blázquez, D. de Bernardis, J. Feist, and P. Rabl, "Can we observe nonperturbative vacuum shifts in cavity qed?", Phys. Rev. Lett. **131**, 013602 (2023) (cit. on p. 8).

[101] D. De Bernardis, T. Jaako, and P. Rabl, "Cavity quantum electrodynamics in the nonperturbative regime", Phys. Rev. A **97**, 043820 (2018) (cit. on p. 10).

[102] A. Vukics, T. Grießer, and P. Domokos, "Elimination of the A-square problem from cavity qed", Phys. Rev. Lett. **112**, 073601 (2014) (cit. on p. 10).

[103] K. Kakazu and Y. S. Kim, "Quantization of electromagnetic fields in cavities and spontaneous emission", Phys. Rev. A **50**, 1830–1839 (1994) (cit. on p. 10).

[104] D. A. Steck, *Quantum and atom optics*, 2007 (cit. on pp. 15, 56).

[105] K. Hepp and E. H. Lieb, "On the superradiant phase transition for molecules in a quantized radiation field: the dicke maser model", Ann. Phys **76**, 360–404 (1973) (cit. on pp. 17, 19).

[106] K. Rzażewski, K. Wódkiewicz, and W. Żakowicz, "Phase transitions, two-level atoms, and the A^2 term", Phys. Rev. Lett. **35**, 432–434 (1975) (cit. on pp. 17, 69).

[107] K. Rzażewski, K. Wódkiewicz, and W. Żakowicz, "Remark on the superradiant phase transition", Phys. Lett. A **58**, 211–212 (1976) (cit. on pp. 17, 69).

[108] F. T. Hioe, "Phase transitions in some generalized dicke models of superradiance", Phys. Rev. A **8**, 1440–1445 (1973) (cit. on pp. 18, 20).

[109] C. F. Lee and N. F. Johnson, "First-order superradiant phase transitions in a multiqubit cavity system", Phys. Rev. Lett. **93**, 083001 (2004) (cit. on pp. 18, 52, 82, 83).

[110] D. Kim, S. Dasgupta, X. Ma, J.-M. Park, H.-T. Wei, L. Luo, J. Doumani, X. Li, W. Yang, D. Cheng, R. H. J. Kim, H. O. Everitt, S. Kimura, H. Nojiri, J. Wang, S. Cao, M. Bamba, K. R. A. Hazzard, and J. Kono, *Observation of the magnonic dicke superradiant phase transition*, 2024 (cit. on p. 18).

[111] F. A. Berezin, "Convex operator functions", Math. USSR Sb. **17**, 269–277 (1972) (cit. on p. 19).

[112] E. H. Lieb, "The classical limit of quantum spin systems", Commun. Math. Phys **31**, 327–340 (1973) (cit. on pp. 19, 112, 177).

[113] G. Giuliani and G. Vignale, *Quantum theory of the electron liquid* (Cambridge University Press, Mar. 2005) (cit. on pp. 23, 58, 62).

[114] I. Amelio, L. Korosec, I. Carusotto, and G. Mazza, "Optical dressing of the electronic response of two-dimensional semiconductors in quantum and classical descriptions of cavity electrodynamics", Phys. Rev. B **104**, 235120 (2021) (cit. on p. 24).

[115] R. D. McKenzie, M. Libersky, D. M. Silevitch, and T. F. Rosenbaum, "Theory of magnon polaritons in quantum ising materials", Phys. Rev. A **106**, 043716 (2022) (cit. on pp. 24, 42, 74, 82).

[116] A. Altland and B. D. Simons, *Condensed matter field theory* (Cambridge University Press, Mar. 2010) (cit. on pp. 26, 41, 43, 140).

[117] R. Feynman and F. Vernon, "The theory of a general quantum system interacting with a linear dissipative system", Ann. Phys. (N. Y.) **24**, 118–173 (1963) (cit. on p. 28).

[118] H. Grabert, P. Schramm, and G.-L. Ingold, "Quantum brownian motion: the functional integral approach", Phys. Rep. **168**, 115–207 (1988) (cit. on pp. 28, 29).

[119] J. L. Alonso, A. Castro, P. Echenique, V. Polo, A. Rubio, and D. Zueco, "Ab initiomolecular dynamics on the electronic boltzmann equilibrium distribution", New J. Phys. **12**, 083064 (2010) (cit. on p. 28).

[120] M. Campisi, P. Talkner, and P. Hänggi, "Thermodynamics and fluctuation theorems for a strongly coupled open quantum system: an exactly solvable case", J. Phys. A: Math. Theor. **42**, 392002 (2009) (cit. on p. 29).

[121] M. Campisi, D. Zueco, and P. Talkner, "Thermodynamic anomalies in open quantum systems: strong coupling effects in the isotropic xy model", Chem. Phys. **375**, Stochastic processes in Physics and Chemistry (in honor of Peter Hänggi), 187–194 (2010) (cit. on p. 29).

[122] G.-L. Ingold, "Path integrals and their application to dissipative quantum systems", in *Coherent evolution in noisy environments* (Springer Berlin Heidelberg, 2002), pp. 1–53 (cit. on p. 29).

[123] P. Pilar, D. D. Bernardis, and P. Rabl, "Thermodynamics of ultrastrongly coupled light-matter systems", Quantum **4**, 335 (2020) (cit. on pp. 35, 38).

[124] Q.-H. Chen, Y.-Y. Zhang, T. Liu, and K.-L. Wang, "Numerically exact solution to the finite-size dicke model", Phys. Rev. A **78**, 051801 (2008) (cit. on p. 35).

[125] H. P. Breuer and F. Petruccione, *The theory of open quantum systems* (Oxford University Press, Oxford, 2002) (cit. on p. 37).

[126] G. L. Bir and G. E. Pikus, *Symmetry and strain-induced effects in semiconductors* (John Wiley and Sons, Nashville, TN, 1974) (cit. on p. 37).

[127] C. Cohen-Tannoudji, B. Diu, and F. Laloe, *Quantum mechanics, volume 2*, 2nd ed. (Wiley-VCH Verlag, Weinheim, Germany, June 2020) (cit. on pp. 37, 38).

[128] A. B. Klimov, L. L. Sánchez-Soto, A. Navarro, and E. C. Yustas, "Effective hamiltonians in quantum optics: a systematic approach", J. Mod. Opt. **49**, 2211–2226 (2002) (cit. on p. 37).

[129] M. Schuler, D. D. Bernardis, A. M. Läuchli, and P. Rabl, "The vacua of dipolar cavity quantum electrodynamics", SciPost Phys. **9**, 066 (2020) (cit. on p. 42).

[130] M. Libersky, R. D. McKenzie, D. M. Silevitch, P. C. E. Stamp, and T. F. Rosenbaum, "Direct observation of collective electronuclear modes about a quantum critical point", Phys. Rev. Lett. **127**, 207202 (2021) (cit. on pp. 42, 74).

[131] C. Gardiner and P. Zoller, *Quantum noise: a handbook of markovian and non-markovian quantum stochastic methods with applications to quantum optics*, Springer Series in Synergetics (Springer, 2004) (cit. on p. 48).

[132] E. del Valle, F. P. Laussy, and C. Tejedor, "Luminescence spectra of quantum dots in microcavities. ii. fermions", Phys. Rev. B **79**, 235326 (2009) (cit. on p. 48).

[133] F. Carollo and I. Lesanovsky, "Exactness of mean-field equations for open dicke models with an application to pattern retrieval dynamics", Phys. Rev. Lett. **126**, 230601 (2021) (cit. on pp. 48, 52, 94).

[134] P. Nataf, T. Champel, G. Blatter, and D. M. Basko, "Rashba cavity QED: a route towards the superradiant quantum phase transition", Phys. Rev. Lett. **123**, 207402 (2019) (cit. on p. 54).

[135] D. Guerci, P. Simon, and C. Mora, "Superradiant phase transition in electronic systems and emergent topological phases", Phys. Rev. Lett. **125**, 257604 (2020) (cit. on p. 54).

[136] A. Sommerfeld, "Zur elektronentheorie der metalle auf grund der fermischen statistik", Z. Phys. **47**, 1–32 (1928) (cit. on p. 60).

[137] "The theory of a fermi liquid", in *Collected papers of l.d. landau* (Elsevier, 1965), pp. 723–730 (cit. on p. 60).

[138] G. Giuliani and G. Vignale, *Quantum theory of the electron liquid* (Cambridge University Press, Cambridge, 2005) (cit. on p. 60).

[139] P. Hohenberg and W. Kohn, "Inhomogeneous electron gas", Phys. Rev. **136**, B864–B871 (1964) (cit. on p. 60).

[140] G. Onida, L. Reining, and A. Rubio, "Electronic excitations: density-functional versus many-body green's-function approaches", Rev. Mod. Phys. **74**, 601–659 (2002) (cit. on p. 60).

[141] H. Störmer, R. Dingle, A. Gossard, W. Wiegmann, and M. Sturge, "Two-dimensional electron gas at a semiconductor-semiconductor interface", Solid State Commun. **29**, 705–709 (1979) (cit. on p. 60).

[142] K. v. Klitzing, G. Dorda, and M. Pepper, "New method for high-accuracy determination of the fine-structure constant based on quantized hall resistance", Phys. Rev. Lett. **45**, 494–497 (1980) (cit. on p. 60).

[143] R. B. Laughlin, "Quantized hall conductivity in two dimensions", Phys. Rev. B **23**, 5632–5633 (1981) (cit. on p. 60).

[144] K. von Klitzing, "The quantized hall effect", Rev. Mod. Phys. **58**, 519–531 (1986) (cit. on pp. 60, 62).

[145] K. von Klitzing, T. Chakraborty, P. Kim, V. Madhavan, X. Dai, J. McIver, Y. Tokura, L. Savary, D. Smirnova, A. M. Rey, C. Felser, J. Gooth, and X. Qi, "40 years of the quantum hall effect", Nat. Rev. Phys. **2**, 397–401 (2020) (cit. on pp. 60, 62).

[146] R. Kubo, "Statistical-mechanical theory of irreversible processes. i. general theory and simple applications to magnetic and conduction problems", J. Phys. Soc. Jpn. **12**, 570–586 (1957) (cit. on p. 62).

[147] D. Tong, *Lectures on the quantum hall effect*, 2016 (cit. on p. 64).

[148] C. Emary and T. Brandes, "Chaos and the quantum phase transition in the dicke model", Phys. Rev. E **67**, 066203 (2003) (cit. on pp. 71, 73, 82, 157).

[149] E. Burzurí, F. Luis, B. Barbara, R. Ballou, E. Ressouche, O. Montero, J. Campo, and S. Maegawa, "Magnetic dipolar ordering and quantum phase transition in anFe8molecular magnet", Phys. Rev. Lett. **107**, 097203 (2011) (cit. on pp. 71, 74, 76, 77).

[150] T. Mori, "Equilibrium properties of quantum spin systems with nonadditive long-range interactions", Phys. Rev. E **86**, 021132 (2012) (cit. on pp. 71, 105, 106).

[151] R. Herrera Romero, M. A. Bastarrachea-Magnani, and R. Linares, "Critical phenomena in light–matter systems with collective matter interactions", Entropy **24**, 1198 (2022) (cit. on pp. 72, 79).

[152] R. Herrera Romero and M. A. Bastarrachea-Magnani, "Phase and amplitude modes in the anisotropic dicke model with matter interactions", Entropy **26**, 574 (2024) (cit. on pp. 72, 73, 79, 82, 157).

[153] M. Jenkins, T. Hümmer, M. J. Martínez-Pérez, J. García-Ripoll, D. Zueco, and F. Luis, "Coupling single-molecule magnets to quantum circuits", New J. Phys. **15**, 095007 (2013) (cit. on pp. 74, 169).

[154] M. Ruggenthaler, N. Tancogne-Dejean, J. Flick, H. Appel, and A. Rubio, "From a quantum-electrodynamical light–matter description to novel spectroscopies", Nat. Rev. Chem. **2**, 0118 (2018) (cit. on p. 74).

[155] Z.-L. Xiang, S. Ashhab, J. Q. You, and F. Nori, "Hybrid quantum circuits: superconducting circuits interacting with other quantum systems", Rev. Mod. Phys. **85**, 623–653 (2013) (cit. on p. 74).

[156] A. A. Clerk, K. W. Lehnert, P. Bertet, J. R. Petta, and Y. Nakamura, "Hybrid quantum systems with circuit quantum electrodynamics", Nat. Phys. **16**, 257–267 (2020) (cit. on p. 74).

[157] D. Gatteschi, R. Sessoli, and J. Villain, *Molecular nanomagnets*, Vol. 5 (Oxford University Press, New York, 2006) (cit. on p. 74).

[158] J. Bartolomé, F. Luis, and J. F. Fernández, *Molecular magnets: physics and applications* (Springer, Berlin, Heildelberg, 2016) (cit. on p. 74).

[159] L. Bogani and W. Wernsdorfer, "Molecular spintronics using single-molecule magnets", Nat. Mater. **7**, 179–186 (2008) (cit. on p. 74).

[160] E. Moreno-Pineda, C. Godfrin, F. Balestro, W. Wernsdorfer, and M. Ruben, "Molecular spin qudits for quantum algorithms", Chem. Soc. Rev. **47**, 501–513 (2018) (cit. on p. 74).

[161] A. Gaita-Ariño, F. Luis, S. Hill, and E. Coronado, "Molecular spins for quantum computation", Nat. Chem. **11**, 301–309 (2019) (cit. on p. 74).

[162] M. Atzori and R. Sessoli, "The second quantum revolution: role and challenges of molecular chemistry", J. Am. Chem. Soc **141**, 11339–11352 (2019) (cit. on p. 74).

[163] J. F. Fernández and J. J. Alonso, "Ordering of dipolar ising crystals", Phys. Rev. B **62**, 53 (2000) (cit. on p. 74).

[164] A. Morello, F. L. Mettes, F. Luis, J. F. Fernández, J. Krzystek, G. Aromí, G. Christou, and L. J. de Jongh, "Long-range ferromagnetic dipolar ordering of high-spin molecular clusters", Phys. Rev. Lett. **90**, 017206 (2003) (cit. on p. 74).

[165] F. Luis, J. Campo, J. Gómez, G. J. McIntyre, J. Luzón, and D. Ruiz-Molina, "Long-range ferromagnetism of mn12 acetate single-molecule magnets under a transverse magnetic field", Phys. Rev. Lett. **95**, 227202 (2005) (cit. on p. 74).

[166] B. Wen, P. Subedi, L. Bo, Y. Yeshurun, M. P. Sarachik, A. D. Kent, A. J. Millis, C. Lampropoulos, and G. Christou, "Realization of random-field ising ferromagnetism in a molecular magnet", Phys. Rev. B **82**, 014406 (2010) (cit. on p. 74).

[167] K. Weighardt, K. Pohl, I. Jibril, and G. Huttner, "Hydrolysis products of the monomeric amine complex ...", Angew. Chem. - Int. Ed. **23**, 77–78 (1984) (cit. on p. 77).

[168] M. Harder, L. Bai, C. Match, J. Sirker, and C. Hu, "Study of the cavity-magnon-polariton transmission line shape", Sci. China: Phys. Mech. Astron. **59**, 117511 (2016) (cit. on p. 78).

[169] S. Gammelmark and K. Mølmer, "Phase transitions and heisenberg limited metrology in an ising chain interacting with a single-mode cavity field", New J. Phys. **13**, 053035 (2011) (cit. on pp. 82–84).

[170] E. Cortese, L. Garziano, and S. De Liberato, "Polariton spectrum of the dicke-ising model", Phys. Rev. A **96**, 053861 (2017) (cit. on p. 82).

[171] J. Rohn, M. Hörmann, C. Genes, and K. P. Schmidt, "Ising model in a light-induced quantized transverse field", Phys. Rev. Res. **2**, 023131 (2020) (cit. on p. 82).

[172] A. Schellenberger and K. P. Schmidt, "(Almost) everything is a Dicke model - Mapping non-superradiant correlated light-matter systems to the exactly solvable Dicke model", SciPost Phys. Core **7**, 038 (2024) (cit. on p. 82).

[173] P. Pfeuty, "The one-dimensional ising model with a transverse field", Ann. Phys. (N. Y.) **57**, 79–90 (1970) (cit. on p. 83).

[174] S. Sachdev, *Quantum phase transitions* (Cambridge University Press, Apr. 2011) (cit. on pp. 84, 163).

[175] V. P. Bykov, "Spontaneous emission from a medium with a band spectrum", Sov. J. Quantum Electron. **4**, 861–871 (1975) (cit. on pp. 86, 87).

[176] S. John and J. Wang, "Quantum electrodynamics near a photonic band gap: photon bound states and dressed atoms", Phys. Rev. Lett. **64**, 2418–2421 (1990) (cit. on p. 87).

[177] B. Gaveau and L. S. Schulman, "Limited quantum decay", J. Phys. A Math. Gen. **28**, 7359–7374 (1995) (cit. on p. 87).

[178] T. Shi, Y.-H. Wu, A. González-Tudela, and J. I. Cirac, "Bound states in boson impurity models", Phys. Rev. X **6**, 021027 (2016) (cit. on p. 87).

[179] J. Román-Roche, E. Sánchez-Burillo, and D. Zueco, "Bound states in ultrastrong waveguide qed", Phys. Rev. A **102**, 023702 (2020) (cit. on p. 87).

[180] E. Cortese, I. Carusotto, R. Colombelli, and S. De Liberato, "Strong coupling of ionizing transitions", Optica **6**, 354 (2019) (cit. on p. 87).

[181] D. De Bernardis, M. Jeannin, J.-M. Manceau, R. Colombelli, A. Tredicucci, and I. Carusotto, "Magnetic-field-induced cavity protection for intersubband polaritons", Phys. Rev. B **106**, 224206 (2022) (cit. on p. 87).

[182] J. Leliaert and J. Mulkers, "Tomorrow's micromagnetic simulations", J. Appl. Phys. **125**, 180901 (2019) (cit. on p. 91).

[183] A. Vansteenkiste, J. Leliaert, M. Dvornik, M. Helsen, F. Garcia-Sanchez, and B. Van Waeyenberge, "The design and verification of mumax3", AIP Adv. **4**, 107133 (2014) (cit. on p. 92).

[184] C. A. González-Gutiérrez, D. García-Pons, D. Zueco, and M. J. Martínez-Pérez, "Scanning spin probe based on magnonic vortex quantum cavities", ACS Nano **18**, 4717–4725 (2024) (cit. on pp. 98, 101).

[185] M. Trif and Y. Tserkovnyak, *Cavity magnonics with domain walls in insulating ferromagnetic wires*, 2024 (cit. on pp. 98, 101).

[186] X.-F. Pan, P.-B. Li, X.-L. Hei, X. Zhang, M. Mochizuki, F.-L. Li, and F. Nori, "Magnon-skyrmion hybrid quantum systems: tailoring interactions via magnons", Phys. Rev. Lett. **132**, 193601 (2024) (cit. on pp. 98, 101).

[187] A. Bondarenko, M. Kounalakis, S. V. Kusminskiy, G. Bauer, and Y. M. Blanter, "Resonant magnetoelastic coupling between magnetic vortex and lattice breathing modes", in 2023 ieee international magnetic conference - short papers (intermag short papers), Vol. 2 (May 2023), pp. 1–2 (cit. on p. 98).

[188] C. Psaroudaki, E. Peraticos, and C. Panagopoulos, "Skyrmion qubits: challenges for future quantum computing applications", Appl. Phys. Lett. **123**, 260501 (2023) (cit. on pp. 98, 101).

[189] S. Sharma, V. S V Bittencourt, and S. Viola Kusminskiy, "Protocol for generating an arbitrary quantum state of the magnetization in cavity magnonics", J. Phys. Mat. **5**, 034006 (2022) (cit. on p. 98).

[190] S. Khan, O. Lee, T. Dion, C. W. Zollitsch, S. Seki, Y. Tokura, J. D. Breeze, and H. Kurebayashi, "Coupling microwave photons to topological spin textures in cu_2oseo_3", Phys. Rev. B **104**, l100402 (2021) (cit. on pp. 98, 101).

[191] L. Liensberger, F. X. Haslbeck, A. Bauer, H. Berger, R. Gross, H. Huebl, C. Pfleiderer, and M. Weiler, "Tunable cooperativity in coupled spin-cavity systems", Phys. Rev. B **104**, l100415 (2021) (cit. on pp. 98, 101).

[192] A. Hrabec, Z. Luo, L. J. Heyderman, and P. Gambardella, "Synthetic chiral magnets promoted by the dzyaloshinskii–moriya interaction", Appl. Phys. Lett. **117**, 130503 (2020) (cit. on p. 98).

[193] M. J. Martínez-Pérez and D. Zueco, "Quantum electrodynamics with magnetic textures", New J. Phys. **21**, 115002 (2019) (cit. on p. 98).

[194] A. Ghirri, C. Bonizzoni, M. Maksutoglu, A. Mercurio, O. Di Stefano, S. Savasta, and M. Affronte, "Ultrastrong magnon-photon coupling achieved by magnetic films in contact with superconducting resonators", Phys. Rev. Appl. **20**, 024039 (2023) (cit. on p. 98).

[195] B. T. McAllister, Y. Shen, G. Flower, S. R. Parker, and M. E. Tobar, "Higher order reentrant post modes in cylindrical cavities and related comments.", J. Appl. Phys. **122**, 144501 (2017) (cit. on p. 99).

[196] M. Goryachev, W. G. Farr, D. L. Creedon, Y. Fan, M. Kostylev, and M. E. Tobar, "High-cooperativity cavity qed with magnons at microwave frequencies", Phys. Rev. Appl. **2**, 054002 (2014) (cit. on pp. 99, 169).

[197] S. Martínez-Losa del Rincón, I. Gimeno, J. Pérez-Bailón, V. Rollano, F. Luis, D. Zueco, and M. J. Martínez-Pérez, "Measuring the magnon-photon coupling in shaped ferromagnets: tuning of the resonance frequency", Phys. Rev. Appl. **19**, 014002 (2023) (cit. on p. 99).

[198] M. J. Martínez-Pérez and D. Zueco, "Strong coupling of a single photon to a magnetic vortex", ACS Photonics **6**, 360–367 (2018) (cit. on pp. 99, 101).

[199] H. Yu, J. Xiao, and H. Schultheiss, "Magnetic texture based magnonics", Phys. Rep. **905**, 1–59 (2021) (cit. on p. 101).

[200] T. Shinjo, T. Okuno, R. Hassdorf, K. Shigeto, and T. Ono, "Magnetic vortex core observation in circular dots of permalloy", Science **289**, 930–932 (2000) (cit. on p. 101).

[201] A. Wachowiak, J. Wiebe, M. Bode, O. Pietzsch, M. Morgenstern, and R. Wiesendanger, "Direct observation of internal spin structure of magnetic vortex cores", Science **298**, 577–580 (2002) (cit. on p. 101).

[202] K. Y. Guslienko, X. F. Han, D. J. Keavney, R. Divan, and S. D. Bader, "Magnetic vortex core dynamics in cylindrical ferromagnetic dots", Phys. Rev. Lett. **96**, 067205 (2006) (cit. on p. 101).

[203] J. Román-Roche, V. Herráiz-López, and D. Zueco, "Exact solution for quantum strong long-range models via a generalized hubbard-stratonovich transformation", Phys. Rev. B **108**, 165130 (2023) (cit. on pp. 104, 181).

[204] V. Herráiz-López, S. Roca-Jerat, M. Gallego, R. Ferrández, J. Carrete, D. Zueco, and J. Román-Roche, "First- and second-order quantum phase transitions in the long-range unfrustrated antiferromagnetic ising chain", Phys. Rev. B **111**, 014425 (2025) (cit. on pp. 104, 123–126, 181).

[205] J. W. Britton, B. C. Sawyer, A. C. Keith, C.-C. J. Wang, J. K. Freericks, H. Uys, M. J. Biercuk, and J. J. Bollinger, "Engineered two-dimensional ising interactions in a trapped-ion quantum simulator with hundreds of spins", Nature **484**, 489–492 (2012) (cit. on p. 104).

[206] M. Knap, A. Kantian, T. Giamarchi, I. Bloch, M. D. Lukin, and E. Demler, "Probing real-space and time-resolved correlation functions with many-body ramsey interferometry", Phys. Rev. Lett. **111**, 147205 (2013) (cit. on p. 104).

[207] C. Monroe, W. C. Campbell, L. M. Duan, Z. X. Gong, A. V. Gorshkov, P. W. Hess, R. Islam, K. Kim, N. M. Linke, G. Pagano, P. Richerme, C. Senko, and N. Y. Yao, "Programmable quantum simulations of spin systems with trapped ions", Rev. Mod. Phys. **93**, 025001 (2021) (cit. on p. 104).

[208] A. Browaeys and T. Lahaye, "Many-body physics with individually controlled rydberg atoms", Nat. Phys. **16**, 132–142 (2020) (cit. on p. 104).

[209] D. Mukamel, "Statistical mechanics of systems with long range interactions", AIP Conf. Proc. **970**, 22–38 (2008) (cit. on pp. 104, 105).

[210] A. Campa, T. Dauxois, and S. Ruffo, "Statistical mechanics and dynamics of solvable models with long-range interactions", Phys. Rep. **480**, 57–159 (2009) (cit. on p. 104).

[211] S. Fey and K. P. Schmidt, "Critical behavior of quantum magnets with long-range interactions in the thermodynamic limit", Phys. Rev. B **94**, 075156 (2016) (cit. on p. 104).

[212] N. Defenu, T. Donner, T. Macrì, G. Pagano, S. Ruffo, and A. Trombettoni, "Long-range interacting quantum systems", Rev. Mod. Phys. **95**, 035002 (2023) (cit. on pp. 104, 105, 127).

[213] N. Defenu, A. Lerose, and S. Pappalardi, "Out-of-equilibrium dynamics of quantum many-body systems with long-range interactions", Phys. Rep. **1074**, 1–92 (2024) (cit. on p. 104).

[214] M. F. Maghrebi, Z.-X. Gong, and A. V. Gorshkov, "Continuous symmetry breaking in 1d long-range interacting quantum systems", Phys. Rev. Lett. **119**, 023001 (2017) (cit. on p. 104).

[215] T. Koffel, M. Lewenstein, and L. Tagliacozzo, "Entanglement entropy for the long-range ising chain in a transverse field", Phys. Rev. Lett. **109**, 267203 (2012) (cit. on p. 104).

[216] T. Kuwahara and K. Saito, "Area law of noncritical ground states in 1d long-range interacting systems", Nat. Commun. **11**, 4478 (2020) (cit. on p. 104).

[217] D. Vodola, L. Lepori, E. Ercolessi, A. V. Gorshkov, and G. Pupillo, "Kitaev chains with long-range pairing", Phys. Rev. Lett. **113**, 156402 (2014) (cit. on p. 104).

[218] F. Ares, J. G. Esteve, F. Falceto, and A. R. de Queiroz, "Entanglement entropy in the long-range kitaev chain", Phys. Rev. A **97**, 062301 (2018) (cit. on p. 104).

[219] S. B. Jäger, L. Dell'Anna, and G. Morigi, "Edge states of the long-range kitaev chain: an analytical study", Phys. Rev. B **102**, 035152 (2020) (cit. on p. 104).

[220] J. T. Schneider, J. Despres, S. J. Thomson, L. Tagliacozzo, and L. Sanchez-Palencia, "Spreading of correlations and entanglement in the long-range transverse ising chain", Phys. Rev. Res. **3**, L012022 (2021) (cit. on p. 104).

[221] O. Viyuela, D. Vodola, G. Pupillo, and M. A. Martin-Delgado, "Topological massive dirac edge modes and long-range superconducting hamiltonians", Phys. Rev. B **94**, 125121 (2016) (cit. on p. 104).

[222] Z.-X. Gong, M. F. Maghrebi, A. Hu, M. L. Wall, M. Foss-Feig, and A. V. Gorshkov, "Topological phases with long-range interactions", Phys. Rev. B **93**, 041102 (2016) (cit. on pp. 104, 108, 117).

[223] J. A. Koziol, A. Langheld, S. C. Kapfer, and K. P. Schmidt, "Quantum-critical properties of the long-range transverse-field ising model from quantum monte carlo simulations", Phys. Rev. B **103**, 245135 (2021) (cit. on pp. 105, 116).

[224] E. Gonzalez Lazo, M. Heyl, M. Dalmonte, and A. Angelone, "Finite-temperature critical behavior of long-range quantum ising models", SciPost Phys. **11**, 076 (2021) (cit. on pp. 105, 112, 116).

[225] A. Campa, A. Giansanti, and D. Moroni, "Canonical solution of a system of long-range interacting rotators on a lattice", Phys. Rev. E **62**, 303–306 (2000) (cit. on p. 105).

[226] T. Mori, "Instability of the mean-field states and generalization of phase separation in long-range interacting systems", Phys. Rev. E **84**, 031128 (2011) (cit. on p. 105).

[227] T. Mori, "Analysis of the exactness of mean-field theory in long-range interacting systems", Phys. Rev. E **82**, 060103(R) (2010) (cit. on p. 105).

[228] T. Mori, "Microcanonical analysis of exactness of the mean-field theory in long-range interacting systems", J. Stat. Phys. **147**, 1020–1040 (2012) (cit. on p. 105).

[229] A. Campa, A. Giansanti, and D. Moroni, "Canonical solution of classical magnetic models with long-range couplings", J. Phys. A Math. Gen. **36**, 6897 (2003) (cit. on pp. 106, 107).

[230] J. Simon, W. S. Bakr, R. Ma, M. E. Tai, P. M. Preiss, and M. Greiner, "Quantum simulation of antiferromagnetic spin chains in an optical lattice", Nature **472**, 307–312 (2011) (cit. on pp. 108, 120).

[231] M. P. Kaicher, D. Vodola, and S. B. Jäger, "Mean-field treatment of the long-range transverse field ising model with fermionic gaussian states", Phys. Rev. B **107**, 165144 (2023) (cit. on p. 108).

[232] E. Yusuf, A. Joshi, and K. Yang, "Spin waves in antiferromagnetic spin chains with long-range interactions", Phys. Rev. B **69**, 144412 (2004) (cit. on pp. 108, 117).

[233] N. Laflorencie, I. Affleck, and M. Berciu, "Critical phenomena and quantum phase transition in long range heisenberg antiferromagnetic chains", J. Stat. Mech.: Theory Exp. **2005**, P12001–P12001 (2005) (cit. on pp. 108, 117).

[234] K. S. D. Beach, *Valence bond description of the long-range, nonfrustrated heisenberg chain*, 2007 (cit. on pp. 108, 117).

[235] A. W. Sandvik, "Ground states of a frustrated quantum spin chain with long-range interactions", Phys. Rev. Lett. **104**, 137204 (2010) (cit. on pp. 108, 117).

[236] L. Yang and A. E. Feiguin, "From deconfined spinons to coherent magnons in an antiferromagnetic Heisenberg chain with long range interactions", SciPost Phys. **10**, 110 (2021) (cit. on pp. 108, 117).

[237] J. Ren, Z. Wang, W. Chen, and W.-L. You, "Long-range order and quantum criticality in antiferromagnetic chains with long-range staggered interactions", Phys. Rev. E **105**, 034128 (2022) (cit. on pp. 108, 117).

[238] P. Adelhardt and K. P. Schmidt, "Continuously varying critical exponents in long-range quantum spin ladders", SciPost Phys. **15**, 087 (2023) (cit. on pp. 108, 117).

[239] J. Zhao, N. Laflorencie, and Z. Y. Meng, "Unconventional scalings of quantum entropies in long-range heisenberg chains", Phys. Rev. Lett. **134**, 016707 (2025) (cit. on pp. 108, 117).

[240] P. Adelhardt, A. Duft, and K. P. Schmidt, *Quantum-critical and dynamical properties of the xxz bilayer with long-range interactions*, 2024 (cit. on pp. 108, 117).

[241] C. Kittel and P. McEuen, *Introduction to solid state physics* (John Wiley & Sons, New York, 2005) (cit. on p. 111).

[242] I. G. Brankov, V. A. Zagrebnov, and I. S. Tonchev, "Asymptotically exact solution of the generalized dicke model", Theor. Math. Phys. **22**, 13–20 (1975) (cit. on p. 112).

[243] R. Gibberd, "Equivalence of the dicke maser model and the ising model at equilibrium", Aust. J. Phys. **27**, 241 (1974) (cit. on p. 112).

[244] D. Vodola, L. Lepori, E. Ercolessi, and G. Pupillo, "Long-range ising and kitaev models: phases, correlations and edge modes", New J. Phys. **18**, 015001 (2015) (cit. on pp. 113, 116, 122).

[245] L. Vanderstraeten, M. VanDamme, H. P. Büchler, and F. Verstraete, "Quasiparticles in quantum spin chains with long-range interactions", Phys. Rev. Lett. **121**, 090603 (2018) (cit. on pp. 113, 122).

[246] G. Francica and L. Dell'Anna, "Correlations, long-range entanglement, and dynamics in long-range kitaev chains", Phys. Rev. B **106**, 155126 (2022) (cit. on pp. 113, 122).

[247] D. Sadhukhan and J. Dziarmaga, *Is there a correlation length in a model with long-range interactions?*, 2021 (cit. on p. 114).

[248] R. Kubo, M. Toda, and N. Hashitsume, *Statistical physics II* (Springer Berlin Heidelberg, Heidelberg, Germany, 1991) (cit. on p. 114).

[249] F. Schwabl, *Statistical mechanics* (Springer Berlin Heidelberg, Heidelberg, Germany, 2006) (cit. on p. 114).

[250] F. Cartarius, G. Morigi, and A. Minguzzi, "Structural transitions of nearly second order in classical dipolar gases", Phys. Rev. A **90**, 053601 (2014) (cit. on p. 116).

[251] R. Landig, L. Hruby, N. Dogra, M. Landini, R. Mottl, T. Donner, and T. Esslinger, "Quantum phases from competing short-and long-range interactions in an optical lattice", Nature **532**, 476–479 (2016) (cit. on pp. 116, 128).

[252] B. Blaß, H. Rieger, G. ő. Roósz, and F. Iglói, "Quantum relaxation and metastability of lattice bosons with cavity-induced long-range interactions", Phys. Rev. Lett. **121**, 095301 (2018) (cit. on pp. 116, 128).

[253] F. Iglói, B. Blaß, G. ő. Roósz, and H. Rieger, "Quantum xx model with competing short- and long-range interactions: phases and phase transitions in and out of equilibrium", Phys. Rev. B **98**, 184415 (2018) (cit. on pp. 116, 128).

[254] G. Sun, "Fidelity susceptibility study of quantum long-range antiferromagnetic ising chain", Phys. Rev. A **96**, 043621 (2017) (cit. on p. 116).

[255] S. Roca-Jerat, M. Gallego, F. Luis, J. Carrete, and D. Zueco, "Transformer wave function for quantum long-range models", Phys. Rev. B **110**, 205147 (2024) (cit. on pp. 116, 123).

[256] Y. Kato and T. Misawa, "Quantum tricriticality in antiferromagnetic ising model with transverse field: a quantum monte carlo study", Phys. Rev. B **92**, 174419 (2015) (cit. on pp. 117, 128).

[257] A. A. Ovchinnikov, D. V. Dmitriev, V. Y. Krivnov, and V. O. Cheranovskii, "Antiferromagnetic ising chain in a mixed transverse and longitudinal magnetic field", Phys. Rev. B **68**, 214406 (2003) (cit. on p. 120).

[258] A. Bar and D. Mukamel, "Mixed order transition and condensation in an exactly soluble one dimensional spin model", J. Stat. Mech.: Theory Exp. **2014**, P11001 (2014) (cit. on p. 120).

[259] D. Mukamel, *Mixed order phase transitions*, 2023 (cit. on p. 120).

[260] P. Lajkó and F. Iglói, "Mixed-order transition in the antiferromagnetic quantum ising chain in a field", Phys. Rev. B **103**, 174404 (2021) (cit. on p. 120).

[261] M. E. Newman and G. T. Barkema, *Monte carlo methods in statistical physics* (Clarendon Press, 1999) (cit. on p. 123).

[262] A. Dosovitskiy, L. Beyer, A. Kolesnikov, D. Weissenborn, X. Zhai, T. Unterthiner, M. Dehghani, M. Minderer, G. Heigold, S. Gelly, J. Uszkoreit, and N. Houlsby, *An image is worth 16x16 words: transformers for image recognition at scale*, 2021 (cit. on p. 123).

[263] L. L. Viteritti, R. Rende, and F. Becca, "Transformer variational wave functions for frustrated quantum spin systems", Phys. Rev. Lett. **130**, 236401 (2023) (cit. on p. 123).

[264] L. L. Viteritti, R. Rende, A. Parola, S. Goldt, and F. Becca, "Transformer wave function for two dimensional frustrated magnets: emergence of a spin-liquid phase in the shastry-sutherland model", Phys. Rev. B **111**, 134411 (2025) (cit. on p. 123).

[265] J.-X. Hou, "From microcanonical ensemble to canonical ensemble: phase transitions of a spin chain with a long-range interaction", Eur. Phys. J. B **93**, 1–6 (2020) (cit. on p. 128).

[266] J. Barré, D. Mukamel, and S. Ruffo, "Inequivalence of ensembles in a system with long-range interactions", Phys. Rev. Lett. **87**, 030601 (2001) (cit. on p. 128).

[267] A. Russomanno, M. Fava, and M. Heyl, "Quantum chaos and ensemble inequivalence of quantum long-range ising chains", Phys. Rev. B **104**, 094309 (2021) (cit. on p. 129).

[268] N. Defenu, D. Mukamel, and S. Ruffo, "Ensemble inequivalence in long-range quantum systems", Phys. Rev. Lett. **133**, 050403 (2024) (cit. on p. 129).

[269] M. M. Khapaev, M. Y. Kupriyanov, E. Goldobin, and M. Siegel, "Current distribution simulation for superconducting multi-layered structures", Supercond. Sci. Technol. **16**, 24–27 (2002) (cit. on p. 169).

[270] A. A. Serga, A. V. Chumak, and B. Hillebrands, "Yig magnonics", J. Phys. D: Appl. Phys. **43**, 264002 (2010) (cit. on p. 170).